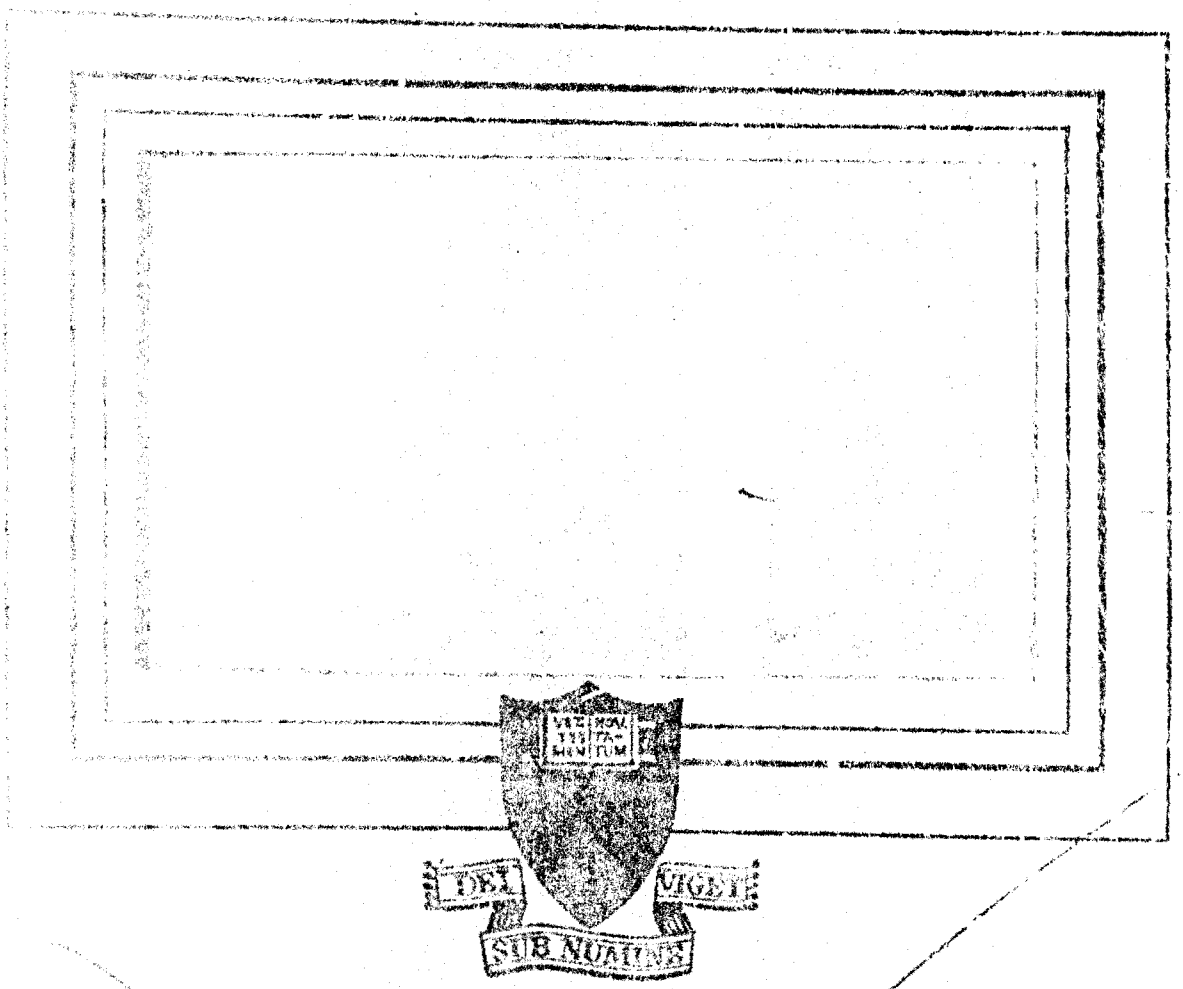

PRINCETON UNIVERSITY

DEPARTMENT OF AEROSPACE AND MECHANICAL SCIENCES

NATIONAL AERONAUTICS AND SPACE ADMINISTRATION
NASA Contract NASr-217

Portions of the Research Represent the
Final Report on NASA Grant NsG-99-60

602 151

NONLINEAR ASPECTS OF COMBUSTION INSTABILITY IN LIQUID PROPELLANT ROCKET MOTORS

Fourth Yearly Progress Report
For the Period 1 June 1963 to 31 May 1964

Report No. 553-d

Department of Aerospace and Mechanical Sciences

205 pp ~ $3.50

Prepared by: David T. Harrje
David T. Harrje
Research Aeronautical Engineer

William A. Sirignano
William A. Sirignano
Research Associate and Lecturer

with contributions from:

Donald H. Lee
Donald H. Lee
Senior Technical Staff Member

Warren C. Strahle
Warren C. Strahle
Research Associate

Ben T. Zinn
B. T. Zinn, - Ford Fellow

Charles E Mitchell
C. E. Mitchell, Assistant-in-Research

C. M. Gartner
E. M. Gartner, Assistant-in-Research

Dennis A. Gary
D. A. Gary, Assistant-in-Research

Approved by: Luigi Crocco D.T.H.
L. Crocco, Robert H. Goddard Professor of Jet Propulsion

1 June 1964
Guggenheim Laboratories for the Aerospace Propulsion Sciences
PRINCETON UNIVERSITY

TABLE OF CONTENTS

I. SUMMARY

The research in liquid rocket motor combustion instability at Princeton University consists of a number of closely interrelated approaches to the problem. The following summary covers the theoretical studies, the basic experimental investigations and the rocket motor parametric studies in the order in which they appear in this progress report.

Further calculations based on the time-lag model of longitudinal mode, nonlinear instability presented in Technical Report No. 677 have been performed. These calculations are presented in Section III-B and show that stability criteria vary with mean-flow Mach number and mode number. A third model, in addition to the two previously presented[6], has been developed (see Section III-C). This model considers both the presence of shock waves in the longitudinal mode and small time-lag or phase between pressure and energy addition at the concentrated combustion zone. Periodic solutions of finite amplitude are found only in operating regimes where the steady-state is unstable so that the "triggering" of an oscillation by a finite disturbance is not possible when the phase is small. This is consistent with the results of Technical Report No. 677, where "triggering" was found to be most probable for a critical phase range, and, based on the trend of numerical calculations, was impossible in the limit of phase going to zero.

In fact, all of the results of the three models of longitudinal mode nonlinear instability and the linear model are shown to be perfectly consistent. The wave forms vary considerably depending upon the various steady-state parameters. Singularly important, in this respect, are the effects of above-resonant versus below-resonant oscillations. (The off-resonant conditions are results of the time-lag).

The case of nonlinear transverse instability is being analyzed presently. An important part of this theoretical program

is the development of a nonlinear boundary condition at the nozzle entrance. This must be obtained by an analysis of the unsteady nozzle flow. This analysis has been carried out to second order and is reported in Section III-D. The nonlinear nozzle analysis is essentially an extension of the linear treatment of the unsteady nozzle flow, the numerical results of which will soon be available.[12]

Pulsed-limits testing to determine the threshold level for initiation of nonlinear transverse combustion instability continues to provide important data on trends in stability for the parameters involved. In Section IV-A LOX, alcohol rocket tests are reported using unbaffled injector designs which further substantiate the important role played by inter-spud spacing in reducing the tendency toward nonlinear instability, especially in the space engine range of 150 psia chamber pressure. Thrust per element[18] and spacing concepts are viewed as being closely related.

Elimination of propellant injection in certain locations along the injection circle were indicated to be effective stability-wise: if 1) the propellant injection gap was sufficiently large resulting in behavior similar to certain baffle effects, or 2) where the gap occurred often, resulting in effects similar to those experienced with spud orientation changes.[1] Higher pressure (300 psia) operation in each case increased the incidence of linear instability. The further increase of chamber pressures to 600 psia and above produced higher mode oscillations. This was found to be a very familiar stability pattern.

Testing with LOX, RP-1 indicated basically similar stability behavior to that experienced with LOX, alcohol. However, higher velocity LOX injection and lower velocity fuel injection tests with the 1 x 12 injector have provided increases in the instability regimes over the equal velocity injector design. Noticeable stability improvement has again been provided through use of the 6 x 2 injector design. Positional and directional effects noticed in the pulsing studies initiated relative mass and mixture ratio surveys of this

injector design. Marked changes in the deviations of relative mass and mixture ratio as well as positional and directional effects were shown to occur as the mixture ratio was altered.

Longitudinal stability testing on the square-motor which has included changes in the propellant used, injector element spacing, orifice diameters (and hence droplet size and relative velocity), numbers of elements, and spray fan interaction have shown certain important relationships as discussed in Section IV-B.

As injector orifice sizes have increased (with a decreased number of injection elements) the incidence of instability has been altered. Starting from a linearly stable design that was provided by the 6 x 6 injector, then moving to a range in which small pulses were required to trigger the instability (4 x 4 design), a distinct linearly unstable regime was finally reached for the largest (.120") diameter orifices. The 4 x 4 nonlinear instability regime was the largest.

RP-1 was also used with LOX in the later case showing similar stability behavior as the alcohol.

In this larger orifice injector case, pulsing has proven to be of only limited effectiveness in extending the stability regime.

Increasing the LOX orifice diameter while leaving the RP-1 orifices untouched produces more rapid combustion with peak c* reached at a shorter chamber length. Instability tendencies were increased via this change. Larger RP-1 orifice tests with the LOX unchanged produced slower burning conditions and eleminated lonti-tudinal mode instability for the chamber lengths tested (to 38½ inches).

The study of the displacement effect using freon shower-head injection into a "pseudo" rocket chamber (see Section IV-C) has yielded the following data:

1. Tangential mode oscillations of less than 50 psi peak-to-peak have resulted in important displacement effects.

2. Not only have large quantities of vapor been cyclically displaced but stream breakup has also been observed.

3. Pressure and velocity measurements substantiate the frequency and spinning mode character of the oscillations.

Another basic experiment probing the effects of oscillating pressure and velocity conditions on droplet distributions (Section IV-D) has indicated that:

1. The number of droplets present at a given axial and radial location in the resonating chamber changes between steady-state and oscillating conditions.

2. Relatively small amplitudes less than 20 psi peak-to-peak are capable of noticeably disturbing the droplet distributions.

3. The photographic techniques evolved allow droplet sizes down to 10 μ diameter to be measured. This direct photomicrography approach was found necessary when the light scattering technique was found incapable of supplying the required droplet characteristics as reported in Technical Report No. 648.

Prediction of the characteristic shape of the lower length limits of longitudinal combustion is found in Section V. This represents one application of theoretical study of droplet burning presented in Technical Report No. 671, together with further data based on a model of unsteady burning in the droplet wake. These predictions agree well with previous longitudinal experimental data indicating trends in the stability limit. Used in conjunction with the sensitive time-lag theory, this approach holds promise in allowing instability regimes to be predicted from calculated droplet sizes. Such correlation is being investigated.

The original time-lag theory of Crocco and Cheng assumed that the mean-flow Mach number in the chamber was small and its square was negligible. That assumption does not apply to present-day rocket chambers of low contraction ratio design. Therefore, that theory is being extended to include higher order Mach number effects. Preliminary results for the corrected stability limits in the case of concentrated combustion are presented in Section VI.

II. INTRODUCTION

This is the fourth in a series of yearly progress reports on the continuing investigation under NASA Contract NASr-217 (formerly NASA Grant NsG-99-60) into the general problem of combustion instability in liquid rocket motors. In these studies, the emphasis has been placed on the nonlinear aspects, both theoretical and experimental. The research involves: theoretical investigations of the unsteady combustion process and the mechanisms involved, rocket thrust chamber and nozzle acoustic characteristics and the interaction between these two important parameters; basic experiments to test the validity of proposed instability mechanisms and provide vital data for use in the theoretical models; and controlled testing of liquid rocket motors with parametric variations in order to isolate and explore the importance of the controlling factors that influence the incidence of nonlinear combustion instability.

In the study of nonlinear combustion instability (i.e., high frequency instability that requires an energy input for initiation which may be internally or externally supplied) it is important to remember that the linear mathematical approaches have often proven extremely helpful in the general understanding of the phenomena involved. In this report linear treatments will be used as well as purely nonlinear theoretical approaches to explore the nature of the instability mechanisms. A most important result of the nonlinear analyses is that "continuity" exists between linear theory and nonlinear theory if the feedback mechanism is a continuous function of the amplitude of the oscillation. This would be true for combustion processes such as vaporization, diffusion and chemical reaction, but would not apply to droplet shattering. These processes are classified as nonlinear processes under the proper amplification conditions.

In this research one of the prime efforts has been to closely relate the theoretical investigations to the basic experiments

and rocket motor parametric studies. To emphasize this aspect of equal importance, this report has been written with a somewhat different format than in the past, where the theoretical and basic experimental studies were separately covered in the Appendices.

As is the case in any status report, a considerable amount of the material covered is in the state of active investigation with only tentative conclusions or observations possible. Every effort has been made to include some mention of all the work in progress so that the report may prove of maximum benefit to those readers engrossed in similar research or confronted with development problems involving combustion instability.

Since the previous yearly progress report (June 1, 1963) a number of technical reports have been distributed, which cover certain aspects of the research in far greater detail than is possible in this report. They include the following, listed chronologically:

"An Optical Method for Observing Breakup and Vaporization of Liquid Jets," W. R. Seebaugh and D. H. Lee, Aeronautical Engineering Report No. 647, June 1963.

"A Theoretical Study of Droplet Burning: Transients and Periodic Solutions," W. C. Strahle, Aeronautical Engineering Report No. 671, December 1963.

"A Theoretical Study of Nonlinear Combustion Instability: Longitudinal Mode," W. A. Sirignano, Department of Aerospace and Mechanical Sciences Report No. 677, March 1964.

"Evaluation of a Light Scattering Technique For Determining the Spray Characteristics of Impinging Liquid Jets," H. R. Bredfeldt, Department of Aerospace and Mechanical Sciences Report No. 648, March 1964.

Current progress in each of these general subject areas is presented in this report together with many other aspects of the research in combustion instability.

In addition to the Princeton University technical reports, the following articles have appeared or have been accepted for publication during the past year.

"Analytical Investigation of Several Mechanisms of Combustion Instability," W. C. Strahle and L. Crocco, Bulletin of the Fifth Liquid Propulsion Symposium, 13-15 November 1963, Chemical Propulsion Information Agency.

"A Shock Wave Model of Unstable Rocket Combustors," W. A. Sirignano and L. Crocco, AIAA Preprint No. 64-143 Solid Propellant Rocket Conference, Palo Alto, California, January (accepted for AIAA Journal publication expected this summer).

"Velocity Effects in Transverse Mode Liquid Propellant Rocket Combustion Instability," F. H. Reardon, L. Crocco and D. T. Harrje (accepted for AIAA Journal publication).

"Problems in Liquid Propellant Instability," D. T. Harrje, Proceedings of the Fourth Meeting of the Technical Panel on Solid Propellant Combustion Instability, Applied Physics Laboratory TG 371-7, April 1964.

"Periodic Solutions to a Convective Droplet Burning Problem: The Stagnation Point," W. C. Strahle (Accepted by the International Combustion Symposium to be held in Great Britain, August 1964).

"Theoretical Studies on Liquid Propellant Rocket Instability," L. Crocco, (Invited paper for the International Combustion Symposium).

Additional background and history of the research on combustion instability at Princeton University may be found in References 1 through 5 and in previous technical reports which will be referenced at appropriate points in the text. Background information on the specific topic of nonlinear combustion instability may be found in References 1-3 and 6.

III. NONLINEAR THEORETICAL APPROACHES-LONGITUDINAL AND TRANSVERSE MODES

A. GENERAL

Theoretical studies of the nonlinear oscillations which commonly occur in rocket combustion chambers and exhaust nozzles have been performed at Princeton over the past few years. The concern has been with the "high-frequency" type of oscillations wherein energy is fed-back to the oscillation by the combustion process and the nozzle acts as a damping device. Shock wave dissipation, if present, provides another means of damping the oscillation.

Both the longitudinal and transverse modes have been analyzed. A shock wave model of the longitudinal mode with no time-lag effects was considered and found to have application to premixed gas rockets. Preliminary results were reported in Ref. 1, while final results are presented in Ref. 6 and 7. A second model of the longitudinal mode with time-lag effects but no shock waves has been investigated and the results were presented in Ref. 6. Further results of this second model are presented in Part B of this section. A third longitudinal-mode model has been analyzed and is presented in Part C of this section. This model considers the presence of shock waves and a small time-lag effect. Analyses of the transverse mode in annular chambers were presented in Ref. 2 and 3. The analysis of transverse oscillations with time-lag effects in a full circular chamber is presently being performed. A portion of that work is presented in Part D of this section.

Theoretical work on nonlinear combustion instability has also been performed by Priem and Guentert[8] and Chinitz, Burstein, and Agosta[9,10]. In their approaches to the problem, an initial disturbance was applied and the resulting flow behavior was determined. That is, it was determined (typically by numerical integration of the equations) whether the disturbance grew or decayed with time. Princeton's work has been different in that periodic solutions have been obtained, chiefly by analytical means.

In all three longitudinal models which were investigated, the assumptions of concentrated combustion zone at the injector end and

of short nozzle were made. The important distinguishing factor of the three models is the characteristic time of the combustion process as compared to the wave travel time in the chamber. The characteristic combustion time in the first model is negligible compared to the wave travel time while in the third model, the combustion time is small but not negligible compared to the wave travel time. Clearly, one may consider the first model as special case of the third in the limit as the combustion time goes to zero. The small combustion time implies that the phase between energy addition and pressure is small and goes to zero as the combustion time goes to zero. The second model involves a combustion time which is of the same order of magnitude as the wave travel time. This means that the phase between energy addition and pressure is of the order of the period of the oscillation.

Specifically, the characteristic combustion time in the second model is introduced by means of the Crocco time-lag postulate. The validity of this postulate has been experimentally demonstrated for linear oscillations but, as of this time, not for nonlinear oscillations. The combustion time in the third model is introduced by means of a convenient postulate which has no experimental support; the gas velocity at the time t at the combustion zone is assumed to be given as a power series in both the thermodynamic conditions at time t and the thermodynamic conditions at the time $t - \tau$. τ has a small value, and may be either positive (lag) or negative (lead). This postulate is made so that the effects of a small phase between energy addition and pressure upon the oscillation could be determined. For the purpose of determining these effects qualitatively, the exact functional form of the combustion zone energy feedback relation is not important provided that the phasing properties are contained in this relation. For this reason, it is believed that the use of this relation is justified.

With the first model, solutions were found which consisted of shock discontinuities followed by exponential decays in pressure and gas velocity as shown in Figure III--1. Nonlinear oscillations were only possible in the region of "linearly" unstable operation with the amplitude increasing with distance from the linear neutral stability

line. The amplitude went to zero at this neutral line implying that the nonlinear and linear results were in agreement. The results of the third model are qualitatively the same with respect to wave form, regions of instability, amplitude vs. distance from neutral line, and continuity between linear and nonlinear results.

With the second model, periodic solutions without shock waves were obtained. These finite-amplitude solutions could be either inside or outside of the linearly-unstable region. Figure III-2 represents a three-dimensional plot of time-lag (τ) vs. interaction index (n) vs. amplitude parameter (ϵ) for periodic oscillations. The amplitude parameter is seen to be proportional to the square root of the displacement from the neutral stability line in the τ, n plane. The periodic solutions without shock waves outside of the linearly unstable region (or in the linearly stable region) were found only at the lower values of the interaction index, n (approximately $n < 2.0$). Note that as n decreases the phase between energy addition and pressure decreases, and goes to zero, as n goes to its minimum value on the neutral stability line. This type of periodic solution was shown to be unstable indicating the possibility of "triggering" action for lower values of the phase. That is, a periodic disturbance with a greater amplitude parameter than some critical value ϵ for given values of τ and n would grow in amplitude resulting in a fully-established oscillation (presumably with shock waves) while a disturbance with smaller than the critical magnitude would decay to zero amplitude. (For details, see Ref. 6). The periodic solutions without shock waves and in the linearly-unstable region were found only at larger values of the interaction index (approximately $n > 2.0$). At these larger values of n, the phase between energy addition and pressure was larger. These were shown to be stable periodic solutions and their wave forms were meaningful and could be calculated. The numerical results for the fundamental mode were presented in Ref. 6 while the results for the harmonics are presented in Part B of this section.

The numerical calculations presented in Ref. 6 indicated that the amplitude of the disturbance necessary to trigger an oscillation

became infinite as phase went to zero. This meant "triggering" action is impossible in that limit which agrees with the results of the third model with small phase where finite amplitude oscillations were found only in regions which were linearly unstable and never in linearly stable regions.

Further agreement is obtained between the second and third models in that the mean pressure level under oscillation is found to be higher (lower) than the steady-state value if energy addition leads (lags) the pressure. Finally, in both models, the frequency is higher (lower)than the resonant value if energy addition leads(lags) pressure.

In the analysis of the transverse oscillations presently being undertaken, the approach is similar to that used by Maslen and Moore[11] in that a perturbation technique is employed and solutions without shock waves are sought.* However, the present problem is considerably more complicated in that the pressure of combustion and the effect of a nozzle are considered here whereas Maslen and Moore considered the case of no mean flow, no energy or mass addition, and a solid wall boundary condition.

The Crocco time-lag postulate is employed in order to represent the feedback of energy to the oscillation. In the initial attempt, the assumption of concentrated combustion zone at the injector end is being made as it was in the studies of the longitudinal oscillations. The short nozzle assumption used in the longitudinal work has no useful counterpart in the transverse case since, while it is reasonable to think of a chamber length much longer than a nozzle length, the chamber and nozzle diameters are of the same order of magnitude. For this reason, quasi-steady results cannot provide a proper boundary condition at the nozzle entrance and it is necessary to analyze the unsteady nozzle flow. Crocco[12] has done this for the linear case. Following similar lines, the work is being extended to the nonlinear case and that effort is reported in Part D of this Section.

---

* Experimental evidence indicates that, typically, shock waves do not occur in the transverse mode in a full chamber.

B. FURTHER CALCULATIONS BASED ON THE NONLINEAR LONGITUDINAL MODEL WITH TIME-LAG EFFECTS

Calculations based on the second nonlinear longitudinal model presented in Ref. 6 have been completed. This particular model considered the case of one-dimensional, unsteady flow in a combustion chamber. The assumptions of a concentrated combustion zone at the injector end and a short nozzle length were made. A phase between energy addition and pressure oscillation was introduced by employment of the Crocco time-lag postulate. In particular, periodic solutions without shock waves were sought. Two types of solutions were found: stable periodic solutions and unstable periodic solutions. The latter type indicates the possibility of "triggering" an oscillation by the application of a finite amplitude disturbance.

Only the numerical results for the fundamental mode with a mean flow Mach number equal to .2 were presented in that report. The results for other Mach numbers, .1 and .3, and for other modes, second and third harmonics, are presented in this report. Figure III-3* shows the results for the fundamental mode with Mach number $u_o = .2$. In Figure III-4 and III-5, the results for the cases of the fundamental mode with $u_o = .1, .3$, respectively, are shown. In Figures III-6 and III-7, the results for the cases of the second and third harmonics, respectively, with $u_o = .2$ are shown.

In the analysis of Ref. 6, the solution was found in the form of a perturbation series in an amplitude parameter ϵ. The solution was approximated to an accuracy of $O(\epsilon^3)$. To first order, the results of the nonlinear analysis were identical with the results of Crocco's linear analysis. To this lowest order, the wave form consisted of a single Fourier component with amplitude ϵ. This component could be either the fundamental or any of the overtones. The neutral stability line for zero-amplitude oscillations was identical to that found by

---

* The calculations, although arithmetical, were quite tedious and were performed with the aid of a 7090 computer. The results were plotted on a cathode ray oscillioscope and photographs of the screen were taken. These photographs are presented in the figures.

Crocco as shown in (a), (b), and (c) of Figures III-3 through III-7. In (a), the frequency in characteristic coordinates* is plotted versus the interaction index n along the neutral line. (b) shows a plot of $\omega\tau$ vs. n where ω is the frequency in time, space coordinates and τ is the sensitive time-lag. τ vs. n is plotted in (c).

It can be seen from (a) that there is a band of frequencies possible rather than discrete values. This is due to the time-lag which introduces another characteristic time besides the wave travel time. The natural frequency for the particular mode occurs at the minimum value of n for neutral oscillation. Both above and below-resonant frequencies are possible. The region inside the "parabola-like" curve is the instability region while the outside of the curve is the stability region. The figures show that the larger the Mach number the wider the instability regions. (b) is identical in all five figures indicating that the ratio of the time-lag to the period of oscillation $\frac{\omega\tau}{2\pi}$ is independent of the mode of oscillation and of Mach number**. τ vs. n for neutral oscillations is seen to be double-valued from (c). The minimum value of n corresponds to a resonant oscillation. The branch of the curve with high (H) values of τ corresponds to below-resonant oscillations while the branch with low (L) values of τ corresponds to above-resonant oscillations. The region of instability is inside the "parabola-like" curve. This region widens as Mach number increases. The instability region moves to lower values of τ as the mode of oscillation becomes higher in such a manner that $\omega\tau$ is unchanged.

There are two effects upon the wave form which appear to second order; the mean pressure level changes from the steady-state***

---

* It was convenient to analyze the wave phenomenon by transforming the equations of motion to a coordinate system formed by the characteristics of the hyperbolic system.

** Actually, if Mach number squared effects are considered, there is a slight dependence. See Section VI.

*** This implies a change in the mean thrust level from the steady-state value dependent upon the particular wave form present at the nozzle entrance. The significance of this change will be determined by further analysis.

value and a second harmonic is added with a phase with respect to the first. ("Second harmonic" means the second Fourier component. If the first Fourier component were the first overtone of the chamber, the second harmonic would be the third overtone.) The amplitude of this second harmonic for one of the Riemann invariants* is given by $\epsilon^2 A$ with the phase given by 2θ. A vs n is plotted in (d) of Figures III-3 through III-7 and θ vs. n is plotted in (e). $\epsilon^2 C_r$ is the change in the mean value of the Riemann invariant and C_r is plotted in (f) of these figures. All three types of curves are seen to be double-valued with an above-resonant branch (L) and a below-resonant branch (H).

A and C_r are seen to tend towards infinity as the resonant point (minimum value of n) is approached. The mean values of A and C_r are higher** for the higher modes. Note that in the above-resonant case (L), the sign of A could be changed (i.e., made positive), if correspondingly, the phase 2θ was translated by the value π. In this way it would be easier to see that the effect of the addition of the second harmonic is not very different for above and below-resonant cases. As shown by (f), the mean pressure level is higher than steady-state for the above-resonant case and lower than steady-state for the below-resonant case. There is no simple pattern in the effect of Mach number upon A and θ, however, the absolute value of C_r decreases as Mach number increases.

The third order effect upon the wave form is that a third harmonic (third Fourier component) is added with a phase with respect to the first. The amplitude of this harmonic is $\epsilon^3 B$ and the phase is 3Δ. B vs. n is plotted in (g) of Figures III-3 through III-7 and Δ vs. n is plotted in (h).

(g) shows that B tends towards infinity as the resonant point is approached. The mean value of the absolute magnitude of B is seen

---

* The Riemann invariants are certain combinations of flow properties which are constant along a characteristic. The speed of sound perturbation at the injector end is directly proportional to the Riemann invariant. See Ref. 6.

** This means higher in absolute value.

to be higher for the higher modes while Δ remains essentially the same with changes in mode and Mach number. No simple pattern is seen in the behavior of B upon Mach number. Note that the amplitude factor B in the above-resonant case (L) may have its sign changed (made positive) if, correspondingly, Δ was translated by $\pi/3$. After this change the phase would be smaller over a wider range of n in both above and below-resonant cases.

On the basis of the calculations above, one may calculate the approximate value of γ and n where an oscillation of a given amplitude occurs. For values of γ and n along the neutral line of (c), the amplitude is zero. The amplitude parameter ϵ increases with the square root of the normal displacement from the neutral line as schematically shown in Figure III-2. Specifically, at a displacement of $D\epsilon^2$ from the neutral line, the amplitude of the first Fourier component for neutral finite-amplitude oscillation is ϵ. D vs. n is plotted in (i) of Figures III-3 through III-7. D may be positive, indicating outward* displacement, or negative, indicating inward displacement. It was shown in Ref. 6 that $D > 0$ corresponds to unstable periodic solutions and $D < 0$ implies stable periodic solutions. (i) shows that $D < 0$ occurs only at n values greater than 2.0. According to the experimental results of Ref. 6, $n < 2$ is the range of physical interest so the theory predicts that stable periodic solutions without shock waves are not likely to occur in practical situations. This conclusion agrees with experimental findings since shocks are usually observed to be present in the wave form of rockets unstable in the longitudinal mode. The fact that unstable periodic solutions are found in the range of n-values of practical interest indicates that "triggering" action is possible there. This agrees at least qualitatively with experimental findings. (See Section IV-B). The values of D become more positive as the mode becomes higher implying that the triggering of an overtone mode requires a lower amplitude disturbance than the triggering a fundamental mode. The lowest Fourier

* "Outward displacement" means into the region of linear stability while "inward displacement" means into the region of linear instability.

component of the disturbance must be identical to the mode being triggered, however, so this does not imply an overtone is more likely to be triggered than the fundamental. There is again no clear pattern in the relationship between D and Mach number, indicating that extropolation from results for one value of Mach number to another value could be gravely in error. This points to the need of the work of Section VI, since the nonlinear parameters presented here depend upon τ and n values along the neutral lines which in turn depend upon the Mach number. Because of the sensitivity of these nonlinear parameters to Mach number, a more accurate analysis of the Mach number effects would be very useful.

The calculation of the wave forms would only be meaningful for stable periodic solutions which are seen to occur only outside of the range of practical interest. However, in case propellants with higher interaction indexes are developed or in order to compensate for possible error in the prediction of the D = 0 point due to approximations in the theory, the wave forms have been calculated and the predictions for n = 4.0 are presented in Figure III-8. The pressure vs. time wave forms were calculated for both injector and nozzle chamber locations, for both the fundamental and second harmonic modes, and for both above-resonant and below-resonant oscillations. The value of ϵ is .1 for the results of Figure III-8.

In (a) of that figure, we have above-resonant oscillation in the fundamental mode at the nozzle entrance. Three approximations are shown: P3 vs. T, which is a first order approximation, P4 vs. T2, the second order approximation, and P6 vs. T4, the third order approximation. The P's are the approximations to the pressure and the T's are the approximations to the time which appear by means of the characteristic coordinate transformation. These T corrections are related to the wave distortion and are larger than the P corrections. The second and third order approximations are essentially identical implying that the third order correction to the wave form is negligible. The important nonlinear effects are the sharpening of the positive pressure peak and the increase in the mean pressure level.*

* The steady-state pressure is 1.

In Figure III-8 (b), the same case of above-resonant, fundamental mode is plotted, except that now the location is the injector-end of the chamber. This wave form (b) is different from the wave form at the nozzle-end of the chamber (a) only in that the amplitude is lower due to the phase in reflection at the injector-end which does not occur at the nozzle-end. This similarity in wave form is expected due to the nature of the wave propagation.

Figure III-8 (c) shows the case of fundamental-mode oscillation at the nozzle-end. It differs from (a) in that the oscillation is now below-resonant causing a sharpening of the negative pressure peak and a decrease in the mean pressure level.

Figure III-8 (d) displays the results for the second-harmonic-mode, above-resonant oscillation at the nozzle end. The comparison with (a) shows that the positive peak is somewhat sharper and the mean pressure is higher with the overtone than with the fundamental. In the case of below-resonant oscillations, the negative peak would be sharper and the mean pressure lower with the overtone than with the fundamental.

For both modes, the peaks tend to sharpen and the deviation of the mean pressure from the steady-state value increases as n decreases.

C. A SHOCK WAVE MODEL OF UNSTABLE ROCKET COMBUSTORS WITH SMALL TIME-LAG EFFECTS

The case of longitudinal oscillations with shock waves in a rocket combustor is investigated in this section. The characteristic time of the combustion process is assumed to be small compared to the wave travel time. A time-lag or phase between pressure and energy addition introduces this characteristic time of the combustion process. The relation between this work and other nonlinear work performed at Princeton is given in Section III A.

The combustion zone length is considered negligibly small compared to the chamber length so that the limiting case of concentrated combustion at the injector-end is considered. The nature of the combustion process determines the boundary condition on the oscillation at this end. The perturbation in gas velocity is related to the perturbations in pressure and temperature. Typically, an increase in one or more of the thermodynamic variables causes an increase in the velocity of the burned gas emitted from the combustion zone since the burning rate increases. Other assumptions are:

1. The flow is one-dimensional.
2. The chamber cross-sectional area is constant.
3. The length of the convergent portion of the nozzle is negligibly small compared to the chamber length so that the limiting case of the short nozzle is considered.
4. A shock wave moves back and forth the length of the chamber with a constant period, reflecting alternately from the nozzle and the combustion ends. Here only one shock wave is considered, so only the fundamental mode is allowed.
5. Flow is homentropic outside of the combustion zone up to and including second order in the wave amplitude. This allows shock waves to occur but no entropy waves are allowed.

6. The chamber gas is calorically perfect.

Under these assumptions, the steady-state flow properties are constant throughout the chamber. All thermodynamic variables are nondimensionalized with respect to their steady-state values. The gas velocity is nondimensionalized with respect to the steady-state speed of sound, space dimension with respect to chamber length and time dimension with respect to chamber length divided by speed of sound.

The coordinate system is taken in such a manner that $x = 0$ at the nozzle entrance location and $x = 1$ at the combustion zone location. Note that this means that the steady-state velocity is negative in sign.

The pressure and temperature at the injector end may be related to the speed of sound by means of the laws of thermodynamics and an equation of state. Therefore, a relationship between the gas velocity perturbation and the speed of sound perturbation may, in principle, be found. Here, it is assumed that the time-lag effect appears in such a manner that this relationship may be written as follows:

$$\frac{u(t)-u_0}{u_0} = \omega \left[K_1 (a(t)-a_0) + K_2 (a(t-\tau)-a_0) \right] +$$

$$+ \delta \left[(a(t)-a_0)^2 + K_3 (a(t)-a_0)(a(t-\tau)-a_0) + K_4 (a(t-\tau)-a_0)^2 \right]$$

$$+ \text{ higher order terms}$$

where u is the gas velocity, a is the speed of sound, t is the time, τ is the time-lag, and ω, δ, k_1, k_2, k_3, and k_4 are positive parameters which describe the combustion process. Zero subscripts denote steady-state values. Note that the relationship has been written in the form of a Taylor series where the third and higher order terms are neglected.

With no loss of generality, we may consider $k_1 + k_2 = 1$. The time-lag is small and is considered as a first order perturbation quantity. This means that

$$a(t-\tau) - a(t) = \left[(a(t-\tau)-a_0) - (a(t)-a_0) \right]$$

must be a second order perturbation quantity since it is the difference between two first-order perturbation quantities whose arguments differ by a first order perturbation quantity. Now, the relationship which provides the boundary condition at the chamber end may be rewritten in the following manner:

$$\frac{u(t)-u_e}{u_e} = \omega\left(a(t)-a_e\right) + \omega K_2 \left[a(t-\tau)-a(t)\right] + \delta\left(a(t)-a_e\right)^2 + \text{higher order terms} \tag{1}$$

The well known compatibility relations may be obtained from the equations of unsteady one-dimensional motion for a fluid. Under our assumptions, the relations (accurate to second order) are:

$$\frac{2}{\gamma-1}\,da + du = 0 \quad \text{along} \quad dx = (u+a)\,dt$$

$$\frac{2}{\gamma-1}\,da - du = 0 \quad \text{along} \quad dx = (u-a)\,dt$$

Let primes imply perturbations so that

$$u = u_o + u' \quad ; \quad a = 1 + a'$$

Furthermore, let

$$\frac{\delta^+}{\delta t} \equiv \frac{\partial}{\partial t} + (u_o+1)\,\frac{\partial}{\partial x} \quad ; \quad \frac{\delta^-}{\delta t} \equiv \frac{\partial}{\partial t} + (u_o-1)\,\frac{\partial}{\partial x}$$

Then, these differential equations are rewritten as follows:

$$\frac{\delta^+}{\delta t}\left(\frac{2}{\gamma-1}a' + u'\right) = -(u'+a')\frac{\partial}{\partial x}\left(\frac{2}{\gamma-1}a' + u'\right) \tag{2a}$$

$$\frac{\delta^-}{\delta t}\left(\frac{2}{\gamma-1}a' - u'\right) = -(u'-a')\frac{\partial}{\partial x}\left(\frac{2}{\gamma-1}a' - u'\right) \tag{2b}$$

The left-hand sides of Equations (2a) and (2b) are of first order while the right-hand sides are of second order. Consider u_1 and a_1 as the first order approximations to u' and a', respectively. Furthermore, consider u_2 and a_2 as second order corrections so that $u_1 + u_2$ and $a_1 + a_2$ are second order approximations to u' and a'. Then, Equation (2a) yields

$$\frac{\delta^+}{\delta t}\left(\frac{2a_1}{\gamma-1} + u_1\right) = 0 \tag{3a}$$

$$\frac{\delta^+}{\delta t}\left(\frac{2a_2}{\gamma-1}+u_2\right)=-(u_1+a_1)\frac{\partial}{\partial x}\left(\frac{2}{\gamma-1}a_1+u_1\right) \tag{4a}$$

and Equation (2b) yields

$$\frac{\delta^-}{\delta t}\left(\frac{2}{\gamma-1}a_1-u_1\right)=0 \tag{3b}$$

$$\frac{\delta^-}{\delta t}\left(\frac{2a_2}{\gamma-1}-u_2\right)=-(u_1-a_1)\frac{\partial}{\partial x}\left(\frac{2}{\gamma-1}a_1-u_1\right) \tag{4b}$$

The general solutions to Equations (3a) and (3b) are found to be the following

$$\frac{2a_1}{\gamma-1}+u_1 = F\left(t-\frac{x}{1+u_0}\right) \tag{5a}$$

$$\frac{2a_1}{\gamma-1}-u_1 = G\left(t+\frac{x}{1-u_0}\right) \tag{5b}$$

where the functions F and G will be determined later from conditions imposed upon the solution. These relations (5a) and (5b) are used to substitute into the inhomogeneous parts of Equations (4a) and (4b).

The particular solutions to Equations (4a) and (4b) are found to be the following

$$\frac{2a_2}{\gamma-1}+u_2=\left(\frac{\gamma+1}{4}\right)\frac{x\,F\left(t-\frac{x}{1+u_0}\right)F_t\left(t-\frac{x}{1+u_0}\right)}{(1+u_0)^2}$$
$$-\left(\frac{3-\gamma}{8}\right)\left(\frac{1-u_0}{1+u_0}\right)F_t\left(t-\frac{x}{1+u_0}\right)\int_0^{t+\frac{x}{1-u_0}}G(\xi)\,d\xi \tag{6a}$$

$$\frac{2a_2}{\gamma-1}-u_2=-\left(\frac{\gamma+1}{4}\right)\frac{x\,G\left(t+\frac{x}{1-u_0}\right)G_t\left(t+\frac{1}{1-u_0}\right)}{(1-u_0)^2}$$
$$-\left(\frac{3-\gamma}{8}\right)\left(\frac{1+u_0}{1-u_0}\right)G_t\left(t+\frac{x}{1-u_0}\right)\int_0^{t-\frac{x}{1+u_0}}F(\xi)\,d\xi \tag{6b}$$

where the subscript t indicates differentiation with respect to time or, equivalently, in this case, differentiation with respect to the argument of the function. Note that the homogeneous solutions to (4a) and (4b) may be included in F and G, respectively, with an error of third order only in (6) which is negligible here. The integrals may be assigned zero as a lower limit since any constant of integration could be combined with F or G.

Equations (5) and (6) may be combined to yield the following

relations:

$$\frac{2a'}{\gamma-1} + u' = F\left(t - \frac{x}{1+u_o}\right) + \left(\frac{\gamma+1}{4}\right) \frac{x F\left(t - \frac{x}{1+u_o}\right) F_t\left(t - \frac{x}{1+u_o}\right)}{(1+u_o)^2}$$

$$- \left(\frac{3-\gamma}{\gamma}\right)\left(\frac{1-u_o}{1+u_o}\right) F_t\left(t - \frac{x}{1+u_o}\right) \int_o^{t + \frac{x}{1-u_o}} G(\xi)\, d\xi \qquad (7a)$$

$$\frac{2a'}{\gamma-1} - u' = G\left(t + \frac{x}{1-u_o}\right) - \left(\frac{\gamma+1}{4}\right) \frac{x G\left(t + \frac{x}{1-u_o}\right) G_t\left(t + \frac{x}{1-u_o}\right)}{(1-u_o)^2}$$

$$- \left(\frac{3-\gamma}{\gamma}\right)\left(\frac{1+u_o}{1-u_o}\right) G_t\left(t + \frac{x}{1-u_o}\right) \int_o^{t - \frac{x}{1+u_o}} F(\xi)\, d\xi \qquad (7b)$$

It is well known that the function $\frac{2}{\gamma-1} a + u$ is continuous to second-order accuracy through a shock discontinuity travelling in the negative x-direction and the function $\frac{2}{\gamma-1} a - u$ is also continuous to second order across a shock moving in the positive x-direction. (See Reference 12b). If the second-order terms in Equation (7a) are neglected, it is seen that the function F is continuous through a shock moving towards the nozzle entrance to at least first-order accuracy. The first-order approximation for F may be substituted into the nonlinear terms of Equation (7a). If F is continuous across the shock, so is F_t. Furthermore, even though G is discontinuous through this type of shock, its integral is continuous. Therefore, the nonlinear terms in Equation (7a) are continuous across this shock. Since $\frac{2a'}{\gamma-1} + u'$ is also continuous to second-order accuracy, this means that F is continuous to second-order accuracy across a shock moving in the negative x-direction. By a similar argument, Equation (7b) would show that G is continuous to second-order accuracy through a shock travelling in the positive x-direction.

Multivaluedness of the solution occurs due to the presence of the shock waves. This nonlinear effect is caused, for example, by the intersection of some of the lines $\left[t - \frac{x}{1+u_o} = \text{constant}\right]$ with a shock moving in the positive x-direction. $F\left(t - \frac{x}{1+u_o}\right)$ has different values depending upon from which side the shock is approached. This is solely a nonlinear effect because the deviation

of the shock path from a $[t - \frac{x}{1+u_o} = \text{constant}]$ line is a nonlinear effect. Of course, the same phenomenon occurs with $G\,(t + \frac{x}{1-u_o})$ near shock waves travelling in the negative x-direction. However, once the shock path is known, the correct value for each x,t point is easily discerned.

The short nozzle boundary condition is used to obtain a relationship between the functions F and G. The Mach number at the entrance of the nozzle $(x = 0)$ is set equal to a constant with time since the wave reflection is a quasi-steady phenomenon in the short nozzle case. Therefore,

$$u'(0,t) = u_o\, a'(0,t) \tag{8}$$

Equations (7a) and (7b) are solved for u' and a' in terms of F and G. Then, the results are substituted into Equation (8) to yield the following nonlinear relation between $F(t)$ and $G(t)$:

$$F(t) - G(t) + \frac{3-\gamma}{8}\left[\frac{1+u_o}{1-u_o}\, G_t(t)\int_0^t F(\xi)\,d\xi - \frac{1-u_o}{1+u_o}\, F_t(t)\int_0^t G(\xi)\,d\xi\right]$$
$$+ \nu\left[F(t)+G(t)\right] - \frac{3-\gamma}{8}\,\nu\left[\frac{1-u_o}{1+u_o}\, F_t(t)\int_0^t G(\xi)\,d\xi + \frac{1+u_o}{1-u_o}\, G_t(t)\int_0^t F(\xi)\,d\xi\right] = 0 \tag{9}$$

where the definition $\nu = -\frac{\gamma-1}{2}\,u_o$ has been made. (Note that ν is a positive number.)

If the nonlinear terms in Equation (9) are neglected, we have

$$(1+\nu)\,F(t) + (\nu-1)\,G(t) = 0$$

This means that the first order approximation to the relationship between F and G is:

$$F(t) = \frac{1-\nu}{1+\nu}\, G(t)$$

If this relation is used to substitute for $F(t)$ in the nonlinear terms of Equation (9), the error would be of third order which is negligible in this analysis. This permits the determination of F as a nonlinear function of G. The result follows:

$$F(t) = \frac{1-\nu}{1+\nu}\left\{G(t) + \frac{3-\gamma}{8}\left[\frac{1-u_o}{1+u_o} - \frac{1-\nu}{1+\nu}\,\frac{1+u_o}{1-u_o}\right] G_t(t)\int_0^t G(\xi)\,d\xi\right\} \tag{10}$$

Now, Equation (10) is employed to substitute for F(t) in Equation (7a) and (7b) with the results:

$$\frac{2a'}{\gamma-1} + u' = \frac{1-v}{1+v} G\left(t-\frac{x}{1+u_o}\right) + \frac{\gamma+1}{4}\left(\frac{1-v}{1+v}\right)^2 \frac{x G\left(t-\frac{x}{1+u_o}\right) G_t\left(t-\frac{x}{1+u_o}\right)}{(1+u_o)^2}$$
$$+ \frac{3-\gamma}{8} \frac{1-v}{1+v} G_t\left(t-\frac{x}{1+u_o}\right)\left\{\frac{1-u_o}{1+u_o}\int_{t+\frac{x}{1-u_o}}^{t-\frac{x}{1+u_o}} G(\xi)\,d\xi\right.$$
$$\left. - \frac{1-v}{1+v}\frac{1+u_o}{1-u_o}\int_o^{t-\frac{x}{1+u_o}} G(\xi)\,d\xi\right\} \qquad (11a)$$

$$\frac{2a'}{\gamma-1} - u' = G\left(t+\frac{x}{1-u_o}\right) - \frac{\gamma+1}{4}\frac{x G\left(t+\frac{x}{1-u_o}\right) G_t\left(t+\frac{x}{1-u_o}\right)}{(1-u_o)^2}$$
$$- \frac{3-\gamma}{8}\frac{1+u_o}{1-u_o}\frac{1-v}{1+v} G_t\left(t+\frac{x}{1-u_o}\right)\int_o^{t-\frac{x}{1-u_o}} G(\xi)\,d\xi \qquad (11b)$$

Another condition, on the function G appears from the combustion zone boundary condition (1). a' and u' at the combustion zone are given by setting x = 1 in Equations (11) and solving the simultaneous system. Noting that γ is a perturbation quantity, we find the following first order approximation from this procedure:

$$G\left(t+\frac{1}{1-u_o}\right) = \frac{1+\omega v}{1+v}\frac{1-v}{1-\omega v} G\left(t-\frac{1}{1+u_o}\right) \qquad (12)$$

It is readily seen from Equation (12) that if $\omega > 1$, $G\left(t+\frac{1}{1-u_o}\right) > G\left(t-\frac{1}{1+u_o}\right)$. In this case, a first order analysis shows an exponential growth of a small perturbation (unstable). If $\omega = 1$, then $G\left(t+\frac{1}{1-u_o}\right) = G\left(t-\frac{1}{1+u_o}\right)$ and the system is neutrally stable. In the case, $\omega < 1$, $G\left(t+\frac{1}{1-u_o}\right) < G\left(t-\frac{1}{1+u_o}\right)$ and a small perturbation decays exponentially (stable).

With no loss of accuracy, Equation (12) is used to substitute for $G\left(t+\frac{1}{1-u_o}\right)$ in the nonlinear terms which result when Equations (1) and (11) are combined. This operation yields the following:

$$G\left(t+\frac{1}{1-u_0}\right) = A\,G\left(t-\frac{1}{1+u_0}\right)$$

$$+\frac{\gamma+1}{4}\left[\frac{KA}{(1+u_0)^2}+\frac{A^2}{(1-u_0)^2}\right] G\left(t-\frac{1}{1+u_0}\right) G_t\left(t-\frac{1}{1+u_0}\right)$$

$$+\frac{3-\gamma}{\gamma} A \frac{1-u_0}{1+u_0} G_t\left(t-\frac{1}{1+u_0}\right) \int_{t+\frac{1}{1-u_0}}^{t-\frac{1}{1+u_0}} G(\xi)\,d\xi$$

$$+\delta v \frac{\gamma-1}{4} \frac{(K+A)^2}{1-\omega v} G^2\left(t-\frac{1}{1+u_0}\right)$$

$$+\omega v K_2 \frac{K+A}{1-\omega v}\left[G\left(t-\tau-\frac{1}{1+u_0}\right)-G\left(t-\frac{1}{1+u_0}\right)\right] \qquad (13)$$

where the definitions have been made

$$A \equiv \frac{1+\omega v}{1+v}\,\frac{1-v}{1-\omega v} \quad ; \quad K \equiv \frac{1-v}{1+v}$$

Now, we will seek periodic solutions for the flow properties. The period of the oscillation for the fundamental mode is the time required for a shock wave to travel once back and forth in the chamber. The shock follows the path ABC shown in Figure III-9. The flow properties in Region III are identical to those in Region I due to periodicity. The period is the time during which the shock travels the path ABC. This time is represented by $T = T_{ABC} = T_{AB} + T_{BC}$. If V is the shock velocity, we have

$$\int_0^{'} dx = \int_0^{T_{AB}} V_{AB}\,dt \quad ; \quad \int_{'}^{0} dx = \int_{T_{AB}}^{T_{AB}+T_{BC}} V_{BC}\,dt \qquad (14)$$

The shock velocities to first order accuracy are given by the well known relations (Reference 12b).

$$V_{AB} = u_0 + 1 + u'_{II} + a'_{II} + \frac{1}{2}\frac{\gamma+1}{\gamma-1}\left(a'_I - a'_{II}\right)$$

$$V_{BC} = u_0 - 1 + u'_{II} - a'_{II} + \frac{1}{2}\frac{\gamma+1}{\gamma-1}\left(a'_{II} - a'_I\right) \qquad (15)$$

In this representation, conditions at the shock AB have been set equal to conditions at the shock CD. The flow properties in (15)

are to be evaluated at the shock with the particular side of the shock given by the Roman numeral subscript. (See Figure III-9).

If Equations (5), (14), and (15) are combined, we may solve for T in an approximate manner. If T_o is the zero order approximation and $T_o + T_1$ is the first order approximation, we obtain (letting $t = 0$ at the point A of shock reflection in Figure III-9)

$$T_o = \frac{2}{1-u_o^2}$$

$$T_1 = \frac{3-\gamma}{8}\left[K\,\frac{1+u_o}{1-u_o} + \frac{1-u_o}{1+u_o}\right]\int_o^{\frac{2}{1-u_o^2}} G(\xi)\,d\xi -$$

$$- \frac{\gamma+1}{8}\left[\frac{K}{(1+u_o)^2} + \frac{1}{(1-u_o)^2}\right]\left[G(0) + G\left(\frac{2}{1-u_o^2}\right)\right] \qquad (16)$$

Since the flow properties are T-periodic, so is $\frac{2a'}{\gamma-1} - u'$, and, therefore, as shown by Equation (11b), G is T-periodic to first order. On the contrary, however, the periodic condition implies that to second order (as is shown by means of Equation (11b))

$$G\left(t + T + \frac{x}{1-u_o}\right) = G\left(t + \frac{x}{1-u_o}\right) +$$

$$+ \frac{3-\gamma}{8} K\,\frac{1+u_o}{1-u_o}\,G_t\left(t + \frac{x}{1-u_o}\right)\int_{t-\frac{x}{1+u_o}}^{t+T-\frac{x}{1+u_o}} G(\xi)\,d\xi$$

Introducing no greater error to the analysis, it is consistent to rewrite this as follows

$$G(\rho + T) = G(\rho) + \frac{3-\gamma}{8} K\,\frac{1+u_o}{1-u_o}\,G_\rho(\rho)\int_o^{\frac{2}{1-u_o^2}T} G(\xi)\,d\xi \qquad (17)$$

where ρ replaces the formal argument $[t + x/(1 \pm u_o)]$. Since to second order accuracy* $G(\rho + T_o) \approx G(\rho + T) + (T_o - T) \times G_\rho(\rho + T) \approx G(\rho + T) - T_1 G_\rho(\rho + T)$, Equation (16) and (17) yield

---

*For positive T_1, this expansion fails very close to the endpoint 0 of the range $0 < \rho < T$ due to the shock discontinuity. For negative T_1, failure occurs near T for the same reason. However, the approach is still correct since the relation gives the asymptotic behavior everywhere in the range as $T_1 \longrightarrow 0$.

$$G\left(\rho + \frac{2}{1-u_o^2}\right) = G(\rho) + \frac{3-\gamma}{8} K \frac{1+u_o}{1-u_o} G_\rho(\rho) \int_0^{\frac{2}{1-u_o^2}} G(\xi)\, d\xi$$

$$- T_1 \; G_\rho(\rho) \tag{18}$$

Setting ρ equal to the argument $[t - 1/(1 + u_o)]$ in Equation (13), that equation may be combined with (16) and (18) to yield the following

$$0 = (A-1) G(\rho) + \frac{\gamma+1}{4} \left[\frac{K}{(1+u_o)^2} + \frac{1}{(1-u_o)^2}\right] G_\rho(\rho) \left\{ G(\rho) - \right.$$

$$\left. - \frac{1}{2} \left[G(0) + G\left(\frac{2}{1-u_o^2}\right) \right] \right\} + \frac{\delta v (\gamma-1)}{(1-v)(1+v^2)} G^2(\rho) +$$

$$+ \frac{2\omega v K_2}{1-v^2} \left[G(\rho - \tau) - G(\rho) \right] \tag{19}$$

Note that (A-1) appears in the first term multiplied by a first order quantity. Since all the other terms in (19) are of second order, (A-1) must be of first order. Therefore, A may be replaced by unity and ωv by v in the nonlinear terms as has already been done in (19). This also means that G can only be determined to first order accuracy from the relationship since the second order correction now does not appear until third order. Furthermore, since G is T_o-periodic to first order accuracy, the integrals which appeared in the nonlinear terms canceled each other.

Since τ is small, the approximation* may be made by means of a Taylor expansion that

$$G(\rho - \tau) - G(\rho) = - \tau \, G_\rho(\rho)$$

and this may be substituted into (19) to obtain the following result

$$\frac{dG}{d\rho} = \frac{rG + \lambda G^2}{C - G} \tag{20}$$

where certain definitions have been made

*Note that near one of the endpoints (0 or T, depending on the sign of τ), this expansion is not correct for nonzero τ due to the discontinuity in $G(\rho)$; however, the correct asymptotic behavior as $\tau \longrightarrow 0$ is given even near these points.

$$r \equiv \frac{4}{\gamma+1} \frac{A-1}{\left[\frac{K}{(1+u_o)^2} + \frac{1}{(1-u_o)^2}\right]}$$

$$\lambda \equiv \frac{2}{\gamma+1} \frac{(-u_o \delta)}{(1-v)(1+v)^2} \frac{1}{\left[\frac{K}{(1+u_o)^2} + \frac{1}{(1-u_o)^2}\right]}$$

$$C \equiv \frac{1}{2}\left[G(0) + G\left(\frac{2}{1-u_o^2}\right)\right] + \tau\phi$$

$$\phi \equiv \frac{\delta}{\gamma+1} \frac{\omega v K_2}{1-v^2} \frac{1}{\left[\frac{K}{(1+u_o)^2} + \frac{1}{(1-u_o)^2}\right]}$$

As explained in References 6 and 7, Equation (20) has a physically reasonable solution only for $C = 0$. This also provides a condition on the solution which is used to determine the constant of integration. We now have

$$\frac{dG}{d\rho} = -r - \lambda G$$

with $$G(0) + G\left(\frac{2}{1-u_o^2}\right) + 2\tau\phi = 0$$

This has the solution

$$G(\rho) = \frac{r}{\lambda}\left[\frac{2}{1+e^{\frac{-2\lambda}{1-u_o^2}}} e^{-\lambda\rho} - 1\right] - \frac{2\tau\phi\, e^{-\lambda\rho}}{1+e^{\frac{-2\lambda}{1-u_o^2}}} \qquad (21)$$

which setting $\tau = 0$ can be shown to be identical to that References 6 and 7, in the case where no time-lag effect was considered. In the limit as $\lambda \to 0$ (or, in other words, $\delta \to 0$), (21) becomes a linear relation indicating a sawtooth waveform.

Equations (5), (10), and (21) may be combined to give a first order approximation to the wave form in Region I. If the isentropic condition is used to relate the pressure perturbation to the speed of sound perturbation, we obtain

$$p - p_o \approx \gamma \frac{r}{\lambda}\left\{\frac{1 - \frac{\lambda}{r}\tau\phi}{1+e^{\frac{-2\lambda}{1-u_o^2}}}\left[e^{-\frac{\lambda x}{1-u_o}} + Ke^{\frac{\lambda x}{1+u_o}}\right]e^{-\lambda t} - \frac{1}{1+v}\right\} \qquad (22a)$$

Similarly, Equations (5) and (21) may be combined to give the waveform in Region II if note is taken that to first order $G\left(t + \frac{x}{1-u_o}\right) = G\left(t - \frac{2}{1-u_o}2 + \frac{x}{1-u_o}\right)$. Again, using the isentropic relationship, we obtain the first order approximation

$$p - p_o \approx \gamma \frac{r}{\lambda} \left\{ \frac{1 - \frac{\lambda}{r} \tau \phi}{1 + e^{\frac{-2\lambda}{1-u_o}}} \left[e^{\frac{2\lambda}{1-u_o}} e^{\frac{-\lambda x}{1-u_o}} + K e^{\frac{\lambda x}{1-u_o}} \right] e^{-\lambda t} - \frac{1}{1+\nu} \right\} \quad (22b)$$

The waveform consists of a shock discontinuity followed by an exponential decay (ϕ is a small number so that $[1 - \lambda \tau \phi / r]$ is positive). As $\lambda \longrightarrow 0$, the waveform goes to a sawtooth. (21) and (5) can be shown to imply that the pressure jump across the shock is constant as the shock travels the length of the chamber. The strength does change in reflection, however, and is greater for the shock travelling in the negative x-direction than for the shock travelling in the positive x-direction.

When τ is positive, (1) shows that energy (or mass) addition lags pressure whereas with τ negative, energy addition leads pressure.* (22) shows a decrease in the mean pressure from the steady-state value when τ is positive and an increase in the mean pressure when τ is negative. This means that when energy addition leads (lags) pressure, the mean pressure is higher (lower) than the steady-state value. This is in qualitative agreement with the results of the second model of Reference 6 where a lead or lag was introduced by means of the Crocco time-lag postulate but no shock waves were present. However, in that case, the absence of the shock caused the "blowup" of the solution as phase went to zero. Note that the deviation of the mean pressure from the steady-state value is of the order of $\tau\phi$ where τ is a perturbation quantity of the order of the amplitude and $\phi = 0\,[\nu]$. Since ν is a very small number, this deviation is much smaller than the amplitude. In Reference 6, it was found to be a second order quantity.

*A small, negative τ or a small time-lead has the same physical effect as a time-lag with a value equal to the period of oscillation minus a small number.

It is seen from (22) that if r/λ were negative, expansion shocks would occur. From its definition r has the same sign as $[A-1]$, so if $\lambda > 0$ and $A < 1$ (or $\omega < 1$), no physically reasonable solution is found. This can be shown to be true even if λ were negative, by means of a topological investigation of the solutions to (20) (See Reference 6). This means that in the "linearly" stable region $\omega < 1$ (and τ small) there can be no oscillation which precludes "triggering" action as the phase between energy addition and pressure asymptotically goes to zero. This result is in agreement with one of the conclusions of Reference 6 where, based on the trend of the calculations, "triggering" seemed impossible in the limit as phase went to zero.

The period of the oscillation may be determined from (16) and (21) to be the following

$$T = \frac{2}{1-u_0^2} + \frac{3-\gamma}{4}\left[\frac{K}{(1-u_0)^2} + \frac{1}{(1+u_0)^2}\right]\frac{r}{\lambda}\left\{\frac{1-u_0^2}{\lambda}\,\frac{1-e^{-\frac{2\lambda}{1-u_0^2}}}{1+e^{-\frac{2\lambda}{1-u_0^2}}} - 1\right\}$$
$$+ \left\{\frac{\gamma+1}{4}\left[\frac{K}{(1+u_0)^2} + \frac{1}{(1-u_0)^2}\right] - \frac{3-\gamma}{4}\left[K\,\frac{1+u_0}{1-u_0} + \frac{1-u_0}{1+u_0}\right] + \frac{1-e^{-\frac{2\lambda}{1-u_0^2}}}{1+e^{-\frac{2\lambda}{1-u_0^2}}}\right\}\tau\phi \qquad (23)$$

The coefficient of τ in (23) can be shown to be positive and quite small in the range of interest. If τ were zero, (23) would give the nonlinear resonant frequency of the chamber with a mean flow present. The time-lag causes a modification of the frequency as shown by (23). In particular, if $\tau > 0$, the frequency is below-resonant; and, if $\tau < 0$, above-resonant. This means that, if energy addition leads (lags) pressure, the oscillation has an above (below)-resonant frequency, which agrees with both the linear results of Crocco[4] and the nonlinear results of Sirignano[6]. These frequency modifications are extremely small, however.

Some mention should be made of the mean mass-burning rate under oscillation. Since there is a deviation in the mean pressure and the mean velocity from their steady-state values, it indicates that the mean burning rate also deviates from its steady-state value. This is not possible for fixed-injection systems since the amount

burned must equal the amount injected. It can be demonstrated, however, that with the pressure (or density) deviation of the order of $\tau\phi$, the burning rate deviation is of the order of $u_o \tau\phi$. So, if u_o is small, the burning rate deviation from the injection rate is negligible compared to the pressure deviation. Furthermore, $u_o \tau\phi$ is always a very small number. Therefore, while this deviation produces a mathematical inconsistency, the numerical errors are quite negligible.

In summary, it can be said that the results of this analysis fit quite well into the "structure of understanding" together with the results of the other two models discussed in Reference 6. Namely, the impossibility of "triggering" action as phase goes to zero is shown, the mean-pressure is shown to be higher (lower) than the steady-state value and the frequency higher (lower) than the resonant frequency if the energy addition leads (lags) the pressure.

NOMENCLATURE

a	speed of sound
A	parameter defined after Equation (13)
c	parameter defined after Equation (20)
F,G	homogeneous solutions to partial differential Equations (2)
k	parameter defined after Equation (13)
k_1, k_2, k_3, k_4	combustion parameters
p	pressure
r	parameter defined after Equation (20)
t	time
T	period of oscillation
u	gas velocity
V	shock velocity
x	longitudinal dimension
γ	ratio of specific heats

δ	combustion parameter
λ	parameter defined after Equation (20)
ν	parameter defined after Equation (9)
ξ	dummy variable of integration
ρ	argument of function G
τ	time-lag
ϕ	parameter defined after Equation (20)
ω	combustion parameter

Subscripts:

o	zero order quantity
1,2	order of correction to solution

Superscript:

Primes:	perturbation quantity

D. TRANSVERSE NOZZLE ADMITTANCE RELATIONS FOR FINITE-AMPLITUDE WAVES

Introduction

There are several fundamental differences between acoustical oscillations in a closed cylindrical chamber and the oscillations that may be present in the combustion chamber of a rocket engine. In the latter case, the oscillations are superimposed on a mean flow created by the combustion process. While in acoustics the amplitudes of the oscillations are small, this may not be the case with the oscillations that may occur in a combustion chamber. In addition, the classical closed-end boundary condition used in the acoustic problem is now replaced by a boundary condition imposed by the presence of a converging-diverging nozzle. When the nozzle is in supercritical operation, the flow down-stream of the nozzle's throat is supersonic and no finite disturbance can travel in the upstream direction. This condition can be expressed by requiring that the solutions for the flow field in the nozzle be regular at its throat.* The regularity condition can be replaced by a complex relation between the pressure, entropy and velocity perturbations. This relation is expected to hold in any location along the converging portion of the nozzle. This relation for three-dimensional perturbations has been termed the transverse admittance relation. Evaluated at the nozzle entrance, it forms the proper boundary condition for the oscillatory flow in the combustion chamber.

The problem of supercritical flow with oscillations in a converging-diverging nozzle was first treated by Tsien[13] who considered the case in which the oscillation of the incoming flow is isothermal. The solution was found for both very low and very high frequencies. Crocco[14] extended this study to include the nonisothermal case and covered the entire frequency range. Both of these investigations were limited to one-dimensional, or longitudinal, oscillations. In a later

---

* No continuous disturbance can travel upstream from the nozzle throat unless the amplitude of the disturbance at the throat is infinite. Shock waves are not considered in the present analysis.

work[15] Crocco extends his one-dimensional analysis to the case of transverse oscillations where he considers the behavior of three-dimensional perturbations on the one-dimensional flow in a deLaval nozzle.

It is the purpose here to extend the above work which is limited to small perturbations, to the case where the perturbations about the one-dimensional mean flow have amplitudes of finite size. The transverse admittance relation resulting from the presence of three-dimensional perturbations about the one-dimensional steady mean flow will be derived. This expression will provide an appropriate boundary condition for the case when the flow oscillations in the combustion chamber have amplitudes of finite size. The latter can result from either the growth of the originally "small" disturbances or the "introduction" of disturbances of finite amplitudes. The admittance relations corresponding to isentropic or irrotational oscillations can be obtained as special cases of the general theory.

The work done in this paper is concerned with the flow in an axi-symmetric nozzle. It could, however, be extended to the special case of a two-dimensional nozzle. The latter case will not be treated here. The admittance relation which will be derived could be used as a boundary condition in the determination flow behavior in any propulsive device followed by a converging-diverging nozzle which is operating in the supercritical range.

Flow Equations

In this derivation, the flow in the converging part of an axi-symmetric nozzle is assumed to be adiabatic inviscid with no body forces and no chemical reaction. The fluid is assumed to be a perfect gas with constant specific heats. The conservation equations in dimensionless form are then as follows:

Conservation of mass

$$\frac{\partial \rho}{\partial t} + \nabla \cdot (\rho \underset{\rightarrow}{q}) = 0 \qquad (2.1)$$

Conservation of momentum

$$\frac{\partial \underset{\rightarrow}{q}}{\partial t} + \frac{1}{2} \nabla (q^2) + (\nabla \times \underset{\rightarrow}{q}) \times \underset{\rightarrow}{q} = - \frac{1}{\gamma \rho} \nabla P \qquad (2.2)$$

Since the fluid is assumed to be inviscid and non-heat conducting, the energy equation in its simplest form expresses the constancy of entropy of a fluid particle after it enters the nozzle.

$$\frac{\partial s}{\partial t} + \underset{\rightarrow}{q} \cdot \nabla s = 0 \tag{2.3}$$

where

$$s = \frac{s^*}{c_p} = \frac{1}{\gamma} \ln P - \ln \rho + \text{constant} \tag{2.4}$$

gives an expression for the nondimensional entropy. The equation of state for a perfect gas was used in the derivation of the last equation.

In the equations above, the reference quantities were chosen as the stagnation quantitives of the unperturbed gas entering the nozzle. The unperturbed flow in the nozzle is assumed to be isoenergetic, isentropic and irrotational. Consequently, its stagnation properties remain constant throughout the unperturbed flow and therefore are suitable reference quantities.

Hence we define:

$$\underset{\rightarrow}{q} = \frac{\underset{\rightarrow}{f^*}}{\bar{c}^{o*}} \; ; \quad P = \frac{p^*}{\rho^{o*}} \; ; \; \rho = \frac{\rho^*}{\bar{\rho}^{o*}} ; \; t^* = \frac{\bar{c}^{o*}}{L^*} t^* \tag{2.5}$$

where * denotes a dimensional quantity, o stagnation values and superposed bar unperturbed (steady) values. L* is a suitably defined characteristic length and is used in the non-dimensionalization of quantities having the dimension of length.

Linearization of the Equations

In analyzing the flow behavior of a supercritical nozzle in which the amplitudes of the unsteady perturbations about the steady-state mean flow are finite in size, it is convenient to assume that the dependent variables appearing in the problem can be written in the following form:

$$
\begin{aligned}
\underset{\rightarrow}{q} &= \underset{\rightarrow}{\bar{q}} + \underset{\rightarrow}{q}^{(1)}\epsilon + \underset{\rightarrow}{q}^{(2)}\epsilon^2 + \cdots \\
p &= \bar{p} + p^{(1)}\epsilon + p^{(2)}\epsilon^2 + \cdots \\
\rho &= \bar{\rho} + \rho^{(1)}\epsilon + \rho^{(2)}\epsilon^2 + \cdots \\
S &= \bar{S} + S^{(1)}\epsilon + S^{(2)}\epsilon^2 + \cdots
\end{aligned}
\tag{3.1}
$$

Where ϵ is some amplitude parameter and the variables written above are respectively the non-dimensional velocity, pressure, density and entropy.

The expressions appearing in (3.1) are substituted into equations (2.1) through (2.4) and the equations are separated according to different powers of ϵ. The zero order equations describing the mean flow conditions are:

$$
\begin{aligned}
&\nabla\cdot(\bar{\rho}\,\underset{\rightarrow}{\bar{q}}) = 0 \\
&\nabla\frac{\bar{q}^2}{2} + (\nabla\times\underset{\rightarrow}{\bar{q}})\times\underset{\rightarrow}{\bar{q}} = -\frac{1}{\gamma\bar{\rho}}\nabla\bar{p} \\
&\underset{\rightarrow}{\bar{q}}\cdot\nabla\bar{S} = 0 \\
&\bar{S} = \frac{1}{\gamma}\ln\bar{p} - \ln\bar{\rho} + \text{constant}
\end{aligned}
\tag{3.2}
$$

These equations can be replaced by simpler ones, obtained from (3.2) when the flow is irrotational:

$$
\nabla\cdot(\bar{\rho}\,\underset{\rightarrow}{\bar{q}}) = 0 \qquad \bar{p} = \bar{\rho}^{\gamma} \quad , \quad \frac{\bar{p}}{\bar{\rho}} = 1 - \frac{\gamma-1}{2}\bar{q}^2 \tag{3.3}
$$

Using the definition of the non dimensional sonic velocity

$$
C = \frac{C^*}{\bar{C}^{o*}} = \left\{\frac{p}{\bar{\rho}}\right\}^{\frac{1}{2}} \tag{3.4}
$$

together with (3.4) we get from (3.3):

$$
\bar{C}^2 = 1 - \frac{\gamma-1}{2}\bar{q}^2 = \bar{\rho}^{\gamma-1} \tag{3.5}
$$

which specifies the mean density variation.

When the nozzle is axi-symmetric the first of equations (3.3) can be used to define a stream function:

$$r\bar{\rho}\,\underset{\rightarrow}{\bar{q}} = \underset{\rightarrow}{e}_{\theta} \times \nabla\psi \tag{3.6}$$

where r is the nondimensional distance from the axis of symmetry and $\underset{\rightarrow}{e}_{\theta}$ the unit vector in the tangential direction.

Under the present assumption of irrotationality of the unperturbed flow, a potential function can also be defined as

$$\underset{\rightarrow}{\bar{q}} = \nabla\phi \tag{3.7}$$

The stream and potential functions introduced are nondimensional.

In the following the unperturbed flow will be assumed to be in the meridional plane.

The equations of order ϵ and their solutions are identical to those obtained by Crocco on his derivation of the transverse admittance relation for the case of small amplitude perturbations. For the sake of completeness, these equations are repeated here:

$$\frac{\partial\rho^{(1)}}{\partial t} + \nabla\cdot(\underset{\rightarrow}{\bar{q}}\,\rho^{(1)} + \underset{\rightarrow}{q}^{(1)}\bar{\rho}) = 0 \tag{3.8a}$$

$$\frac{\partial \underset{\rightarrow}{q}^{(1)}}{\partial t} + \nabla(\underset{\rightarrow}{\bar{q}}\cdot\underset{\rightarrow}{q}^{(1)}) + (\nabla\times\underset{\rightarrow}{q}^{(1)})\times\underset{\rightarrow}{\bar{q}} + \frac{\rho^{(1)}}{\bar{\rho}}\nabla(\tfrac{1}{2}\bar{q}^2) + \frac{1}{\gamma\bar{p}}\nabla p^{(1)} = 0 \tag{3.9a}$$

$$\frac{\partial s^{(1)}}{\partial t} + \underset{\rightarrow}{\bar{q}}\cdot\nabla s^{(1)} \tag{3.10a}$$

$$s^{(1)} - \frac{p^{(1)}}{\gamma\bar{p}} + \frac{\rho^{(1)}}{\bar{\rho}} = 0 \tag{3.11a}$$

The equations of order ϵ^2 are similar to those found by Crocco except for their inhomogeneous parts. They are written as follows:

$$\frac{\partial \rho^{(2)}}{\partial t} + \nabla \cdot \left(\bar{\rho}\, \underset{\rightarrow}{q}^{(2)} + \rho^{(2)} \underset{\rightarrow}{\bar{q}} \right) = - \nabla \cdot \left(\rho^{(1)} \underset{\rightarrow}{q}^{(1)} \right) \tag{3.8b}$$

$$\frac{\partial \underset{\rightarrow}{q}^{(2)}}{\partial t} + \nabla \left(\underset{\rightarrow}{\bar{q}} \cdot \underset{\rightarrow}{q}^{(2)} \right) + \left(\nabla \times \underset{\rightarrow}{q}^{(2)} \right) \times \underset{\rightarrow}{\bar{q}} + \frac{\rho^{(2)}}{\bar{\rho}} \frac{1}{2} \nabla \underset{\rightarrow}{\bar{q}}^{2} + \frac{1}{\gamma \bar{\rho}} \nabla p^{(2)}$$

$$= - \left\{ \frac{\rho^{(1)}}{\bar{\rho}} \frac{\partial \underset{\rightarrow}{q}^{(1)}}{\partial t} + \frac{\rho^{(1)}}{\bar{\rho}} \nabla \left(\underset{\rightarrow}{\bar{q}} \cdot \underset{\rightarrow}{\bar{q}}^{(1)} \right) + \frac{\rho^{(1)}}{\bar{\rho}} \left(\nabla \times \underset{\rightarrow}{q}^{(1)} \right) \times \underset{\rightarrow}{\bar{q}} + \frac{1}{2} \nabla \left(\underset{\rightarrow}{q}^{(1)} \cdot \underset{\rightarrow}{q}^{(1)} \right) + \left(\nabla \times \underset{\rightarrow}{q}^{(1)} \right) \times \underset{\rightarrow}{q}^{(1)} \right\} \tag{3.9b}$$

$$\frac{\partial s^{(2)}}{\partial t} + \underset{\rightarrow}{\bar{q}} \cdot \nabla s^{(2)} = - \underset{\rightarrow}{q}^{(1)} \cdot \nabla s^{(1)} \tag{3.10b}$$

$$s^{(2)} - \frac{\rho^{(2)}}{\gamma \bar{\rho}} + \frac{\rho^{(2)}}{\bar{\rho}} = - \frac{1}{2} \left[\frac{1}{\gamma} \left(\frac{\rho^{(1)}}{\bar{\rho}} \right)^{2} - \left(\frac{\rho^{(1)}}{\bar{\rho}} \right)^{2} \right] \tag{3.11b}$$

A comparison between the systems of equations corresponding to $O(\epsilon)$ and $O(\epsilon^2)$ shows that their homogeneous parts are identical.

The solution of the second-order system of equations, along lines paralleling the solution of the first-order system of equations will be found. Before this is done an appropriate set of independent coordinates will be chosen.

Choice of the Independent Variables

Abandoning the vectorial representation, it is useful to choose the independent variables in a way appropriate to the introduction of the boundary conditions at the nozzle walls. In the axi-symmetric case, following Crocco, it is convenient to let the steady-state potential function ϕ replace the axial variable, and the steady-state stream function replace the radial variable. Indicating by δs and δn elementary (non-

dimensional) lengths in the direction of the unperturbed stream lines and of their normals on the meridional plane, see Figure III-10, equations (3.6) and (3.7) can then be written as follows:

$$\bar{q} = \frac{\partial \phi}{\partial s} \qquad r \bar{\rho} \bar{q} = \frac{\partial \psi}{\partial n} \tag{4.1}$$

The third independent variable, θ, indicates the variation in the tangential direction.

Separation of the Variables

In order to be able to solve equations (3.8b) through (3.11b) the following assumptions are made:

(i) The unperturbed flow is one-dimensional and the corresponding variables describing it depend only on ϕ.

(ii) Assumption (i) also implies that the angle of obliquity of the stream lines with respect to the axis of symmetry is sufficiently small so that its cosine is practically 1 and the element of normal δn along the surface ϕ = constant can be identified with dr. Hence equation (4.1) can be integrated, providing

$$\psi = \bar{\rho}(\phi)\, \bar{q}(\phi)\, \frac{r^2}{2} \tag{5.1}$$

(iii) The solution will be restricted to the case where the axial component of vorticity is zero. This assumption is necessary in order to achieve separation of variables in the continuity equation. This assumption is equivalent to saying that $V^{(s)}_{(n\nu_q)}(\phi)$ and $W^{(s)}_{(n\nu_q)}(\phi)$, defined in Equation (5.8), are equal to one another. This assumption will be further elaborated on other parts of this report.

Rewriting equations (3.8b) through (3.11b) in a (ϕ, ψ, θ) coordinate system and separating the momentum equation (3.9b) into its three components results in the following system of equations:

continuity:

$$\frac{\partial}{\partial t}\left(\frac{\rho^{(2)}}{\bar{\rho}}\right)+\bar{g}^{2}\frac{\partial}{\partial\phi}\left(\frac{u^{(2)}}{\bar{g}}\right)+2\bar{\rho}\bar{g}\frac{\partial}{\partial\psi}\left(\psi\left(\frac{v^{(2)}}{r\bar{\rho}\bar{g}}\right)\right)$$

$$+\left(\frac{\bar{\rho}\bar{g}}{2}\right)\frac{\partial}{\partial\theta}\left(\frac{r\omega^{(2)}}{\psi}\right)+\bar{g}^{2}\frac{\partial}{\partial\phi}\left(\frac{\rho^{(2)}}{\bar{\rho}}\right)=$$

$$-\left\{\bar{g}^{2}\frac{\partial}{\partial\phi}\left(\frac{\rho^{(1)}}{\bar{\rho}}\frac{u^{(1)}}{\bar{g}}\right)+2\bar{\rho}\bar{g}\frac{\partial}{\partial\psi}\left(\psi\frac{\rho^{(1)}}{\bar{\rho}}\frac{v^{(1)}}{r\bar{\rho}\bar{g}}\right)\right.$$

$$\left.+\frac{\bar{\rho}\bar{g}}{2\psi}\frac{\partial}{\partial\theta}\left(\frac{\rho^{(1)}}{\bar{\rho}}r\omega^{(1)}\right)\right\}$$

(5.2)

Φ- momentum:

$$\frac{\partial}{\partial t}\left(\frac{u^{(2)}}{\bar{g}}\right)+\frac{\partial}{\partial\phi}\left(\bar{g}^{2}\frac{u^{(2)}}{\bar{g}}\right)+\frac{\partial}{\partial\phi}\left(\frac{p^{(2)}}{\gamma\bar{\rho}}\right)-\frac{1}{2}S^{(2)}\frac{d\bar{g}^{2}}{d\phi}$$

$$=\frac{1}{4\bar{c}^{2}}\frac{d\bar{g}^{2}}{d\phi}\left[\frac{\gamma}{\bar{c}^{2}}\left(\frac{p^{(1)}}{\gamma\bar{\rho}}\right)^{2}-\bar{c}^{2}\left(\frac{\rho^{(1)}}{\bar{\rho}}\right)^{2}\right]-\left\{\frac{1}{2}\bar{g}^{2}\frac{\partial}{\partial\phi}\left(\frac{u^{(1)}}{\bar{g}}\right)^{2}+\frac{1}{2}\left(\frac{u^{(1)}}{\bar{g}}\right)^{2}\frac{d\bar{g}^{2}}{d\phi}\right.$$

$$+\frac{\partial}{\partial\phi}\left(\psi\bar{\rho}\bar{g}\left(\frac{v^{(1)}}{r\bar{\rho}\bar{g}}\right)^{2}\right)+\frac{1}{4\psi}\frac{\partial}{\partial\phi}\left(\bar{\rho}\bar{g}(r\omega^{(1)})^{2}\right)+\left(\frac{\rho^{(1)}}{\bar{\rho}}\right)^{2}\frac{\partial}{\partial\phi}\left(\bar{g}^{2}\frac{u^{(1)}}{\bar{g}}\right)$$

$$+\bar{\rho}\bar{g}\frac{1}{2}\left[(r\omega^{(1)})\frac{1}{\psi}\left(\frac{\partial}{\partial\theta}\left(\frac{u^{(1)}}{\bar{g}}\right)-\frac{\partial}{\partial\phi}(r\omega^{(1)})\right)-\right.$$

$$\left.\left.\left(\frac{v^{(1)}}{\bar{\rho}\bar{g}r}\right)4\psi\left(\frac{\partial}{\partial\phi}\left(\frac{v^{(1)}}{\bar{\rho}\bar{g}r}\right)-\frac{\partial}{\partial\psi}\left(\frac{u^{(1)}}{\bar{g}}\right)\right)\right]+\left(\frac{\rho^{(1)}}{\bar{\rho}}\right)\frac{\partial}{\partial t}\left(\frac{u^{(1)}}{\bar{g}}\right)\right\}$$

(5.3)

Ψ - momentum:

$$\frac{\partial}{\partial t}\left(\frac{V^{(1)}}{\bar{\rho}\bar{g}r}\right)+\bar{g}^{-2}\frac{\partial}{\partial\phi}\left(\frac{V^{(2)}}{\bar{\rho}\bar{g}r}\right)+\frac{\partial}{\partial\psi}\left(\frac{p^{(2)}}{r\bar{\rho}}\right)=-\left\{\bar{\rho}\bar{g}\ \frac{\partial}{\partial\psi}\left[\psi\left(\frac{V^{(1)}}{\bar{\rho}\bar{g}r}\right)^2\right]\right.$$

$$+\frac{1}{4}\bar{g}\bar{\rho}\ \frac{\partial}{\partial\psi}\left(\frac{(r\omega^{(1)})^2}{\psi}\right)+\bar{g}^{-2}\frac{u^{(1)}}{g}\left[\frac{\partial}{\partial\phi}\left(\frac{V^{(1)}}{\bar{\rho}\bar{g}r}\right)\right]$$

$$\left.+\left(\rho^{(1)}/\bar{\rho}\right)\bar{g}^{-2}\frac{\partial}{\partial\phi}\left(\frac{V^{(1)}}{\bar{\rho}\bar{g}r}\right)+\left(\frac{\rho^{(1)}}{\bar{\rho}}\right)\frac{\partial}{\partial t}\left(\frac{V^{(1)}}{\bar{\rho}\bar{g}r}\right)\right\} \tag{5.4}$$

Θ - momentum:

$$\frac{\partial}{\partial t}\left(r\omega^{(2)}\right)+\bar{g}^{-2}\frac{\partial}{\partial\phi}\left(r\omega^{(2)}\right)+\frac{\partial}{\partial\theta}\left(\frac{p^{(2)}}{\bar{\rho}r}\right)=-\left\{\bar{\rho}\bar{g}\ \psi\frac{\partial}{\partial\theta}\left(\frac{V^{(1)}}{\bar{\rho}\bar{g}r}\right)^2+\frac{\bar{g}\bar{\rho}}{4\psi}\frac{\partial}{\partial\theta}\left(r\omega^{(1)}\right)^2\right.$$

$$\left.+\left(\frac{u^{(1)}}{g}\right)\bar{g}^{-2}\frac{\partial}{\partial\phi}\left(r\omega^{(1)}\right)+\frac{\rho^{(1)}}{\bar{\rho}}\bar{g}^{-2}\frac{\partial}{\partial\phi}\left(r\omega^{(1)}\right)+\frac{\rho^{(1)}}{\bar{\rho}}\frac{\partial}{\partial t}\left(r\omega^{(1)}\right)\right\} \tag{5.5}$$

Entropy Equation:

$$\frac{\partial}{\partial t}\left(s^{(2)}\right)+\bar{g}^{-2}\frac{\partial s^{(2)}}{\partial\phi}=-\left\{\frac{u^{(1)}}{g}\bar{g}^{-2}\frac{\partial s^{(1)}}{\partial\phi}+\left(\frac{V^{(1)}}{r\bar{\rho}\bar{g}}\right)^2\bar{\rho}\bar{g}\ \psi\frac{\partial s^{(1)}}{\partial\psi}\right.$$

$$\left.+\left(r\omega^{(1)}\right)\frac{\bar{\rho}\bar{g}}{2\psi}\frac{\partial s^{(1)}}{\partial\theta}\right\} \tag{5.6}$$

Equation of state:

$$\bar{c}^2\ s^{(2)}-\left(\frac{p^{(2)}}{\gamma\bar{\rho}}\right)+\bar{c}^2\left(\frac{\rho^{(2)}}{\bar{\rho}}\right)=-\frac{1}{2}\left[\frac{\gamma}{\bar{c}^2}\left(\frac{p^{(1)}}{\gamma\bar{\rho}}\right)^2-\bar{c}^2\left(\frac{\rho^{(1)}}{\bar{\rho}}\right)^2\right] \tag{5.7}$$

Note that the dependent variables appear in equations (5.2) through (5.7) in the following particular grouping:

$$\rho^{(2)}/\bar{\rho}\,,\quad u^{(2)}/\bar{q}\,,\quad V^{(2)}/r\bar{\rho}\bar{q}\,,\quad r\omega^{(2)}\,,\quad p^{(2)}/\gamma\bar{p}\,,\quad S^{(2)}$$

Consequently it will be more convenient to solve for these quantities rather than the explicit unknowns.

The inhomogeneous parts of equations (5.2) through (5.7) are composed of solutions of the first-order equations and are thus assumed to be known. It is also important to note that the homogeneous parts of these equations are identical to the system of equations of order ϵ.

Equations (5.2) through (5.7) have two kinds of solutions corresponding respectively to tangentially spinning and standing waves. Since the second-order equations are linear and the standing or spinning type solutions can be expressed in terms of combinations of exponentials, it will be easier to solve the second-order equations once by assuming that the dependence of the solutions on time and θ has the following general form: $\sum_{m,n} e^{i(m\omega t + n\nu\theta)}$. The final result is obtained by assigning m and n their correct values. These will be determined from the form of the expressions appearing in the inhomogeneous parts of the second-order equations.

Since the homogeneous system of the second-order equations is separable but the inhomogeneous system is not, it becomes necessary to assume that the unknowing appearing in the second-order equations can be expanded in terms of the eigenfunctions which satisfy the homogeneous system (i.e., $e^{in\nu\theta} J_{n\nu}(S_{n\nu,s}\sqrt{\psi})$ is such an eigenfunction) of equations, the boundary conditions at $\psi = \psi_w$ and the condition of periodicity of the solution in the θ direction. The second-order solutions are thus assumed to have the following form:[1]

(1) The various functions appearing in (5.8) may be complex functions of their arguments.

$$\left(\rho/\bar{\rho}\right) = \sum_{m,n} e^{i(m\omega t + n\nu\theta)} \sum_{\ell=1}^{\infty} R^{(2)}_{(mn\ell)}(\phi)\, J_{n\nu,\ell}\left(S_{mn\ell}\frac{\sqrt{\psi}}{\sqrt{\psi_w}}\right)$$

$$\left(u^{(2)}/\bar{g}\right) = \sum_{m,n} e^{i(m\omega t + n\nu\theta)} \sum_{\ell=1}^{\infty} U^{(2)}_{(mn\ell)}(\phi)\, J_{n\nu,\ell}\left(S_{mn\ell}\frac{\sqrt{\psi}}{\sqrt{\psi_w}}\right)$$

$$\left(V^{(2)}/r\bar{\rho}\bar{g}\right) = \sum_{m,n} e^{i(m\omega t + n\nu\theta)} \sum_{\ell=1}^{\infty} V^{(2)}_{mn\ell}(\phi)\frac{d}{d\psi}\left(J_{n\nu,\ell}\left(S_{mn\ell}\frac{\sqrt{\psi}}{\sqrt{\psi_w}}\right)\right)$$

$$\left(r\omega^{(2)}\right) = \sum_{m,n} e^{i(m\omega t + n\nu\theta)} \sum_{\ell=1}^{\infty} in\nu\, W^{(2)}_{(mn\ell)}(\phi)\, J_{n\nu,\ell}\left(S_{mn,\ell}\frac{\sqrt{\psi}}{\sqrt{\psi_w}}\right)$$

$$\left(P^{(2)}/\gamma\bar{\rho}\right) = \sum_{m,n} e^{i(m\omega t + n\nu\theta)} \sum_{\ell=1}^{\infty} P^{(2)}_{(mn\ell)}(\phi)\, J_{n\nu,\ell}\left(S_{mn\ell}\frac{\sqrt{\psi}}{\sqrt{\psi_w}}\right)$$

$$\left(S^{(2)}\right) = \sum_{m,n} e^{i(m\omega t + n\nu\theta)} \sum_{\ell=1}^{\infty} S^{(2)}_{(mn\ell)}(\phi)\, J_{n\nu,\ell}\left(S_{mn\ell}\frac{\sqrt{\psi}}{\sqrt{\psi_w}}\right) \tag{5.8}$$

where ω represents the nondimensional angular frequency, which relates to the dimensional frequency as follows:

$$\omega = \frac{L^*}{\epsilon^*}\omega^* \tag{5.9}$$

and m and n take on a particular set of values.

It is also assumed that the known expressions appearing in the inhomogeneous parts of Equations (5.2), (5.3), (5.6) and (5.7) could be expanded in an eigenfunction expansion of the following general

form:

$$F_1(\phi)G_2(t,\theta,r) = F_1(\phi)\sum_{m,n} e^{i(m\omega t+n\nu\theta)}\sum_{\beta=1}^{\infty}\bar{A}_{n\nu,\beta}J_{n\nu}\left(S_{n\nu,\beta}\frac{\sqrt{\Psi}}{\sqrt{\Psi_\omega}}\right) \qquad (A)$$

where $e^{in\nu\theta}$ and $J_{n\nu}(S_{n\nu,\beta}\sqrt{\Psi})$ are eigenfunctions of the homogeneous system of equations. In order to illustrate the manner in which the above expansion is to be used, consider for example the expansion of the first term in the inhomogeneous part of equation (5.2) for the case of a spinning wave:

$$\bar{\rho}^2(\phi)\frac{\partial}{\partial\phi}\left(\frac{u^{(1)}}{\bar{\rho}}\,\frac{\rho^{(1)}}{\bar{\rho}}\right) = \bar{\rho}^2(\phi)\frac{d}{d\phi}\left(R^{(1)}\frac{d\Phi^{(1)}}{d\phi}\right)\cos^2(\omega t+\nu\theta)\,J_\nu^2\left(S_{\nu h}\frac{\sqrt{\Psi}}{\sqrt{\Psi_\omega}}\right)$$

$$= \bar{\rho}^2(\phi)\frac{d}{d\phi}\left(R^{(1)}\frac{d\Phi^{(1)}}{d\phi}\right)\frac{1}{2}\Big(1+\cos 2(\omega t+\nu\theta)\Big)\,J_\nu^2\left(S_{\nu h}\frac{\sqrt{\Psi}}{\sqrt{\Psi_\omega}}\right)$$

$$= \bar{\rho}^2(\phi)\frac{d}{d\phi}\left(R^{(1)}\frac{d\Phi^{(1)}}{d\phi}\right)\frac{1}{2}\left\{\sum_{\beta=1}^{\infty}A_{0,\beta}J_0(S_{\beta}\sqrt{\Psi})+\frac{1}{2}\left(e^{2i(\omega t+\nu\theta)}+e^{-2i(\omega t+\nu\theta)}\right)\sum_{\beta=1}^{\infty}A_{2\nu,\beta}J_{2\nu}(S_{2\nu,\beta}\sqrt{\Psi})\right\}$$

where $R^{(1)}(\phi)$ and $\frac{d\Phi^{(1)}}{d\phi}(\phi)$ are assumed to be known from the solution of the first order equation. The above expansion shows that m and n will take on the following values:

$$m = n = 0; \qquad m = n = 2; \qquad m = n = -2$$

The constants $A_{0,\beta}$ and $A_{2,\beta}$ can be obtained by expanding the function $J_\nu^2\left(S_{\nu h}\frac{\sqrt{\Psi}}{\sqrt{\Psi_\omega}}\right)$ in two Dini-series one in terms of $J_0\left(S_{0,\beta}\frac{\sqrt{\Psi}}{\sqrt{\Psi_\omega}}\right)$, and, the other, in terms of $J_{2\nu}\left(S_{2\nu,\beta}\frac{\sqrt{\Psi}}{\sqrt{\Psi_\omega}}\right)$.

To achieve separation of the equations corresponding to $O(\epsilon^2)$ it is also necessary to assume that the terms appearing in the inhomogeneous part of equation (5.4) (Ψ - momentum) could be expanded as follows:

$$F_2(\phi)G_2(t,\Psi,\theta) = F_2(\phi)\sum_{m,n} e^{i(m\omega t+n\nu\theta)}\sum_{\beta=1}^{\infty}\bar{B}_{n\nu,\beta}\frac{d}{d\Psi}\left(J_{n\nu}\left(S_{n\nu,\beta}\frac{\sqrt{\Psi}}{\sqrt{\Psi_\omega}}\right)\right) \qquad (B)$$

It is also necessary to assume that the terms appearing in the inhomogeneous part of equation (5.5) (θ - momentum) could be expanded as follows:

$$F_3(\phi)G_3(t,\Psi,\theta) = F_3(\phi)\sum_{n,m} i^{nv}\, e^{i(m\omega t + n\nu\theta)} \sum_{\beta=1}^{\infty} \bar{C}_{nv\beta}\, J_{nv}\left(S_{nv\beta}\frac{\sqrt{\Psi}}{\sqrt{\Psi_w}}\right) \tag{C}$$

Expansions (B) and (C) could be obtained by integrating $F_2(\phi)G_{r2}(t,\Psi,\theta)$ and $F_3(\beta)G_3(t,\Psi,\theta)$ with respect to Ψ and θ respectively and then expanding the integrated functions in a Dini-series of the same form as expansion (A) on page 47. Differentiation of the resulting series with respect to Ψ and θ results in expansions of the same form as (B) and (C). It is, of course, necessary to assume that the integrated functions and their expansions are of such nature that term-by-term differentiation is allowable. The validity of the above statements is also important in proving that $V^{(2)}_{nv\beta}(\phi) = W^{(2)}_{nv\beta}(\phi)$. The latter is a necessary condition for the separation of second-order equations.

It is convenient at this point to introduce the function $\Phi^{(2)}_{(nv\beta)}$ defined as follows

$$u^{(2)}_{(nv\beta)}(\phi) = \frac{d\Phi^{(2)}_{nv\beta}(\phi)}{d\phi} \tag{5.10}$$

Substitution of Equations (5.8) and (5.10) into Equations (5.2) through (5.6), expanding the terms appearing in the inhomogeneous parts of these equations in the manner described in the last paragraph and use of assumption iii (i.e., $V^{(2)}_{nv\beta}(\phi) = W^{(2)}_{nv\beta}(\phi)$) result in the following set of equations corresponding to particular values of the subscripts $(n\nu,\beta)$.†*

†For brevity, the following notations will be used: $' = \frac{d}{d\phi}$; $'' = \frac{d^2}{d\phi^2}$

*In the derivation of the following equations the dimensions were conveniently scaled so that $\Psi_{wall} = 1$.

$$mi\omega\, R^{(2)}_{(m,l,\beta)}(\phi) + \bar{\beta}^2 \Phi^{(2)''}_{(m,l,\beta)}(\phi) - \frac{\bar{p}\bar{\beta}}{2} S^2_{(m,l,\beta)}(\phi) V^{(2)}_{(m,l,\beta)}(\phi) + \bar{\beta}^2 R'^{(2)}_{(m,l,\beta)}(\phi) = E^{(2)}_{(m,l,\beta)}(\phi) \quad (5.11)$$

$$mi\omega\, \Phi^{(2)'}_{(m,l,\beta)}(\phi) + \frac{d}{d\phi}\left(\bar{\beta}^2 \Phi^{(2)'}_{(m,l,\beta)}(\phi)\right) + P'^{(2)}_{(m,l,\beta)}(\phi) = \frac{d\bar{\beta}^2}{d\phi} + S^{(2)}_{(m,l,\beta)}(\phi) + B^{(2)}_{(m,l,\beta)}(\phi) \quad (5.12)$$

$$mi\omega\, V^{(2)}_{(m,l,\beta)}(\phi) + \bar{\beta}^2 V^{(2)'}_{(m,l,\beta)}(\phi) + P^{(2)}_{(m,l,\beta)}(\phi) = C^{(2)}_{(m,l,\beta)}(\phi) \quad (5.13)$$

$$mi\omega\, W^{(2)}_{(m,l,\beta)}(\phi) + \bar{\beta}^2 W^{(2)'}_{(m,l,\beta)}(\phi) + P^{(2)}_{(m,l,\beta)}(\phi) = D^{(2)}_{(m,l,\beta)}(\phi) \quad (5.14)$$

$$S^{(2)'}_{(m,l,\beta)}(\phi) + \frac{mi\omega}{\bar{\beta}^2} S^{(2)}_{(m,l,\beta)}(\phi) = A^{(2)}_{(m,l,\beta)}(\phi) \quad (5.15)$$

$$P^{(2)}_{(m,l,\beta)}(\phi) - \bar{c}^2 R_{(m,l,\beta)}(\phi) = \bar{c}^2 S^{(2)}_{(m,l,\beta)}(\phi) - G^{(2)}_{(m,l,\beta)}(\phi) \quad (5.16)$$

The functions $E^{(2)}_{(m,l,\beta)}(\phi)$, $B^{(2)}_{(m,l,\beta)}(\phi)$, $C^{(2)}_{(m,l,\beta)}(\phi)$, $D^{(2)}_{(m,l,\beta)}(\phi)$, $A^{(2)}_{(m,l,\beta)}(\phi)$ and $G^{(2)}_{(m,l,\beta)}(\phi)$ are defined in Appendix A.

It will be interesting at this point to consider the expression for the second-order vorticity and examine more carefully the statements made in assumption iii $\nabla \times \underset{\rightarrow}{q} = \nabla \times \bar{\underset{\rightarrow}{q}} + \nabla \times \underset{\rightarrow}{q}^{(1)}\epsilon + \nabla \times \underset{\rightarrow}{q}^{(2)}\epsilon^2 + \cdots$ where

$$\nabla \times \underset{\rightarrow}{q}^{(2)} = \begin{vmatrix} \frac{e_\phi}{\bar{\beta}} & \frac{e_\psi}{\bar{\beta} r} & r e_\theta \\ \frac{\partial}{\partial \phi} & \frac{\partial}{\partial \psi} & \frac{\partial}{\partial \theta} \\ \frac{u^{(2)}}{\bar{\beta}} & \frac{v^{(2)}}{r\bar{\beta}} & r w^{(2)} \end{vmatrix}$$

$$- \bar{\rho}\bar{g}\left[\frac{\partial}{\partial\psi}(rw^{(2)}) - \frac{\partial}{\partial\theta}\left(\frac{v^{(2)}}{\bar{\rho}\bar{g}r}\right)\right]\underset{\sim}{e}_{\phi}$$

$$+ \bar{g}/r\left[\frac{\partial}{\partial\theta}\left(\frac{u^{(2)}}{\bar{g}}\right) - \frac{\partial}{\partial\phi}(rw^{(2)})\right]\underset{\sim}{e}_{\psi}$$

$$+ \bar{\rho}\bar{g}^{2}r\left[\frac{\partial}{\partial\phi}\left(\frac{v^{(2)}}{\bar{\rho}\bar{g}r}\right) - \frac{\partial}{\partial\psi}\left(\frac{u^{(2)}}{\bar{g}}\right)\right]\underset{\sim}{e}_{\bullet}$$

$$= \bar{\rho}\bar{g}\sum_{m,n} inv\, e^{i(m\omega t+nv\theta)}\sum_{g}\left(W^{(2)}_{(nv,g)}(\phi) - V^{(2)}_{(nv,g)}(\phi)\right)\left(\frac{d}{d\psi}J_{nv}(S_{(nv,g)}\sqrt{\psi})\right)$$

$$+ \bar{g}/r\sum_{m,n} inv\, e^{i(m\omega t+nv\theta)}\sum_{g}\left(V^{(1)'}_{(nv,g)}(\phi) - W^{(2)'}_{(nv,g)}(\phi)\right)J_{nv}(S_{(nv,g)}\sqrt{\psi})$$

$$+ \bar{\rho}\bar{g}^{2}r\sum_{m,n} e^{i(m\omega t+nv\theta)}\sum_{g}\left(V^{(2)'}_{(nv,g)}(\phi) - \bar{\Phi}^{(2)'}_{(nv,g)}(\phi)\right)\frac{d}{d\psi}\left(J_{(nv)}(S_{(nv,g)}\sqrt{\psi})\right)$$

(5.17)

From Equation (5.17) it can be seen that the requirement $W^{(1)}_{n,g}(\phi) = V^{(2)}_{n,g}(\phi)$ introduces the same restriction as in the first-order equations; i.e., the second-order vorticity component along the streamlines must be identically zero. Further implications of above restriction will be discussed later on.

Reduction of the System

For convenience, the superscript (2) and subscripts (nv, g) used in previous sections will be left out of the following derivation.

Substract equation (5.14) from (5.13) to get:

$$\bar{g}^{2}(W-V)' + mi\omega(W-V) = \mathbb{D} - \mathbb{C} = 0 \qquad (6.1)$$

(Because $\mathbb{D} = \mathbb{C}$. See definition of these quantities in appendix A and discussion on bottom of page 48 .

The general solution of (6.1) is

$$W - V = C_0 f_0^{(m)} \tag{6.2}$$

where

$$f_0^{(m)}(\phi) = e^{-mi\omega} \int_0^{\phi} \frac{d\phi'}{\bar{g}^2(\phi')} \tag{6.3}$$

The constant C_0 must be taken equal to zero in order that V = W, which is a necessary condition for the separations of the continuity equation.

From (5.15) and (5.16) we get:

$$S = f_0^{(m)}(\phi) \left\{ \int_0^{\phi} \frac{A(\phi')}{f_0^{(m)}(\phi')} \, d\phi' + \sigma \right\}$$

$$= \frac{1}{\bar{C}^2} \left[P(\phi) - \bar{C}^2 R(\phi) \right] + \frac{1}{\bar{C}^2} G(\phi) \tag{6.4}$$

where $\sigma = S(\phi = 0)$

Integrate (5.12) to get:

$$\bar{g}^2 \frac{d\bar{\Phi}}{d\phi} + mi\omega \bar{\Phi} + P = \frac{1}{2} \int_0^{\phi} S(\phi') \frac{d\bar{g}^2}{d\phi'} \, d\phi' + \int_0^{\phi} \mathbb{B}(\phi') \, d\phi'$$

$$= \frac{1}{2} \sigma \int_0^{\phi} \frac{d\bar{g}^2}{d\phi'} f_0^{(m)}(\phi') \, d\phi' + \int_0^{\phi} \left(\frac{1}{2} f_0^{(m)}(\phi') \frac{d\bar{g}^2}{d\phi'} \int_0^{\phi'} \frac{A(\phi'')}{f_0^{(m)}(\phi'')} \, d\phi'' \right) d\phi' + \int_0^{\phi} \mathbb{B}(\phi') \, d\phi$$

$$= \sigma f_1 + K \tag{6.5}$$

where

$$f_1 = \int_0^{\phi} \frac{1}{2} \frac{d\bar{q}^2}{d\phi'} f_0^{(m)}(\phi')\, d\phi'$$

$$K = \int_0^{\phi} \left(\frac{1}{2} f_0^{(m)}(\phi') \frac{d\bar{q}^2}{d\phi} \int_0^{\phi'} \frac{A(\phi'')}{f_0^{(m)}(\phi'')}\, d\phi' + \int_0^{\phi} B(\phi')\, d\phi' \right) \tag{6.6}$$

The pressure is eliminated between (6.5) and (5.13) to get:

$$\bar{q}^2 \frac{d}{d\phi}(\Phi - V) + mi\omega(\Phi - V) = \sigma f_1 + K - C = \sigma f_1 + L$$

where

$$L = K - C$$

The solution of the above equation is:

$$\Phi - V = f_0^{(m)} \left\{ \int_0^{\phi} \frac{\sigma f_1(\phi')}{\bar{q}^2 f_0^{(m)}(\phi)}\, d\phi' + \int_0^{\phi} \frac{L(\phi')}{\bar{q}^2 f_0^{(m)}(\phi')}\, d\phi' + C_1 \right\} = \sigma f_2 + C_1 f_0^{(m)} + M \tag{6.7}$$

where

$$f_2 = f_0^{(m)}(\phi) \int_0^{\phi} \frac{f_1(\phi')}{\bar{q}^2 f_0^{(m)}(\phi')}\, d\phi' \quad \text{and} \quad M = f_0^{(m)}(\phi) \int_0^{\phi} \frac{L(\phi')}{\bar{q}^2 f_0^{(m)}(\phi')}\, d\phi \tag{6.8}$$

From (6.4):

$$P_{(\phi)} = \bar{C}^2(\phi) \sigma f_0^{(m)}(\phi) + \bar{C}^2 f_0^{(m)}(\phi) \int_0^{\phi} \frac{A(\phi')}{f_0^{(m)}(\phi')}\, d\phi' + \bar{C}^2(\phi) R(\phi) - G(\phi)$$

Using the last expression for $P(\phi)$ in equation (6.5) yields the following equation:

$$\bar{q}^2 \frac{d\Phi}{d\phi} + mi\omega\Phi + \bar{C}^2 R = \sigma f_1 - \bar{C}^2 \sigma f_0^{(m)} - \bar{C}^2 f_0^{(m)} \int_0^{\phi} \frac{A(\phi')}{f_0^{(m)}(\phi')}\, d\phi' + G + K$$

$$= \sigma (f_1 - \bar{C}^2 f_0^{(m)}) + X = N$$

where:

$$\overline{\overline{X}} = \kappa - \bar{c}^2 f_0^{(m)} \int_0^{\phi} \frac{A(\phi')}{f_0^{(m)}(\phi')} d\phi' + G$$

and

$$N = \sigma (f_1 - \bar{c}^2 f_0^{(m)}) + \overline{\overline{X}}$$

Combining (5.11) and (6.7) gives the following relation:

$$\bar{g}^2 \frac{dR}{d\phi} + mi\omega R + \bar{g}^2 \frac{d^2\bar{\Phi}}{d\phi^2} - \frac{\bar{\rho}\bar{I}}{2} S^2_{m\nu,g} \bar{\Phi} = E - (\sigma f_2 + C_1 f_0^{(m)}) \frac{\bar{\rho}\bar{I}}{2} S^2_{m\nu,g}$$

$$- M \frac{\bar{\rho}\bar{I}}{2} S^2_{m\nu,g} = Q$$

where $Q = -(\sigma f_2 + C_1 f_0^{(m)}) \frac{\bar{\rho}\bar{I}}{2} S^2_{m\nu,g} + E - M \frac{\bar{\rho}\bar{I}}{2} S^2_{m\nu,g}$

Eliminating R between the above differential equations results in the following second-order differential equation for $\bar{\Phi}$:

$$\bar{g}^2 (\bar{c}^2 - \bar{g}^2) \frac{d^2\bar{\Phi}}{d\phi^2} - \bar{g}^2 \left(\frac{1}{\bar{c}^2} \frac{d\bar{g}^2}{d\phi} + 2 mi\omega \right) \frac{d\bar{\Phi}}{d\phi}$$

$$+ \left(m^2\omega^2 - mi\omega (\bar{g}^2/\bar{c}^2)(\tfrac{\gamma-1}{2}) \frac{d\bar{g}^2}{d\phi} - \frac{\bar{\rho}\bar{I}}{2} S^2_{m\nu,g} \bar{c}^2 \right) \bar{\Phi} = \bar{c}^2 Q - mi\omega N - \bar{g}^2 \bar{c}^2 \frac{d}{d\phi} \left(\frac{N}{\bar{c}^2} \right) \tag{6.9}$$

Defining

$$f_3 = \frac{f_1}{\bar{c}^2 f_0^m} \tag{6.10}$$

and using the definitions of Q, N and M and the relations

$$\bar{g}^2 \frac{df_0^{(m)}}{d\phi} + mi\omega f_0^{(m)} = 0 \tag{6.11}$$

and

$$f_2 = f_0^m \int_0^{\phi} \frac{f_1}{\bar{g}^2 f_0^m} d\phi' = \frac{f_0^{(m)}}{mi\omega} \int_0^{\phi} f_1 \, d\left(\frac{1}{f_0^m} \right)$$

$$= \frac{f_0^{(m)}}{mi\omega} \left[\bar{c}^2 f_3 - \tfrac{1}{2} (\bar{g}^2 - \bar{g}^2(\omega)) \right] \tag{6.12}$$

the inhomogeneous part of equation (6.9) becomes:

$$-\bar{c}^2 f_0^{(m)} \left[\sigma \left\{ \bar{g}^2 \frac{df_2}{d\phi} + \frac{S_{m,g}^2}{2} \bar{\rho}\bar{g} \frac{1}{2mi\omega} (2\bar{c}^2 f_3 + \bar{g}_{(0)}^2 - \bar{g}^2) \right\} + C_1 \frac{S_{m,g}^2}{2} \bar{\rho}\bar{g} \right]$$

$$+ \left\{ \bar{c}^2 (E - \frac{\bar{J}\bar{I}}{2} S_{m,g}^2 M) - mi\omega \bar{X} - \bar{g}^2 \bar{c}^2 \frac{d}{d\phi} \left(\frac{\bar{A}}{\bar{c}^2} \right) \right\}$$

Now equation (6.9) can be written in the following form

$$\mathcal{L}(\bar{\Phi}) = -\bar{c}^2 f_0^{(m)} (C_1 F^{(1)} + \sigma F^{(2)}) + F^{(3)} \tag{6.13}$$

where $\mathcal{L}(\bar{\Phi})$ represents the left-hand side of equation (6.9) and the functions $F^{(j)}$ $j = 1, 2, 3$, are expressed in terms of known functions.

$$F^{(1)} = \frac{\bar{J}\bar{I}}{2} S_{m,g}^2$$

$$F^{(2)} = \bar{g}^2 \frac{df_2}{d\phi} + \frac{S_{m,g}^2}{2} \bar{\rho}\bar{g} \frac{2\bar{c}^2 f_3 + \bar{g}_{(0)}^2 - \bar{g}^2}{2mi\omega} \tag{6.14}$$

$$F^{(3)} = \bar{c}^2 (E - \frac{\bar{J}\bar{I}}{2} S_{m,g}^2 M) - mi\omega \bar{X} - \bar{g}^2 \bar{c}^2 \frac{d}{d\phi} \left(\frac{\bar{A}}{\bar{c}^2} \right)$$

Admittance Condition at an Entrance of an Axisymmetric Nozzle

The general solution of equation (6.9) is a combination of the general solution of the homogeneous equation and the particular solution of (6.13). If these solutions are known the general solution can be written as follows:

$$\bar{\Phi} = C_1 \bar{\Phi}^{(1)} + \sigma \bar{\Phi}^{(2)} + \bar{\Phi}^{(3)} + C_2 \bar{\Phi}_h + C_3 \tilde{\bar{\Phi}}_h \tag{7.1}$$

where $\bar{\Phi}_h$ and $\tilde{\bar{\Phi}}_h$ are two independent solutions of the homogeneous part of equation (6.9):

$$\mathcal{L}(\bar{\Phi}_h) = 0$$

C_2 and C_3 are arbitrary constants. Now note that above equation has the following singular points:

$$\bar{g} = 0, \quad \bar{g} = \bar{c} = \bar{c}_{throat} = \left(\frac{2}{\gamma+1}\right)^{\frac{1}{2}} \text{ and } \quad \bar{g} = \infty$$

For supercritical nozzle with finite nozzle entrance only the singularity at the throat (where $\phi = 0$) is of interest.

Assuming that all the singularities of the solution, Φ , appear in $\tilde{\Phi}_h$ then the condition requiring the regularity of the solution at the nozzle's throat can be expressed by requiring $C_3 = 0$. Consequently the proper solution of (6.9) is:

$$\Phi = C_1 \Phi^{(1)} + \sigma \Phi^{(2)} + \Phi^{(3)} + C_2 \Phi_h \tag{7.2}$$

From (7.2) together (5.10), (6.7), (6.4), (6.5), and assumption iii, the following relations are obtained:

$$\begin{aligned}
U - \frac{d\Phi^{(3)}}{d\phi} &= C_1 \frac{d\Phi^{(1)}}{d\phi} + \sigma \frac{d\Phi^{(2)}}{d\phi} + C_2 \frac{d\Phi_h}{d\phi} \\
V - \Phi^{(3)} + M &= C_1 (\Phi^{(1)} - f_0^{(m)}) + \sigma (\Phi^{(2)} - f_2) + C_2 \Phi_h \\
P + \bar{g}^2 U + m\omega \Phi^{(3)} - K &= -C_1 m\omega \Phi^{(1)} - \sigma m\omega (\Phi^{(2)} - \tfrac{f_1}{m\omega}) - C_2 m\omega \Phi_h \\
S - f_0^{(m)} \int_0^{\phi} \frac{A(\phi')}{f_0^{(m)}(\phi)} d\phi' &= 0 + \sigma f_0^{(m)} + 0
\end{aligned} \tag{7.3}$$

If these are considered to be a system of linear equations for the determination of C_1, σ and C_2 with given values of U, V = W , P , and S for a given ϕ , we see that only three of these values can be arbitrarily prescribed. In other words, a relation must exist between any such set of four values. This relation is obtained from the relation of compatibility of the four linear Equations ; i.e., from the vanishing of the following determinant;

$$\begin{vmatrix}
U - \frac{d\Phi^{(3)}}{d\phi} & \frac{d\Phi^{(1)}}{d\phi} & \frac{d\Phi^{(2)}}{d\phi} & \frac{d\Phi_h}{d\phi} \\
V - \Phi^{(3)} + M & (\Phi^{(1)} - f_0^{(m)}) & (\Phi^{(2)} - f_2) & \Phi_h \\
P + \bar{g}^2 U + m\omega \Phi^{(3)} - K & -m\omega \Phi^{(1)} & (f_1 - m\omega \Phi^{(2)}) & -m\omega \Phi_h \\
S - f_0^{(m)} \int_0^{\phi} \frac{A(\phi')}{f_0^{(m)}(\phi)} d\phi' & 0 & f_0^{(m)} & 0
\end{vmatrix} = 0 \tag{7.4}$$

$$u\left[\bar{g}^2(\bar{c}^2\xi^{(1)}-\zeta)-m i\omega\right]+V m i\omega\,\bar{c}^2\xi^{(1)}+P(\bar{c}^2\xi^{(1)}-\zeta)$$

$$-S\bar{c}^2\left[\frac{\bar{g}^2-\bar{g}_{(0)}^2}{2}\xi^{(1)}+m i\omega\,\xi^{(2)}-f_1\zeta\right]+m i\omega\,\bar{\Phi}^{(3)}\zeta$$

$$-\frac{d\bar{\Phi}^{(3)}}{d\phi}m i\omega-M m i\omega\,\bar{c}^2\xi^{(1)}+K(\bar{c}^2\xi^{(1)}-\zeta)$$

$$-Z\bar{c}^2\left[\frac{\bar{g}^2-\bar{g}_{(0)}^2}{2}\xi^{(1)}+m i\omega\,\xi^{(2)}-f_2\zeta\right] \qquad (7.6)$$

Above relation holds for any value of ϕ . In particular, (7.6) it holds at the nozzle's entrance where it provides the admittance relation for the combustion chamber flow. For the second-order equations, there are infinitely many admittance relations corresponding to different values of the subscripts ($n\nu, g$) appearing in the eigenfunction expansions used for their solution. The function $\bar{\Phi}^{(3)}$ which appears in the inhomogeneous part of the admittance relation is the particular solution of equation (6.13) which corresponds to $F^{(3)}$ (defined in equation (6.14)) and it is assumed to be known.

The transverse-admittance relation for the first-order equation can be obtained from the second-order admittance relation by putting its inhomogeneous part equal to zero and letting $m = 1$.

The admittance relation simplifies in the isentropic case by taking $S = 0$ identically. If the perturbed flow is irrotational, it must also be isentropic. This implies that $C_1 = \quad = 0$ and consequently Equations (7.3) become:

$$U-\frac{d\bar{\Phi}}{d\phi}=C_2\frac{d\Phi_h}{d\phi}$$

$$V-\bar{\Phi}^{(3)}=C_2\Phi_h$$

$$P+\bar{g}^2U+m i\omega\,\bar{\Phi}^{(3)}-K=-C_2\,m i\omega\,\Phi_h \qquad (7.7)$$

The above relation will be simplified further by observing that now the expressions for $\bar{\Phi}^{(3)}$ and K will be considerably simpler.

Eliminating C_2 from (7.7), one obtaines:

$$\frac{U - \frac{d\bar{\Phi}^{(1)}}{d\phi}}{\frac{d\Phi_h}{d\phi}} \cdot \frac{V - \bar{\Phi}^{(1)}}{\Phi_h} = \frac{P + \bar{\gamma}^2 U + mi\omega \bar{\Phi}^{(1)} - K}{-mi\omega \Phi_h} \tag{7.8a}$$

$$\frac{U - \frac{d\bar{\Phi}^{(1)}}{d\phi}}{V - \bar{\Phi}^{(1)}} = \zeta \tag{7.8b}$$

$$\frac{-mi\omega \left(U - \frac{d\bar{\Phi}^{(1)}}{d\phi}\right)}{P + \bar{\gamma}^2 U + mi\omega \bar{\Phi}^{(1)} - K} = \zeta$$

which represents two admittance conditions when applied to the entrance of the nozzle.

For purely-axial oscillations, Equations (5.13) and (5.14) become meaningless and one has to disregard Equation (6.7) which is related to Equation (5.13). The corresponding admittance relation can be obtained from (7.3) by disregarding the second equation and all terms in C_1. Using this procedure, one finds the following admittance relation:

$$U(\bar{\gamma}^2 \zeta + mi\omega) + P\zeta + S\bar{c}^2 \left[mi\omega \xi^{(2)} - f_3 \zeta\right] =$$

$$- mi\omega \bar{\Phi}^{(2)} \zeta + \frac{d\bar{\Phi}^{(1)}}{d\phi} mi\omega + K\zeta + Z\bar{c}^2 \left[mi\omega \xi^{(2)} - f_3 \zeta\right] \tag{7.9}$$

For one-dimensional isentropic oscillations above admittance relation is replaced by:

$$\frac{-mi\omega \left(U - \frac{d\bar{\Phi}^{(1)}}{d\phi}\right)}{P + \bar{\gamma}^2 U + mi\omega \bar{\Phi}^{(1)} - K} = \zeta \tag{7.10}$$

Note that this equation has the same form as one of these appearing in (7.8b), although the similarity is only formal since the

values of $\mathcal{Y}$ (or $\mathcal{Y}_h$) depend on entirely different equations. Note further that these nonlinear admittance relations may be used only for an oscillation without shock waves. It is very likely that shocks would be present in a purely axial mode.

NOMENCLATURE

ρ - Density

P - Pressure

S - Entropy

$\underline{q}$ - Velocity

U - Axial component of velocity.

V - Radial component of velocity.

w - Tangential component of velocity.

$R^{(i)}$ - Function indicating axial variation of $(\rho^{(i)}/\bar{\rho})$

$P^{(i)}$ - Function indicating axial variation of $(p^{(i)}/\gamma\bar{p})$

$U^{(i)}$ - Function indicating axial variation of $(u^{(i)}/\bar{q})$

$V^{(i)}$ - Function indicating axial variation of $(V^{(i)}/r\bar{\rho}\bar{q})$

$W^{(i)}$ - Function indicating axial variation of $(\omega^{(i)}r)$

C - Speed of sound.

r - Distance from axis of symmetry.

t - Time

Ψ - Stream function.

ϕ - Potential function.

θ - Angle, indicating tangential variation.

ω - Frequency

γ - Ratio of specific heats.

C_p - Specific heat at constant pressure.

δs - Infinitesimal variation in axial direction (along Ψ = constant).

δn - Infinitesimal variation in radial direction (along ϕ = constant).

$S_{(m,\beta)}$ - Eigenvalue, solution of the equation $\frac{d}{d\Psi} J_{m\gamma}(\sqrt{\Psi}) = 0$.

ϵ - Amplitude parameter.

$\underline{e}$ - Unit vector.

σ - Entropy perturbation at the nozzle throat.

$\mathcal{L}(\ )$ - Second order differential operator

$\Phi(\phi)$- Defined as $U_\phi^{(i)} = \frac{d}{d\phi}\Phi^{(i)}(\phi)$.

C_1, C_2, C_3 - Constants appearing in the solution for $\bar{\Phi}$.

NOTE:

The functions A, B, C, D, E and G are defined in Appendix A. The functions $f_o^{(m)}$, f_1, f_2, f_3, K, L, M, N, Q, $\bar{X}$ and $F^{(j)}$ (j=1,2,3) are defined in sub section D-6.

Z , ζ and $\xi^{(j)}$ (j=1,2) are defined in sub section D-7.

SUPERSCRIPTS:

* - Dimensional quantity

o - Stagnation quantity

— - Steady State quantity

(i)- i = 1, 2 . . . . indicates order of the equation.

SUBSCRIPTS:

(n/β) - n = 0, ± 1, ± 2, . . . β = 1, 2, ... Indicates mode under consideration.

w - wall

h - Homogeneous

t - Throat

ϕ, ψ, θ - Indicates direction of unit vectors.

IV. NONLINEAR COMBUSTION INSTABILITY MECHANISMS: EXPERIMENTAL

A. TRANSVERSE MODE NONLINEAR ROCKET MOTOR STUDIES

For several years parametric studies of transverse mode nonlinear combustion instability have been carried out at Princeton University using 9-inch diameter rocket hardware. These pulsed-limits studies have been instrumental in defining problem areas for more basic study as well as reproducing in model-size rocket chambers certain aspects of the combustion conditions found in high-thrust engines. Trends in the variations of the instability regimes encountered in this testing point to possible means of avoiding certain linear and nonlinear high frequency instability problems in full-size hardware designs.

A number of important parameters were outlined in last year's report[1] and will be briefly summarized here before proceeding to the current studies. Using the ethyl alcohol, liquid oxygen propellant combination, together with a pulsing device based on a grain charge and burst disk arrangement,[1-3] the incidence of nonlinear combustion instability was influenced by:

1.) Orientations of the spuds, where tangential injector orifice alignment (radial spray fans) showed major differences. Extremes of stability were shown by 6 x 2 (six groups consisting of two spuds similarly oriented), the most stable arrangement, and 12 x 1 and 1 x 12 groupings which proved to be the least stable.

2.) Rotation of the spuds to the radial orifice alignment was shown to markedly improve the stability when compared to the 1 x 12 tangential arrangement.

3.) Inter-fan spacing (distance between fuel and oxidizer spray fans in a single spud) changes influenced stability with the zero spacing arrangement clearly superior (i.e., fuel fan end-impinging on the oxidizer fan).

4.) Chamber pressure variations indicated that increased pressures favored higher modes and/or linear instability.

and

5.) Inter-Spud spacing changes showed that larger spacing arrangements were more difficult (or impossible) to trigger into nonlinear combustion instability.

These studies have been continued for both the ethyl alcohol, oxygen and RP-1, oxygen propellant combinations. Certain additional data on these past five parameters have been obtained and will be covered first.

Before proceeding to the details of the test data it would be well to review the mechanism believed responsible for many of the effects observed. Associated with transverse pressure oscillations are velocities and hence particle displacements. Stability of the combustion process is involved with these displacements since the effect is selective i.e., the more readily vaporized propellant is displaced with reference to the droplets of the other thus varying the local mixture ratio and hence the local combustion rates. The theoretical treatment for this phenomenon (first observed by the research group at Rocketdyne) was covered by Reardon in Reference 16 . This topic is also covered in a soon to be published paper[17].

The situation existing in actual rocket engines from the standpoint of determining the mass and mixture ratio distributions of the propellants involved and then charting the course of the displaced vapor becomes quite complex. In the studies at Princeton University the propellants are normally injected at a single injection radius. Distribution data for this relatively simple arrangement will be discussed in detail in this section. The displacement paths and how they vary with distance from the center of the injector (originating as a circle, evolving into an eclipse and finally into a circular arc at the chamber wall) also complicates the situation. A discussion of these paths and the inter relationships with ellipitical spray fans of various orientations is to be found in Appendix A of Reference 1.

Thus with regard to the various effects that are discussed next, it must be remembered that due to the interwoven considerations as mentioned above <u>trends in stability characteristics</u> as influenced by the parameter variations will be investigated. The true magnitude of any of these effects could only be ascertained in the final hard-

ware design with numbers of radial injection locations.

That the stability threshold of a rocket chamber can be influenced by increasing or decreasing the inter-spud spacing was shown in Reference 1. Perhaps the best illustration of these spacing influences was found in Figure 18 of that Reference and is repeated here for comparison as Figure IV-1. Here the standard instability regime can be seen as determined for the 1 x 12 grouping (1.84 inch inter-spud spacing) as compared to the completely stable mixture ratio-perturbation amplitude field for the 1 x 8 (2.76 inch spacing) and completely unstable field (of increased amplitude) for the 1 x 16 (1.38 inch spacing).

To evaluate whether the chamber Mach number was influencial in establishing the degree of stability in the inter-spud spacing investigation was the purpose of a series of tests in progress at the time of the last report. One group of tests used spuds with orifices of twice the standard area (.084" diameter vs. .059" diameter). These spuds when placed in the 8 spud configuration providing the same total propellant flow as 16 standard spuds. Thus, the Mach number was maintained constant while spacing and orifice sizes were the variables. Testing at the 150 psi level with these double-size orifice area spuds yielded the same stable results indicated in Figure IV-1 for the 1 x 8 standard spud.

Another approach taken to provide equivalent chamber Mach number conditions involved the use of a 12 spud injector plate to which 4 more centrally located spuds were added (referred to as 1 x (12 + 4), Figure IV-2). Such testing preserved the 12 spud spacing (1.84 inches) while producing the Mach number associated with the 16 spud arrangement. The data obtained in these tests are shown in Figure IV-2 and IV-3. In the $O \longrightarrow \bar{F}$ (see nomenclature) tests (Figure IV-2) the instability regime is actually slightly smaller than that found in Figure IV-1 for 1 x 12. Checking with the instability limits data in Reference 1 for $\bar{O} \rightarrow F$ (also in Figure IV-2) and for comparisons for the higher pressure results (Figure IV-3) the following

can be said: At 150 psia the $\bar{O} \longrightarrow F$ data also indicates a somewhat more limited range of instability as compared to that previously recorded for 1 x 12 (Figure 19, Reference 1), certainly not even approaching the 1 x 16 case. At 300 and 600 psi the instability regimes and modes closely compare to the previously obtained 1 x 12 data (Figure 26, Reference 1)with the characteristic standing modes and higher modes entering the scene as the pressure was raised.

The conclusions based on both the large injector orifice tests and the added spud tests, in which the chamber Mach number for the 16 spud arrangement was duplicated in each case are as follows:

1. Inter-spud spacing has been shown to be an important stability parameter for the 150 psia chamber pressure regime.
2. Minor differences indicated that Mach number influences were present but were not a controlling characteristic.

Reardon has discussed the influence of thrust per element (F/E) in recent Aerojet reports[18,19]. There exists a close connection between (F/E) and inter-spud (or inter-element) spacing. In a fixed thrust rocket design both parameters must change simultaneously, whereas in the Princeton tests just described the parameters were independently varied over a limited range, i.e., F/E varied from 80 to 160 lbs/element while the spacing (considering all the tests) varied from 1.36 to 2.76 inches.

Other spud arrangements to test non-uniform inter-spud spacings were also investigated. Both 16 spud and 12 spud injector face plates were used in these studies. The approach was that of leaving certain selected spud locations blank. For example, with the 16 spud face plate, groups of 3 spuds followed by 1 blank space were used and assigned the nomenclature 4 (3 + 1 B). The purpose of these tests was to determine whether non-uniformities in the propellant injection (spaced appropriately) could alter the instability regimes.

Evaluating the 4 (3 + 1 B) tests for the four pulse direction-propellant placement arrangements (see nomenclature this section) the following points are observed from Figures IV-4 and -5. $O \longrightarrow \bar{F}$ tests produced the broad instability regime characteristic of the 1 x 16 tests

(Figure IV-1) with decreased amplitudes. $\bar{O} \longrightarrow F$ pulsing (also Figure IV-4) showed instability to 2.3 mixture ratio similar to 1 x 16 data[1]. $F \longrightarrow \bar{O}$ studies (Figure IV-5) failed to produce the reversed spin instability shown in both 1 x 16 and 1 x 12 results[1]. And finally, $\bar{F} \longrightarrow 0$ tests indicated the existance of instability in separate regions at high and low mixture ratio where 1 x 12 tests were entirely stable and 1 x 16 tests were unstable.

In another series of tests the 12 position injector face plate was used with 2 spud and 1 blank groupings. Testing at the 150 psia level indicated stable operation under $0 \rightarrow \bar{F}$ pulsed conditions. This would correspond to 1 x 8 results. Thus when the spacing alternates between each pair of spuds (i.e. 1.84, 3.68, 1.84, 3.68 etc.) the blank space appears to be effective.

Based on the stable behavior encountered at 150 psia, tests were also run at 300 psia. These higher chamber pressure results (as shown in Figure IV-6) indicate the presence of spinning or standing first tangential mode oscillations for $\bar{O} \rightarrow F$ and $0 \rightarrow \bar{F}$ pulse gun and propellant placement. For comparison, the 300 psia tests with the 1 x 8 double-size orifice area spuds are summarized in Figure IV-7. These results also indicate the same stability behavior although of somewhat higher amplitude. Spot checks with the 1 x 8 arrangement and the standard orifice size reduced the amplitudes close to those found in the testing of the 4 (2 + 1 B) injector.

In a final series of tests checking the effect of non-uniform propellant injection on combustion instability regimes the spacing was increased to a two-spud gap at 180° intervals. Using the 16 position injector face, the arrangement consisted of 4 spuds followed by two blanks or 2 (4 + 2 B). The test data are presented in Figures IV-8 and -9. Although possessing the same number of spuds as the last tests described, the stability behavior was entirely different at 150 psia chamber pressure. First, tangential <u>standing</u> mode oscillations were present* for all four pulsings conditions ($\bar{O} \rightarrow F$, $0 \rightarrow \bar{F}$, $F \rightarrow \bar{O}$ and $\bar{F} \rightarrow 0$) except for the lower mixture ratios opera-

*The pressure antinodal line passed through the blank spaces.

tion. Even a number of the lower mixture ratio tests damped very slowly (one taking 600 millisec., Figure IV-8). Thus it would appear that the wider gap acts much like a baffle* [2,20] in altering the chamber environment to one favoring the standing type oscillations. Furthermore, it again has been shown that four spuds in a group (under the general rule of three or more) behave much as the full compliment (in this case a 16 spud injector).

Raising the chamber pressure to 300 psia, linear first tangential standing mode oscillations replaced the nonlinear type. At 600 psi linear instability persisted with first tangential, first radial and mixed 1T 1R modes present. As has been previously discussed both in this section and in Reference 1 , this transition first to standing mode oscillations and then to higher modes appears to be characteristic of the injection elements used (data in Figure IV-9).

Briefly, the following conclusions can be drawn about this variety of spacing tests.

1. Similar to the effects observed with orientation[1] if three or more spuds are grouped, followed by a spacing change, only minor improvements in stability are derived. On the other hand, when alternating spacing was investigated (i.e., two spuds followed by one blank) stability was improved.

2. Use of wider gaps in the propellant distribution (i.e. two spuds positions blank at 180° intervals) resulted in effects similar to those observed with the diametral baffle, i.e., previous spinning first tangential mode was replaced with standing 1T mode oscillations.

3. Higher pressures (300 and 600 psia) resulted in the same trends as the previous studies reported in Reference 1 . The linear instability tendencies increased with pressure as did the incidence of higher modes, 2nd tangential or 1st radial and combined modes.

From a practical design standpoint certain difficulties would be present in using voids in the propellant injection density to improve stability characteristics. One would be the problem to locally cool the injector face if no propellant was being injected. This region may receive equivalent heat flux or even increased heat transfer (if

*Appendix B provides a new approach to simple baffle design.

a strong recirculation pattern is established in that location) and would demand careful design attention. Such considerations would also apply to any form of increased spacing and must be allowed for in the injector design (i.e., no stagnation regions, sufficient cross velocities in the ring groves, proper material choice to reduce hot spots, etc.).

RP-1 Testing

In previous rocket testing at Princeton jet fuels and especially a purer hydrocarbon, iso-octane[20b], were used with liquid oxygen. The tests referred to were concerned with longitudinal mode combustion instability and the results were compared to those obtained testing with ethyl alcohol. The conclusions based on linear combustion instability data were that the instability regimes were similar but slightly smaller for LOX, iso-octane. This, incidently, could be predicted by the droplet and wake burning theory covered in Section V. Therefore, similar values for the combustion parameters τ and n were found.

In considering RP-1 for nonlinear combustion instability testing, other factors must also be taken into account.

In determining any vapor displacement effects, how slowly the droplets of one propellant vaporize accomplishes similar objectives as the rapid vaporization of the displaced propellant. From this standpoint, RP-1 would appear to be somewhat more prone to vapor displacement effects than ethyl alcohol due to its slower vaporization rate.

In the first RP-1 tests to be described, the identical injector elements were used as in the alcohol tests, i.e., like-on-like doublets with .059 inch orifices. Since the nominal mixture ratio for LOX, RP-1 is 2.3 (maximum c* point, versus 1.4 for LOX, alcohol). The LOX velocity is increased, producing finer droplets near the injector face (where D_{30} = 137μ versus 160μ for LOX-alcohol assuming $\Delta V = V_J$, Equation 11, Ingebo[21]) and hence providing a means for more rapid vaporization. The fuel velocity,

on the other hand, is decreased thereby increasing droplet sizes ($D_{30\ RP-1} = 194\mu$ versus $D_{30\ Alc} = 155\mu$). Both changes may be looked upon as favoring displacement effects provided that the combustion distribution has not been significantly altered* in the combustion chamber. Tests are currently in progress using the appropriate sizes of injector orifices necessary to restore equivalent stream velocities at the 2.3 nominal design mixture ratio. These tests will be discussed later.

The injector chosen first was the 1 x 12 tangentially oriented fan arrangement - the "standard" for the pulsed-limits testing with LOX, alcohol. Equivalence ratio is used to cross correlate the RP-1 and alcohol data. It would appear from these tests (for all four pulse conditions) that the instability regimes were noticeably widened. These data are shown in Figures IV-10 and IV-11. Only the $O \longrightarrow \bar{F}$ tests indicated a small instability regime expansion ($<$ .2 mixture ratio at the low mixture ratio end). The amplitudes were characteristically of the order of 260 psi peak-to-peak approaching the equivalence ratio and amplitude conditions experienced with LOX, alcohol and the closer-spaced 1 x 16 arrangement.[1] Higher pressure testing with this arrangement produced linear instability of both spinning and standing first tangential modes similar to so many of the higher pressure tests.

Use of the 6 x 2 orientation approach, which had proven to be quite successful in limiting the instability regimes with alcohol and LOX, was checked next with RP-1. Spinning first tangential mode instability was found with certain propellant and pulse gun arrangements. Conditions of complete stability occurred a number of times in mixture ratio regions formerly unstable depending on the exact location of the pulse. The particular data referred to is shown in Figures IV-12 to -14 for a number

*If the larger fuel droplets produced should result in the rate of combustion decreasing near the injector face then the additional time for mixing and evening out of fuel and oxidizer concentrations that would take place axially could result in a supression of such displacement effects.

of pulse gun and propellant arrangements at 150 and 300 psi. Compared to the 1 x 12 LOX, RP-1 tests these data represented improved stability but fell considerable short of the near stable operation at 150 - 600 psia chamber pressure that had been indicated with LOX, Alcohol 6 x 2 testing. However, $\bar{F} \longrightarrow 0$ data (not shown) was completely stable and the 300 psia chamber pressure results indicated lower amplitude standing first tangential mode instability.

To determine the exact distributions of fuel and oxidizer present in the regions near the points of injection (from both a mass and mixture ratio standpoint) and thus hopefully explain the positional effects observed with the pulses, the 6 x 2 injector was placed in the spray booth.[22] There, using at first a liquid collector probe similar to that developed by Rupe[23] and later switching to 9 x 9 matrix collector (81-¼" tubes at ½" center distances [22]), the necessary samples were taken and analyzed. The local mixture ratio and relative mass were determined using RP-1 as the fuel and appropriate density sugar water to simulate the LOX.

To speed the initial data processing, the local mixture ratio and relative mass were computed on IBM 1620 equipment using the height data from the collected columns of RP-1 and simulated oxidizer as an input. These data were then used in conjunction with adjacent samplings to provide an overall mass and mixture ratio map. Simplified versions of such maps are shown in Figures IV-15 and -17 for 1.4 and 2.4 mixture ratios. Studying these data one can see where three relatively large oxidizer rich zones exist between spuds 12-1, 4-5 and 8-9 on the outer edge of the injector under both 1.4 and 2.4 mixture ratio operation. Similar broad fuel-rich zones are found at 2-3, 6-7 and 10-11 locations toward the center of the injector (especially visible in Figure IV-15). Whether any effect of sectionalizing the injector via propellant-rich zones is responsible for the improved stability (similar to the wide gaps previously mentioned or the effect due to baffles) remains an interesting interpretation. On this question it should be noted that

when an 8 x 2 arrangement was used with LOX, Alcohol the results were not nearly as good from a stability standpoint as 6 x 2.

Also of interest is the fact that the LOX momentum is so predominant in the 1.4 data shown in Figure IV-15 and -16 that the mixture ratio averages greater than two above the center of the spud never reaching the 1.4 mixture ratio at which the injector was operated.

To take all these data into account in the prediction of spin direction is no easy task. This approach for the moment has been side stepped in favor of simply seeing if the injector is really "balanced" in the circumferential directions. With this in mind, a one-dimensional view of the mixture ratio and relative mass, as seen along the injection diameter, is illustrated in Figure IV-16 for 1.4r and in Figure IV-18 for 2.4r. The broader LOX and RP-1 regions as previously mentioned are clearly visible in these figures. The mixture ratio for the 1.4r data at the spud center is more clearly defined in this circumferential slice and it would be difficult to justify the overall mixture ratio that was present. Referring back to Figure IV-15, apparently the fuel was displaced inwardly (possibly due to oxidizer momentum considerations).

The data obtained for the 2.4 case points out that the mixture ratio and relative mass fluctuations are considerably less intense than the 1.4r. This is very obvious when one compares Figure IV-18 to IV-16. Both samplings were done at three inches from the injector face. Viewing the local mixture ratio as a measure of the combustion that has occurred up to that point, one would conclude that in the 2.4 case a higher percentage of the total combustion has taken place. This improved mixing, whether due to the relative velocities between fuel and oxidizer and/or a more rapid blossoming of the LOX due to the higher Δ p, has a direct influence on any displacement effects present. How to weigh each of these effects is a subject currently being pondered. For the moment, however, let us consider the following attempt.

Using the one-dimensional approach some terms must first be defined. In considering available oxygen for displacement, the availability could be considered to begin at stoichiometric mixture ratio; approximately 3.4 if the injector is evaluated for LOX, RP-1 and 2.1 for LOX, Alcohol. Then the simple relationship to use is:

$$M_{o_{avail}} = M_{o_{total}} \frac{r - r_{stoich.}}{r + 1}$$

where $M_{o_{avail}}$ is the relative mass available, $M_{o_{total}}$ is the total relative mass, r is the mixture ratio.

Adding up these contributions at each spud location with direction being assigned via the oxidizer to fuel preference[1], it was found in the 1.4r that a difference in "balance" of 19% existed between the two directions. At 2.4r there was an 84% unbalance. The direction of predicted spin at 2.4 mixture ratio agreed with Figures IV-12 through -14. These can only be considered preliminary results until additional mixture ratio and relative mass surveys can be completed. Such surveys are being considered as a Senior Thesis topic beginning this summer.

Returning to the discussion of the rocket firings, the first series of data on the injector elements designed for 2.3 mixture ratio have now been completed. The results with $0 \longrightarrow \bar{F}$ testing place the spinning mode instability regime between 2.1 and 3,15 mixture ratio. Compared to Figure IV-10, this indicates a considerable contraction especially since the 45-20 grain charge burst disk combination was used in these tests. Based on equivalence ratio, these limits represent a contraction from the LOX, Alcohol instability regimes*, Figure IV-1.

Zero inter-fan spacing (item 3 on the first page of this section) was shown to be extremely effective in controlling high frequency combustion instability for LOX, RP-1 as was the case for alcohol. The tests run to date include only the 1.4 mixture ratio

*In contrast, however, $\bar{F} \longrightarrow 0$ pulses have produced 1T instability as with the 1.4r RP-1 spuds, a situation not found for LOX, alcohol.

design spuds. The one caution in interpreting these tests is that the c* performance is down because in essence only one ring of fuel and one ring of oxidizer are provided.[1]

To provide controls on inter-spud spacing beyond those obtainable with the orientation of spuds non-evenly spaced locations have been provided in one injector face. Preliminary tests indicated a marked influence of pulse gun positioning. For this reason the tests have been interrupted while the injector is analyzed in the spray booth.

It is hoped that the basic experiment being conducted on the vapor displacement mechanism (see part C of this Section) will provide the vital data needed on the amplitude and phase of the vapor and droplet movement. Only with a greater knowledge of these inter-relationships can intelligent stability predictions be made with regard to this instability mechanism.

NOMENCLATURE

Injector Code:

$$a \times (b + cB),\ d\ L \text{ on } L\ e\ f\ \bar{g}$$

a = Number of groups

b = Number of spuds in group

c = Number of blank spaces (B) in group

d = Inter-fan spacing between the like-on-like (L on L) spray fans

e = Design mixture ratio based on equal velocity of 75 ft/sec

f = Orientation of center line formed by like-on-like orifices: tangential (T) or radial (R)

g = Propellant spray fan away from chamber wall

$\bar{g}$ = Propellant spray fan nearest the chamber wall either $\bar{O}$ or $\bar{F}$

Pulse Arrangements:

$\bar{g} \rightarrow g$, where $\rightarrow$ indicates pulse direction.

B. LONGITUDINAL NONLINEAR ROCKET STUDIES USING THE SQUARE-MOTOR

The square-motor approach to study the effects associated with high density, closely spaced injection elements was outlined in Reference 1. Before covering the most recent results determined in the study, it would be well to briefly review the previous data.

The square-motor as its name implies is a thrust chamber made of three and four inch long, copper, square chamber sections. The design allows chamber length variations to forty inches using a hydraulic jack to hold and seal the various elements (injector, group of chamber sections and nozzle, see Figure 28, Reference 1). The various injectors under test provide a propellant-injection density greater than .5 lb. per in^2 - a considerable step above other Princeton rocket hardware that flow less than 20% of that amount. The injector evaluations are based on the incidence of linear type longitudinal instability which can be partially controlled by use of a multiorifice nozzle[2] to vary the nozzle admittance or by checking the incidence of nonlinear longitudinal oscillations using injector-end or nozzle-end pulsing (gun powder and burst disk combination).

The tests previously reported[1] with the larger injection orifices (and associated higher flow rates), the pulsing effects and nozzle changes indicated that large amplitude (200 to 300 psi peak-to-peak) longitudinal-mode oscillations could be produced. That only the smallest pulse was necessary (15 grain - 1 K disk) to initiate these high amplitude oscillations was also shown. Both pulse locations could produce the instability although the nozzle location generated longitudinal mode oscillations from the start (versus mixed mode initiation from the injector-end pulses). These were similar to the natural rapid instability transition observed with this chamber-injector combination (Figures 31 and 33 of Reference 1).

The tests described above used an injector which could be fabricated in four simple patterns using a 4 x 4 like-on-like design.

For clarity, Figure 29 from Reference 1 is repeated here as Figure IV-19. Type I injector uses aligned, like propellant spray fans that end impinge on themselves in alternate rows of fuel and oxidizer. Fuel fans end impinge on oxidizer fans in the unlike end impingement Type II. Type III injector allows for end impingement of one propellant on itself with side impingement from the other propellant. Finally, Type IV rotates the fans approximately 26° to avoid end impingement.

In Reference 1 the stability behavior of Type I was reported for LOX, Alcohol as producing linear longitudinal combustion instability at high and low mixture ratios at lengths greater than 14 inches. Multiorifice nozzle tests extended the instability to cover the entire operating range of mixture ratio.

The Type IV injector, on the other hand, indicated linear instability at only very low mixture ratio at a length of 38 inches. Using the 15-1K pulses, however, the range of instability was extended to ten inches. The Type II injector exhibited similar stability behavior.

The Type III injector design was then tested and the results are illustrated in Figure IV-20. There are two versions of the Type III design, the one shown in Figure IV-19 (where the LOX end impinges on the side of the fuels which are end-impinging on themselves) and the reversed design. The former is referred to as Type III pulsed $0 \longrightarrow 0$ and the data in Figure IV-20 depict the high amplitude oscillations over the entire operational mixture ratio range. These oscillations exist for lengths greater than twelve inches for this design. All of the tests shown have been pulses at either the nozzle or the injector end.

The other Type III injector (pulsed $F \longrightarrow F$) yielded longitudinal instability amplitudes of approximately one half the magnitude as those shown in Figure IV-20 at the shorter lengths (at 39 inches the amplitudes were similar). The lower length instability limit extended to eleven inches between 1.1 and 2.1 mixture ratio. Thus,

neither design exhibited improved stability* over Type II and Type IV.

To investigate even larger orifice sizes on this program (the injector orifice diameters for the 4 x 4 type injectors was .059"), an injector design with even fewer injection elements was conceived. Using four-spud elements placed on 1.33 inch centers, each spud injects only a single propellant. The orifice size was .120 inches. Since spuds were used, both the unlike end impinging characteristics of Type II and the rotated feature of Type IV can be provided by merely rotating the spuds.

Typical data from such tests are shown in Figure IV-21 for the Type IV injector design using LOX-Alcohol. Here it is found that without pulsing, instability extends down to at least twenty inches. At that length the amplitudes are quite low (38 to 151 psi, often intermittent) while with the Type II design, the instability range was similar but the amplitudes at twenty inches were still more than 200 psi peak-to-peak.

As in the case of the transverse mode tests (reported in the previous part of this section) RP-1 replaced the alcohol in the test program. As was previously discussed in such a propellant switch-over (using the identical injector design), changes will occur in the relative velocity between the two injected propellants and in the droplet sizes produced.

The Type II pattern shows the least change from the results described for LOX, Alcohol. Lower length limits are comparable extending to approximately nineteen inches as seen in Figure IV-22). The upper limit of instability is found to increase in mixture ratio as the length increases to 30 inches. A change of this type was also indicated in Figure IV-21 for the same equivalence ratio.

The Type IV injector design stability data shown in Figure IV-23 also indicates a changing stability limit from a mixture ratio standpoint as the length increases. The lower length limit in these data is shifted to over 26 inches. In both Figure IV-22 and -23 pulsing at these upper mixture ratio limits showed only minor effects.

---

* Based on injector-end pulsing to emphasize effects of the injector pattern where Type II and IV were stable below 15 inches.

Several size pulses were used in these small shifts of the stability limits. It is hoped that these or similar tests will provide a means for checking experimentally some of the theoretical longitudinal nonlinear models covered in Section III.

With the LOX, RP-1 combination, the high velocity flow on the LOX side restricted the high mixture ratio operation to 3.2r. As a first step the orifices on two spuds were increased to .170 inch diameter. Testing with the Type II arrangement and the large LOX orifices increased the limits of the instability regime to the 1.8 to 3.8r range for lengths greater than 23 inches. Intermittent longitudinal oscillations were present above 2.8r at nineteen inches. With the Type IV design and large LOX holes, high amplitude instability was found over the operational mixture ratio range at 23 inches with intermittent traces down to nineteen inches. Thus, the addition of the large LOX orifices and unchanged fuel injection increased the instability regime for both injector types but especially in the case of Type IV.

Reversing the propellants so that the large orifices were on the fuel side produced the following effect: Type II (large F) was stable for all mixture ratios at 29½ and 38½ inches with damping taking less than 50 milliseconds after the initial pulse. Type IV (large F) was stable for all mixture ratios at 22½, 25½ and 38½ inches with even more rapid damping than Type II. One can see from such tests that the increasing of the sizes of the fuel droplets and/or slowing down the fuel velocity provided a considerable improvement in the longitudinal mode stability characteristics. Changes on the oxidizer side via larger, more slowly moving droplets increased the unstable regime. Injection characteristics of both propellants are shown to be capable of markedly influencing the incidence of instability.

Looking at c* versus length, data for unstable operation of the Type IV injector with .12 inch diameter LOX orifices as compared to .17 inch diameter, some idea of the effect on combustion

distribution is seen. From Figure IV-24, the .17 inch diameter LOX orifice tests are found to peak at a length of approximately 25 inches for 1.8 to 3.4r while c* peaks do not occur for the .12 inch LOX orifice until 34 inches for 1.8r and over 38 inches for 2.4r. Even this later mixture ratio trend indicates that as the LOX velocity is further increased the peak c* occurs at a longer length.

With the Type II injector both the .12 and .17 inch diameter orifice reached peak C* near 25 inches. The Type II instability regimes also changed only slightly with orifice size compared to the major length changes in the instability regime for the Type IV configuration. This is further proof of the close connection between the axial combustion distribution and the longitudinal stability characteristics of a rocket motor. Local mixture ratio conditions at barious distances from the injector face will be studied to see how well cold-flow tests can predict the final combustion distributions.

The experimentally observed effect of combustion distribution on the stability is presently being compared to the predictions of the time-lag theory for the distributed case.

In addition, this distributed-combustion theory is being extended to include higher Mach number effects following similar lines to the analysis of Section VI which involved the concentrated combustion case.

C. VAPOR DISPLACEMENT MECHANISM - BASIC EXPERIMENT IN THE "PSEUDO" ROCKET

The significance of vapor and liquid droplet displacement as a factor in the initiation and/or in the sustaining mechanism of the tangential mode of high frequency combustion instability in liquid propellant rocket engines has been questioned for some time[16]. As indicated in the preceding Yearly Report (Reference 1) the results of analytical studies (Appendix A of Reference 1) as well as experimental tests carried out on liquid propellant rocket motors at Princeton University (also covered in an earlier part of this Section) have shown that the displacement of vaporizing propellants by the oscillating gas flow in an unstable rocket motor is an important factor in the combustion process. The experimental program described in this portion of the report is an outgrowth of the desire to study this effect in a systematic manner.

Activity on the project during its initial year encompassed: the development of a 15KV, spark lighted, schlieren-shadowgraph system (wherein both the liquid and gas phases could be readily distinguished); the optimization of test fluids to be used in the experiments; and the analysis of vaporizing liquids in quiescent surroundings. Details of these results can be found in Technical Report 647 (Ref.24). Research activities during the past year have brought the experiment to a fully-developed state and the ability to obtain significant data describing the phenomena is now at hand.

A new graduate student was brought into the program last summer during the period when efforts were being expanded in the design and construction of a "pseudo" rocket motor. The intent of the experiment utilizing this apparatus is to simulate as nearly as possible certain significant rocket engine parameters present during the tangential mode of instability. The inherent limitations of this "cold" motor approach were well recognized but the value of gaining at least partial insight into the effect was felt to greatly outweigh the shortcomings. A schematic diagram of the "pseudo" motor, is shown in Figure IV-25.

The unit was modeled after the 1500 pound thrust rocket engines used at Princeton. In this way it was hoped to utilize data from each program to the benefit of the other.

The "pseudo" rocket chamber is 9 inches in diameter and 6 inches long. A photograph of the apparatus in its present form is shown in Figure IV-26. The injector end of the chamber contains a porous metal plate through which nitrogen gas may be passed to simulate the through-flow of combustion products. The vaporizing liquid is injected via a single jet of large length to diameter ratio. This simple type of injection, providing well-established turbulent flow conditions, 25 represents the first injection element to be tested and hopefully will be followed by impinging types if the experiment will permit it. The chamber side walls contain two diametrically opposed one inch thick optical glass windows two inches wide by four inches long. The nozzle end of the motor consists of a flat plate containing evenly-spaced multiple exhaust nozzles to assist in the attainment of uniform flow through the chamber. A nitrogen shock tube is located in the chamber wall such that the delivered pressure perturbation enters tangentially into the chamber. The chamber has been designed to provide positions for as many as five Kistler type crystal pressure transducers in the exhaust plate, two Kistler or Dynisco pressure transducers in the side wall as well as thermocouples and an axially-adjustable hot-wire anemometer entering through the exhaust plate.

One item of great importance in this experiment is the acoustic environment provided by chamber dimensions employed and the use of nitrogen gas at somewhat less than ambient temperature ($\sim 528^{\circ}$R). Thus, the first tangential mode of this cylindrical chamber is approximately 880 cycles per second. The first longitudinal mode would appear at 1130 cps while the 1L, 1T combined mode and the second tangential modes would be predicted for just over 1400 cps.

As might be expected, various problems arose in adapting the original optical system to the present apparatus and indeed in perfecting the apparatus itself. The placement and focusing of the optical

components proved to be very critical since small changes in the position of the spark source and/or mirrors greatly decreased the clarity and contrast of the photographs. Alignment of the windows also was quite critical. These windows, of course were designed to be perpendicular to the collimated light beam within close tolerances to avoid distortion.

First, the optical system was focused without the windows. When the initially procured optically ground pyrex glass windows were inserted it was found that, due to internal stresses and density gradients in the glass, the liquid droplets and vapor were partially obscured. These windows were replaced by optically ground and polished plate glass windows. With these new windows the fine detail of the jet could be observed and the liquid stream, the droplets and vapor could be distinguished as in the previous research.[24] Increased contrast attained by varying filter and film combinations was also partially responsible for the improved photographic data.

All the above adjustments were made using either helium or Freon 21 as the simulated propellant with the chamber at atmospheric pressure. It had previously been determined that the normal boiling point of Freon 21 was such that it vaporized readily thus meeting the specification deemed desirable for simulation of the actual propellant. During the development of the equipment, however, as the chamber pressure was increased (by blocking off some of the small nozzles which make up the exit plate as well as increasing the flow of N_2 carrier gas) it was found that the Freon 21 no longer vaporized sufficiently due to its higher boiling temperature at these pressures. As a consequence at increased chamber pressure different Freons (Freon 14 for P_c 75 psig and Freon 12 for P_c 125 psig) will be required to adequately vaporize and allow observation of the phenomena.

Concurrent with the development of the apparatus a comparative analysis of gas densities in actual rocket engines and those occurring in the experimental apparatus was made which indicated that a pressure of 14.7 psia in the apparatus was equivalent to 230 psia in a typical LOX/RP-1 rocket engine or 360 psia in a LOX/LH_2 engine. The

controlling relationship is simply:

$$P_p = P_c \frac{M_c \; T_p}{M_p \; T_c}$$

where P is pressure, M is the molecular weight and T the temperature. The subscript p is for the pseudo rocket chamber and c actual combustion chamber being modeled. The experimental chamber is designed for use up to 300 psig. Thus from a density standpoint, the apparatus can simulate a wide range of chamber pressures which are currently of practical interest, and those which may be of interest if extremely high chamber pressures (3000 psia or greater) are utilized.

Although the problems just discussed were time consuming, the primary problem encountered with the apparatus was involved in the operation of the nitrogen shock tube. In its original form, a solenoid was designed to drive a pointed steel dart through a burst disk thereby initiating disk rupture and releasing the nitrogen pulse. In actual practice it was found that the solenoid did not have sufficient power to break the disks in a consistent manner, hence the release of the pulse was not reproducible. As a result, the shock tube was redesigned so that the dart is now forced through the burst disk by energy from an air cylinder. The latched air cylinder shaft is released by the original solenoid. (See Figure IV-26).

Utilizing previous work accomplished under Grant NsG-99-60 (Ref.20)the gun tube was designed to contain a volume of approximately 1.4 cubic inches (3-3/4" long of 1/2" tube). Tests were run using this tube with 1700 psig in the gun and with chamber pressure varying from 0-300 psig. The oscillating pressure in the chamber was measured by Kistler pressure transducers (Model #601) at various radial positions in the exhaust plate. The A. C. component of the output of the transducers was recorded on tape and the traces were then printed at 80 inches/sec on an oscillograph. These conditions of pressure and volume in the pulse gun produced initial amplitudes of the pulse in the order of only 3 psi peak-to-peak. The pressure traces indicated that the

oscillating portion of the pulse decayed in a few milliseconds. In order to determine relative pulse strengths, to check the instrumentation, as well as compare data with the results of previous work (Ref.20), several tests were made using gunpowder charges instead of the nitrogen gas. In this way peak-to-peak pressure of approximately 100 psi were attained. These tests agreed quite well with the earlier investigation producing frequencies of 880 cps as expected. It was known that the strength of the oscillating pressure component and its duration were functions of pressure level of the initial pulse and the quantity of gas injected into the chamber. Therefore the tube length was increased to 3 times, and finally to 9 times its original length with the pressures increasing from 1000 to 3000 psig. Upon studying the pulse traces it was found that many overtones were present and the frequencies did not agree too well with the theoretical frequencies. In addition, the peaks of the pulse were much sharper than expected.

Upon close observation of the apparatus it was found that the porous injector plate had buckled, apparently as a result of the powder charge over pressure. When the tests were repeated after the porous plate had been repaired, the frequencies agreed well with the theory and the peaks of the wave were noticeably smoother. Utilizing a volume nine times the original, together with 3000 psig nitrogen, a peak-to-peak amplitude of 15 psi was obtained. In addition, it was determined that with the high amplitude pulses the overtones died out more quickly than the primary frequency and the pulse shape became more like a sine wave with peak-to-peak amplitudes of 3-5 psi. Band pass filters were installed in the transducer output circuits to remove extraneous noise and harmonics. It had been anticipated that peak-to-peak oscillations of the order found with the highest pressure pulse would be required to observe significant droplet and vapor movement in the jet.

At this point in the development of the apparatus a variable delay trigger circuit was installed. In operation this circuit is activated by the initial shock wave passing over one of the pressure transducers in the exhaust plate. The transducer output then initiates

the 15K spark source at desired delay times between 0 millisec and 40 millisec thus producing a photograph on the film plate. The circuit proved to be accurate and reproducible to within 3 tenths of a millisecond.

Some difficulties were also encountered with the apparatus in attaining reproducible discharge of the nitrogen gas with the shock tube due to uneven rupturing of the burst disks. This was corrected by redesigning the cutting head on the steel dart which punctures the diaphragm.

At this point the entire apparatus was considered operational and specific experiments were undertaken. It was concluded that the 'pseudo' motor would be operated initially at approximately 10 psig since this was equivalent to 400 psia representing a reasonable chamber pressure level. This chamber pressure was, of course, somewhat less than that required to assure sonic flow across the exhaust nozzles, but it was felt that this condition would not effect the significance of the experiments. Experiments at higher pressure will be made in the future to determine the validity of this assumption.

In practice, a run consists of setting up the 15KV spark source, darking the room, opening the film shutter, setting the delay circuit for the desired time period, establishing the flow of vaporizing liquid, establishing the nitrogen thorough-flow, energizing the delay circuit, and closing the shutter. Each test sequence takes approximately 30 seconds. The optimum use of the equipment requires that a number of photographs be taken before they can be conveniently developed and analyzed as a series.

Analysis of initial test data indicated that with 1200 psig in the shock tube and with the smallest volume in use (1.4 inches^3), the vaporizing Freon jet was blow completely out of the viewing window until long after the pressure trace showed that the pulse had decayed. This result was somewhat unexpected since, as indicated previously, it was felt that larger perturbations would be required to disturb the jet to this extent. It was concluded that the continued

unidirectional disturbance of the jet was caused by the nitrogen flow from the shock gun "choking" at exit port thus creating a steady rotational flow component in the chamber. It was also evident that a severely turbulent zone of the injected nitrogen gas existed in the upper portion end of the chamber. The specific knowledge that this turbulence was caused by the pulse gun was confirmed in a series of auxiliary experiments where pulses were introduced without the use of liquid injection or the nitrogen through flow. In the experimental set up the pulse gun had been mounted so as to fire directly at the jet approximately one inch below the point of liquid injection. The interaction of the rotational flow component as well as the photographic interference of the turbulence made it desirable to change the position of the gun so that it would be introduced on the opposite side of the chamber from the injector near the exhaust end.

A minature probe with a pressure transducer on the tip was placed immediately in front of the gun port to determine the gun emptying time. The flow from the gun indicated that a "choked" flow condition was occuring and that the time to decay was greater than desired in the experiment. It was concluded that while this effect was undesirable, that by reducing the pulse strength it could be distinquished from the effects of the oscillating pressure component and thus need not curtail the experimental program. An improved technique using a piston in the pulse gun so as to discharge all of the flow instantaneously is being investigated. Several series of tests were made on the system in the foregoing configuration wherein only pressure transducers and thermocouples were employed. These tests indicated that indeed vapor and droplets from the jet were moved in some interesting patterns but the movement was not readily capable of being correlated with the pressure traces from the Kistler pressure transducers in the exhaust plate. It was felt that much of the difficulty arose from the general turbulence level present in the bottom of the chamber as a result of the shock pulse. Because of this problem as well as a desire to obtain velocity data a hot wire anemometer was added to the

chamber and a pressure transducer was placed in the chamber side wall. Typical of the data obtained with the current system is the following:

Chamber Pressure	10 psig
Injector Pressure Drop	124.6-131.6 psig
Pulse Gun Pressure	1200 psig
Burst Disks	1100 Aluminum (0.016" thick)
Freon Injector Temp.	$69^{\circ}F$
Chamber Temp.	61°-$58^{\circ}F$
Shock Tube	1.4 $in.^3$

A sequence of ten photographs were taken at varying intervals out to approximately 5 milliseconds.

The oscillographic data obtained from the test sequence is shown in Figure IV-27. The figure clearly shows the poor quality of the transient pressure record when the transducer is located in the exhaust plate and the improvement in quality obtained by moving the pressure transducer closer to the injector end on the chamber wall. The traces have been filtered for all frequencies below 400 cps and above 2000 cps. The misalignment of the phasing of the traces on the record is due to the fact that the various probes are located at different circumferential positions in the chamber. The timing marks shown in the figure refer to times from the initial shock wave passing over the pressure transducer located in the exhaust plate. The upper trace is a velocity measurements using hot-wire anemometer instrumentation. Both the pressure and velocity data clearly indicate approximately 850 cps fluctuations close to the characteristic frequency calculated for the pulsing. These preliminary data, indicate that an inphase relationship exists. This phase relationship is characteristic of the spinning mode and indicates that a perturbed state consistent with that seen in an actual unstable combustion chamber has been attained.

In Figure IV-28 the shock wave has passed the far viewing window and has not yet passed the liquid jet itself. The structure

of the jet is typical of those studied earlier under quiescent conditions. The opaque positions define the liquid phase and the cellular structure defines the Freon vapor. Note that the jet is vaporizing in a uniform manner and that some small droplets can be seen moving down and away from the core. The turbulence from the nitrogen pulse is clearly visable in the lower right hand corner as a mottled zone.

Figure IV-29 was taken approximately 0.8 of a millisecond later. The shock wave has passed the jet with negligible effect. Note a slight indication of the movement of vapor to the right side of the jet in the unobscured upper portion of the photograph. This movement is in the direction of the pulse (i.e. from left to right on the near side of the chamber). The liquid portion of the jet appears to be unaffected. At 1.2 millisec later when the disturbance should have made approximately 2 revolutions in the chamber (1½ in relation to the jet) the jet appears as shown in Figure IV-30. Here the liquid portion of the jet has been broadened and many droplets appear to be at the jet surface. The vapor is clearly uniformally displaced to the right side of the jet and is spread out over a larger area than before.

As shown in Figure IV-31 another 0.8 millisec later, the jet was spread out considerably. Here the first vestiges of a sine wave-like vapor sheath begins to appear along the axial path. In Figure IV-32 (from 3.9 millisec) the jet has taken on even more obvious displacement variations along the axial dimension. The jet appears to be shedding fine droplets and vapor at the peaks of the waves in alternately opposite directions. The jet also appears to have formed a shape of approximately three cycles as it flows through the chamber. Theoretically at the frequency of the fundamental tangential mode there should be 2.6 cycles in this length. Here the dispersion of the jet is quite noticeable and in places one can see completely through what was the liquid jet core. In Figure IV-33 the jet is beginning to drift into a much broader pattern and seems to be more of a unidirectional behavior (time 4.8 ms.).

The results of the experiment to date have established

more clearly a picture of what physically happens to vaporizing liquid streams under a transverse perturbation. Specifically, in resume, the result to data show:

1. Transverse pulses can completely destroy a vaporizing jet.

2. Very small perturbations can readily effect the position and shape of the jet. This may lend some credence to the thought that linear or non-linear instability may be one continuous phenomena and that the effect can readily grow from small perturbations.

3. The vapor and fine droplets surrounding the jet while under the influence of the oscillating field take on a cyclic axial shape at a frequency approximating that of the fundamental mode of the perturbation.

4. In the range of oscillation amplitudes tested, the spray and principal portions of the vapor produced by the oscillating transverse flow appear to remain in a position local to the jet. The rotational flow component tends, after some time, to displace significantly the droplets and vapor.

During the course of the experiment it is intended that an impinging jet will be installed in place of the single jet now in use in an attempt to observe the behavior of a range of injection elements. In addition, it is felt that a much better insight into the role that baffles play in inhibiting instability can be obtained by incorporating various baffle configuration and observing the behavior of the vaporizing jet both in the baffle cavities and beyond the baffle tips. Such studies could vastly increase the knowledge of how a baffle accomplishes it stabilizing functions, Appendix B discusses one approach to simplified baffle design.

D. BASIC EXPERIMENTS IN DROPLET RESONANT PHENOMENA

The research conducted on this particular project is undertaken to determine what, if any, mechanism exists between droplet velocities, droplet size distribution and pressure oscillations in a "pseudo" rocket environment. This environment is created in a six inch diameter cylindrical chamber of variable length (see Fig. IV-34). The injector being studied is mounted at one end of the chamber. A series of windows positioned parallel to the spray axis are used to observe the first 4-1/4" of the spray. If desired, the windows may be moved to greater axial distances from the injector face. The chamber is pressurized through radial vents around the windows. Nitrogen flowing through these vents keeps the windows free of fine droplet spray. The nitrogen exhausts through a variable-speed siren at the opposite end of the chamber, thus providing the desired pressure oscillations. These oscillations simulate certain characteristic fluctuating pressure conditions found in rocket thrust chambers experiencing combustion instability. The longitudinal mode of pressure variation is normally produced in the chamber, although other modes can be studied.

The chamber pressure limit is 450 psi with the plexiglass section; the resonant frequencies of current interest are 500 and 1000 cps (first and second longitudinal modes); the injector pressure drop has a range of 0-400 psi; peak-to-peak pressure changes as high as 20 psi have been obtained under oscillating conditions. All of these values are in the range of the rocket engines presently being tested under this contract. Only water has been studied to date.

One phase of this study was completed last fall and was recently published as a technical report.[25] That work evaluated a diffractive light scattering technique which predicts the Sauter Mean Diameter of the spray, a parameter which was to be used in observing variations under oscillating flow. However, the interpretation of the experimental results based on the light scattering

theory was found to deviate considerably from theoretical expectations. Results from theoretical computations indicate that these deviations can be produced by a particular type of particle distribution, i.e., a dominant normal distribution of particles at small droplet diameters followed by a narrow tail of droplets extending to relatively large droplet sizes. High speed photographic spray analysis indicated that this form of droplet distribution does exist in the spray fans of the impinging jet injectors tested.

It was shown that, in addition, for impinging jets the correct Sauter Mean Diameter can be evaluated within the theoretical limitations if specific data reduction procedures are followed, but that the Sauter Mean Diameter in itself does not have sufficient sensitivity to describe the spray characteristics adequately. Had the light scattering technique fulfilled all the experimental requirements, a significant simplification would have been possible in the analysis of the droplet variations under oscillation as well as steady-state operation. Therefore, a somewhat more conventional approach had to be adopted: photomicrography and individual droplet analysis which would provide the necessary droplet size distribution data. More specifically, the method used is required to stop the motion of the droplets and record their size accurately, i.e., to a size range down to 10 μ.

Considering the camera system for use in the photomicrographic approach, a number of requirements were taken into account. First, it is well known that any lens camera has a depth of field which is dependant upon the desired circle of confusion. In measuring droplet sizes, however, the tolerable circle of confusion is a function of the droplet size (smaller droplets need a smaller absolute error in depth of field to be able to have the same relative error in droplet size as larger droplets). Thus, a drop size distribution obtained from a camera photograph is based on a count of droplets in a volume (the area seen by the camera times the depth of field) which is different for each size droplet. In

comparing the data obtained in this research to earlier data from similar tests, it was necessary to take this correction into account.

Since the primary concern of this experiment is in distinguishing differences in spray characteristics between steady-state and oscillating pressure, consistent errors such as this can be ignored. It would, of course, be more beneficial to be able to correct for these errors so that the data taken can be viewed in a proper perspective relative to other similar studies and be compared to other works in the future. However, since the evaluation of steady-state characteristics of sprays (similar to those here) have been undertaken by others,[21, 26, 29] no attempt will be made to repeat these more complete studies.

To compensate for the depth of field effect, the following relationship from Mack and Martin[28] is useful:

$$\Delta s = \frac{2s}{\frac{Ma}{c} - \frac{c}{Ma}}$$

where the depth of field is (Δs), object distance is s, magnification is M, aperture is a, and tolerable circle of confusion is c.

For values of c encountered in these tests, the second term in the denominator may be neglected giving a linear relation:

$$s = \frac{2s}{Ma} c$$

To check this depth of field Bredfeldt[25] used wires of known diameters as reference targets. By controlled camera movement and a study of the resulting photographs for the onset of out of focus condition, the depth of field as a function of wire size was determined. With the new camera arrangement built around the same telephoto lens, a recheck of the equation was necessary. It was felt that targets geometrically and optically more similar to the droplets should prove even more useful. A microscope slide of glass spheres of various sizes in the droplet size range was made. Depth

of field tests as described for the wires were conducted using this slide at the precise location of the droplet spray. The data verified the linear relation between depth of field and circle of confusion. The corrections for depth of field which are mentioned later in this report are obtained by dividing the population of each droplet size by its corresponding depth of field. The resulting drop size distributions represent a complete distribution for all the droplets within a well-determined volume (the area photographed times a unit length of depth of field).

Next to be considered was the choice of film and development which was dependent upon photographically satisfying two conditions. The droplets have to be photographed 1) under lighting conditions which vary with different optical spray depths, and 2) with sufficient contrast to quickly and accurately record a droplet image. Since films with high contrast have, in general, small exposure latitudes, these two conditions cannot be satisfied by the choice of film alone. Therefore tests were conducted to determine the optium film and developer to be used. The final procedure uses Kodak Plus-X Portrait Film (because of it's fine grain and wide exposure latitude) developed in Kodak D-8 developer providing high contrast. These negatives are then enlarged to a final magnification of about 30 on "0" grade paper (Kodak Polycontrast A, without filter).

Also to be considered was the choice of the final value of mangification of the camera system which was based on a trade off among several variables. For a given film grain size as the magnification increases smaller and smaller objects (in this case droplets) can be recorded. However, there are three limitations to the maximum magnification which can be used.

The first comes from the depth of field equation discussed earlier. That equation reveals an inverse relationship between depth of field and magnification. Thus, if for larger magnifications the depth of field becomes too small, the number of photographs

which must be taken to obtain a large enough droplet count becomes excessively large. This leads to cumbersome and time consuming data processing. This limitation to date has not become a serious problem.

The second limitation arises from the need to maintain proper exposure. As the magnification increases so does the distance between the lens and film, and therefore the exposure. Since the time of exposure is determined by the speed necessary to stop the motion of the droplets, this limitation is really dependent upon the light source intensity. With sufficiently fast films the magnification used (five times size) would have easily fit within the exposure limits. However, based on available film for the 70 millimeter automatic advance camera that was suitable for this work, there was a definite magnification limitation.

Finally, the very practical limitation arose as to the overall size of the camera system. The test laboratory which houses the entire apparatus is of relatively limited size. This laboratory geometry was certainly one factor in limiting the camera to five power magnification which proved to be adequate in resolving the 10 μ droplets.

With these considerations in mind the final camera system was designed and checked out (see Figure IV-35). The lens system consists of a 200 mm telephoto unit with an f 3.5 speed rating. The lens system is mounted at one end of a four foot tube with the film advance apparatus mounted at the other end. Thus, the image to lens distance is fixed resulting in a constant magnification factor at a fixed image to object distance (controlled by the limited depth of field). Movement of the camera system is remotely controlled via linear actuators to provide axial and transverse positioning of the object plane. The 70 mm film is remotely advanced using a Beattie camera back. Thus, a series of photomicrographs are taken in rapid sequence when the predetermined operating conditions are attained. A typical series of photographs is shown in Figure IV-36. The shutter remains open during the series since an intermittent light source is

used.

To satisfy the requirements for the light source portion of the overall optical system it is necessary to provide a diffuse light source Reference 21. Use of collimated light systems would lead to contributions from portions of the spray in the field of view but before or after the depth of field. The diffuse light source allows for even illumination of the droplets within the region of interest.

Sufficient light is another requirement for properly backlighting the droplets and allowing the film images to be of sufficient clarity. Again the diffuse light source can more easily attain this objective.

Before choosing a light system, a method of photographing sprays through the use of fluorescent dyes which has been developed at the University of Wisconsin [29] was first considered. In this technique a thin sheet of high intensity light is focused through the spray perpendicular to the camera axis. The light causes a fluorescent dye in the spray droplets to radiate. These radiating droplets are then the only ones to be photographed. Although adoption of this technique would have required extensive rebuilding of the simulated combustion chamber used in the tests, it did have one desirable advantage. By narrowing the light beam to the camera depth of field for the smallest droplet, every droplet in the light beam would be photographed in focus. The correction for depth of field would then not be necessary.

However, although Reference 29 did use this fluorescent technique to obtain spray results which would have been satisfactory for our purposes it was felt that the time required for adoption of the chamber would not be worth the elimination of the depth of field varition. After all, as mentioned previously, the depth of field correction can, for the purposes of this research, be considered a consistent error which will not effect the differences in spray characteristics which are sought.

The light source that was finally decided upon uses the spark

from a 15 kv capacitor discharge of about 1μ sec duration. The light is kept in a diffused beam and passes through the spray and directly into the camera lens. This back lighting of the droplets combined with the photographic processes previously discussed provides excellent contrast as can be seen referring again to Fig. IV-36. The duration of the spark is sufficient short to stop all droplet motion in the data taken so far. However, at higher injector pressure differences slight blurring of the droplets due to their motion may be encountered especially at locations closer to the injector face.

In the comparison of the processed data to earlier work the velocity of the impinging jets, spray, and surrounding gas (N_2) were needed. The jet velocities were obtained by calibrating the injector orifice flows for a given pressure drop across them. The gas velocities are determined by assuming isentropic choked flow through the outlets. This assumes, however, a one-dimensional flow of gas which in the region of the windows is not quite true. As mentioned earlier, all of the N_2 is injected radially into the chamber through vents around the windows. The velocity of the spray is obtained through use of a streak camera. This camera will also be used in studying wave patterns of droplets (see Ref. 30) close to the injector face by studying the frequency of streaks in the traces.

The first series of tests were made with a 90°, .040 inch diameter impinging jet injector. It is similar to those presently used in instability tests except for the smaller diameter of the jets. Future tests are planned using significantly larger and smaller injector orifice diameters. The present injector orifice size was chosen based on previous data [25] and the absence of window fogging problems.

Before any attempt was made to determine differences in distributions between oscillating pressure and steady-state flow, it was necessary to obtain steady-state spray characteristics and to compare these results to earlier reported evaluations of these characteristics. (References 26 and 27.)

The wave frequencies (so called Christmas tree effect) ob-

served by Bredfeldt in steady-state tests with this spray injector were found to be 3100 cps. These agree with other works [27]. However, these data were taken for sprays in quiescent air so they may differ from the results that will be obtained from the streak camera for sprays in the simulated combustion chamber.

The processing of the steady-state data for number-size distributions has been accomplished by comparing the individual droplets on the 30 times magnification photographs to a plastic template of circles. The differences in successive circle diameters correspond to about 8½ μ of actual droplet size. To enable these data to be compared with other similar data for impinging jet injectors the distributions had to be grouped to represent ranges of diameters (Δ D's) in which each successive range was in a ratio of $\sqrt{2}$ to the previous range. Consideration of this correction along with the depth of field correction allows the distributions obtained to be plotted four different ways: 1) uncorrected, or directly as obtained from the photographs, 2) with a correction for the depth of field, 3) with a correction for a Δ D ratio of $\sqrt{2}$, 4) with both the depth of field and Δ D correction.

Data obtained 3-3/4 inches downstream of the injector for a chamber pressure of 100 psig, injector pressure drop of 50 psi (and a corresponding jet velocity of 52 ft/sec) and based on a count of 3032 droplets are plotted by these four methods of analysis in Figure IV-37. Bimodal tendencies as reported in Reference [27] can be seen here in only #1 and #4. This again is in agreement with the literature, Reference [27]. The data taken for that reference were from a collimated light shadowgraph technique. Such a technique has no depth of field effect. The data were processed on a droplet counting machine which had a Δ D ratio of $\sqrt{2}$. The conditions correspond to the #4 plot of Fig. IV-37. The data from an earlier work, Reference 21, which is reevaluated in Reference [26] were taken using with a photographic method similar to that used here and processed using a Δ D ratio of one. No mention is made in the report of a correction for depth of

field. These data correspond to the #1 plot. In these two reference cases bimodal distributions were obtained similar to those obtained here. Furthermore, the variations of the mean values of the modes due to variations in the injector diameters [27] indicates that the mean mode values obtained in this experiment are in agreement with the tendency indicated by these earlier works. A list of these modes appears in Table I, Figure IV-38.

This is however a qualitative comparison. A more quantitative comparison with previous work can be made by following the analysis of Reference 21 . In that work the drop size distribution data were analyzed by using the Nukiyama-Tanasawa expression:

$$\frac{dR}{dD} = \left(\frac{3.915}{D_{30}}\right)^6 \quad \frac{D^5}{120} \quad e^{-3.915D/D_{30}}$$

where R is the volume fraction of drops having diameters $<D$ and D_{30} is the characteristic volume number mean droplet diameter. The D_{30} values obtained from this expression were then used to formulate the empirical expression:

$$\frac{D_j}{D_{30}} = 2.64 \quad \sqrt{D_j V_j} + .97 \quad D_j \Delta V$$

where D_j is the impinging jet diameter, V_j it's velocity and ΔV the velocity difference between the background gas stream and the liquid jet.

In appl ing this analysis to the data the values of the D_{30} calculated in the Nukiyama-Tanasawa expression do not agree with either the actual D_{30} values (based on the definition, $(D_{30})^3 = \frac{\sum ND^3}{\sum N}$) or the values needed to satisfy the empirical expression. Comparative values are listed in Table II , Figure IV-38.

This lack of agreement in the data is not understood. It is felt that when a more complete knowledge of the stream velocities ligament breakup region and final droplet size distributions is

obtained from photomicrograph data analysis that these questions will be answered. The emphasis, however, will be on determining the changes in droplet characteristics between a steady-state and an oscillating environment.

Pressure oscillation data was taken at the resonant frequency of 500 cps with a peak-to-peak pressure variation of approximately 5 psi. Preliminary analysis of these droplet photomicrographs indicate a tendency for definite groupings of droplets to develop under unsteady conditions (as viewed through window #2, 2-1/8 inch point). These groupings are more pronounced than in the steady-state photomicrographs and possibly a phase relationship is indicated between the droplets and the oscillation frequency. This preliminary conclusion is based on the droplet distributions observed under oscillating conditions as shown in Figure IV-39. Should such resonant effects be present, then coupling between the combustion process and the chamber acoustics could result in combustion instability. This possibility is discussed in Reference 31 and in Section V.

Another effect also appears to be evident when the droplet size distribution data are plotted versus similar steady-state information (see Figure IV-40). The total droplet density (number of droplets counted per picture) is considerably lower under the oscillating conditions. Assuming that the same mass flow is being provided by the injector for the same pressure drop across it, this effect could be due to a number of causes. One, the water droplets may be shattering (or even evaporating) into particles too small to be photographed ($< 10\ \mu$ diameter) prior to reaching window #2. Secondly, the opposite case may occur, i.e., the ligaments known to form in such sprays may be extending further downstream and therefore would contain more mass than they do in steady-state. However, a visual comparison of steady-state and unsteady photomicrographs indicates a reduced number of ligaments present with oscillating conditions. Another possibility is that although the droplet density may be lower on the axis, it may be greater out in the radial direction

indicating a transverse broadening of the spray fan in terms of mass flux. Preliminary analysis indicates that this condition is present. Additional photomicrographs will allow these possibilities to be fully investigated. It is hoped that the results from the streak camera will show any variations in droplet wave frequencies and droplet velocities for both the steady and oscillating conditions. The results described here are admittedly from a very small sampling of data. The visual counting of droplets is a relatively slow process. Many photographs have been taken which are presently waiting to be processed. Now that the techniques of obtaining the data have been established, the processing and analysis of the data will play an important role in the progress of the research.

It is planned that tests covering the effect of variables such as: chamber pressure, frequency, injector pressure drop, orifice size, transverse and radial location, etc., will be completed over the next months.

V. DROPLET AND DROPLET WAKE BURNING - MECHANISM FOR COMBUSTION INSTABILITY

Introduction

In order to more fully understand and control the occurrence of combustion instability in liquid rocket motors, it is important that the responsible mechanisms be well understood. Even without such information the lumped parameter approach (utilizing the combustion parameters τ and n from the pressure sensitive time lag approach of Crocco[4]) has proven extremely useful in describing instability regimes. However, without a detailed knowledge of the mechanism involved often only an indirect attack on the problems has been possible. For example, well-defined limits of instability could be used to predict other stability boundaries or instability regimes for similar rocket motor injector designs.[32] However, one could not determine beforehand, based on known physical or chemical characteristics, where or when instability would occur if the rocket was not quite similar to those previously experimentally investigated (this particularly pertains to the injection orifices).

An analytical investigation of several mechanisms* has been carried out by Strahle and Crocco.[31] The mechanisms under consideration were (1) the oscillatory burning or vaporization of liquid droplets when based upon quasi-steady theories of vaporization, (2) the effect of droplet displacement from mear positions caused by chamber gas pressure oscillations at the injector face.

The conclusions reached in this theoretical study may be summarized as follows:

There were strong physical and mathematical reasons for rejecting some commonly advanced mechanisms of instability, although these mechanisms could be a contributing factor. The evaluation was

*Other, more promising mechanisms were also analysed and are summarized beginning on the following pages. They are droplet burning and droplet wake burning.

based on whether or not the mechanism could account for the initiation of spontaneous instability resulting from small perturbations in a rocket engine.

The spacial droplet number density was eliminated as a possible mechanism because the drag was estimated to be too small to cause the necessary relative movement during the cycle time. By this same reasoning, positional displacement of droplets affecting the positional vaporization rate were also unable to contribute. The vaporization rate, when based on quasi-steady theories, was judged inadequate. This was based on response to a pressure wave, response to velocity effects when the droplets were close to a velocity node and phase problems between velocity and pressure. Thus, the validity of quasi-steady vaporization theory was questioned when used in conjunction with high frequency oscillations. It was pointed out that a valid time-dependent theory of the vaporization process would be necessary to explain some observed instability phenomena.

Evaluation of the pressure oscillation effects on the formation of droplets near the injector face was concluded to play no part unless this particular mechanism undergoes a strong resonance in the frequency range of interest (see Section IV-D). The reason stated was that since combustion occurs in a region, rather than at a discrete location at or near the injector face, any non-resonant effects would average out prior to combustion. This would mean that a strong mechanism must be in the region of the steady-state combustion rather than only at the injector face.

In References[33,34] the analysis of instability mechanisms, concentrating on droplet and droplet wake burning, is covered in great detail. These studies pointed out that, for simple droplet models, frequencies commensurate with the diffusion times produced extremely strong response in vaporization rate. In the limit of very high frequency it was found that the vaporization rate perturbation could become infinite as the square root of frequency, but that the burning rate perturbations (important in the feedback mechanism) would

remain bounded.

Using a flat plate model, it was found that for many practical configurations effects of periodic liquid heat-up and finite evaporation kinetics could be ignored.

To take into account convective effects conditions of high free stream Reynolds number flow were considered over a liquid body. Only for sufficiently low Reynolds numbers, large droplet sizes, high temperatures, and fast reaction kinetics could the pressure be low enough from a practical point of view and still retain the collapsed flame assumption. It was found from the steady-state theory that, even with the collapsed flame, a significant fraction (order of 1/2 total) of the vaporized mass would be convected into the droplet wake rather than burned in the boundary layer.

The burning rate perturbation can undergo striking changes with frequency for the assumed wave type (longitudinal mode) if one assumes that a droplet acts partly as a flat plate and partly as a stagnation point. The most important parameters in determining this behavior are the stoichiometric heat of reaction, q, and the ratio of the free stream oxidizer mass fraction to the stoichiometric mass ratio of oxidizer to fuel, Y_o/j. The velocity effect was shown to be of paramount importance to this behavior.

The theory, in many ways, only roughly approximated the conditions present in an actual combustor. Nine points were cited in Technical Report 671, pages 151-152, and a detailed study of each would be required to determine the effects. Cited as probably the most important effect was that a great deal of mass would be carried into the wake and not burned in the leading edge boundary layer; therefore, it was concluded that the problem of wake flames should be treated in the unsteady state. Even with such limitations, this droplet burning theory explains many of the qualitative features of longitudinal rocket engine instability[33] if the burning rate perturbation is accepted as the appropriate feedback function.

In a paper titled "The Unsteady Laminar Jet Flame at Large

Frequencies of Oscillation and Application to the Wake of a Burning Droplet," Strahle introduces the important case of wake burning. Below Re = 400 the wake should be laminar and stable[37]. If the flame cannot exist from the forward stagnation point and the droplet acts as a flame holder, this configuration (i.e., droplet burning in a free convection field and behaving as an overventilated laminar diffusion flame[38]) can still be expected to be valid but with the added complication of an unknown ignition point. This flameholder model is shown in Figure V-1.

Partial premixing of the fuel and oxidizer components would be initiated at the droplet leading edge. The leading edge would be blown by vaporization; therefore, separation would occur quite early. The wake then would essentially consist of three parts, the re-circulation region, a trailing edge vaporization region and the burning core flow region. In the core, conditions would be fuel-rich; the external flow, of course, would be oxidizer-rich. Under the proper initial conditions near the droplet (verified from steady-state experiments) modifications to the controlling relationships could be found from the solutions to the unsteady laminar jet flame, and should hold qualitatively over the majority of the burning wake region. It is this droplet wake burning theory that will now be applied to longitudinal combustion instability.

Development

One result of the unsteady wake theory is that the burning rate perturbation is given by

$$\frac{\dot{m}_{r_f})_r}{\bar{m}_{r_f}} - \frac{\gamma - T_f}{\gamma} + \frac{3\bar{m}_{r_f} k}{4\bar{r}_f \gamma} \sin\frac{\pi}{4}\frac{1}{\sqrt{\omega}} + \frac{2R_f}{\bar{r}_f \varphi} + \Theta\left[\frac{1}{\omega}\right] \quad (1)$$

$$\frac{R_f}{\bar{r}_f \varphi} = -\frac{T_f}{\gamma}\left\{\frac{T_f - 1}{k} + \frac{1}{\bar{r}_f^2}\int_0^{\bar{r}_f} r\,(\dot{+} - T)\,dr\right\} + \Theta\left[\frac{1}{\omega}\right] \quad (2)$$

Here $\dot{m}_{r_f})_r / \bar{m}_{r_f}\,\varphi$ is the local burning rate perturbation component

in phase with the local pressure perturbation, φ, divided by the steady-state local burning rate, where φ is nondimensionalized by the stagnation chamber pressure. This ratio is the important quantity with reference to engine stability and must be approximately one or greater, and positive, for instability to occur. γ is the ratio of specific heats. q is the stoichiometric heat of reaction divided by the free stream enthalpy, $c_p^* T_\infty^*$. $\bar{r}_f$ is the wake flame radius in the steady-state (a function of axial distance) and is nondimensionalized by the droplet radius. It therefore has a range of approximately one to zero. $\bar{m}_{F_f}$ is the steady-state fuel burning rate divided by 2 and nondimensionalized by $\rho_\infty^*(u_\infty^* - u_c^*)$ at an axial location for the flame. It is obtainable only by a solution to the steady-state wake problem and ranges from order one near the droplet to zero at the flame tip. T is the temperature distribution in the wake nondimensionalized by T_∞^* and is a function of axial and radial distance. It likewise is only known after a complete steady-state solution to the wake is carried out. T_f is the flame temperature given by

$$T_f = \left[1 + q\,\frac{Y_{O\infty}}{j} + T_c\,\frac{Y_{O\infty}}{jY_{F_c}}\right] \Big/ \left[1 + \frac{Y_{O\infty}}{jY_{F_c}}\right] \qquad (3)$$

Y_O/j is the free stream oxidizer mass fraction divided by the stoichiometric mass ratio of oxidizer to fuel. T_c is the center-line gas temperature near the ignition point in the wake. Y_{F_c} is the fuel vapor mass fraction at the same axial location. r is radial distance from the centerline. Finally, ω is the dimensionless frequency

$$\omega = \frac{\omega^* \rho_\infty^* a^{*2}}{\mu_\infty^*} \qquad (4)$$

This high frequency solution contains no terms up to $\Theta[1/\omega]$ of the "velocity effect" and is purely a "pressure effect" (see Technical Report 671[33]) and is known to provide good qualitative behavior for an analogous stagnation point problem down to $\omega = 4$ or 5. Such behavior will also be assumed here and Equations (1) and (2) will be

assumed exact. These equations hold when the droplets are stationary with respect to the chamber. It is claimed here from unpublished work that to $\mathcal{O}[1/\omega]$ it is also valid when the droplets are moving. The reason for this is that the movement causes a Doppler effect of $\mathcal{O}[M]$ in the timewise frequency seen by the droplets. The velocity (or incompressible) effect results being $\mathcal{O}[1]$ are therefore not affected and still die out as $1/\omega$. The pressure effect, of $\mathcal{O}[M]$, is modified by the velocity effect times the extra terms introduced by this Doppler effect of $\mathcal{O}[M]$. This creates terms of $\mathcal{O}[M]$, the action of the Doppler effect on a pressure effect creating terms of $\mathcal{O}[M^2]$ which are negligible. Thus, the pressure effect is only altered by terms which still die out as $1/\omega$ which are neglected in Equations (1) and (2).

Some insight into the lower length limit of longitudinal mode combustion instability can be gained from Equations (1) - (4). First, from Equation (4) we can calculate the frequency for such a lower length limit based on Reference[32].

$$\omega^* \approx 3000 \text{ cps (approximately 8 inch cylindrical length)}$$

For the .035 inch diameter injection orifices used in those tests we can calculate the droplet size using Ingebo's[21] data:

$$a^* \approx 3 \times 10^{-4} \text{ ft.} \approx 100\mu$$

The chamber density at 600 psi would be:

$$\rho^*_{gg} \approx .2 \text{ lb/ft}^3$$

From Priem's data[35] the viscosity would be approximately equal to

$$\mu^*_{\sim} = 5 \times 10^5 \text{ lb/ft - sec}$$

Then the dimensionless frequency is

$$\omega \approx 6.8$$

which is in the high frequency range. Therefore, the equations will be assumed valid at the short length limit. They cannot be valid at the upper length since the functions are monotonic in frequency; once m_{F_f} becomes sufficient to cause instability (if it does at all) the system would remain unstable. Supposedly, the neglected terms

would become important at long length. It now remains to show that Equations (1) and (2) do indeed predict stability below a certain length.

Various approximations will now be introduced. Since the wake is axially symmetric, near the axis T goes as ar^2+b with a and b constant. If this functional dependence is assumed to hold all the way to r_f

$$T = \frac{T_f - T_c(\xi)}{r_f^2} r^2 + T_c(\xi)$$

where ξ is axial length from the initial point, $T_c(0) = T_c$. Now the integration in Equation (2) may be performed with the result

$$\frac{R_f}{\bar{r}_f \varphi} = -\frac{T_f}{\gamma}\left\{\frac{T_f - 1}{2} + \frac{\ln\left[1+\frac{T_f - T_c(\xi)}{T_c}\right]}{2(T_f - T_c(\xi))} - \frac{T_f - T_c(\xi)}{4} - \frac{T_c(\xi)}{2}\right\}$$

Now assume in the above, that T_c is linear in ξ because of the core heat-up with axial length

$$T_c(\xi) = (T_f - T_c)\xi + T_c$$

Then the average T_c is approximately $T_f/2$ if $T_c \ll 1$, which will be assumed. Also, assume that the average $r_f = 1/2$ and

$$\frac{R_f}{\bar{r}_f \varphi} \cong -\frac{T_f}{\gamma}\left\{\frac{\ln 2}{T_f} + \frac{T_f}{8} - \frac{1}{2}\right\}$$

Now Equations (1) and (2) are combined to yield

$$\frac{\dot{m}_{F_f})_r}{\bar{m}_{F_f}\varphi} \approx 1 - \frac{T_f^2}{4\gamma} - \frac{2}{\gamma}\ln 2 + \frac{\bar{m}_{F_f}\beta}{\gamma+\omega}\sin\Psi_4$$

Concerning chamber instability $(\dot{m}_{F_f}/\bar{m}_{F_f}\varphi)_r$ must be a certain magnitude to overcome the nozzle damping.[f] Holding the nozzle type and chamber pressure fixed, a mixture ratio traverse produces a small shifting of the position of the steady-state flame front. This shifting, however, produces only a very small change in

the required feedback unless the flame front is very near a pressure node. Therefore, this magnitude can be picked for all mixture ratios. It is analogous to twice the minimum interaction index required for instability. Let us choose $(\mathcal{M}_{F_f}/\bar{m}_{F_f}\varphi)_r = b$. Then there results

$$\omega = \left\{ \frac{\bar{m}_{F_f} \ell \sin \pi/4}{\frac{T_f^2}{4} + 2\ln 2 + r(b-1)} \right\}^2 \tag{5a}$$

Now it is known from Technical Report 671[33] that while trends are predicted quite low in the frequency range by Equation (5), absolute numbers are not. Furthermore, absolute numbers for $\bar{m}_{F_f}$ are not available without a complete solution to the wake problem. However, if a reference point is known, designated by a subscript zero, Equation (5) may be written

$$\frac{\omega}{\omega_0} = \left\{ \frac{(\bar{m}_{F_f}\ell)/(\bar{m}_{F_{f_0}}\ell_0)}{\left[\frac{T_f^2}{4} + 2\ln 2 + \gamma(b-1)\right] / \left[\frac{T_{f_0}^2}{4} + 2\ln 2 + \gamma(b_0-1)\right]} \right\}^2 \tag{5b}$$

and it may be possible to estimate trends for $m_{F_f}/m_{F_{f_o}}$ as well as for other quantities. Now from Equation (4)

$$\omega = \frac{\omega^* \rho_\infty^* a^{*2}}{\mu_\infty^*} \frac{L^*}{L^*} \frac{c^*}{c^*} = \left\{ \pi + \Theta[M] \right\} \frac{c^*}{L^*} \frac{\rho_\infty^* a^{*2}}{\mu_\infty^*}$$

where L^* is chamber length and c^* is the chamber gas speed of sound. Then

$$\frac{L^*}{L_0^*} = \frac{\omega_0}{\omega} \frac{(\rho^*/\rho_0^*)(c^*/c^*)}{(\mu^*/\mu_0^*)} \left(\frac{a}{a_0^*} \right)^2 \tag{6}$$

This states the lower length stability limit variation if one point is known. It remains to compute these quantities for an actual system.

In a rocket chamber the ambient temperature, T_∞^*, must increase with length to the adiabatic flame temperature for the

particular engine mixture ratio. By energy considerations T_f^* must be above this flame temperature initially (since burning is assumed at stoichiometric mixture ratio) and decrease to it in time. Thus on the average $T_f > 1$. Changes in the adiabatic chamber temperature with mixture ratio should also be reflected in similar changes in T^*_{∞}. It will be assumed that $T^*_{\infty} / T^*_{\infty_o}$ is the same as the same ratio for the adiabatic flame temperature. This quantity, which appears in q/q_o, can therefore be calculated from equilibrium calculations concerning the chamber gases of complete combustion. Similarly, c^*/c^*_o and ρ^*/ρ^*_o are known. μ^* is assumed proportional to T^*_{∞} so that μ^*/μ^*_o is known. T_c affects the results only slightly if it is low enough and may be assumed constant. Similarly, T_{F_c} is primarily determined by the droplet characteristics and may be assumed constant. This, of course, is open to question if the ignition point in the wake seriously changes with mixture ratio. This is a possibility. It will be assumed that Y_{o_∞} is proportional to the mixture ratio and that at, say, a mixture ratio of one (O/F) $Y_{o_\infty} = .2$ on the average. At present there is no guide to this choice, if the steady-state distributions of oxidizer are not known. For the alcohol, oxygen system $j \approx 2.1$ and $q_o \approx 10$. Note q^* is independent of T^* under the assumptions of the wake theory so that only T^*_{∞} in the denominator affects q. All quantities are now available for the computation of T_f.

The computation of the variation of $\bar{m}_{F_f}$ is extremely difficult. If, however, the flame lies on the outside of the velocity inflection point in the mixing region, an increase in Y_{o_∞} will move the flame toward the center line where a larger velocity gradient exists. This in turn will increase the burning rate. It will be assumed that this is the case and that the dependence on Y_{o_∞} is the same as that for the droplet theories. In reality, this quantity depends in a complex manner on the ignition point velocity profile, Y_{o_∞}/j, and Y_{F_c}. Exact or even more probable behavior of this function can only be determined through experiment. At any rate it

$$\bar{m}_{F_f} / \bar{m}_{F_{f_o}} = (Y_{o_\infty} / Y_{o_{\infty_o}})^t \qquad (7)$$

where $t \sim 0.8$ and itself varies with Y_{o_∞} in a mild manner.

The final quantity for determination is a^*. Now strictly, a^* is not the droplet size but is a wake thickness and will vary depending not only upon droplet size but upon the burning and convective environment. Another fundamental assumption is that a^* is proportional to droplet size alone. This is to be interpreted as a mean size of the distribution and over the lifetime. This mean will be assumed proportional to the injected mean. Then Ingebo's correlation[21] suggests

$$a^* \propto r_j^{*\,1-n} V_F^{*-n} \qquad (8)$$

where n is between 1/2 and 1. This does not include a chamber density or pressure effect since in those experiments ρ_∞^* or p^* was not varied. Such an effect must exist, however, and the most likely candidate is a ρ^* dependence. Justification for what assumption should be made can be found in unpublished Princeton data which show only a small effect on the short length limit with a pressure increase as long as the pressure is sub-citical for the fuel. Reardon's Aerojet compilations show a very small increase in the length with a pressure increase. Equation (6) then states that $a^* \propto \rho^{-p}$, where $p \sim .4 - .5$. Thus, p will be assumed equal to .5. Similar justification will be used in computing n. A knowledge of an actual stability limit will be used to compute n; if the numbers are reasonable, i.e., $n > 0$, it will be considered not only fortunate but a rather important confirmation of the application of the theory. It should be noted that one confirmation is already given by the wake theory in that the imaginary counterpart of Equation (1) is negative, indicating a lag of the burning rate behind pressure. This was confirmed by the time lag theory and associated experimentation at the short length limit.

The final quantity for consideration is the fuel injection

velocity variation. If chamber pressure is held constant and mixture ratio varied

$$V_F \propto (O/F)^{-s} \tag{9}$$

where $s \approx 0.45$ in the range of interest and is actually a weak function of O/F itself.

Now combining Equations (5b) and (6)-(9), there results the computational equation with $(O/F)_o = 1.0$ and $(q/q_o) = (T_o/T)$

$$\frac{L}{L_o} = \left\{\frac{(T_c^2/4)+\ell \ln \ell + \gamma(b-1)}{(T_c^2/4)+\ell \ln \ell + \gamma(b_o-1)}\right\}^{\ell} (O/F)^{\ell(sn-t)} \left(\frac{c}{c_o}\right)\left(\frac{T}{T_o}\right)\left(\frac{r_j}{r_{j_o}}\right)^{\ell(1-n)} \tag{10}$$

$$= z^{\ell} (O/F)^{\ell(sn-t)} \left(\frac{c}{c_o}\right)\left(\frac{T}{T_o}\right)\left(\frac{r_j}{r_{j_o}}\right)^{\ell(1-n)}$$

which defines z. The enclosed table represents computations made for the old 3" cylindrical engine fuel-on-oxidizer impinging injector with $r_j^* = r_{j_o}^* = 0.035$ in. The propellants are ethanol and liquid oxygen at a chamber pressure of 300 psia. The reference point is $O/F = 1.0$, $L_o = 8.0$ inches. The injector design point is $O/F = 1.4$.

$p = 300$ psia $\quad Y_{F_c} = .9 \quad T_c = .2 \quad q_o = 10$

O/F	$T_{chamber}$ (^oF)	$C_{chamber}$ (ft/sec)	$T/T_o = q_o/q$	c/c_o	$Y_{o/j}$	T_f	L/L_o
1.0	4300	3770	1	1	0.10	1.817	1
1.4	5560	3940	1.292	1.044	0.14	1.827	.798
1.65	5840	3725	1.359	1.019	0.18	1.968	.833
2.2	5820	3875	1.352	.988	0.22	2.150	.937

$b = 1 \quad s = .45 \quad t = .8 \quad r_j = r_{j_o} \quad z_o = 2.211$

$$(O/F)^{.45n - .8} = \sqrt{(L/L_o)\ (c_o/c)(T_o/T)} \Big/ z$$

O/F	g	$O/F^{.45n-.8}$	n
1.0	1	1	
1.4	1.005	.765	.011
1.65	1.041	.739	.436
1.8	1.066	.728	.580
2.2	1.152	.727	.880

It is noted that in all cases $n > 0$ which, at least is reasonable even if accurate numbers are not known. It should be borne in mind that at $O/F = 1.0$ the stability map has almost closed; in fact, all stability maps close rapidly at low O/F. It is felt that such application is stretching the theory considerably since it would then be applied near both the upper and lower length limit. For this application it is preferable to only consider the results for $O/F > 1.4$. At low O/F the motor performance also deteriorates rapidly making the assumption b = constant invalid. In fact, b would increase, tending to raise the computed n to more realistic values. A salient characteristic of the low length limit is that it is concave toward long lengths on a plot of O/F vs length. To match this characteristic is a major achievement here. It can be done with a variable n, although for the injector used, there is no information to tell whether or not this is realistic. It can also be done with a fixed n. For, say, $n = 1/2$ L/L_o at first decreases due to O/F to a negative power in Equation (10). At sufficiently large O/F, however, g^2 becomes overpowering and tends to increase L/L_o. This accounts for another characteristic of stability maps: at high O/F only a gentle slope to the right occurs. This is due to the compensating effects of n and g. The fact that different injection types should produce different types of instability maps clearly appears through the form of variation of a^*. However, exactly what these dependences are is not yet clearly defined. For instance, in the fuel-on-oxidizer injection system, the resultant momentum axis of the impinging jets changes with O/F. This is not true for the like-on-like system.

Concerning changes in r_j, a* probably increases with r_j for $n < 1$. This in turn increases the lower length limit, a fact observed experimentally at Princeton. It produces an effective increase of the sensitive time lag. Such a fact is also borne out on the larger engines built today; there is no longitudinal instability at quite long lengths. Injectors of the same orifice size but of different type also follow the predicted trend. For a showerhead which produces a larger drop size than impinging jets of the same size, instability does not occur until quite long lengths. Concerning other propellant types, RP-1 while having a larger heat of combustion than ethanol also produces a larger T^*_{cc} such that q is roughly independent of propellant type. Then while μ increases c also increases and there is a compensating effect in Equation (6). The question of propellant change once again revolves about the drop size. The factors involved include surface tension and liquid density and viscosity as well as the gas phase properties and injector type. It may well be possible to determine the drop size change from instability data. Therefore, using Reference 32 , it is concluded from the lower length limit locations that a switch from ethyl alcohol to iso-octane as a fuel produced a smaller drop size. This would also be predicted from the injectors used since r_j was decreased in the iso-octane injector over that used for alcohol (.031 vs. .035 inch diameter), lending further support to the theory. Unpublished RP-1 data suggests no change, all other factors being the same.

Comparison with n, γ Theory

Including the phase effect Equations (1) and (2) along with our approximations for R_f may be written from the wake theory as

$$\dot{m}_{Ff}/\bar{\dot{m}}_F \varphi = -A + \frac{B}{\sqrt{\omega}} - i\frac{B}{\sqrt{\omega}}$$

$$A = \frac{T_f \ell}{4\gamma} + \frac{\ell}{\gamma} \ln \ell - 1$$

$$B = \frac{3}{4} \sin \pi/4 \; \frac{\bar{\dot{m}}_{Ff}}{\bar{r}_f} \ell \qquad (11)$$

From the n-τ theory

$$\frac{m_{F_f}}{\overline{m}_{F_f}\varphi} = n\left(1 - e^{-i\omega^* \tau^*}\right) \tag{12}$$

The equivalence of these two relations can only be made at a stability limit, where periodic solutions actually exist. Therefore, variations in n and τ^* with actual droplet parameters are under the constraint that one moves on a stability line. Separating into real and imaginary parts, Equations (11) and (12) become

$$n = \frac{\left(\frac{B}{\sqrt{\omega}} - A\right)^2 + \frac{B^2}{\omega}}{2\left(\frac{B}{\sqrt{\omega}} - A\right)} \tag{13}$$

$$\sin \omega^* \tau^* = -\frac{B}{\sqrt{\omega}\, n} \tag{14}$$

Abandoning the time lag theory postulate that n and τ^* are frequency independent, we now say that at the short length limit they may vary with ω while still retaining the form of Equation (12). Given the droplet parameters which appear in A and B, Equations (13) and (14) may be used to determine n and τ^* as functions of frequency, ω . It remains to be ascertained if the relationships between n , τ^*, and ω can be similar to those obtained from the time-lag theory, and if so, in what range of droplet parameters does the similarity occur.

NOMENCLATURE

a	droplet diameter
c	speed of sound
c_p	specific heat at constant pressure
i	imaginary number ($\sqrt{-1}$)
j	stoichiometric mass ratio of fuel to oxidizer
L	chamber length at high-frequency stability limit
m	total mass flux in radial direction
M	Mach number
$\mathcal{M}$	space dependent part of m perturbation
n	interaction index or exponent in Equation (8)
O/F	mixture ratio
p	pressure or exponent in droplet diameter and density relation
q	stoichiometric heat of reaction
r	radial coordinate
R_f	perturbation magnitude of flame movement
R_e	Reynolds number
S	exponent in Equation (9)
t	exponent in Equation (7)
T	temperature
Y	mass fraction
$\mathcal{J}$	defined by Equation (10)
γ	ratio of specific heats
μ	viscosity
ξ	axial variable
ρ	density
ω	frequency

Subscripts:

c	core centerline value (at $\xi = 0$ unless indicated by ξ in argument)
f	quantity at flame

F	fuel or fuel side of flame
0	oxidizer, oxidizer side of flame, or initial value
∞	free stream value

Superscripts:

$-$	steady-state quantity
*	dimensional quantity

VI. HIGH-SUBSONIC MACH NUMBER EXTENSION TO THE LINEARIZED THEORY

Using a simplified model for the rocket engine, whereby all combustion was concentrated* in a narrow zone, Crocco and Cheng studied the stability behavior of the flow system in the rocket chamber when small perturbations on the steady-state operation were introduced. The analysis assumed that the flow Mach numbers in the chamber were so low that steady-state thermodynamic properties were constant on either side of the flame front. In effect this involved ignoring terms which were of the magnitude of the Mach number squared.

Since that time, rocket engine configurations have been built with increasingly lower contraction ratios ($M > .5$ is not uncommon), which makes the terms of the order of the Mach number squared more important.

In the past year work has been done to extend the analysis of Crocco and Cheng to include these effects of higher chamber Mach numbers. Most of the assumptions and the methods of analysis of the original work are retained. In general, a steady-state flow system using the concentrated combustion front is used, small perturbations on the steady-state are applied, and the stability behavior is examined. The chamber oscillations are supported by means of variations in the burning rate which are described by means of the time-lag concept.

A combustion chamber is separated into two regions; Region 0, which contains stagnant gaseous combustion products with liquid propellant droplet flowing through it with constant velocity $U_{\ell_o}^*$, and Region 1 which contains gaseous combustion products of the same composition flowing with some uniform axial velocity U_1^*. The flame front separates the two regions. The propellant droplets are considered to be instantaneously and completely burned at the flame front. One-dimensional flow is assumed. The following equations describing the steady-state conditions in the chamber are written:

*They studied the stability behavior of the flow system for the more general case of distributed combustion, as well.

$$\bar{\rho}_1^* \, \bar{u}_{1_0}^* = \bar{\rho}_1^* \, \bar{u}_1^* \qquad \text{continuity} \qquad (1)$$

$$\bar{p}_0^* + \bar{\rho}_1^* \, \bar{u}_{1_0}^{2*} = \bar{p}_1^* + \bar{\rho}_1^* \, u_1^{*2} \qquad \text{momentum} \qquad (2)$$

$$h_0^* = h_1^* + \tfrac{1}{2} \, \bar{u}_1^{*2} \qquad \text{energy} \qquad (3)$$

The starred quantities are dimensional. The quantities are non-dimensionalized with respect to conditions in Region 0 in the following manner:

$$\bar{\rho}_1 = \frac{\bar{\rho}_1^*}{\bar{\rho}_0^*} \qquad \bar{u}_{1_0} = \frac{u_{1_0}^*}{c_0^*} \qquad \bar{p}_0 = \frac{\bar{p}_0^*}{\bar{p}_0^*} = 1 = \bar{\rho}_0^* = \bar{T}_0^* = h_0^*$$

$$\bar{u}_1 = \frac{u_1^*}{c_0^*} \qquad \bar{h}_1 = \frac{h_1^*}{h_0^*} = \frac{(\gamma-1)}{\gamma} \frac{\bar{h}_1^*}{RT_0^*} = \bar{T}_1$$

$$t = \frac{t^*}{L^*/c_0^*} = \frac{t^*}{\theta} \qquad X = \frac{X^*}{L^*}$$

The equations are rewritten:

$$\bar{\rho}_1 \, \bar{u}_1 = \bar{\rho}_1 \, \bar{u}_1 \qquad (4)$$

$$1/\gamma + \bar{\rho}_1 \, \bar{u}_1^2 = \frac{\bar{p}_1}{\gamma} + \bar{\rho}_1 \, \bar{u}_1^2 \qquad (5)$$

$$\bar{h}_1 = \bar{T}_1 = 1 - \frac{\gamma-1}{2} \, \bar{u}_1^2 \qquad (6)$$

The perfect gas assumption yields:

$$\frac{\bar{p}}{\bar{\rho}} = \bar{T} \qquad (7)$$

Combining (4) and (5) :

$$\bar{p} = 1 + \gamma \bar{\rho}_1 \, \bar{u}_1 (\bar{u}_{1_0} - \bar{u}_1) \qquad (8)$$

or

$$\bar{p}_1 = \left[1 - \frac{\gamma \bar{u}_1^2 (k-1)}{1-\left(\frac{\gamma-1}{2}\right)\bar{u}_1^2}\right] \tag{9}$$

where $$k \equiv \frac{\bar{u} f_0}{\bar{u}_1}$$

Non-steady state conservation equations are written for either Region 1 or Region 0 as:

<u>continuity</u>:

$$\frac{\partial u}{\partial t} + u \frac{\partial \rho}{\partial x} + \rho \frac{\partial u}{\partial x} = 0 \tag{10}$$

<u>momentum</u>:

$$\rho \frac{\partial u}{\partial t} + \rho u \frac{\partial u}{\partial x} + \frac{1}{\gamma} \frac{\partial \rho}{\partial x} \tag{11}$$

The energy equation is replaced by the isentropic assumption as follows:

$$p = \rho^{\gamma} \tag{12}$$

Let

$$p = \bar{p} + p' \quad \rho = \bar{\rho} + \rho' \quad u = \bar{u} + u'$$

where p', ρ', u' are perturbation quantities so small that their products and squares can be ignored.

If the steady-state equations are subtracted from (10) and (11), they become:

$$\frac{\partial \rho'}{\partial t} + \bar{u} \frac{\partial \rho'}{\partial x} + \bar{\rho} \frac{\partial u'}{\partial x} = 0 \quad \text{continuity} \tag{13}$$

$$\bar{\rho} \frac{\partial u'}{\partial t} + \bar{\rho} \bar{u} \frac{\partial u'}{\partial x} = \frac{1}{\gamma} \frac{\partial p'}{\partial x} \quad \text{momentum} \tag{14}$$

These equations correspond to the wave equation for a one-dimensional, uniform flow field. The general solution can be written:

$$u' = f_1' \left[x-(\bar{u}+\bar{c})t\right] + f_2' \left[x-(\bar{u}-\bar{c})t\right]$$

$$\rho' = \frac{\bar{\rho}}{\bar{c}} (f_1'-f_2')$$

$$p' = \gamma \frac{\bar{p}}{\bar{c}} (f_1'-f_2')$$

Note that the functions f_1', and f_2' are not the same in Regions 0 and 1.

Since f_1' and f_2' are arbitrary functions of their arguments, and since periodic solutions for u', ρ', p' are desired, the functions f_1' and f_2' are written:

$$f_1' = C_r \exp S(t - a_r x) \tag{15}$$

$$f_2' = C_s \exp S(t - a_s x) \tag{16}$$

where

$$a_r = \frac{1}{\bar{u}+\bar{c}} \qquad a_s = \frac{1}{\bar{u}-\bar{c}}$$

$$S = \Lambda + i\Omega$$

Using (15) and (16), the perturbations become

$$u' = \nu(x) \exp St \tag{17}$$

$$\rho' = \frac{\bar{\rho}}{\bar{c}} \sigma(x) \exp St \tag{18}$$

$$p' = \frac{\gamma\bar{p}}{\bar{c}} \sigma(x) \exp St \tag{19}$$

where $$\nu(x) = C_r \exp(-a_r S x) + C_s \exp(-a_s S x) \tag{20}$$

$$\sigma(x) = C_r \exp(a_r S x) - C_s \exp(-a_s S x) \tag{21}$$

(20) and (21) represent four equations, two for Region 0 and two for Region 1, so that there are four constants to be determined.

Two boundary conditions and two matching conditions are available to determine the four constants.

At the injector face $\mu' = 0$ and $x = 0$ and, therefore, Equations (17) and (20) yield

$$\frac{C_{r_0}}{C_{s_0}} = -1 \tag{22}$$

At the chamber exit plane $x = 1$ and

$$\frac{\left(\frac{u'}{\bar{u}_1}\right)}{\left(\frac{\rho'}{\bar{\rho}_1}\right)} = \frac{\left(\frac{v_1(x)}{\bar{u}_1}\right)}{\left(\frac{\nabla_1(x)}{\bar{c}_1}\right)} = \alpha$$

where α is the nozzle specific admittance coefficient (Reference 4.) Then, Equations (17), (18), (20), and (21) yield

$$\frac{C_{r_1}}{C_{s_1}} = -\left[\frac{1+\frac{\bar{u}_1\alpha}{\bar{c}_1}}{1-\frac{\bar{u}_1\alpha}{\bar{c}_1}}\right] \exp S(a_{r_1} - a_{s_1})$$

$$= B \exp S(a_{r_1} - a_{s_1}) \tag{23}$$

where $B \equiv \left[\frac{1+\frac{\bar{u}_1\alpha}{\bar{c}_1}}{1-\frac{\bar{u}_1\alpha}{\bar{c}_1}}\right]$

Using (22) and (23), the space-dependent parts of the perturbation become

$$v_0(x) = C_{s_0} \exp(-s a_{s_0} x)\left\{1 - \exp[-s(a_{r_0} - a_{s_0})x]\right\} \tag{24}$$

$$\nabla_0(x) = -C_{s_0} \exp(-s a_{s_0} x)\left\{1 + \exp[-s(a_{r_0} - a_{s_0})x]\right\} \tag{25}$$

$$v_1(x) = C_{s_1} \exp(-s a_{s_1} x)\left\{1 - B \exp[s(a_{r_1} - a_{s_1})(1-x)]\right\} \tag{26}$$

$$\nabla_1(x) = -C_{s_1} \exp(-s a_{s_1} x)\left\{1 + B \exp[s(a_{r_1} - a_{s_1})(1-x)]\right\} \tag{27}$$

At the flame front, the steady-state conservation equations for mass and momentum are:

$$\bar{\rho}_l \bar{u}_{l_0} = \bar{\rho}_1 \bar{u}_1 \qquad \text{mass}$$

$$\frac{\bar{p}_0}{\gamma} + \bar{\rho}_l \bar{u}_{l_0}^2 = \bar{\rho}_1 \bar{u}_1^2 + \frac{\bar{p}_1}{\gamma} \qquad \text{momentum}$$

The assumption has been made earlier that $\bar{\rho}_l \bar{u}_{l_0}$ is a constant, independent of time. This implies that the same amount of mass is always entering the flame front due to the liquid droplets. The amount of mass leaving the flame front is dependent upon both the amount of gas and liquid entering the flame front and the amount of gas produced in the flame front. Under steady-state conditions, no gas enters the flame front, and gas is produced in the flame front at the same rate liquid mass enters. Under a perturbation of the steady-state pressure, the burning rate also undergoes a perturbation. Under such a perturbation the change in the amount of mass produced in the flame front is equal to the difference between the incoming liquid mass flow and the outgoing mass flow less the incoming mass flow. That is

$$\Delta m = -\bar{\rho}_l \bar{u}_{l_0} + \rho_1 u_1 - \rho_0 u_0' \qquad (28)$$

Similarly, the amount of momentum produced under steady-state conditions must be equal to the incoming liquid momentum plus the pressure difference between the pressure in Region 0 and the pressure in Region 1. Under a perturbation, the amount of incoming liquid momentum is constant. The change in the amount of momentum which must be produced is thus equal to the difference in pressures between Regions 0 and 1 under the perturbation, plus the outgoing gas momentum less the incoming gas momentum less the incoming liquid momentum. This relationship may be written:

$$\Delta mv = \frac{p_1 - p_0}{\gamma} - \bar{\rho}_l \bar{u}_{l_0}^2 - \rho_0 u_0'^2 + \rho_1 u_1^2 \qquad (29)$$

The assumption is now made that Δmv, the amount of momentum produced

in the flame front is equal to the product of Δm, the change in mass produced in the flame front under perturbation and $\bar{u}_{l_o}$. That is, it is assumed that all mass produced in the flame front is released with constant velocity equal to the velocity of the incoming liquid droplets. This relationship is written:

$$\Delta m_f = (\Delta m)\,\bar{u}_{l_o} . \tag{30}$$

Using (28) as substituting (30) into (29), (29) may be rewritten (neglecting the higher order term $u_o'^2$):

$$-\bar{\rho}_l\,\bar{u}_{l_o}^2 + \rho_1 u_1 \bar{u}_{l_o} - u_o' \bar{u}_{l_o} = \frac{p_1 - p_o}{\gamma} - \bar{\rho}_l\,\bar{u}_{l_o}^2 + \rho_1 \bar{u}_1^2 \tag{31}$$

Rewriting the quantities used above as the sum of their steady-state values and a small perturbation of this steady-state value, the following equation results when the steady-state momentum equation is subtracted:

$$\frac{p_o' - p_1'}{\gamma} = 2\bar{\rho}_1\,\bar{u}_1 u_1' + k\,\bar{u}_1(\bar{\rho}_1\bar{u}_1'\rho_1' - u_o') \tag{32}$$

This equation is solved to yield the ratio between the perturbation quantities p_o' and p_1':

$$\frac{p_o'}{p_1'} = \frac{1 + \bar{\rho}_1\bar{u}_1\frac{u_1'}{\rho_1'}(2-k) - \frac{k}{\gamma}\frac{\bar{u}_1^2}{\bar{T}_1}}{1 + k\,\bar{u}_1\frac{u_o'}{p_o'}} \tag{33}$$

Mass conservation at the flame front requires that $\Delta m = \dot{m}_b$ if $\dot{m}_b$ is change in burning rate under a small perturbation. It follows that

$$\frac{\Delta m - \bar{\rho}_1\bar{u}}{\bar{\rho}_1\,\bar{u}_1} = \frac{\dot{m}_b - \bar{\dot{m}}_b}{\bar{\dot{m}}_b} \equiv \mu_b \tag{34}$$

where μ_b is the fractional increase in burning rate.

The assumption is now made that all propellant elements have the same sensitive time-lag. In this case, μ_b may be

expressed as (see Crocco and Cheng, Ch. I)

$$\mu_b = -\frac{d\tau}{dt}$$

where τ is the sensitive time-lag.

In general:

$$\tau - \bar{\tau} = -\frac{n}{\bar{f}(t-\bar{\tau})} \int_{t-\tau}^{t} \frac{\bar{f}(t')}{\bar{p}(t')} p'(t')\, dt' \qquad (35)$$

f(t) represents the processes which must accumulate before combustion can occur. That is, combustion occurs at time t according to the criterion

$$\int_{t-\tau}^{t} f(t')\, dt' = E_A$$

where E_A has a certain value.

n is an interaction index dependent upon propellant properties and defined as $n = \frac{p}{\rho}\left(\frac{\partial f}{\partial p} + \frac{\partial T}{\partial p}\frac{\partial f}{\partial T} + \frac{dZ}{dp}\frac{\partial f}{\partial Z} \cdots\right)$ where Z is an arbitrary variable.

Since all preparatory processes take place in Region 0, $\bar{f}(t)$ is a constant and $\bar{p}(t') = \bar{p}_o = 1$.

Thus, (35) may be written

$$\tau - \bar{\tau} = -n \int_{t-\bar{\tau}}^{t} p'(t')\, dt'$$

$$\frac{d\tau}{dt} = -n\left[p'(t) - p'(t-\bar{\tau})\right]$$

$$\mu_b = n\left[p'(t) - p'(t-\bar{\tau})\right]$$

The time used in the last expression above is a Lagrangian Coordinate time; in order to be consistent this is rewritten

$$\mu_b = n\left[p'(\psi, t) - p'(\xi, t-\bar{\tau})\right] \qquad (36)$$

t is now time in the coordinate system stationary with respect to the combustion chamber. ξ is the position of the flame front, is the axial position at which the propellant element that burns

at time t first becomes sensitive.

The assumption is now made that Ψ is so close to ξ for the time lags under consideration that $p'(\xi, t) \approx p'(\Psi, t)$. This implies that the production of mass may vary with time but the location of the flame front does not.

Under this assumption (36) may be written

$$\mu_b = n\gamma\, \sigma_0 \left[\exp(st) - \exp s(t-\tau)\right] \tag{37}$$

$$= n\gamma\, \sigma_0 \exp st \left[1 - \exp(-s\tau)\right] \tag{38}$$

This expression may be combined with (34) to yield

$$n\gamma\, \sigma_0 \exp st \left[1 - \exp(-s\tau)\right] = \frac{\rho_1' \bar{u}_1 + \bar{\rho}_1 u_1' - u_0'}{\bar{\rho}_1 \bar{u}_1} \tag{39}$$

This may be written in the form

$$\bar{u}_1 \bar{\rho}_1 n\gamma \left[1 - \exp(-s\tau)\right] = \frac{\bar{u}_1 + \frac{\bar{T}_1}{\bar{\rho}_1}\frac{u_1'}{p_1'}}{\frac{\bar{T}_1}{\bar{\rho}_1}} - \frac{u_0'}{\rho_0'} \tag{40}$$

From (17) and (18), it is found that

$$\frac{u_1'}{p_1'} = \frac{V_1(x)}{\sigma_1(x)} \qquad \frac{u_0'}{\rho_0'} = \frac{V_0(x)}{\sigma_0(x)}$$

If these two relationships and (33) are substituted in (40) the following equation results:

$$\bar{u}_1 \bar{\rho}_1 n\gamma \left[1 - \exp -(s\tau)\right]$$

$$= \frac{\bar{u}_1\left[1 + \beta \exp \Psi\right] - \bar{\tau}_1\left[1 - \beta \exp \Psi\right]\left[1 + \frac{n\bar{T}_1}{\gamma}\left(\frac{1-\exp(-2\beta)}{1+\exp(\beta+2sx)}\right)\right] + \frac{1-\exp(-2sx)}{1+\exp(-2sx)}}{D(1+\beta \exp \Psi) - (2-k)\,\bar{u}_1\,\bar{c}_1\,\bar{T}_1\left[1 - \beta \exp \Psi\right]} \tag{41}$$

where $\Psi = s\bar{A}(1-x)$, $D = \bar{T}_1 - \frac{n^2 k}{\gamma}$, $\bar{A} = \frac{2\bar{\tau}_1}{\bar{c}_1^2 - \bar{u}_1^2}$

X represents the axial position of the flame front. This equation may be reduced to the form:

$$P + M\exp(-2sx) + \left[N + L\exp(-2sx)\right]\exp \Psi$$

$$+ \left[E + E\exp(-2sx)\right]\exp(-s\tau) + \left[F + F\exp(-2sx)\right]\exp(\Psi - s\tau) = 0 \tag{42}$$

where E, F, L, M, N, and P are defined later.

In order to find the neutral stability relationships, Λ is set = 0, $S = i\omega$, and the corresponding $\bar{\tau} = \delta$.

If (42) is separated into its real and imaginary parts, the following two equations are obtained:

$$a + c\cos s - d\sin s + e\cos\phi + f\sin\phi + g\cos(s-\phi) - h\sin(s-\phi) = 0 \quad (43)$$

$$b + d\cos s + c\sin s + f\cos\phi - e\sin\phi + g\sin(s-\phi) + h\cos(s-\phi) = 0 \quad (44)$$

where

$$s \equiv \omega\bar{\Lambda} \qquad \phi \equiv \omega\delta$$

$$a \equiv P + M\cos 2\omega x \;;\; b \equiv -M\sin 2\omega x$$

$$c \equiv N(B_{re}\cos 2\omega x + B_{Im}\sin 2\omega x) + L\left(B_{Re}\cos(2\omega x + sx) + B_{Im}\sin(2\omega x + sx)\right)$$

$$d \equiv N(B_{Im}\cos 2\omega x - B_{Re}\sin 2\omega x) + L\left[B_{Im}\cos(2\omega x + sx) - B_{Re}\sin(2\omega x + sx)\right]$$

$$e \equiv E + E\cos 2\omega x \;;\; f \equiv -E\sin 2\omega x$$

$$g \equiv F\left[B_{Re}(\cos 2\omega x + \cos(2\omega x + sx)) + B_{Im}(\sin 2\omega x + \sin(2\omega x + sx))\right]$$

$$h \equiv F\left[B_{Im}(\cos 2\omega x + \cos 2\omega x + sx) - B_{Re}(\sin 2\omega x + \sin(2\omega x + sx))\right]$$

$$P \equiv \bar{u}_1\bar{\rho}_1 n\gamma\left(D - \bar{u}_1\bar{c}_1\bar{T}_1(2-k)\right) - \left(D - \bar{u}_1\bar{c}_1\bar{T}_1(2-k)\right) - (\bar{u}_1 - \bar{c}_1)\left(1 + \frac{2}{\gamma}\bar{u}_1\right)$$

$$M \equiv \left(D - \bar{u}_1\bar{c}_1\bar{T}_1(2-k)\right)(\bar{u}_1\bar{\rho}_1 n\gamma + 1) - (\bar{u}_1 - \bar{c}_1)\left(1 - \frac{2}{\gamma}\bar{u}_1\right)$$

$$N \equiv \left(D + \bar{u}_1\bar{c}_1\bar{T}_1(2-k)\right)(\bar{u}_1\bar{\rho}_1 n\gamma - 1) - (\bar{u}_1 + \bar{c}_1)\left(1 + \frac{2}{\gamma}\bar{u}_1\right)$$

$$L \equiv \left(D + \bar{u}_1\bar{c}_1\bar{T}_1(2-k)\right)(\bar{u}_1\bar{\rho}_1 n\gamma + 1) - (\bar{u}_1 + \bar{c}_1)\left(1 - \frac{2}{\gamma}\bar{u}_1\right)$$

$$E \equiv -\bar{u}_1\bar{\rho}_1 n\gamma\left(D - \bar{u}_1\bar{c}_1\bar{T}_1(2-k)\right)$$

$$F \equiv -\bar{u}_1\bar{\rho}_1 n\gamma\left(D + \bar{u}_1\bar{c}_1\bar{T}_1(2-k)\right)$$

B_{re} and B_{Im} are the real and imaginary parts of B.

$$B_{re} = \frac{\bar{\rho}_1^2\bar{c}_1^2 - \bar{u}_1^2\left(\alpha_r^2 + \alpha_{Im}^2\right)}{\left(\bar{\rho}_1\bar{c}_1 - \bar{u}_1\alpha_r\right)^2 + \bar{u}_1^2\alpha_{Im}^2}$$

$$B_{Im} = \frac{2\bar{\rho}_1\bar{c}_1\alpha_{Im}}{\left(\bar{\rho}_1\bar{c}_1 - \bar{u}_1\alpha_r\right)^2 + \bar{u}_1^2\alpha_{Im}^2}$$

α_{re} and α_{Im} are the real and imaginary parts of the nozzle specific admittance ratio.

After some manipulations, (43) and (44) are solved to give

the following relationships for s and ϕ :

$$\cos s = \frac{-A\mathcal{B} + C\sqrt{\mathcal{B}^2 - A^2 + C^2}}{\mathcal{B}^2 + C^2} \tag{45}$$

$$\cos \beta = \frac{-IH + J\sqrt{H^2 - I^2 + J^2}}{H^2 + J^2} \tag{46}$$

$$A \equiv a^2 + b^2 + c^2 + d^2 - (e^2 + f^2 + g^2 + h^2)$$
$$\mathcal{B} \equiv 2(ac + bd - eg - fh)$$
$$C \equiv 2(bc - ad + eh - fg)$$
$$I \equiv a^2 + b^2 + e^2 + f^2 - (d^2 + c^2 + g^2 + h^2)$$
$$H \equiv 2(ae + bf - gc - dh)$$
$$J \equiv 2(af - be - hc + dg)$$

The right-hand sides of Equations (45) and (46) above are complicated functions of ω and n. Since no simple solution has been found for the general case, an iteration procedure has been adopted. In this procedure for given values of π_1, k, and γ, an ω is selected. A trial value of n is then chosen and the right and left-hand sides of Equation (45) are calculated and compared to each other. Succeeding values of n are chosen until the left-hand side is equal to the right hand side. This will give a value of n which corresponds to the selected value of ω. Using these values of ω and n $\phi = \omega\delta$ may be calculated. Thus, a value of $\omega\delta$ for the given n is also obtained. Using this technique, the neutral stability curves for ω vs n and $\omega\delta$ vs n, may be plotted. Since $\delta = \frac{\omega\delta}{\omega}$ the neutral stability curve for δ vs n is also obtained.

In the simple case of combustion concentrated at the injector face and short nozzle, $X = 0$, $B_{Im} = 0$, and the equations are greatly simplified:

$$\text{Cos } s = -\frac{A}{B} \tag{47}$$

$$\text{Cos } \phi = -\frac{I}{H} \tag{48}$$

where A , B , I , H are no longer functions of ω , and the iteration procedure is not necessary.

Results and Conclusions

At the present time, numerical results are available only for the simple case of short nozzle and combustion concentrated at injector. Numerical analysis is proceeding for the more involved cases of arbitrary axial location and long nozzles.

Equations (47) and (48) were solved using Chamber exit Mach numbers of $M_E = .417$ and $M_E = .207$. The solutions are shown in Figs. VI-1, -2, -3. Some effects of increasing Mach number are readily seen. First, there is a shifting of the minimum n which will support unstable oscillations toward larger values of n . This can be seen by comparing the minimum n for $M_E = .417$ and $M_E = .207$ in Figure -1 or -2. The linear (in Mach number) analysis of Crocco and Cheng predicted a minimum n of .46 regardless of Mach number. As can be seen from Figure -1 or -2, agreement with this value is close for $M_E = .207$. However, for $M_E = .417$ a noticeable increase occurs ($n_{min} = .54$). This seems to indicate that a larger forcing function is required at the fundamental frequencies of the chamber in order to produce instability as the Mach number in the chamber is increased. The effect is not too large, for a $M_E = .620$, n_{min} increases only to .56.

A second effect, due to consideration of all orders of Mach number, may also be seen in Figures -1, -2, and -3. This effect is the existence of a maximum n above which no stable region can be found. At this maximum n, ω , the dimensionless frequency, is exactly half-way between the fundamental frequencies of the chamber. The fundamental frequencies of the chamber are the frequencies which would be present in the chamber if, at both ends, it reflected compression waves as compression waves, and expansion waves as expansion waves with no phase or delay in reflection. In Figure -1, these fundamental frequencies are found as the frequencies

corresponding to the peaks of the stability curve at n_{min}. These fundamental frequencies have the values of $\omega = \frac{\ell\pi}{\lambda}$ where $\ell = 1, 2, 3...$ The frequencies of oscillation at n max are furthest from the fundamental values and thus are hardest to support. At n_{max}, however, these oscillations can be supported. This implies that for n greater than n_{max}, oscillations at any frequency can be supported and the chamber is absolutely unstable.

Chamber Mach number has a profound effect upon the value of n_{max}. As can be seen from Figure -1, n max for $M_E = .417$ is equal to 1.85. For $M_E = .207$, however, n_{max} is so large as to be off the scale. This is in agreement with the results of Crocco for the case of low Mach number. He predicted no n_{max}, and it is found, when all orders of Mach number are considered, that for low M_E, n_{max} has a value which is above the range of n of practical interest, and, in the limit of very small Mach numbers, n_{max} tends to infinity.

Another consequence of considering all orders of Mach number is the shifting down of the ω vs. n curve and the shifting up of the δ vs n curve. This effect can be seen in Figures -1 and -3 if one looks at the curves for the same mode numbers at the two different M_E's, .417 and .207. It should be noted here that the m numbers come from Figure 2. From the solution of (47), it is found that $\omega\delta$ has the closed curve shape seen in Figure 2 and that the horizontal line of symmetry may be located at $\omega\delta = (2m+1)\pi$ where m = 0 , 1 , 2 , 3 , ... In Figure -3 results using m = 0 and m = 1 are shown. Since $\delta = \frac{\omega\delta}{\omega}$ an m and an ℓ must be specified for a given δ curve. In Figure -3, the m and on the various curves correspond to the m and ℓ of the corresponding ω and $\omega\delta$ curves which were cross-plotted to yield the δ vs n curve.

The shifting of the ω vs n curve to lower ω for higher Mach numbers at the fundamental frequencies can be explained as an effect due to the change of wave propagation time in the chamber.

The time required for a wave to travel from one end of the chamber to the other and back again in steady-state is:

$$T^* = \frac{L^*}{c_1 + u_1} + \frac{L^*}{c_1 - u_1} = \frac{2\bar{T}_1 L^*/c_0^*}{c_1^2 - u_1^2} \cdot \frac{c_0^*}{c_0^*} = \frac{2\bar{T}_1}{c_1^2 - u_1^2} \cdot \frac{L^*}{c_0^*}$$

L^*/c_0^* is the factor we used earlier to nondimensionalize time. Thus the equation above becomes in non-dimensional form:

$$T = \frac{2\bar{T}_1}{c_1^2 - u_1^2} \tag{49}$$

This expression is precisely equal to $\tilde{\Lambda}$. Since, for fundamental frequencies $\omega = \frac{2\ell\pi}{\tilde{\Lambda}}$, then using (49):

$$\omega = \frac{2\ell\pi}{T} \tag{50}$$

This implies that as the wave travel time increases, the fundamental frequency decreases for given ℓ. Since T increases with Mach number, ω must decrease with Mach number.

The values of $\omega\delta$ at n_{min} are $\omega\delta = (2m+1)\pi$, therefore, $\omega\delta$ does not shift at n_{min} for increasing Mach number. The quantity δ is the product of $\frac{1}{\omega}$ and $\omega\delta$ and therefore it must shift up at n_{min} for increasing Mach number.

Some general comments should be made about the curves in Figures -1, -2, and -3. First, all the curves plotted are continuous and have infinite slopes at n_{max} and n_{min}. This can be shown analytically for the simple case of short nozzle and concentrated combustion at the injector. Secondly, if the Mach number is allowed to become very small, the curves exactly duplicate the results of the linear analysis for n in the range of practical interest (up to about 5). At very large n, however, there will exist an n_{max} even for very small Mach numbers and the curves will still be continuous. The curve of Figure -3 will become several curves, all continuous, if all possible combinations of m and ℓ are considered. These curves will cover practically the whole area between n_{min} and

n_{max} with unstable regions. The curves are, in general, slightly more spread out for given m and $\mathcal{L}$ for larger Mach numbers, thus predicting an increase in the size of the instability regions.

In conclusion, for the simple case of short nozzle and concentrated combustion, two effects on stability are to be recognized as higher Mach numbers are considered. The first is the shifting of n_{min} to higher values of n indicating increasing stability. The second is the spreading out of the δ vs n curve away from n_{min} which indicates decreasing stability.

NOMENCLATURE

C*	local speed of sound
C^*_o	speed of sound in stagnant burned gases
L*	chamber length from injector to entrance of nozzle
$\theta = \frac{L^*}{C^*_o}$	time required for wave to travel chamber length in stagnant gas
X*	axial length from injector end of chamber
U*	mean gas velocity in axial direction
M_E	Mach number at entrance to nozzle
p*	pressure of burnt gas
ρ^*	density of burnt gas
T*	temperature of burnt gas
h*	enthalpy of burnt gas
ρ_l^*	density of liquid propellant element
U*	velocity of liquid propellant element
k	constant relating $\bar{u}$ and $\bar{u}_1$
λ^*	amplification coefficient
Ω^*	angular frequency
ω^*	neutral angular frequency
n	interaction index
τ^*	time lag
δ^*	critical value of time lag corresponding to neutral oscillations

$\alpha = \alpha_R + i\alpha_I$ specific admittance ratio of deLaval nozzle

γ^* axial location of the concentrated combustion front

superscript* indicates dimensional quantity

superscript' indicates a small perturbation

subscript$_o$ indicates quantity evaluated in Region 0

subscript$_1$ indicates quantity evaluated in Region 1

subscript$_\ell$ indicates quantity pertaining to liquid propellant element

$\bar{\ }$ over a quantity indicates steady-state

subscripts$_{R_e}$ and $_{I_m}$ indicate the real and imaginary parts of a quantity, respectively.

APPENDIX A

EXPRESSIONS FOR TRANSVERSE WAVES

Expansions of the inhomogeneous parts of the second-order equations will follow:

I. **EXPRESSIONS FOR SPINNING WAVE.**

Continuity Equation:

$$-\left\{\sum_{j=1}^{\infty}\left[\left(A_{oj}\,\bar{r}^{2}\frac{d}{d\phi}\left(R^{(1)}\frac{d}{d\phi}\Phi^{(1)}\right)+B_{oj}\,z\,\bar{r}\,\bar{r}\left(R^{(1)}V^{(1)}\right)\right)\frac{1}{2}\right)J_{o}\left(S_{oj}\sqrt{\Psi}\right)\right.$$

$$+\frac{1}{2}\left(A_{2\nu j}\,\bar{r}^{2}\frac{d}{d\phi}\left(R^{(\nu)}\frac{d}{d\phi}\Phi^{(\nu)}\right)+\left(B_{2\nu j}\,z-C_{2\nu j}\,\nu^{2}\right)\bar{r}\,\bar{r}\,R^{(\nu)}V^{(\nu)}\right)\frac{1}{2}\left(e^{2i(\omega t+\nu\theta)}\right.$$

$$\left.\left.+\,e^{-2i(\omega t+\nu\theta)}\right)J_{2\nu}\left(S_{2\nu j}\sqrt{\Psi}\right)\right]\right\}=-\left\{\sum_{j=1}^{\infty}\left(E_{oj}\,J_{o}\left(S_{oj}\sqrt{\Psi}\right)\right.\right.$$

$$\left.\left.+\,E_{2\nu,j}\,\frac{1}{2}\left(e^{2i(\omega t+\nu\theta)}+e^{-2i(\omega t+\nu\theta)}\right)J_{2\nu}\left(S_{2\nu j}\right)\right\}\right.$$

ϕ- momentum:

$$\sum_{s=1}^{\infty}\Bigg[\Bigg(A_{0s}\Bigg\{\frac{1}{4}\frac{d\bar{r}^2}{d\phi}\left[\frac{\gamma}{c^2}P^{(s)2}-R^{(s)2}\right]+R^{(s)}\frac{dP^{(s)}}{d\phi}-\frac{1}{2}S^{(s)}R^{(s)}\frac{d\bar{r}^2}{d\phi}$$

$$-\frac{\bar{r}^2}{2}\frac{d}{d\phi}\left(\frac{d\bar{r}^{(s)}}{d\phi}\right)^2-\frac{1}{2}\left(\frac{d\bar{\Phi}^{(s)}}{d\phi}\right)^2\frac{d\bar{r}^2}{d\phi}\Bigg\}-D_{0s}\Bigg\{\frac{d}{d\phi}\left(\bar{r}\bar{\rho}V^{(s)2}\right)-\bar{r}\bar{\rho}\frac{d}{d\phi}\left(V^{(s)}\right)^2$$

$$+2\bar{r}\bar{\rho}V^{(s)}\frac{d}{d\phi}\left(\bar{\Phi}^{(s)}\right)\Bigg\}-C_{0s}\Bigg\{\frac{\lambda^2}{4}V^{(s)2}\frac{d}{d\phi}\left(\bar{r}\bar{\rho}\right)+\frac{\lambda^2}{2}\bar{r}\bar{\rho}V^{(s)}\frac{d}{d\phi}\bar{\Phi}^{(s)}\Bigg\}\Bigg)\frac{1}{2}J_0\left(\zeta_{0s}\sqrt{\Psi}\right)$$

$$+\frac{1}{2}\Bigg(A_{2s}\Bigg\{\frac{1}{4}\frac{d\bar{r}^2}{d\phi}\left[\frac{\gamma}{c^2}P^{(s)2}-R^{(s)2}\right]+R^{(s)}\frac{dP^{(s)}}{d\phi}-\frac{1}{2}S^{(s)}R^{(s)}\frac{d\bar{r}^2}{d\phi}-\frac{\bar{r}^2}{2}\frac{d}{d\phi}\left(\frac{d\bar{r}^{(s)}}{d\phi}\right)^2$$

$$-\frac{1}{2}\left(\frac{d\bar{\Phi}^{(s)}}{d\phi}\right)^2\frac{d\bar{r}^2}{d\phi}\Bigg\}-D_{2s}\Bigg\{V^{(s)2}\frac{d}{d\phi}\left(\bar{r}\bar{\rho}\right)+2\bar{r}\bar{\rho}V^{(s)}\frac{d}{d\phi}\bar{\Phi}^{(s)}\Bigg\}$$

$$+\lambda^2C_{2s}\Bigg\{\frac{1}{4}V^{(s)2}\frac{d}{d\phi}\left(\bar{\rho}\bar{r}\right)+\frac{1}{2}\bar{r}\bar{\rho}V^{(s)}\frac{d}{d\phi}\bar{\Phi}^{(s)}\Bigg\}\Bigg)\frac{1}{2}\left(e^{\lambda\left(\alpha\cos\left(\gamma+\omega t\right)\right)}+e^{-\lambda\left(\alpha\cos\left(\gamma+\omega t\right)\right)}\right)J_{2s}\left(\zeta_{2s}\sqrt{\Psi}\right)\Bigg]$$

$$= \sum_{g=1}^{\infty} \left\{ B_{0,g} J_0(S_{0g}\sqrt{\Psi}) + B_{2\nu,g} \tfrac{1}{2}\left(e^{2i(\omega t+\nu\theta)} + e^{-2i(\omega t+\nu\theta)}\right) J_{2\nu}(S_{2\nu,g}\sqrt{\Psi}) \right\}$$

Ψ - Momentum:

$$\sum_{g=1}^{\infty} \left\{ \left(A_{0g} \left\{ \tfrac{1}{2} R^{(1)} P^{(1)} - \tfrac{\bar{\gamma}^2}{2} \frac{d\bar{\Phi}^{(1)}}{d\phi} \frac{dV^{(1)}}{d\phi} \right\} - D_{0g} \left\{ \bar{\rho}\bar{g}\, V^{(1)^2} \right\} - \nu^2 C_{0,g} \left\{ \frac{V^{(1)^2}}{4} \bar{\rho}\bar{g} \right\} \right) \frac{d}{d\Psi} \frac{J_0(S_{0,g}\sqrt{\Psi})}{2} \right.$$

$$+ \tfrac{1}{2} \left(A_{2\nu,g} \left\{ \tfrac{1}{2} R^{(1)} P^{(1)} - \tfrac{1}{2} \bar{\gamma}^2 \frac{d\bar{\Phi}^{(1)}}{d\phi} \frac{dV^{(1)}}{d\phi} \right\} - D_{2\nu,g} \left\{ \bar{\rho}\bar{g}\, V^{(1)^2} \right\} \right.$$

$$\left. \left. + \nu^2 C_{2\nu,g} \left\{ \frac{V^{(1)^2}}{4} \bar{\rho}\bar{g} \right\} \right) \tfrac{1}{2} \left(e^{2i(\omega t+\nu\theta)} + e^{-2i(\omega t+\nu\theta)} \right) \frac{d}{d\Psi} J_{2\nu}(S_{2\nu,g}\sqrt{\Psi}) \right\}$$

$$= \sum_{g=1}^{\infty} C_{0,g}\, J_0(S_{0g}\sqrt{\Psi}) + C_{2\nu,g} \tfrac{1}{2} \left(e^{2i(\omega t+\nu\theta)} + e^{-2i(\omega t+\nu\theta)} \right) J_{2\nu}(S_{2\nu,g}\sqrt{\Psi}$$

Θ - Momentum:

$$\left\{ \sum_{g=1}^{\infty} \tfrac{1}{2} \left[A_{2\nu,g} \left(\tfrac{1}{2} R^{(1)} P^{(1)} - \tfrac{1}{2} \bar{\gamma}^2 \frac{d\bar{\Phi}^{(1)}}{d\phi} \frac{dV^{(1)}}{d\phi} \right) - D_{2\nu,g} \left\{ \bar{\rho}\bar{g}\, V^{(1)^2} \right\} \right. \right.$$

$$\left. \left. + \nu^2 C_{2\nu,g} \left\{ \tfrac{1}{4} \bar{\rho}\bar{g}\, V^{(1)^2} \right\} \right] \tfrac{1}{2} \left(e^{2i(\omega t+\nu\theta)} - e^{-2i(\omega t+\nu\theta)} \right) J_{2\nu}(S_{2\nu,g}\sqrt{\Psi}) \right\} 2i\nu$$

$$= \left\{ \sum_{g=1}^{\infty} D_{2\nu,g} \tfrac{1}{2} \left(e^{2i(\omega t+\nu\theta)} - e^{-2i(\omega t+\nu\theta)} \right) J_{2\nu}(S_{2\nu,g}\sqrt{\Psi}) \right\} 2i\nu$$

Entropy Equation:

$$- \sum_{g=1}^{\infty} \left\{ \left[A_{0g} \bar{g}^2 \frac{d\bar{\Phi}^{(1)}}{d\phi} \frac{dS^{(1)}}{d\phi} + \bar{\rho}\bar{g}\, V^{(1)} S^{(1)} \left(2 D_{0g} + \frac{\nu^2}{2} C_{0g} \right) \right] \tfrac{1}{2} J_0(S_{0g}\sqrt{\Psi}) \right.$$

$$+ \tfrac{1}{2} \left[A_{2\nu,g} \bar{g}^2 \frac{d\bar{\Phi}^{(1)}}{d\phi} \frac{dS^{(1)}}{d\phi} + \bar{\rho}\bar{g}\, V^{(1)} S^{(1)} \left(2 D_{2\nu,g} - \frac{\nu^2}{2} C_{2\nu,g} \right) \right] \tfrac{1}{2} \left(e^{2i(\omega t+\nu\theta)} \right.$$

$$\left. \left. + e^{-2i(\omega t+\nu\theta)} \right) J_{2\nu}(S_{2\nu,g}\sqrt{\Psi}) \right\}$$

$$= \sum_{g=1}^{\infty} - \left\{ A_{0,g} J_0(S_{0g}\sqrt{\Psi}) + A_{2\nu,g} \tfrac{1}{2} \left(e^{2i(\omega t+\nu\theta)} + e^{-2i(\omega t+\nu\theta)} \right) J_{2\nu}(S_{2\nu,g}\sqrt{\Psi}) \right\}$$

Equation of State:

$$\sum_{\beta} \left\{ A_{o\beta} \left(\frac{\bar{c}^2}{2} R^{(1)^2} - \frac{\gamma}{2\bar{c}^2} P^{(1)^2} \right) \frac{1}{2} J_0 (S_{o\beta} \sqrt{\Psi}) \right.$$

$$+ \frac{1}{2} A_{2\nu\beta} \left(\frac{\bar{c}^2}{2} R^{(1)^2} - \frac{\gamma}{2\bar{c}^2} P^{(1)^2} \right) \frac{1}{2} \left(e^{2i(\omega t + \nu\theta)} + e^{-2i(\omega t + \nu\theta)} \right) J_{2\nu} (S_{2\nu\beta} \sqrt{\Psi})$$

$$= \sum G_{o\beta} J_0 (S_{o\beta} \sqrt{\Psi}) + G_{2\nu\beta} \frac{1}{2} \left(e^{2i(\omega t + \nu\theta)} + e^{-2i(\omega t + \nu\theta)} \right) J_{2\nu} (S_{2\nu\beta} \sqrt{\Psi})$$

II. SOLUTION FOR STANDING WAVE

The symbols A, B, C, D and E appearing in the equations below have the same definitions as the corresponding symbols appearing in the expressions of part (I) page 132 (corresponding to spinning wave solution).

Continuity Equation:

$$= - \sum_{\beta=1}^{\infty} \left\{ E_{o\beta} \left[\frac{1}{2} + \frac{1}{4} \left(e^{2i\omega t} + e^{-2i\omega t} \right) \right] J_0 (S_{o\beta} \sqrt{\Psi}) \right.$$

$$\left. + E_{2\nu\beta} \left[\frac{1}{4} \left(e^{2i\nu\theta} + e^{-2i\nu\theta} \right) \left(1 + \frac{1}{2} \left(e^{2i\omega t} + e^{-2i\omega t} \right) \right) \right] J_{2\nu} (S_{2\nu\beta} \sqrt{\Psi}) \right\}$$

ϕ Momentum:

$$\sum_{\beta=1}^{\infty} \left\{ B_{o\beta} \left[\frac{1}{2} + \frac{1}{4} \left(e^{2i\omega t} + e^{-2i\omega t} \right) \right] J_0 (S_{o\beta} \sqrt{\Psi}) \right.$$

$$\left. + B_{2\nu\beta} \left[\frac{1}{4} \left(e^{2i\nu\theta} + e^{-2i\nu\theta} \right) \left(1 + \frac{1}{2} \left(e^{2i\omega t} + e^{-2i\omega t} \right) \right) \right] J_{2\nu} (S_{2\nu\beta} \sqrt{\Psi}) \right\}$$

ψ - Momentum:

$$\sum_{\beta=1}^{\infty} \left\{ C_{o\beta} \left[\frac{1}{2} + \frac{1}{4} \left(e^{2i\omega t} + e^{-2i\omega t} \right) \right] \frac{1}{\sqrt{\Psi}} J_0 (S_{o\beta} \sqrt{\Psi}) + C_{2\nu\beta} \left[\frac{1}{4} \left(e^{2i\nu\theta} + e^{-2i\nu\theta} \right) \left(1 + \frac{1}{2} \left(e^{2i\omega t} + e^{-2i\omega t} \right) \right) \right] \frac{1}{\sqrt{\Psi}} J_{2\nu} (S_{2\nu\beta} \sqrt{\Psi}) \right\}$$

Θ - Momentum:

$$\sum_{g=1}^{\infty} 2(1)\left\{\mathbb{D}_{2l,g}\left[\frac{1}{8}(e^{2i\omega\theta}-e^{-2i\omega\theta})\left(1+\frac{1}{2}(e^{2i\omega t}+e^{-2i\omega t})\right)\right] J_{2l}(S_{2l,g}\sqrt{\Psi})\right\}$$

Entropy Equation:

$$\sum_{g=1}^{\infty} -\left\{A_{0g}\left[\frac{1}{2}+\frac{1}{4}(e^{2i\omega t}+e^{-2i\omega t})\right] J_0(S_{0g}\sqrt{\Psi})\right.$$
$$\left. + A_{2lg}\left[\frac{1}{4}(e^{2i\omega\theta}+e^{-2i\omega\theta})\left(1+\frac{1}{2}(e^{2i\omega t}+e^{-2i\omega t})\right)\right] J_{2l}(S_{2lg}\sqrt{\Psi})\right\}$$

Equation of State:

$$\sum_{g=1}^{\infty}\left\{G_{0g}\left[\frac{1}{2}+\frac{1}{4}(e^{2i\omega t}+e^{-2i\omega t})\right] J_0(S_{0g}\sqrt{\Psi})+\right.$$
$$\left. + G_{2lg}\left[\frac{1}{4}(e^{2i\omega\theta}+e^{-2i\omega\theta})\left(1+\frac{1}{2}(e^{2i\omega t}+e^{-2i\omega t})\right)\right] J_{2l}(S_{2lg}\sqrt{\Psi})\right\}$$

From the expansion forms of the inhomogeneous parts of the second-order equations (for standing as well as tangentially spinning waves) it can be seen that m and n, defined in Equation (5.8) take on the following values: $0, \pm 2$.

The expansion forms of the functions, depending on the independent variable Ψ, appearing in the inhomogeneous parts of the second-order equations will follow:

$$J_\nu^2(S_{\nu h}\sqrt{\Psi}) - \sum_{g=1}^{\infty} A_{n\nu g}\, J_{n\nu}(S_{n\nu g}\sqrt{\Psi})$$

$$\frac{d}{d\Psi}\left\{\Psi J_\nu(S_{\nu h}\sqrt{\Psi})\frac{d}{d\Psi}(S_{\nu h}\sqrt{\Psi})\right\} = \sum_{g=1}^{\infty} B_{n\nu g}\, J_{n\nu}(S_{n\nu g}\sqrt{\Psi})$$

$$\frac{1}{\Psi} J_\nu^2(S_{\nu h}\sqrt{\Psi}) = \sum_{g=1}^{\infty} C_{n\nu g}\, J_{n\nu}(S_{n\nu g}\sqrt{\Psi})$$

$$\Psi\left[\frac{d}{d\Psi} J_\nu(S_{\nu h}\sqrt{\Psi})\right]^2 - \sum_{g=1}^{\infty} D_{n\nu g}\, J_{n\nu}(S_{n\nu g}\sqrt{\Psi})$$

$$\Psi J_\nu(S_{\nu h}\sqrt{\Psi})\frac{d}{d\Psi} J_\nu(S_{\nu h}\sqrt{\Psi}) = \frac{\Psi}{2}\frac{d}{d\Psi} J_\nu^2(S_{\nu h}\sqrt{\Psi}) = \sum_{g=1}^{\infty} E_{n\nu g}\, J_{n\nu}(S_{n\nu g}\sqrt{\Psi})$$

For the second order solution n takes on the values 0 and $\pm$ 2. Also note that the relation $J_{2\nu}(S_{2\nu,q}\sqrt{\Psi}) = J_{-2\nu}(S_{2\nu,q}\sqrt{\Psi})$ (when 2ν is an integer) was used in expanding the functions appearing in the inhomogeneous parts of the second-order equations.

APPENDIX B

CONCEPT IN ROCKET BAFFLE DESIGN

Introduction

It is well known that the occurrence of transverse spinning mode high frequency combustion instability in the liquid propellant rocket engine can often be eliminated by the use of baffles. These baffles are solid surfaces which protrude from the injector plate, are perpendicular to it, and extend some determined distance into the rocket combustion chamber. The pattern or arrangement of these baffles required to prevent combustion instability cannot as yet be predicted a priori, and generally it may be said that such design is still an art rather than a science.

In some situations, however, there are certain rational guidelines to this design. It appears for some configurations that a design which segments the chamber into smaller sections will be successful in preventing the spinning mode in the chamber although the standing mode may still be present [16]. This is true even if the protrusion distance is rather small compared to the chamber length provided that the baffle protrudes part-way into a region of active combustion. If this is true, then segmenting a chamber by baffles changes the acoustic modes of oscillation of the full chamber to those permitted by the baffle cavities. Even standing modes can be altered in type, and in frequency of oscillation, from those permitted for the full chamber. This is important as larger and larger rocket engines are considered since as a rocket engine size increases the natural frequencies of the chamber decrease. However, it is well known that the higher the frequency, the more stable will be the engine [16]. This is caused by the frequency-dependent energy feedback to an acoustic wave from the combustion process. It appears that above a certain frequency (dependent upon propellant and injector type) this feedback is insufficient to sustain the wave by overcoming the damping due to the exit nozzle. Therefore, if baffles really do alter the acoustic nature of the chamber in the manner described above

(note that there are some observed exceptions to this postulate), it is clear that a sufficiently large number of cavities can increase the frequencies of the allowable modes to a point where combustion instability is impossible in the transverse modes.

If it is assumed that this design principle is adopted, it is reasonable to ask if there is an optimum baffle pattern or shape. Of course, "optimum" must be defined. By this it will be meant that

1. The natural fundamental frequency of the cavities is as high as possible for any given number of cavities.
2. The baffles must not have a complicated shape that would entail manufacturing problems nor cause excessive engine weight.
3. There will be a dispersive device in the baffle shape such that given an oscillation at the natural frequency of the cavity, the amplitude will not be uniform over the cavity but will be less than that at the point of maximum amplitude.

It will be shown that, given the above-mentioned assumption concerning the effect of a baffle, a shape meeting the specifications does exist.

Analysis

The effect of the combustion process in determining the natural frequency of the transverse oscillations is of the order of the mean Mach number of the flow and are considered negligible compared to unity. This would be a small correction even for large Mach numbers[16]. For transverse oscillations, variations in the longitudinal direction are also of this same order and are neglected here. A linearized analysis gives a satisfactory first approximation to the natural frequency of oscillation within the cavity. The oscillation is described by the wave equation

$$\frac{\partial^2 \phi}{\partial t^2} - \left(\frac{\partial^2 \phi}{\partial x^2} + \frac{\partial^2 \phi}{\partial y^2} \right) = 0 \qquad (1)$$

where ϕ is the velocity potential, t is the time coordinate and x and y are the transverse dimensions in a cartesian system. The velocity potential has been nondimensionalized with respect to steady-state speed of sound times chamber diameter, time with respect speed of sound divided by chamber diameter and space dimensions with respect to chamber diameter.

A solution is assumed to be of the form

$$\phi = \Phi(x,y)\, e^{i\omega t}$$

Substitution into Equation (1) yields

$$\frac{\partial^2 \Phi}{\partial x^2} + \frac{\partial^2 \Phi}{\partial y^2} + \omega^2 \Phi = 0 \qquad (2)$$

Now, the frequency ω would be determined by the shape of the cavity by means of the application of boundary conditions to Equation (2). The general class of cavities considered here is shown in Figure B-1. One cavity dimension is much larger than the other. The cavity may or may not be symmetric about the maximum width line. For convenience, R(0) is taken as zero and ϵ is defined as the maximum width such that Y(0) = 1. $\epsilon \ll 1$ is the important characteristic of this type of configuration.

The gradients in the y-direction are much larger than the gradients in the x-direction. It is convenient, therefore, to scale the y-direction by the factor ϵ such that

$$y = \epsilon \eta + R(x)$$

Note that this technique was originally applied to the problem of a long, slender vibrating membrane[36].

Under this scale transformation Equation (2) becomes*

$$\frac{\partial^2 \Phi}{\partial \eta^2} + \epsilon^2 \omega^2 \Phi = -\epsilon^2 \frac{\partial^2 \Phi}{\partial x^2} \qquad (3)$$

The boundary conditions state that the normal velocity at the baffles (which are the cavity walls) be zero. This means, as can be seen from Figure B-1, that

*Terms of the order of $\frac{dR}{dx}$ and $\frac{d^2R}{dx^2}$ have been assumed negligible in the region of interest (vicinity of maximum width). This is conservative in that the inclusion of these terms shows that the design is still more favorable.

$$\frac{\partial \phi}{\partial y} = \frac{dR}{dx}\frac{\partial \phi}{\partial x} \quad \text{along} \quad y = R(x)$$

$$\frac{\partial \phi}{\partial y} = \frac{dR}{dx}\frac{\partial \phi}{\partial x} + \epsilon \frac{dY}{dx}\frac{\partial \phi}{\partial x} \quad \text{along} \quad y = R(x) + \epsilon Y(x)$$

This may be transformed to the following:

$$\frac{\partial \bar{\phi}}{\partial \eta} = \epsilon \frac{dR}{dx}\frac{\partial \bar{\phi}}{\partial x} \quad \text{along} \quad \eta = 0$$

$$\frac{\partial \bar{\phi}}{\partial \eta} = \epsilon \frac{dR}{dx}\frac{\partial \bar{\phi}}{\partial x} + \epsilon^2 \frac{dY}{dx}\frac{\partial \bar{\phi}}{\partial x} \quad \text{along} \quad \eta = Y(x) \qquad (4)$$

In solving Equation (3) with the boundary conditions (4), the following form of the solution is assumed

$$\bar{\Phi}(x,\eta) = e^{\Psi(x,\eta)}$$

Now, Equation (3) becomes

$$\frac{\partial^2 \Psi}{\partial \eta^2} + \left(\frac{\partial \Psi}{\partial \eta}\right)^2 + \epsilon^2 \omega^2 = -\epsilon^2 \left[\frac{\partial^2 \Psi}{\partial x^2} + \left(\frac{\partial \Psi}{\partial x}\right)^2\right] \qquad (5)$$

and the boundary conditions (4) are now

$$\frac{\partial \Psi}{\partial \eta} = \epsilon \frac{dR}{dx}\frac{\partial \Psi}{\partial x} \quad \text{along} \quad \eta = 0$$

$$\frac{\partial \Psi}{\partial \eta} = \epsilon \frac{dR}{dx}\frac{\partial \Psi}{\partial x} + \epsilon^2 \frac{dY}{dx}\frac{\partial \Psi}{\partial x} \quad \text{along} \quad \eta = Y(x) \qquad (6)$$

The following series solutions for Ψ and ω are assumed:

$$\Psi = \epsilon^{-1}\Psi_{-1} + \Psi_0 + \epsilon\Psi_1 + \cdots$$

$$\omega = \epsilon^{-1}\omega_{-1} + \omega_0 + \epsilon\omega_1 + \cdots$$

These series are substituted into Equation (5) and we find after separation that

$$\frac{\partial \Psi_{-1}}{\partial \eta} = 0$$

which means that the lowest order coefficient, Ψ_{-1}, is a function of x only. The separated equation which governs Ψ_0 is found

to be

$$\frac{\partial^2 \psi_0}{\partial \eta^2} + \left(\frac{\partial \psi_0}{\partial \eta}\right)^2 + \omega_{-1}^2 = -\left(\frac{d\psi_{-1}}{dx}\right)^2 \qquad (7)$$

The boundary conditions (6) become

$$\frac{\partial \psi_0}{\partial \eta} = \frac{dR}{dx}\frac{d\psi_{-1}}{dx} \quad \text{along} \quad \eta = 0$$
$$\frac{\partial \psi_0}{\partial \eta} = \frac{dR}{dx}\frac{d\psi_{-1}}{dx} \quad \text{along} \quad \eta = Y(x) \qquad (8)$$

The final transformation to be used is $\psi_0 = \log \theta$. This transforms Equation (7) as follows:

$$\frac{\partial^2 \theta}{\partial \eta^2} + \left[\omega_{-1}^2 + \left(\frac{d\psi_{-1}}{dx}\right)^2\right]\theta = 0$$

The boundary conditions (8) are written

$$\frac{\partial \theta}{\partial \eta} = \left(\frac{dR}{dx}\frac{d\psi_{-1}}{dx}\right)\theta \quad \text{along} \quad \eta = 0$$
$$\frac{\partial \theta}{\partial \eta} = \left(\frac{dR}{dx}\frac{d\psi_{-1}}{dx}\right)\theta \quad \text{along} \quad \eta = Y(x)$$

Note that x appears only as a parameter above, so that the equation may be treated as an ordinary differential equation. The lowest eigenfunction is

$$\theta = \cos\left[\frac{\pi\eta}{Y(x)} - \arctan\left(\frac{dR}{dx}\frac{d\psi_{-1}}{dx}\right)\right] \qquad (9)$$

with the governing relation for ψ_{-1} as follows:

$$\omega_{-1}^2 + \left(\frac{d\psi_{-1}}{dx}\right)^2 = \frac{\pi^2}{Y(x)} \qquad (10)$$

In order to prevent the solution from going to infinity, the positive value of $\frac{d\psi_{-1}}{dx}$ is taken for negative values of x while the negative slope is taken for positive values of x. This means $\frac{d\psi_{-1}}{dx}(0) = 0$. The differential equation for ψ_{-1} cannot be solved with a general $Y(x)$. However, by using a Taylor series for $Y(x)$ the equation may be solved for a small region around the maximum width point. Noting that $\frac{dY}{dx}(0) = 0$, we say

$$Y(x) = Y(0) + \frac{1}{2}\frac{d^2Y}{dx}(0)\,x^2 + O(x^3)$$

Since $\frac{d\Psi_{-1}}{dx}(0) = 0$, Equation (10) yields $\omega_{-1} = \frac{\pi}{Y(0)}$. Therefore, Equation (10) may be rewritten as follows

$$\frac{d\Psi_{-1}}{dx} = - \frac{\sqrt{- \frac{d^2Y}{dx^2}(0)}}{(Y(0))^{1/2}} \pi x$$

Note this means that the phase in Equation (9) is of order x^2. Integrating, we have

$$\Psi_{-1} = - \frac{\sqrt{- \frac{d^2Y}{dx^2}(0)}}{(Y(0))^{1/2}} \pi \frac{x^2}{2}$$

The constant of integration is neglected since it would only be a multiplicative factor on the final solution. Tracing back through the series of transformations and noting that $Y(0) = 1$ we find

$$\begin{aligned}
\Phi &= e^{\epsilon^{-1}\Psi_{-1} + \Psi_0 + O(\epsilon)} = e^{\epsilon^{-1}\Psi_{-1}} e^{\Psi_0} + O(\epsilon) \\
&= e^{\epsilon^{-1}\Psi_{-1}} e^{\log \Theta} + O(\epsilon) = \Theta\, e^{\epsilon^{-1}\Psi_{-1}} + O(\epsilon) \\
&= e^{-\left[\sqrt{-\frac{d^2Y}{dx^2}(0)}\right] \pi \frac{x^2}{2\epsilon}} \cos \pi\eta + O(\epsilon)
\end{aligned} \tag{11}$$

Terms of order x^2 were neglected in writing the argument of the cosine function since their effect is of order larger than ϵ only outside of the region of large amplitude as shown by the exponential term.

The physical interpretation of Equation (11) is simple. The amplitude of the oscillation is a maximum at the maximum width line ($x = 0$) and decays rapidly in an exponential manner in either direction from this line (the amplitude is only significant in a region of size equal to $\sqrt{\epsilon}$). This decay occurs due to the dispersive mechanism provided by the narrowing of the cavity away from the maximum width line. The difference in the curvatures (at the maximum width line) of the two baffles surrounding the cavity is most critical in determining this decay rate. The larger the difference (or the larger the rate of "narrowing"), the greater the

decay rate as shown by the factor $\left[\sqrt{\frac{d^2Y}{dx^2}(0)}\right]$ appearing in the exponential term.

The natural frequency was found to be

$$\omega \approx \frac{1}{\epsilon}\,\omega_{-1} = \frac{\pi}{\epsilon}$$

This means the frequency is approximately determined by the maximum width ϵ and, therefore, is very large when $\epsilon << 1$.

Possible Configuration

One possible shape is shown in Fig. B-2 (assuming that three baffles are sufficient to raise the frequency of the acoustic mode to acceptable values). Circular shapes are one special case of this elliptical shape. (It should not be construed that elliptical chambers are preferred or even practical.) The frequency is maximized by making four cavities of minimum width. This can be done by locating the maximum-cavity-width centerline transverse to the minimum width axis of a symmetric chamber. The difference in radii of curvature at the maximum width points can be adjusted equally between the cavities or adjusted at will. The only constraint on the rest of the shape is that there is never another point at which the maximum width is equalled or exceeded. There are, therefore, an infinity of shapes which are theoretically equally acceptable. Of course, the analysis requires $\epsilon << 1$ and how good the theory is for ϵ not too small can only be determined by experiment. Clearly, it will fail for $\epsilon = 1/2$ since a well defined acoustic mode exists for the half chamber if the full chamber is nearly circular.

Discussion and Conclusions

Under the assumption that the purpose of a combustion chamber baffle is to segment a chamber into cavities with higher natural frequencies of gas oscillation than those of the full chamber, an interesting result from wave theory and its application have been presented. Baffle design criteria have been developed that are related to the specification of two quantities at the maximum width point of each cavity, i.e., this maximum width and the difference in the radii of curvature of the two cavity walls at

this point. With this concept it is possible to maximize the acoustic frequencies allowable in the chamber, do this with a smooth somewhat arbitrary shape, and to provide a degree of dispersion, i.e., the amplitude decays with distance from the maximum width point.

The maximization of frequency is known to have beneficial effects concerning combustion instability. The arbitrariness of shape away from the maximum width point allows freedom concerning manufacturing and weight problems. The dispersive mechanism is important if the amplitude level is important in determining stability characteristics of an engine. However, even given the assumption concerning the baffle effect it should be remembered that $\epsilon \ll 1$ is required and the meaning of "very much less than" can only be determined experimentally. The theory is at best an asymptotic representation of the true state of affairs and should not be blindly applied. Since the allowable number of baffles in an engine is necessarily limited (the magnitude of ϵ is limited) care must be taken in interpreting experimental results.

Nomenclature

$R(x)$	profile of baffle
t	time
x,y	transverse dimensions
$Y(x)$	width of cavity
ϵ	maximum width of cavity
η	translated y-dimension
Θ	defined in Appendix
Φ	velocity potential
$\bar{\Phi}$	amplitude of velocity potential
Ψ	defined in Appendix
ω	frequency

REFERENCES

1. Crocco, L., Harrje, D. T., Lee, D. H., Strahle, W. C., Sirignano, W. A., Bredfeldt, H. R., and Seebaugh, W. R., "Nonlinear Aspects of Combustion Instability in Liquid Rocket Motors", (Third Yearly Progress Report), Princeton University Aeronautical Engineering Report 553c, June 1, 1963.

2. Crocco, L., Harrje, D. T., Strahle, W. C., and Sirignano, W. A., "Nonlinear Aspects of Combustion Instability in Liquid Propellant Rocket Motors", (Second Yearly Progress Report), Princeton University Aeronautical Engineering Report 553b, June 1, 1962.

3. Crocco, L., Harrje, D. T., Sirignano, W. A., and Ashford, D. M., "Nonlinear Aspects of Combustion Instability in Liquid Propellant Rocket Motors", (First Yearly Progress Report), Princeton University Aeronautical Engineering Report No. 553, June 1961.

4. Crocco, L., and Cheng, S. I., "Theory of Combustion Instability in Liquid Propellant Rocket Motors", AGARD Monograph No. 8, Butterworths Scientific Pub., Ltd., London, 1956.

5. Crocco, L., Harrje, D. T., Reardon, F. H., and Strahle, W. C., "Combustion Instability in Liquid Propellant Rocket Motors", (Thirty-fifth Progress Report), Princeton University Aeronautical Engineering Report No. 216-ii, June, 1961.

6. Sirignano, W. A., "A Theoretical Study of Nonlinear Combustion Instability: Longitudinal Mode", Technical Report No. 677, Department of Aerospace and Mechanical Sciences, Princeton University, March 1964.

7. Sirignano, W. A., Crocco, L., "A Shock Wave Model of Unstable Rocket Combustors", (to be published in AIAA Journal, summer 1964).

8. Priem, R. J., and Guentert, D. C., "Combustion Instability Limits Determined by a Nonlinear Theory and a One-Dimensional Model", NASA TN D-1409, October, 1962.

9. Chinitz, W., and Agosta, V. D., "Combustion Instability: Shock Wave Propagation in a Liquid Propellant Rocket Motor", Polytechnic Institute of Brooklyn, Department of Mechanical Engineering (PRL-62-13), June, 1962.

10. Burstein, S. Z., and Agosta, V. D., "Combustion Instability: Non-Linear Analysis of Wave Propagation in a Liquid Propellant Rocket Motor", Polytechnic Institute of Brooklyn, Department of Mechanical Engineering, March, 1962.

11. Maslen, S. H., and Moore, F. K., "On Strong Transverse Waves Without Shocks in a Circular Cylinder", Journal of Aeronautical Sciences, Vol. 23, No. 6, 1956, pp. 583-593.

12. Crocco, L., "Behavior of Supercritical Nozzles Under Three-Dimensional Oscillatory Conditions"- Currently in Preparation.

12b. Courant, R., and Friedricks, K. O., "Supersonic Flow and Shock Waves", Interscience Publishers, Inc., New York, 1948, pp 1-91.

13. Tsien, H. S. "The Transfer Functions of Rocket Nozzles", Journal of the American Rocket Society, Vol. 22, May, 1952.

14. Appendix B of Reference 4.

15. Crocco, L., Harrje, D. T., Reardon, F. H., "Combustion Instability in Liquid Propellant Rocket Motors", (Thirteeth Quarterly Progress Report), Princeton University Aeronautical Engineering Report No. 216-dd, December, 1959.

16. Reardon, F. H., Crocco, L., and Harrje, D. T., "An Investigation of Transverse Mode Combustion Instability in Liquid Propellant Rocket Motors", Princeton University Aeronautical Engineering Report 550, June 1, 1961.

17. Reardon, F. H., Crocco, L., and Harrje, D. T., "Velocity Effects in Transverse Mode Liquid Propellant Rocket Combustion Instability", (accepted for publication AIAA Journal).

18. Reardon, F. H., "M-1 Thrust Chamber Transverse Mode Combustion Instability Analysis", Aerojet-General Corporation, Liquid Rocket Plant, Report TCR 9621-012, 15 August 1963.

19. "Gemini Stability Improvement Program", Aerojet-General Corporation, Liquid Rocket Plant, Report Gemsip MR-4, 19 March 1964.

20. Allen, W. D., "Experimental Studies of Transverse Waves in a Cylindrical Chamber", Princeton University Aeronautical Engineering Report No. 608, June 8, 1962.

20b. Crocco, L., Harrje, D. T., Reardon, F. H., "Transverse Combustion Instability in Liquid Propellant Rocket Motors, ARS Journal, Vol. 32 pg. 366, March, 1962.

21. Ingebo, R. D., "Drop-Size Distribution for Impinging - Jet Breakup in Airstreams Simulating the Velocity Conditions in Rocket Combustors", NACA TN 4222, 1958.

22. Lee, D. H., "Propellant Distribution Surveys of F-1 Injector Elements", Department of Aerospace and Mechanical Sciences Report No. 680, March, 1964.

23. Rupe, J. H., "Experimental Studies of the Hydrodynamics of Liquid Propellant Injection, External Publication No. 388, Jet Propulsion Laboratory, June 7, 1957.

24. Seebaugh, W. R., and Lee, D. H., "An Optical Method for Observing Breakup and Vaporization of Liquid Jets", Princeton University, Aeronautical Engineering Report No. 647, June, 1963.

25. Bredfeldt, H. R., "Evaluation of a Light Scattering Technique for Determining the Spray Characteristics of Impinging Liquid Jets", Technical Report No. 648, Department of Aerospace and Mechanical Sciences, Princeton University, March, 1964.

26. Foster, H. H., and Heidmann, M. F., "Spatial Characteristics of Water Spray Formed by Two Impinging Jets at Several Jet Velocities in Quiescent Air", NASA TN D-301, July, 1960.

27. Heidmann, M. F., and Foster, H. H., "Effect of Impingement Angle on Drop-Size Distribution and Spray Pattern of Two Impinging Jets", NASA TN D-872, July, 1962.

28. Mack, J. E., and Martin, M. J., "The Photographic Process", First Edition, McGraw Hill, 1939.

29. Benson, G. M., El-Wakil, M. M., Uyehara, O. A., and Myers, P. S., "The Determination of Cross-Sectional Drop Size Distributions of Liquid Sprays by a Fluorescent Technique." (Final Report of study sponsored by National Science Foundation under Contract No. 2130-G2565 for period July 1956-June 1958); University of Wisconsin, Madison, Wisconsin.

30. Heidmann, M. F., Priem, R. J., and Humphrey, J. C., "A Study of Sprays Formed by Two Impinging Jets." NASA TN 3835, March, 1957.

31 Strahle, W. C., and Crocco, L., "Analytical Investigation of Several Mechanisms of Combustion Instability." (Bulletin of the Fifth Liquid Propulsion Symposium, 13-15, November, 1963), Chemical Propulsion Information Agency.

32. Crocco, L., Grey, J., and Harrje, D. T., "Theory of Liquid Propellant Rocket Combustion Instability and its Experimental Verification", ARS Journal, Vol. 30, No. 2, February, 1960, pp. 159-168.

33. Strahle, W. C., "A Theoretical Study of Unsteady Droplet Burning: Transients and Periodic Solutions", Princeton University (Ph.D. Thesis), Aeronautical Engineering Laboratory Report No. 671, December, 1963.

34. Strahle, W. C., "The Unsteady Laminar Jet Flame at Large Frequencies of Oscillation and Application to the Wake of a Burning Droplet", (submitted to the AIAA Journal).

35. Priem, R. J., and Heidmann, M. F., "Propellant Vaporization as a Design Criterion for Rocket-Engine Combustion Chambers", NASA Technical Report R-67, 1960.

36. Kruskal, M. D., "Asymptotology." Princeton University, Plasma Physics Laboratory AEC Research and Development Report No. MATT-160.

37. Moller, W., "Experimentalle Untersuchungen zur Hydrodynamik der Kugel", Phy. Zeit. 39, 57-76, 1938.

38. Spaulding, D. B., "Experiments on the Burning and Extinction of Liquid Fuel Spheres", Fuel 32, 169, 1953.

Wave shapes

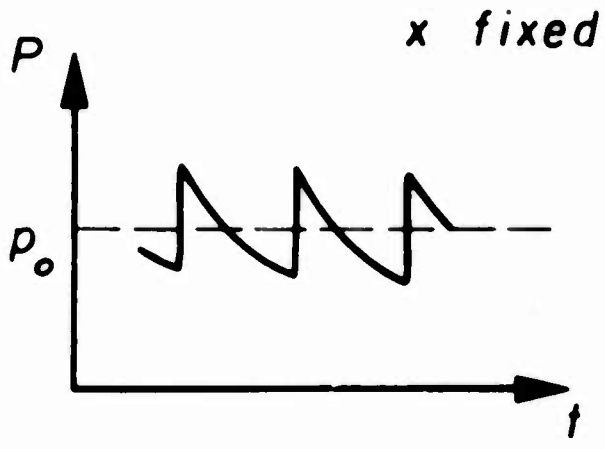

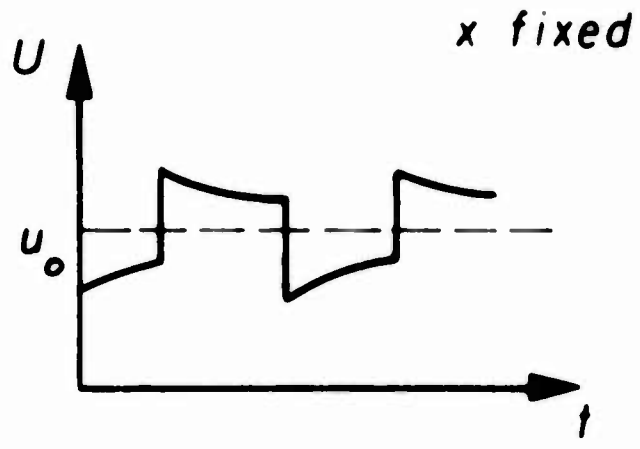

wave direction →

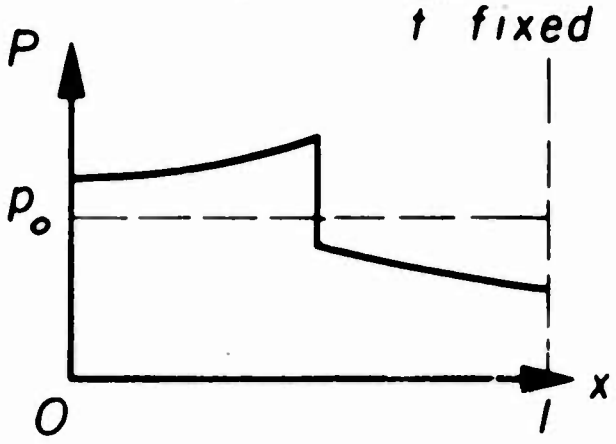

wave direction ←

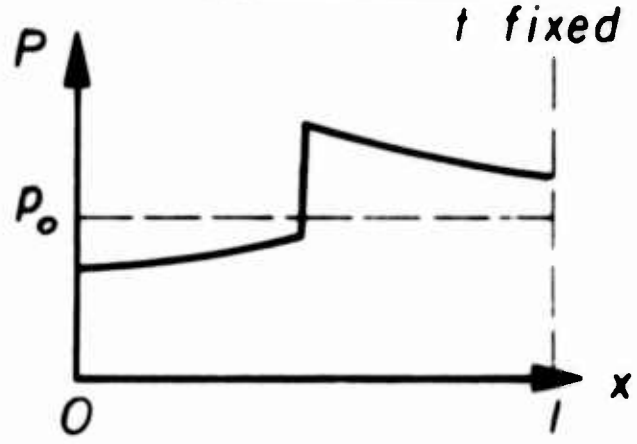

wave →

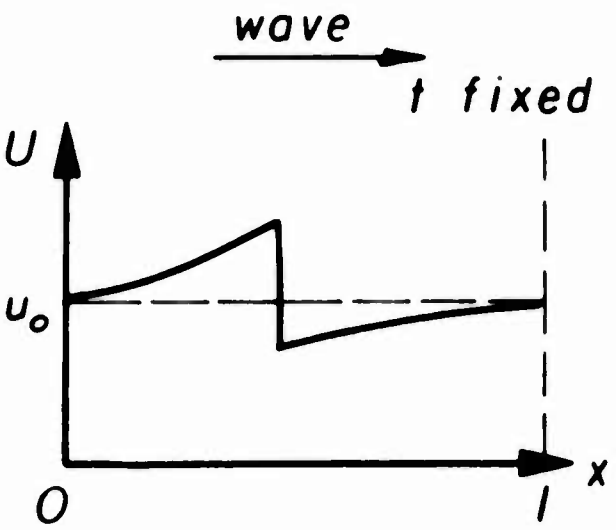

wave ←

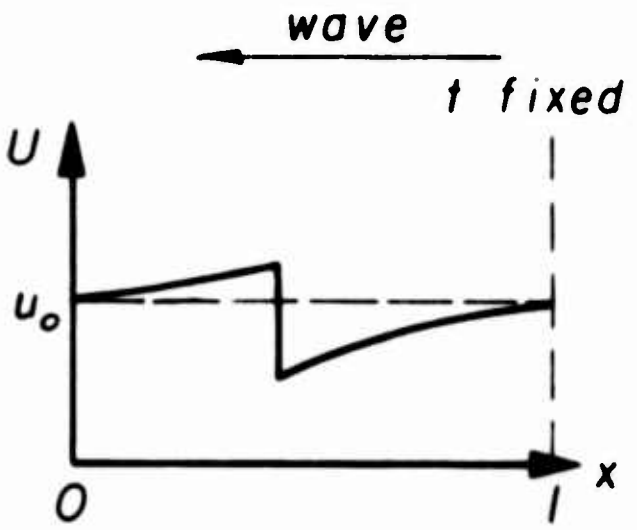

Figure III-1

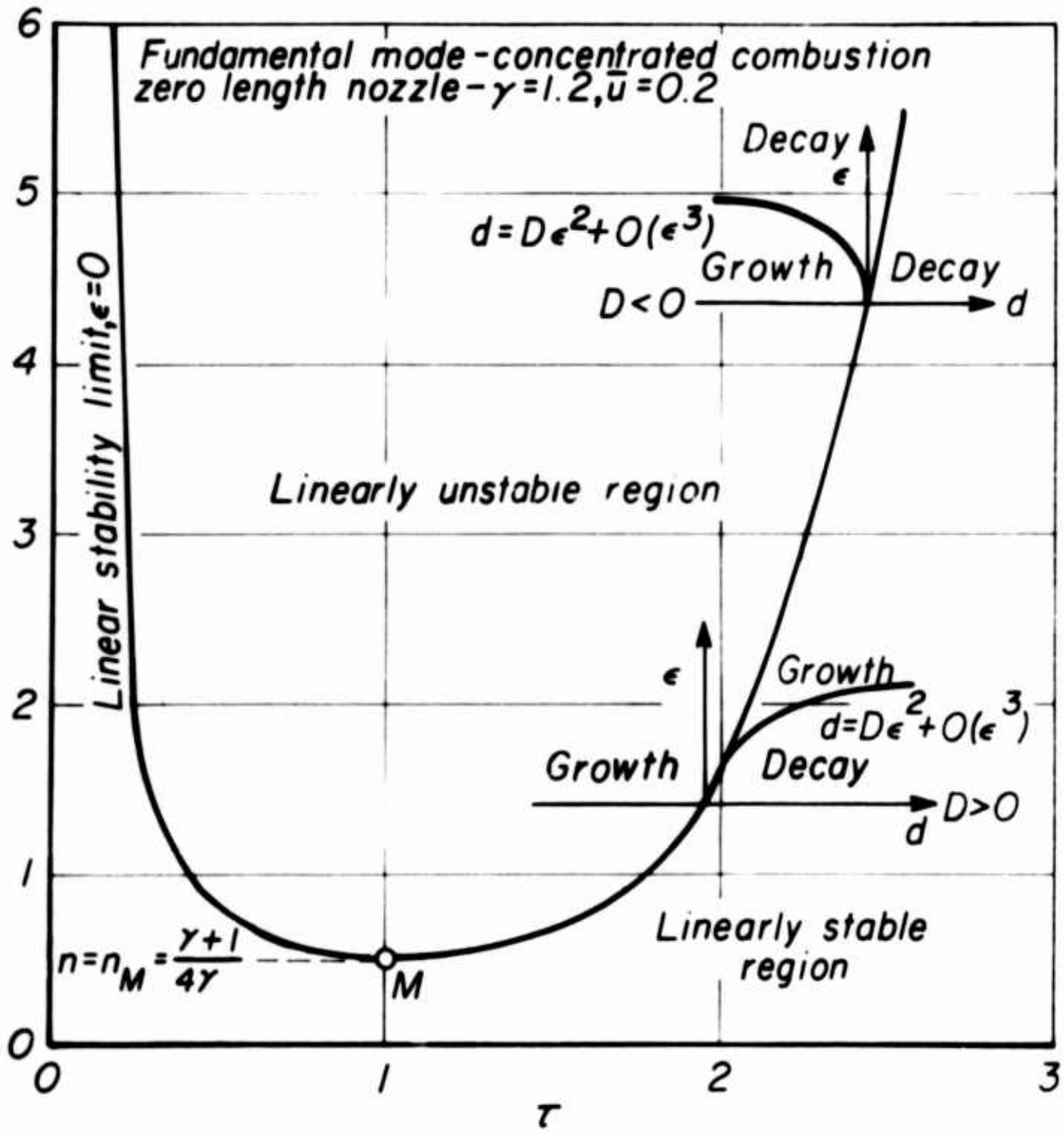
Fundamental mode-concentrated combustion
zero length nozzle-γ=1.2, ū=0.2
Linear stability limit, ε=0
Linearly unstable region
Linearly stable region
Decay
ε
d=Dε²+O(ε³)
Growth
Decay
D<0
d
ε
Growth
d=Dε²+O(ε³)
Growth
Decay
D>0
d
n=n_M=(γ+1)/4γ
M
n
τ
0
1
2
3
0
1
2
6
5
4
3
2
1
0

Figure III-2

Results of nonlinear longitudinal model with time-lag effect.
u_0 = 2 fundamental mode

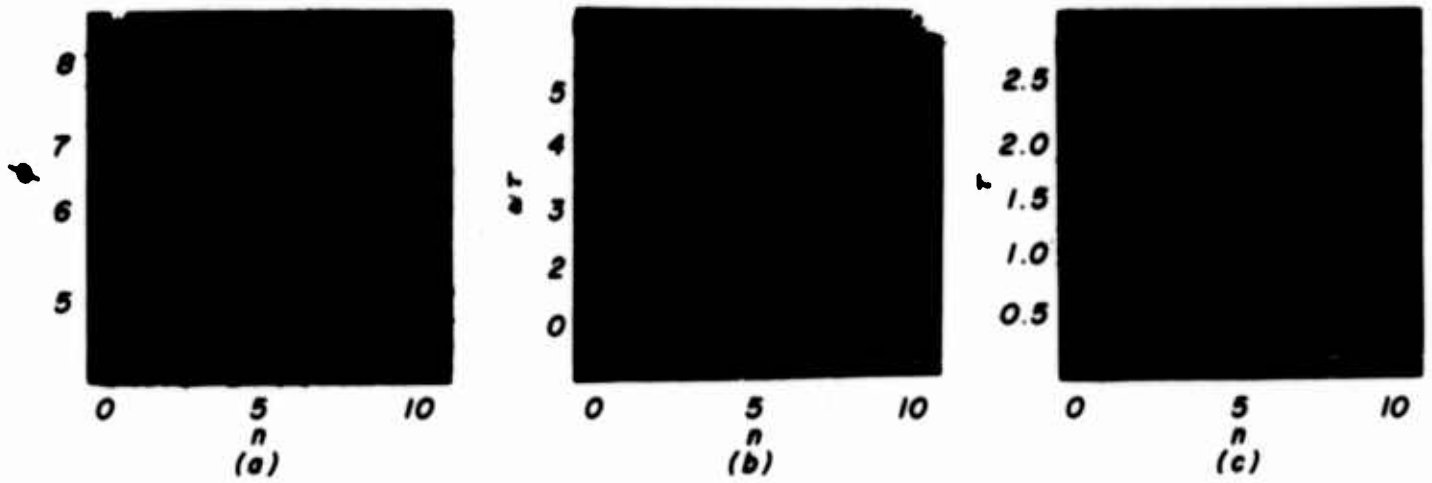

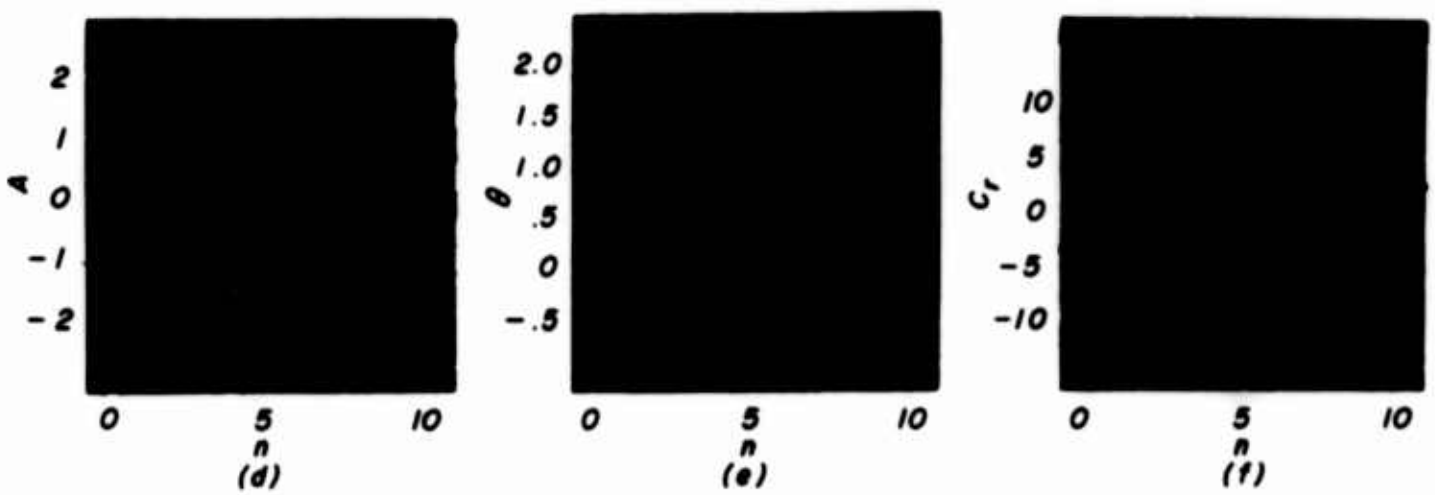

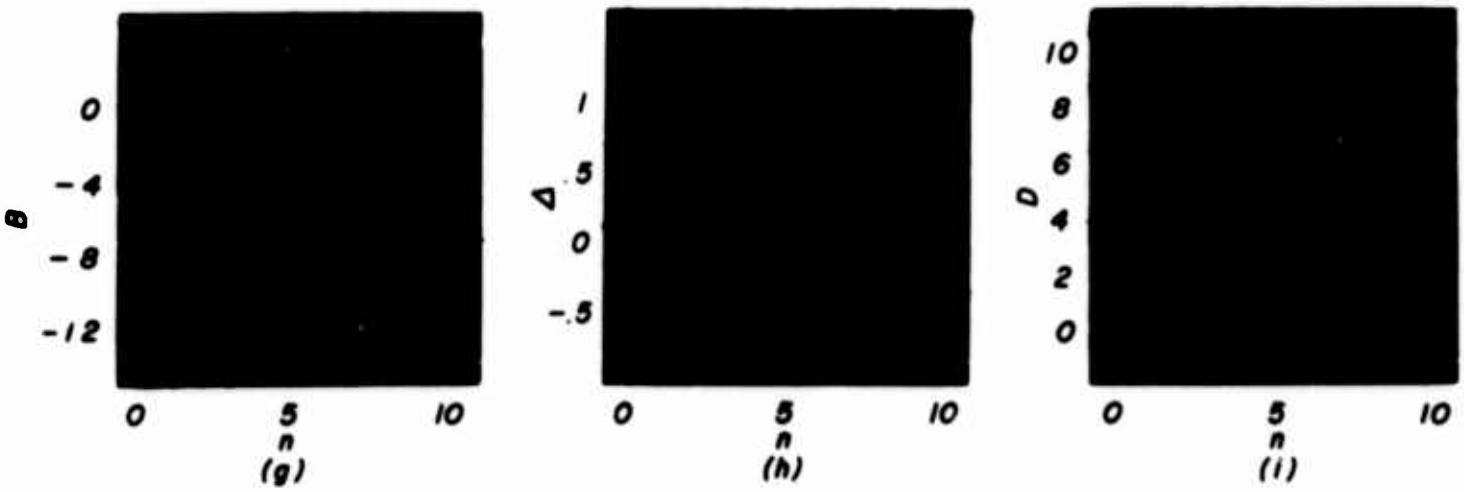

Figure III-3

Results of nonlinear longitudinal model with time-lag effect.
u_0 = .1 fundamental mode

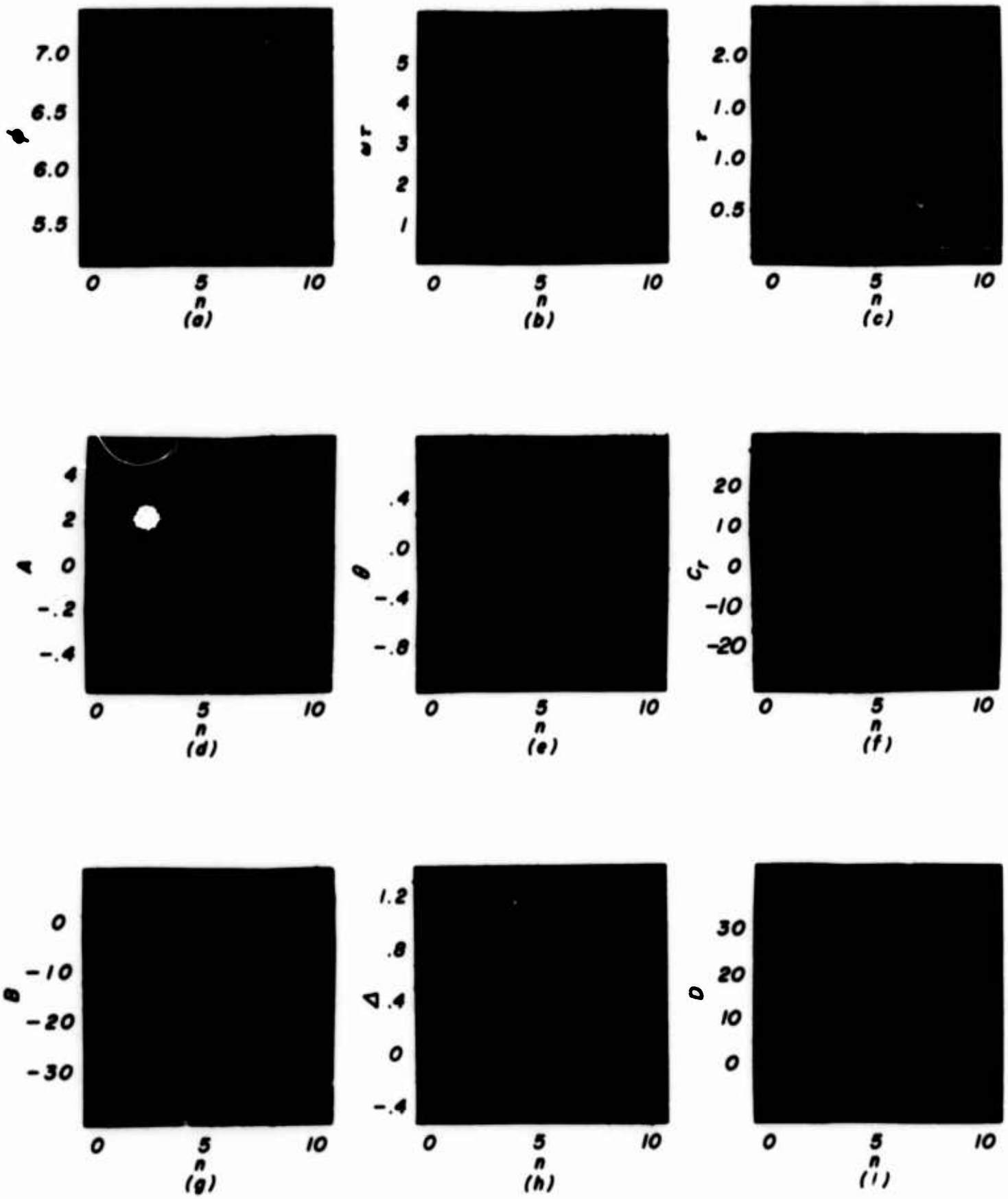

Figure III-4

Results of nonlinear longitudinal model with time-lag effect.
u_o = .3 = fundamental mode

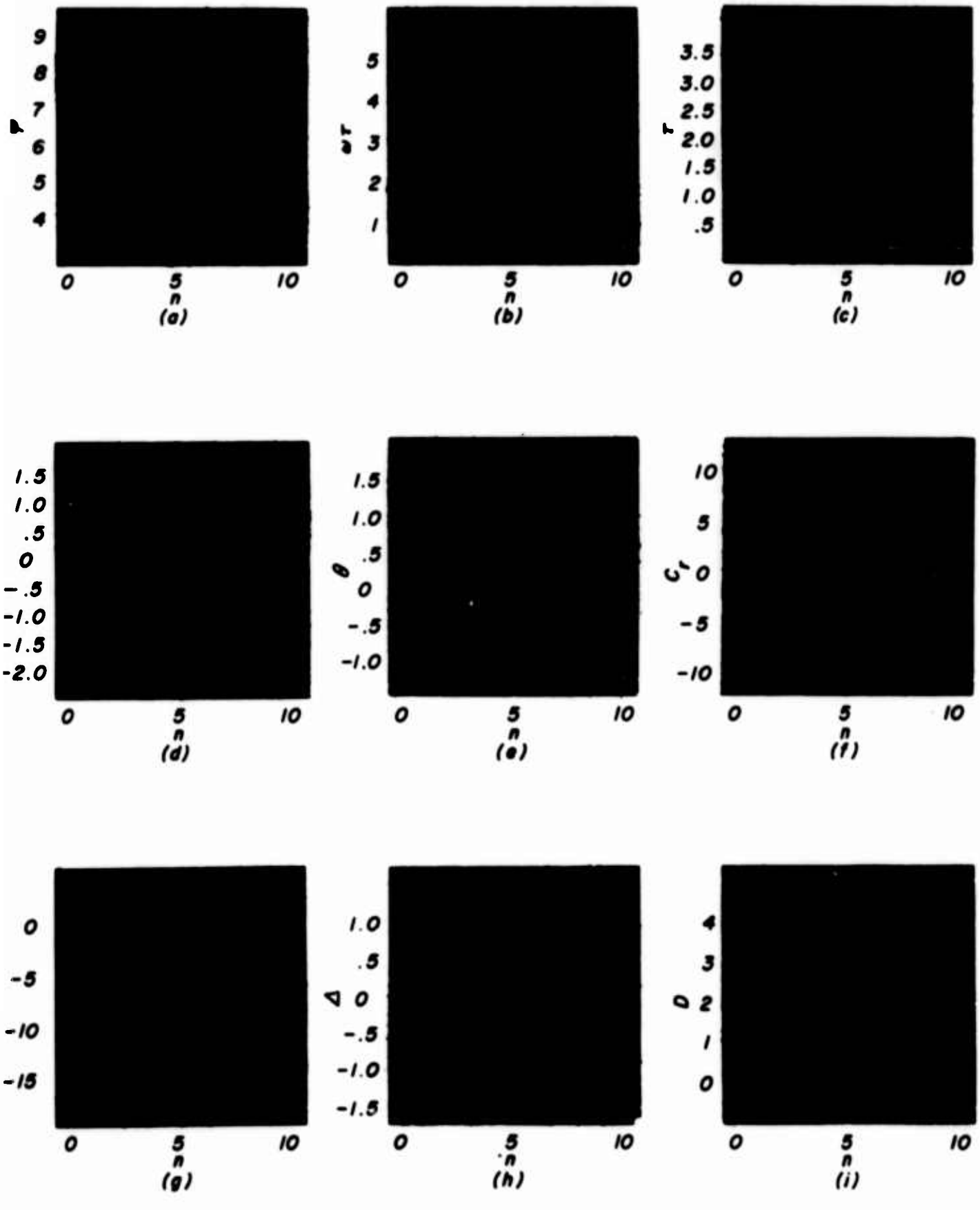

Figure III-5

Results of nonlinear longitudinal model with time-lag effect.
u_0=.2 second harmonic mode

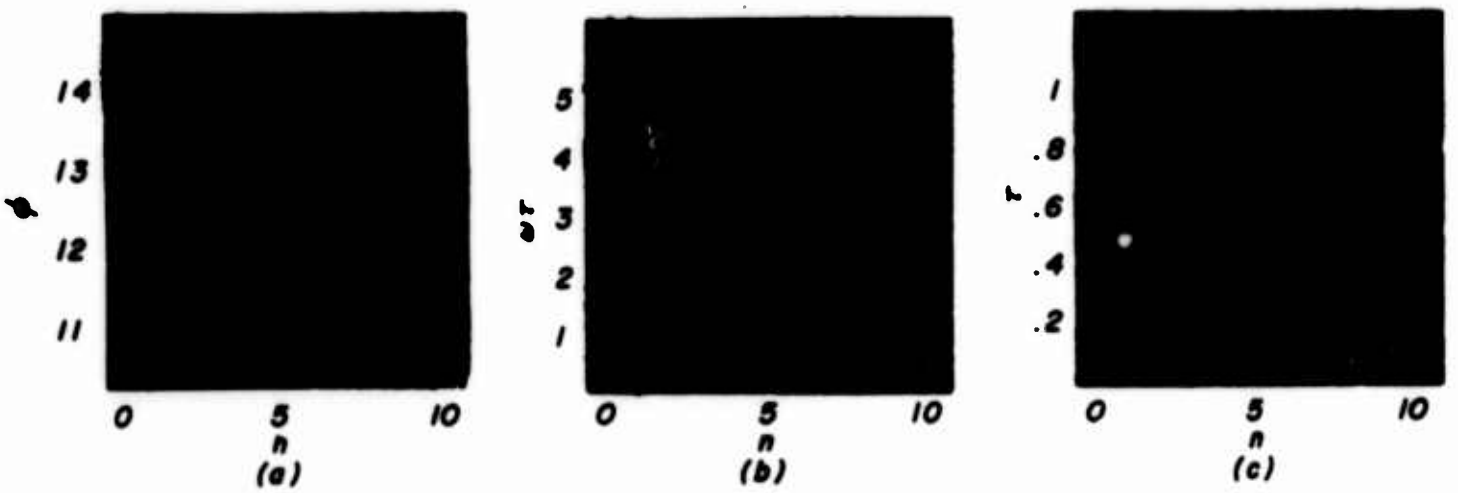

Figure III-6

Results of nonlinear longitudinal model with time-lag effect:
u_0 = .2 third harmonic mode

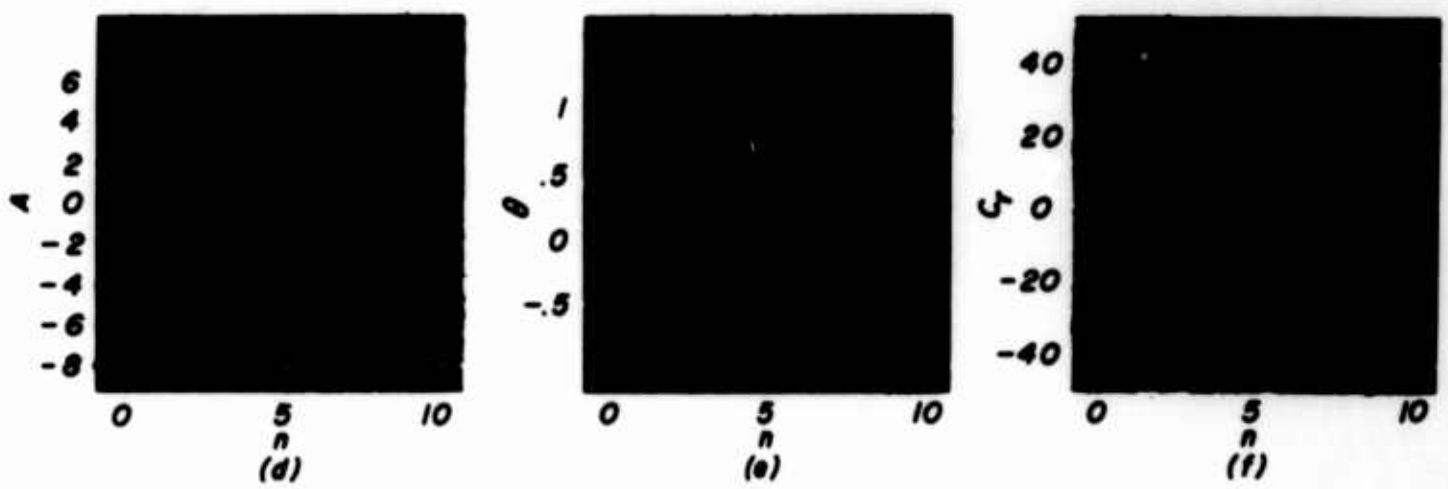

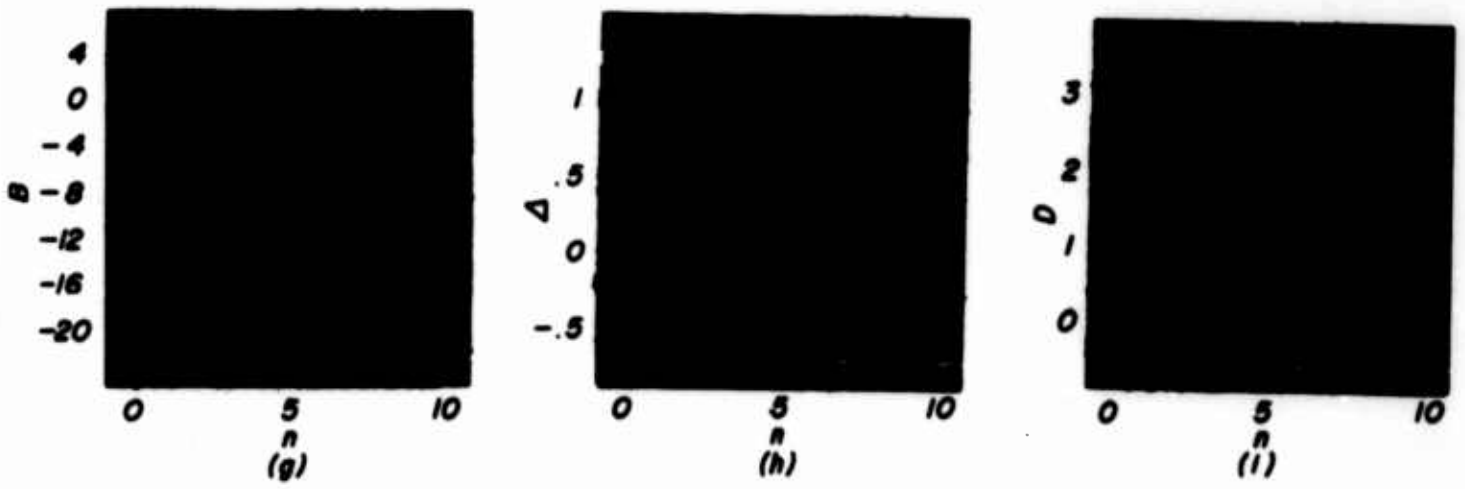

Figure III-7

Pressure versus time
Fixed chamber location

Nozzle-fundamental mode
Above-resonant oscillation
(a)

Injector-fundamental mode
Above-resonant oscillation
(b)

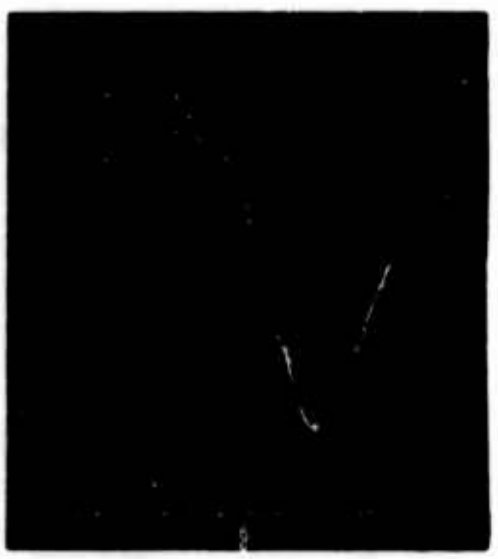

Nozzle-fundamental mode
Below-resonant oscillation
(c)

Nozzle- second harmonic
Above-resonant oscillation
(d)

Figure III-8

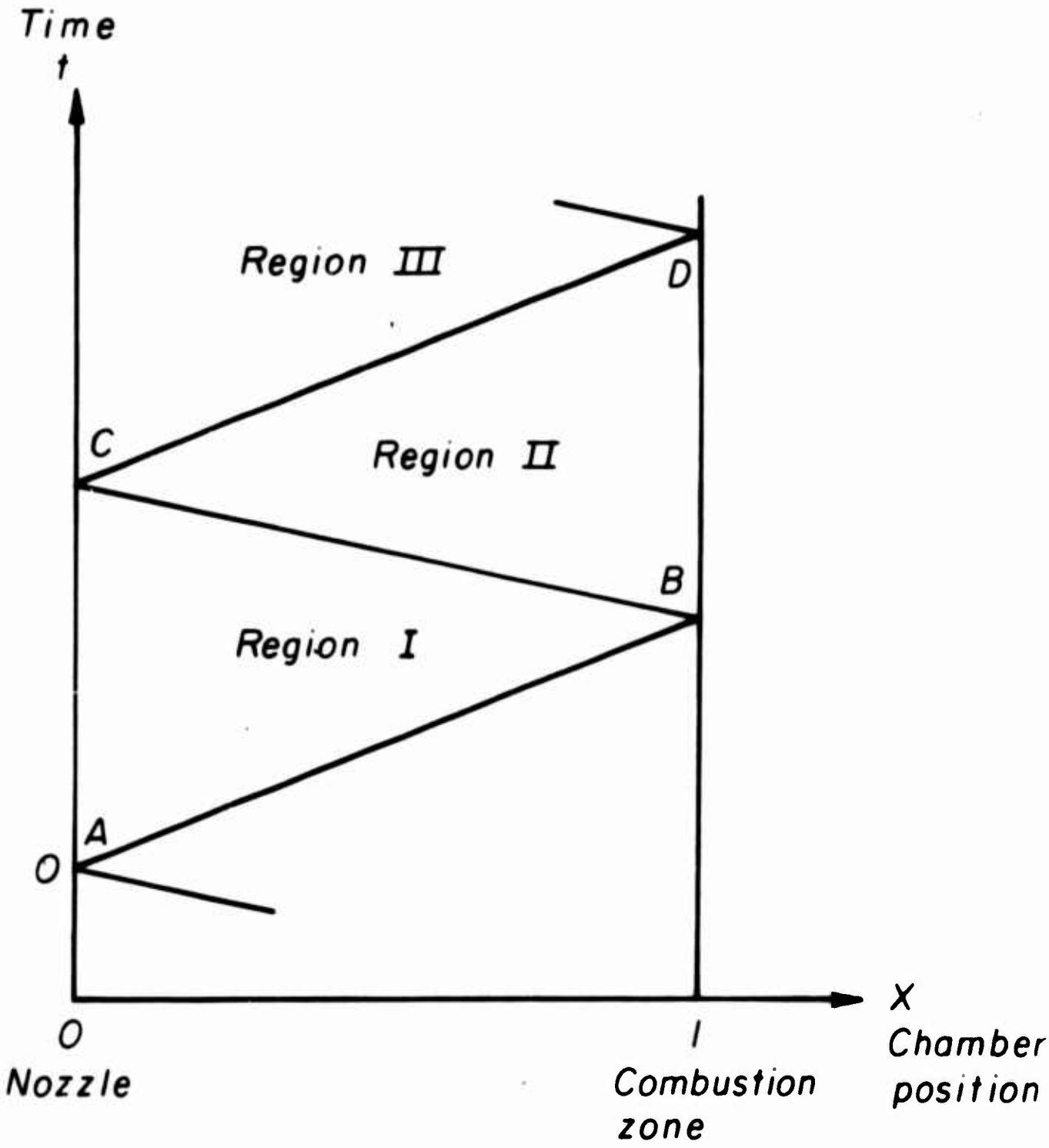
Shock path
Time
t
Region III
D
C
Region II
B
Region I
A
O
X
O
Nozzle
l
Combustion
zone
Chamber
position

Figure III - 9

Coordinate system used for the solution of the oscillatory nozzle flow

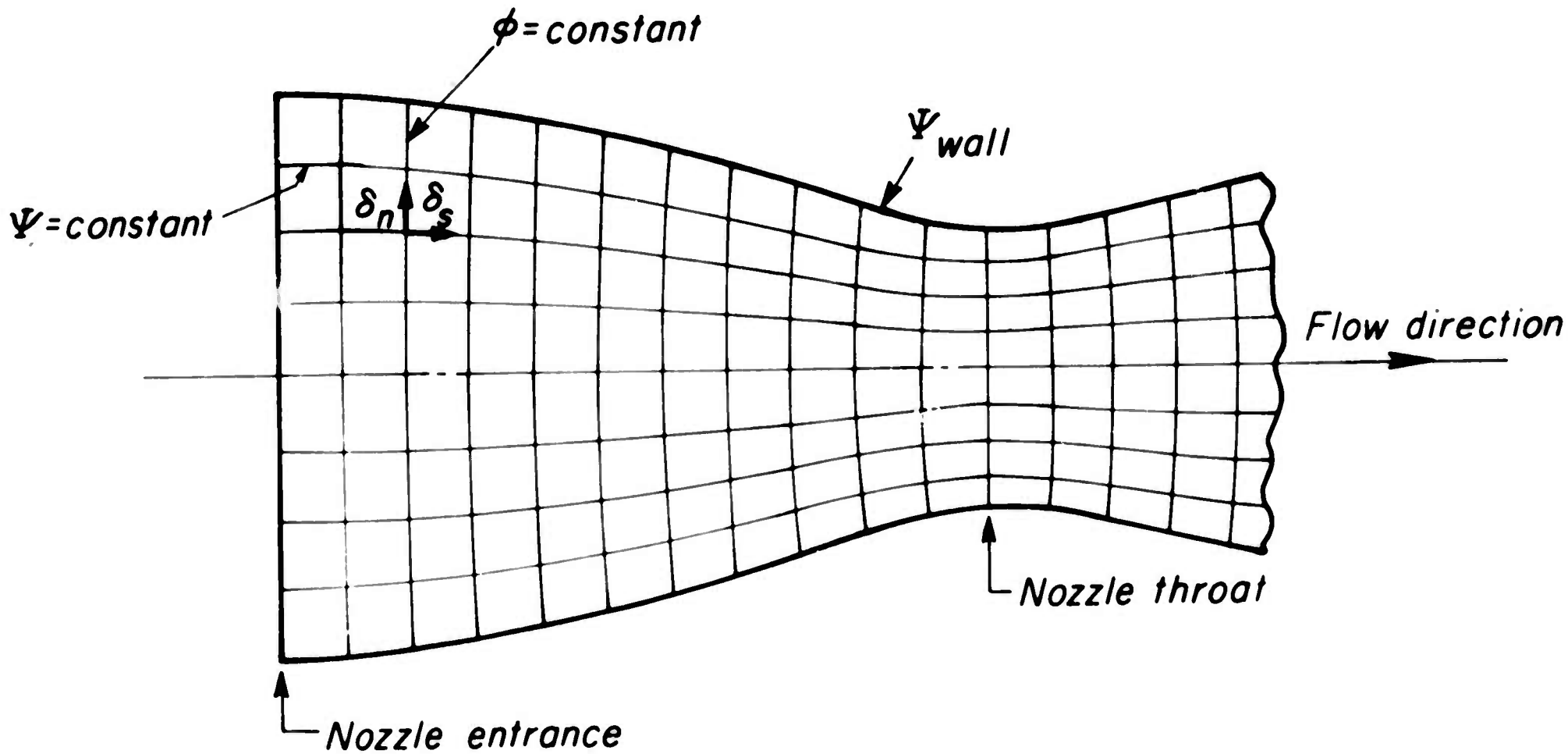

Figure III-10

Pulsed instability limits tests

0.2" like-on-like, O → F, alcohol-oxygen, 9"-7" chamber,

150 psia, 1000 lb thrust

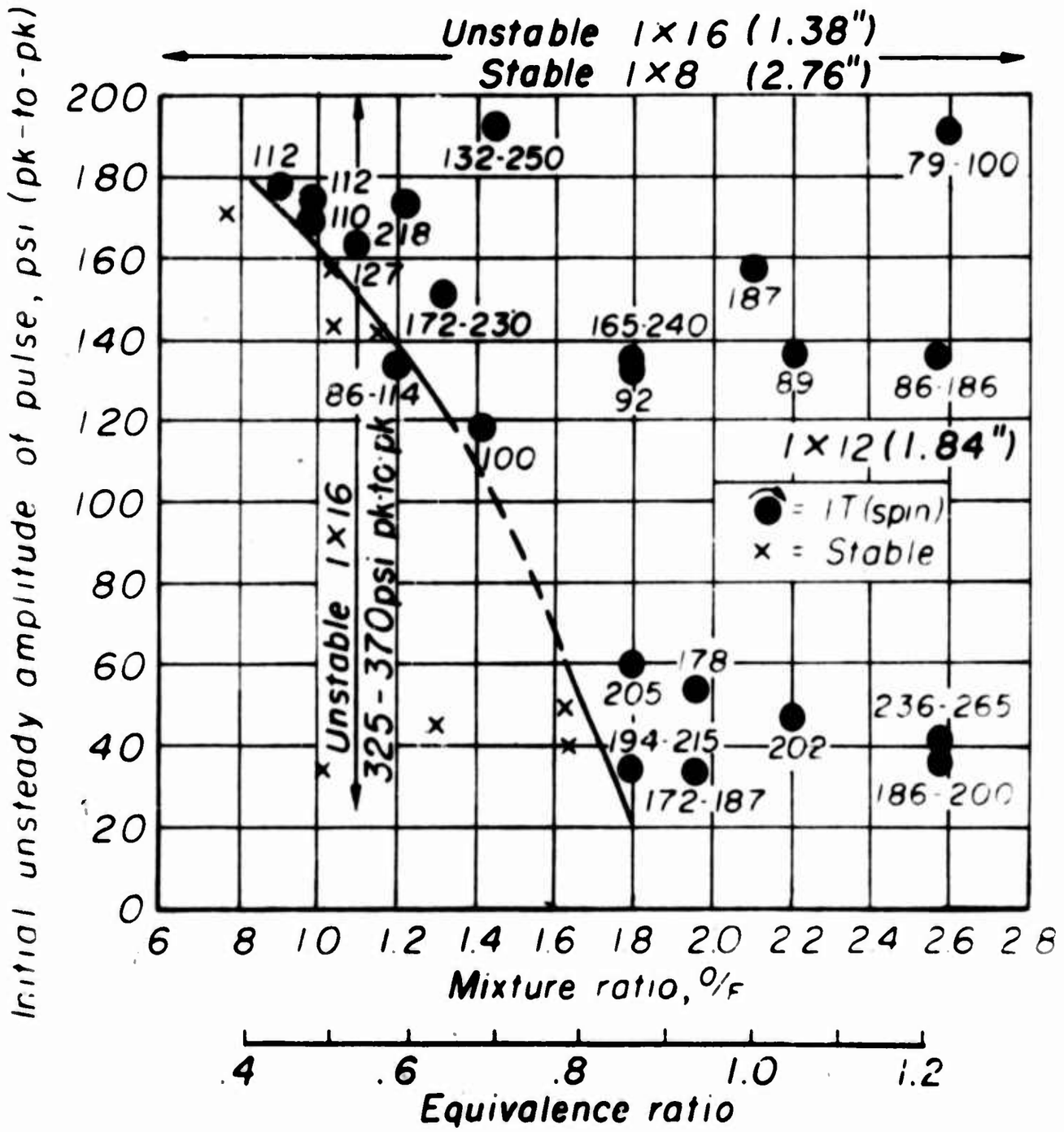

Figure IV-1

. LOX, Alc, pulsed - limits stability results using the 1 X (12+4), .2L on L 1.4 T injector $\bar{O} \rightarrow F$ and $O \rightarrow \bar{F}$ testing at five pulse sizes, 150 psia chamber pressure, 9" dia. chamber, 7" dia. injection, 1300 lb thrust

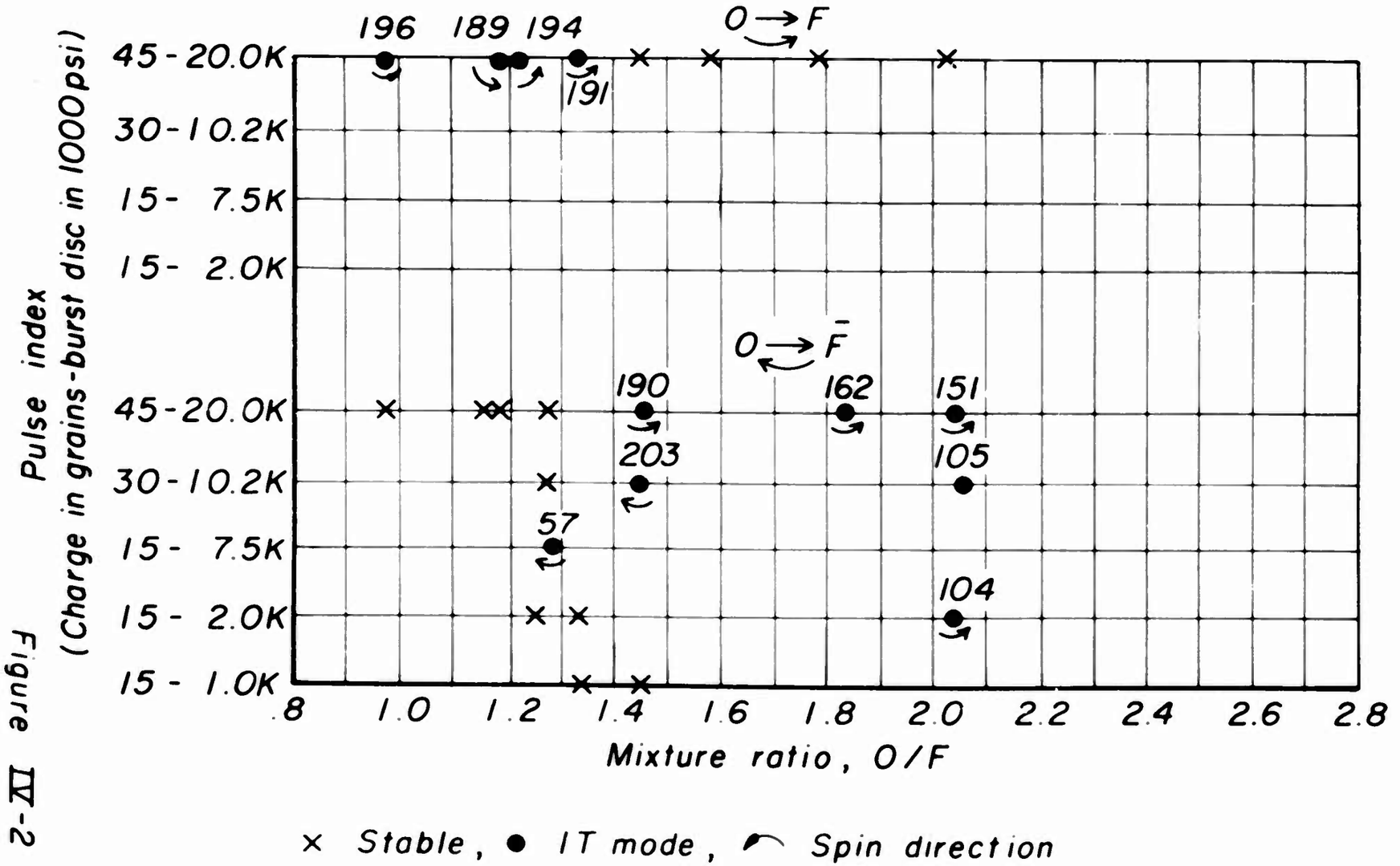

× Stable, ● IT mode, ↶ Spin direction

Figure IX-2

LOX, Alc. pulsed-limits stability results using the 1x(12+4), .2 LonL 1.4T injector $\bar{O}\rightarrow F$ and $O\rightarrow\bar{F}$ testing at one pulse size, at two chamber pressures 9" dia. chamber, 7" dia. injection, 1300 lb thrust

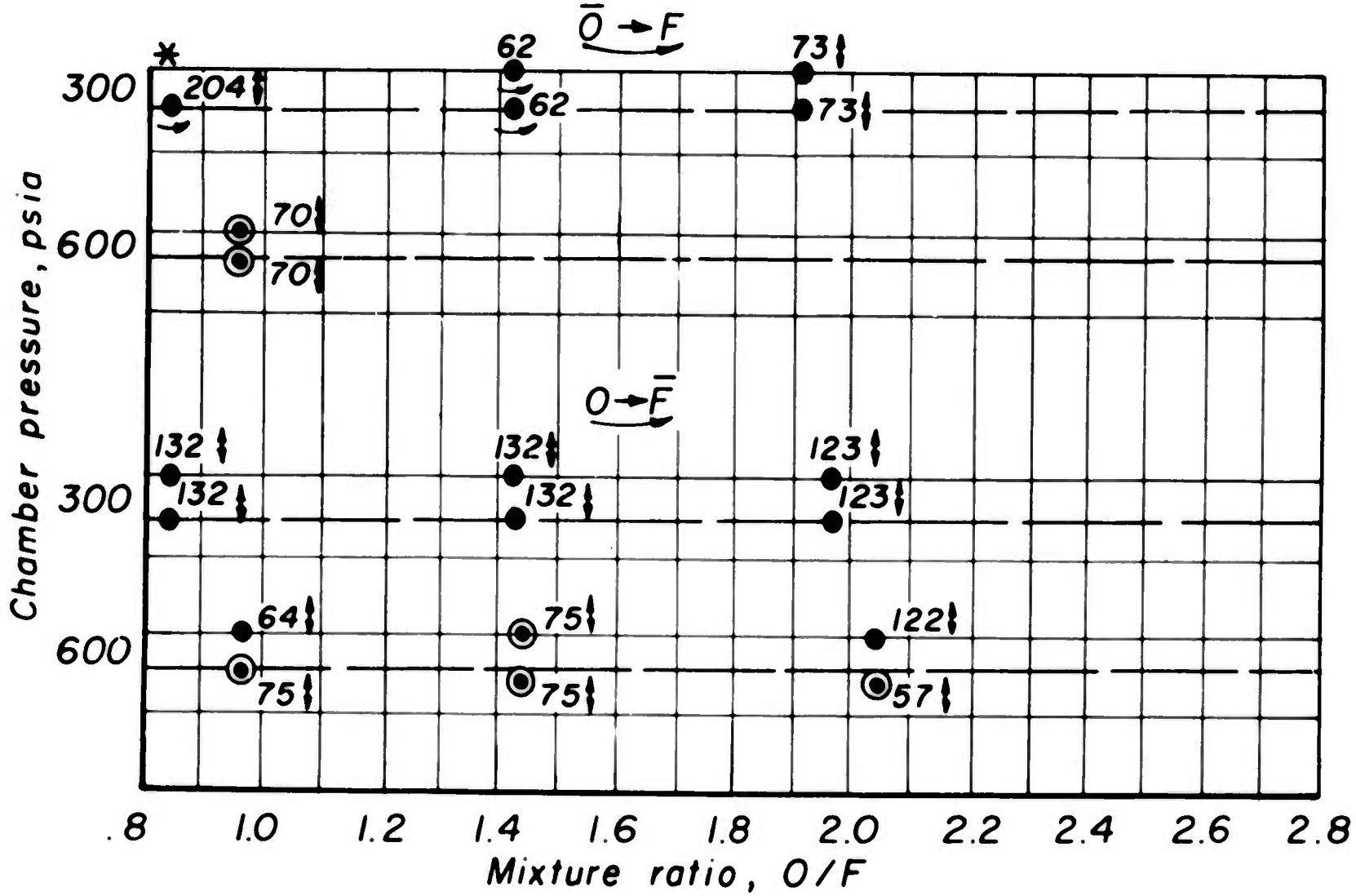

* No pulse, ● First tangential mode, ↶ Spin direction,
—— Before pulse, ◉ Second tangential mode,
| Max. amplitude, frequency and amplitude oscillating

Figure IV-3

LOX, Alc. pulsed-limits stability results using the 4x(3+1B).2 LonL 1.4T injector $\bar{O}\rightarrow F$ and $O\rightarrow\bar{F}$ testing at two pulse size, 150 psia chamber pressure, 9" dia. chamber, 7"dia. injection, 10001b thrust

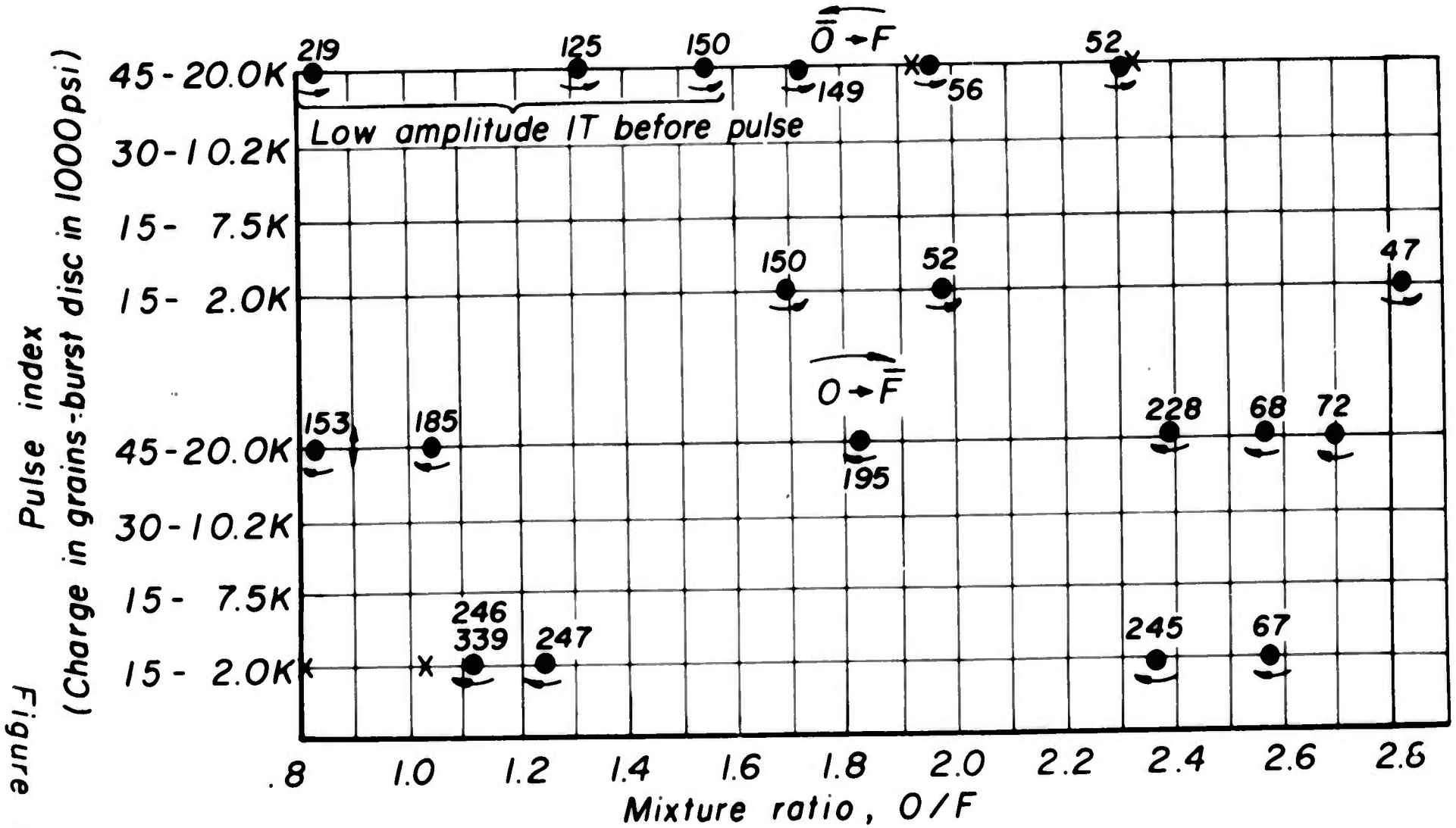

Figure IX-4

LOX, Alc. pulsed-limits stability results using the 4x(3+1B).2L on L 1.4T injector $F \rightarrow \bar{O}$ and $\bar{F} \rightarrow O$ testing at one pulse sizes, 150 psia chamber pressure, 9" dia. chamber, 7" dia. injection, 10001b thrust

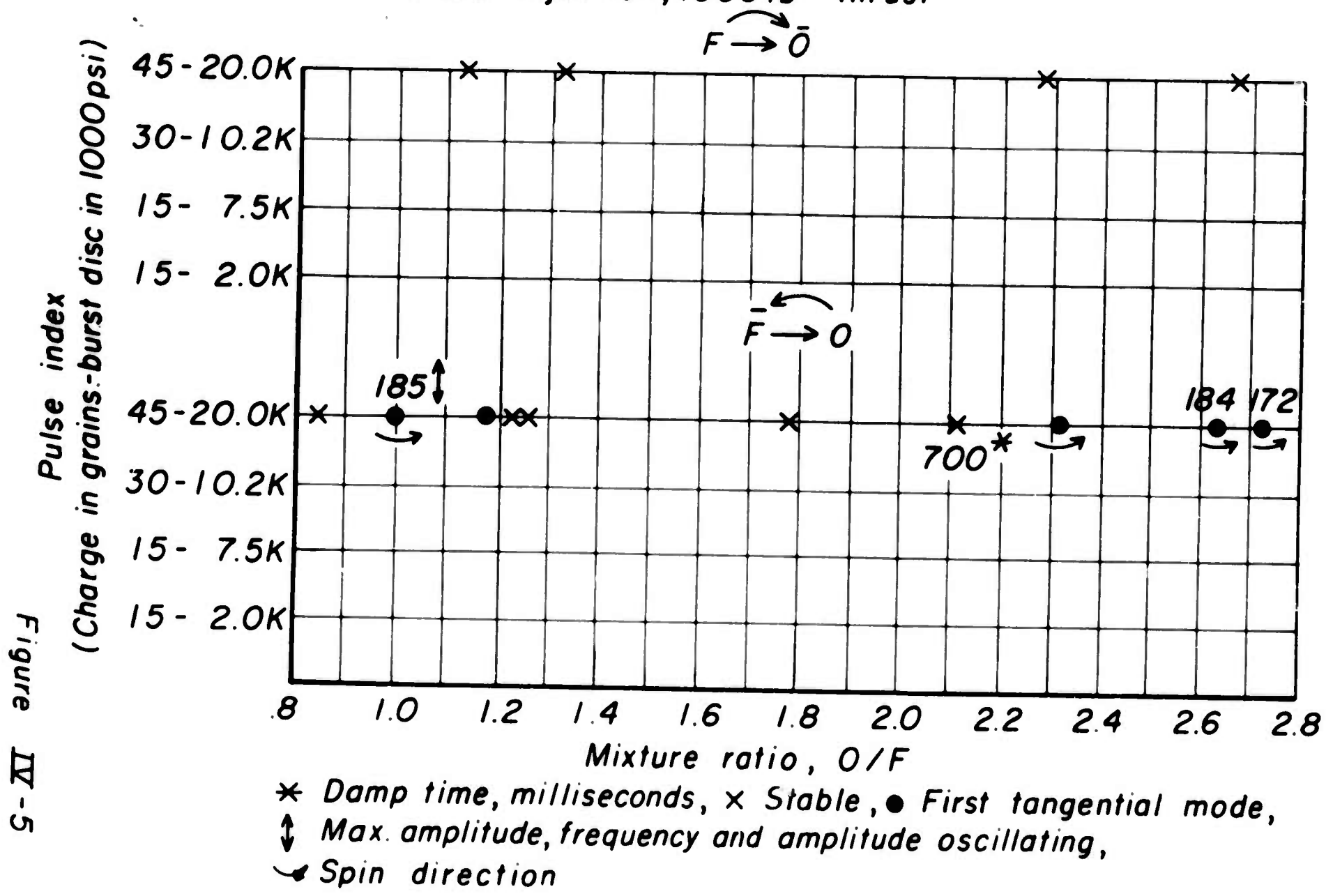

Figure IX-5

JPR 2174

LOX, Alc pulsed-limits stability results using the 4x(2+1B).2 LonL 1.4 T injector $\bar{O} \rightarrow F$ and $O \rightarrow \bar{F}$ testing at one pulse size, 300 psia chamber pressure, 9" dia. chamber, 7" dia. injection, 667 lb thrust

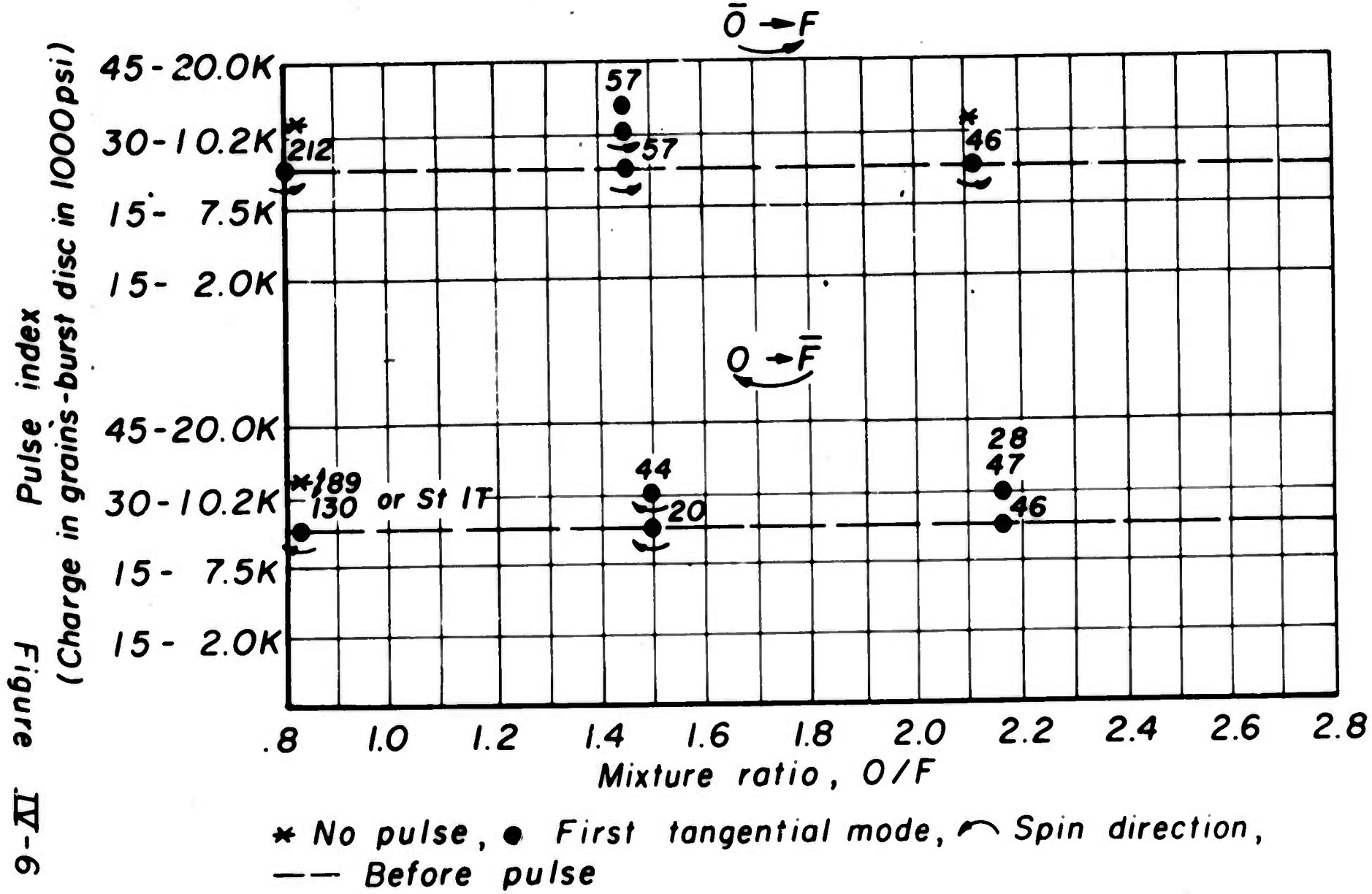

Figure IV-6

* No pulse, ● First tangential mode, ↶ Spin direction,
—— Before pulse

LOX - RP-1 pulsed-limits stability results using the 1 x 8+, .2 LonL, 1.4 T injector $\bar{O} \rightarrow F$ and $O \rightarrow \bar{F}$ testing at one pulse size (45-20K), at two chamber pressure, 9" dia. chamber, 7" dia. injection, 1334 lb thrust

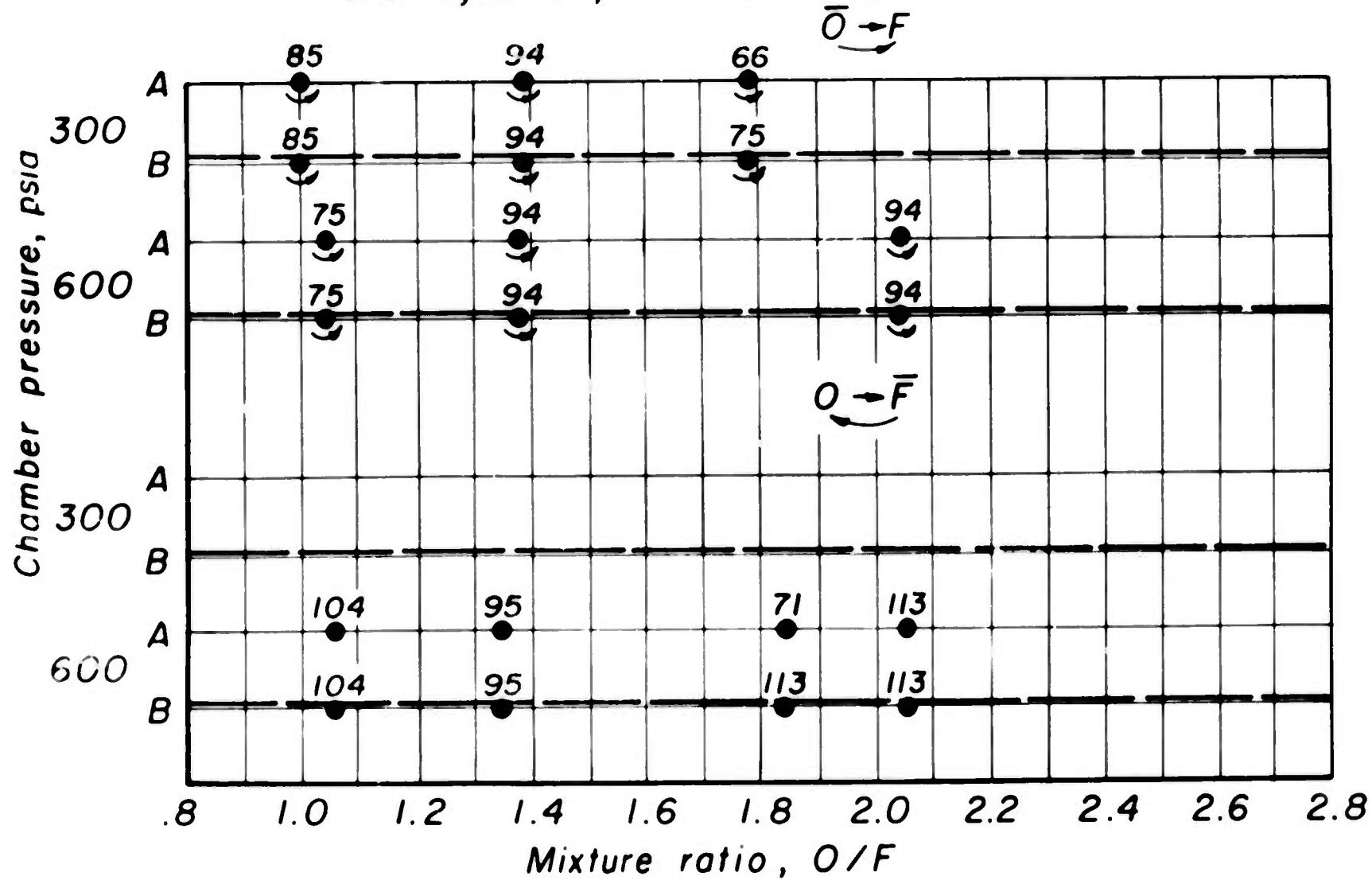

+ .084" diameter orifices, ● First tangential mode,
↷ Spin direction, A After pulse, B Before pulse

Figure IV-7

LOX, Alc. pulsed - limits stability results using the 2x(4+2B).2 L on L 1.4 T injector O → F̄ and F → Ō testing at one pulse size, 300 psia chamber pressure, 9" dia. chamber, 7" dia. injection, 667 lb thrust

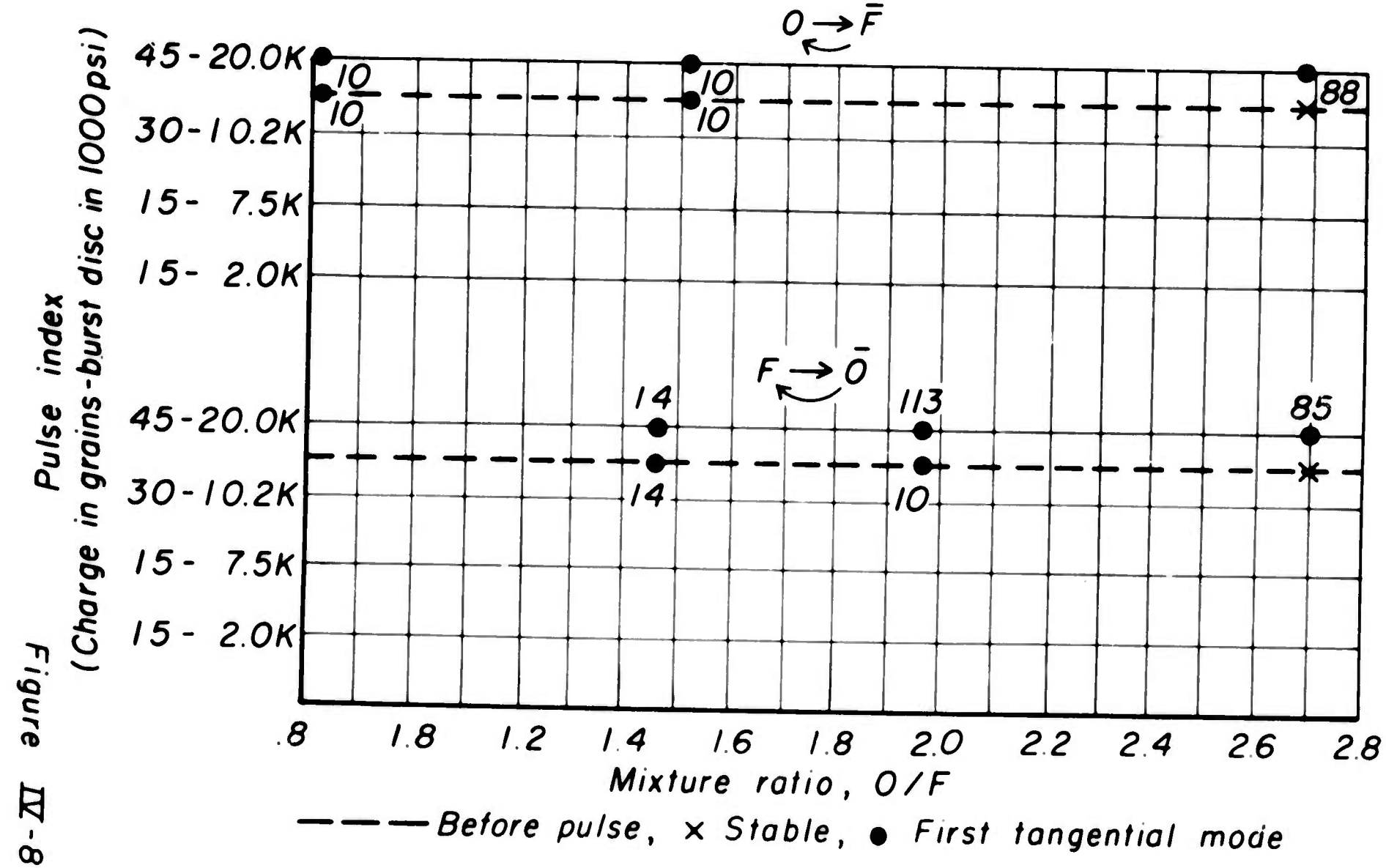

Figure IX-8

. LOX, Alc. pulsed - limits stability results using the 2x(4+2B).2 L onL 1.4 T injector $\bar{O} \rightarrow F$ and $O \rightarrow \bar{F}$ testing at one pulse size, 600 psia chamber pressure, 9" dia. chamber, 7" dia. injection, 667 lb thrust

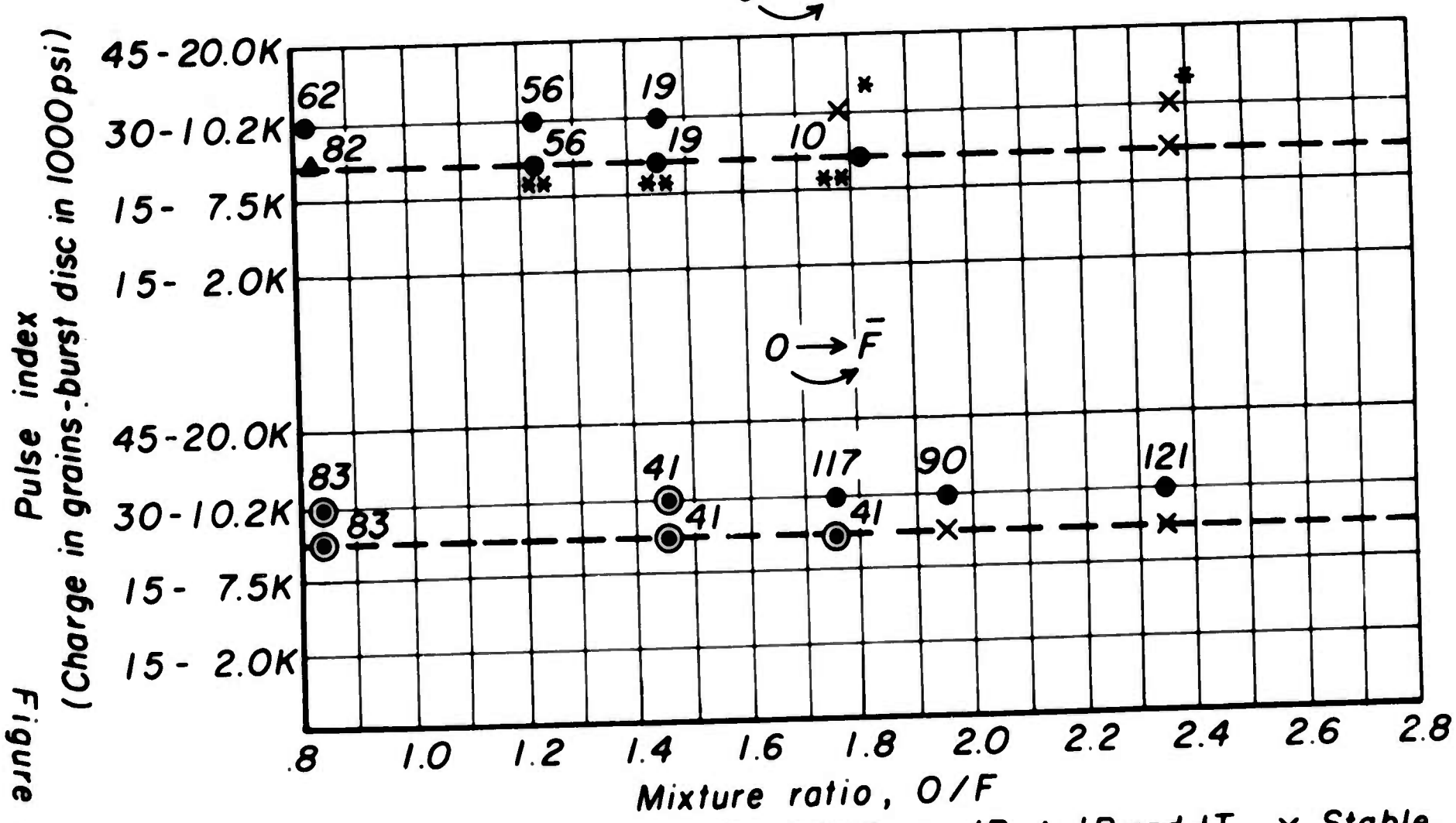

— — Before pulse, ◉ ≈6000 cps, IR, ▲ IR and IT, × Stable,
* Long decay (O) .4 sec, ** Traces of 6000 cps early in runs,
● First tangential mode

Figure IX-9

LOX, RP-1 pulsed-limits stability results using the 1×12, .2 LonL 1.4T injector $\bar{O} \rightarrow F$ and $O \rightarrow \bar{F}$ testing at two pulse sizes, 150 psia chamber pressure, 9" dia. chamber, 7" dia. injection, 10001b thrust

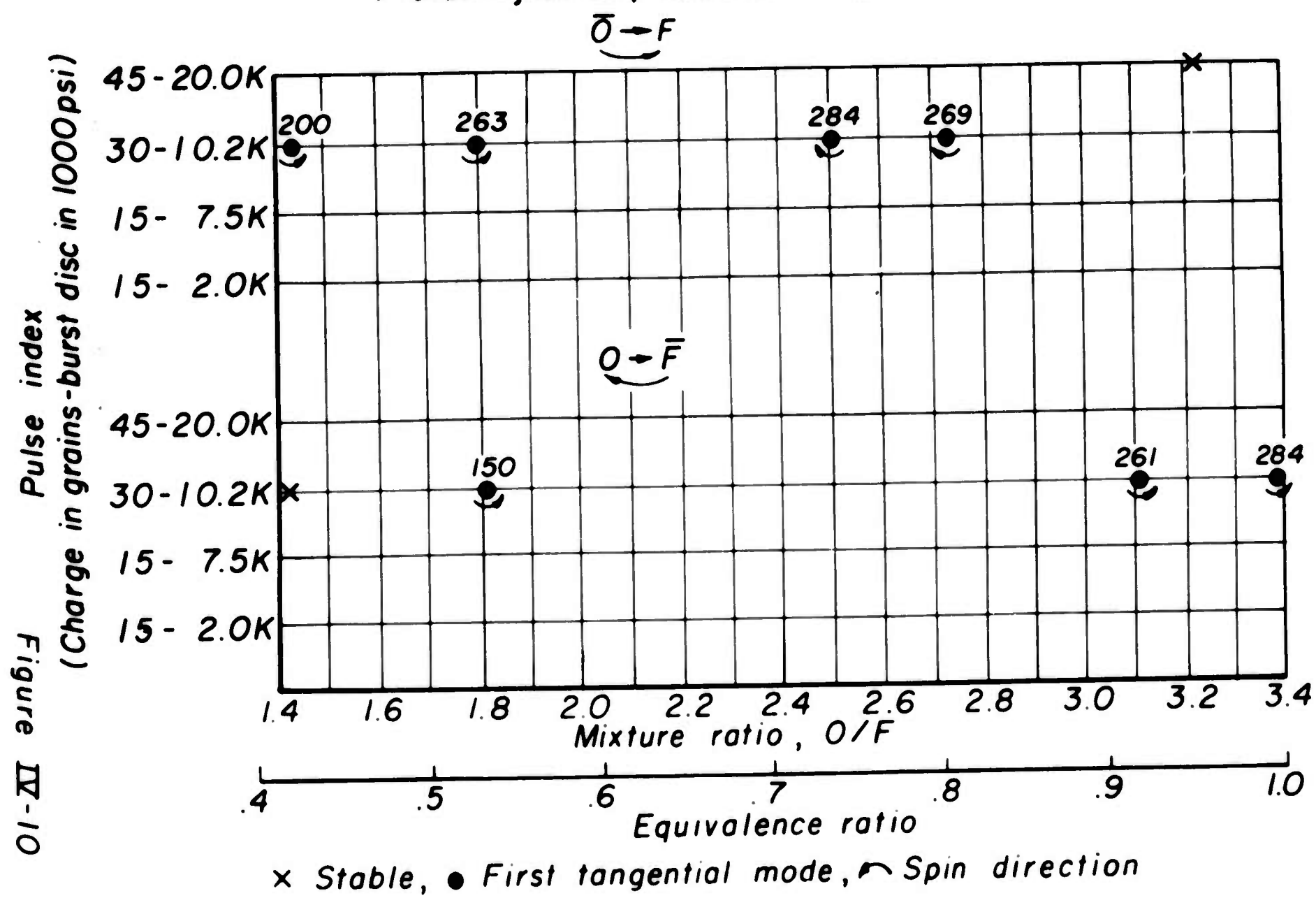

Figure IX-10

JPR 2376

LOX, RP-1 pulsed-limits stability results using the 1×12, .2 LonL 1.4T injector F→$\bar{O}$ and $\bar{F}$→O testing at two pulse sizes, 150 psia chamber pressure, 9" dia. chamber, 7" dia. injection, 10001b thrust

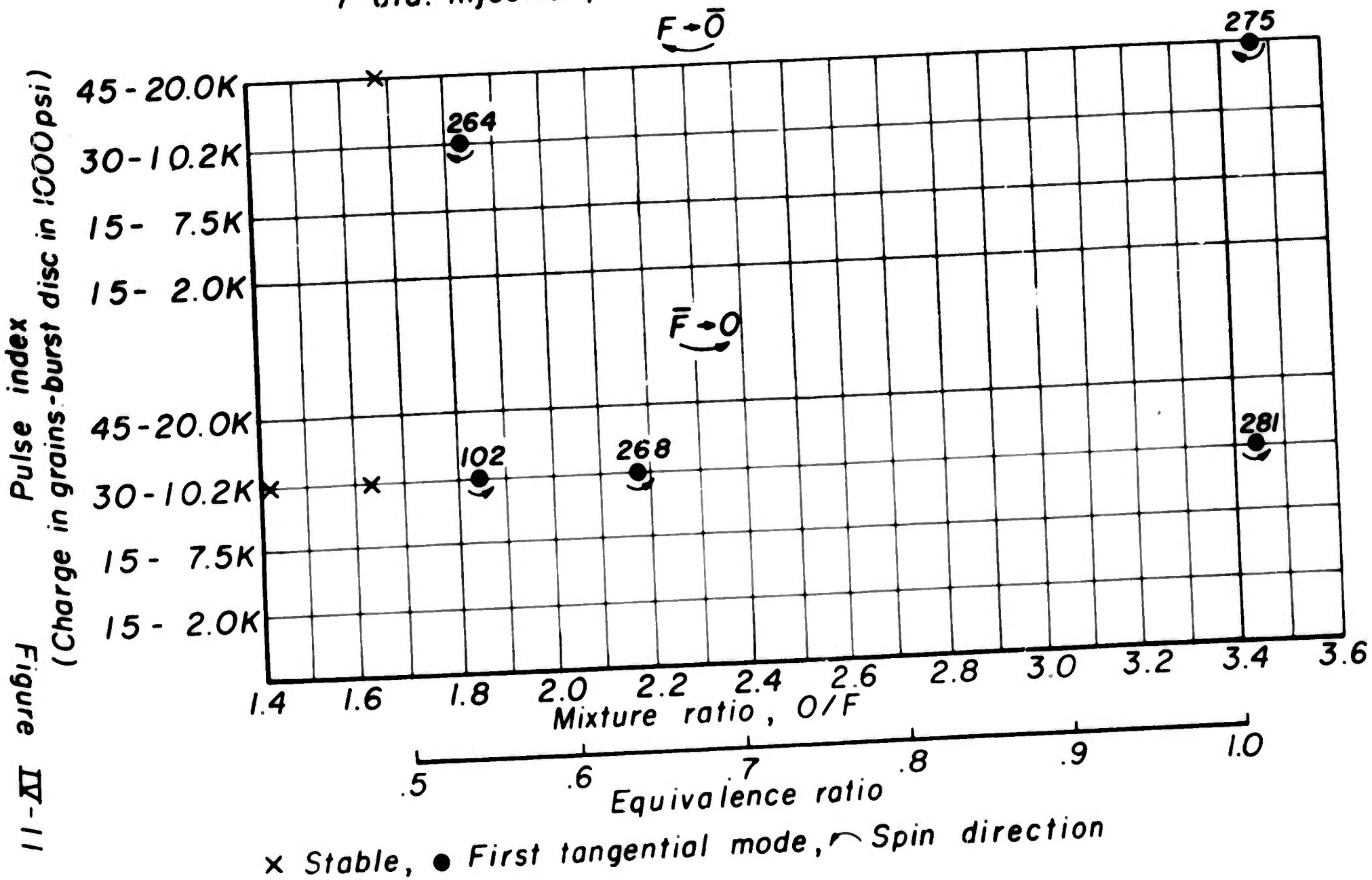

Figure IX-11

LOX, RP-1 pulsed-limits stability results using the 6×2,.2 L on L 1.4 T. injector ($O \rightarrow \bar{F}$), and ($O \rightarrow \bar{F}$)$_2$ testing at one pulse sizes, 150 psia chamber pressure, 9" dia. chamber, 7" dia. injection, 10001b thrust

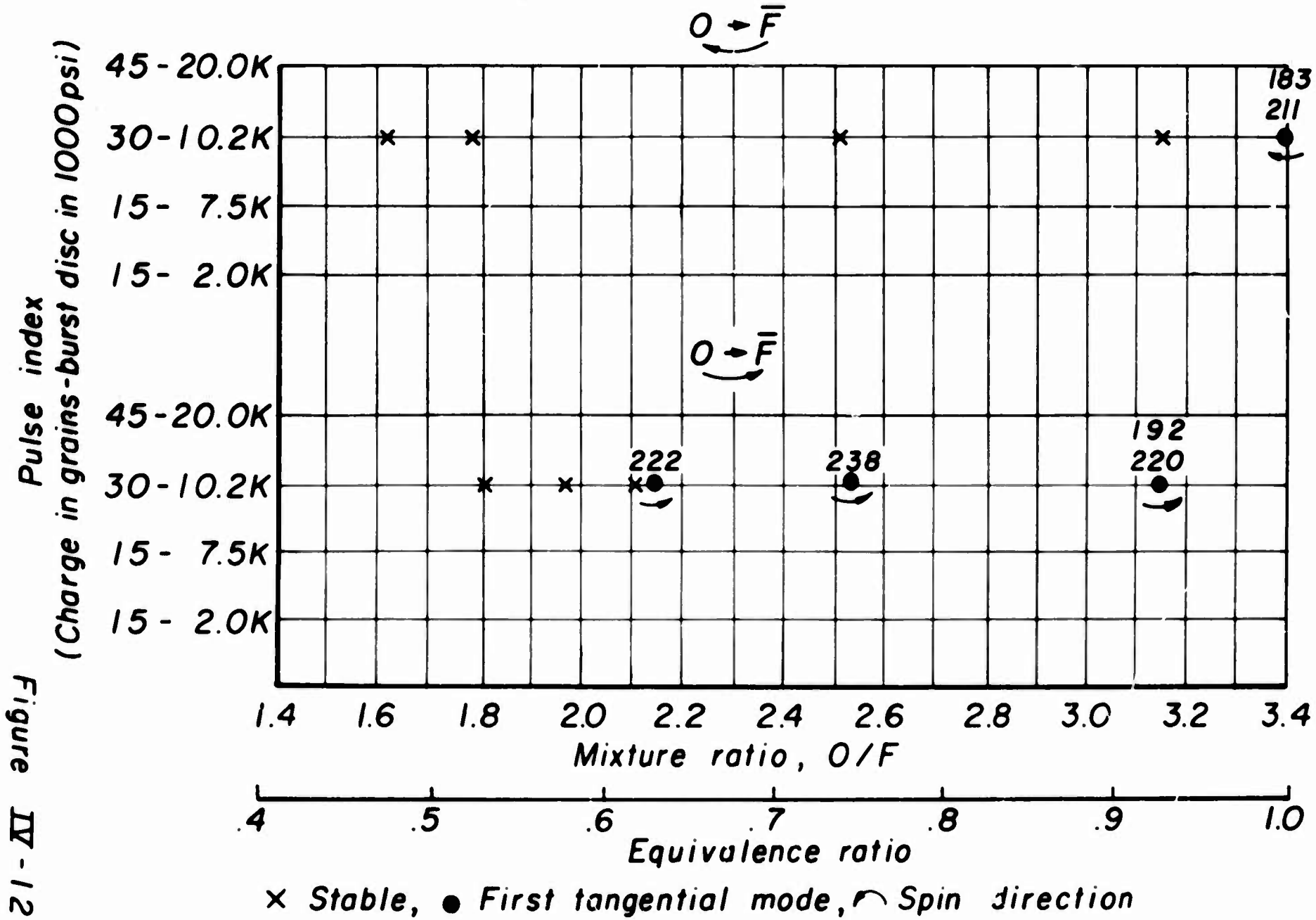

Figure IV-12

LOX, RP-1 pulsed-limits stability results using the 6 X 2, .2 L on L 1.4T injector ($F \rightarrow \bar{O}$)$_1$ and ($F \rightarrow \bar{O}$)$_2$ testing at one pulse sizes, 150 psia chamber pressure, 9" dia. chamber, 7" dia. injection, 1000 lb thrust

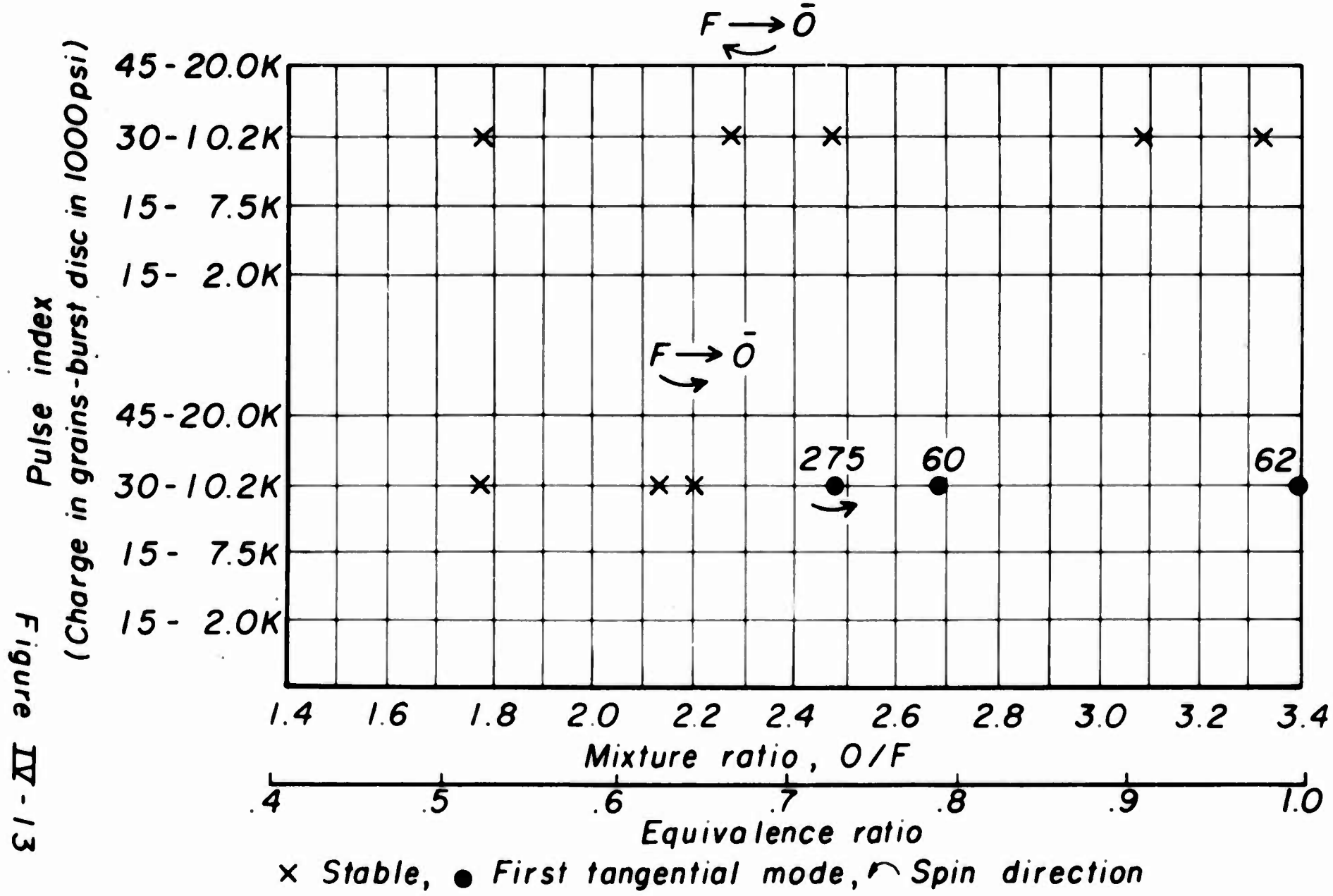

× Stable, ● First tangential mode, ↶ Spin direction

Figure IX-13

LCX, RP-1 pulsed-limits stability results using the 6 X 2, .2 L on L 1.4T. injector($\bar{O} \rightarrow F$)$_1$ and ($\bar{O} \rightarrow F$)$_2$ testing at one pulse size, 150 psia chamber pressure, 9" dia. chamber, 7" dia. injection, 1000 lb thrust

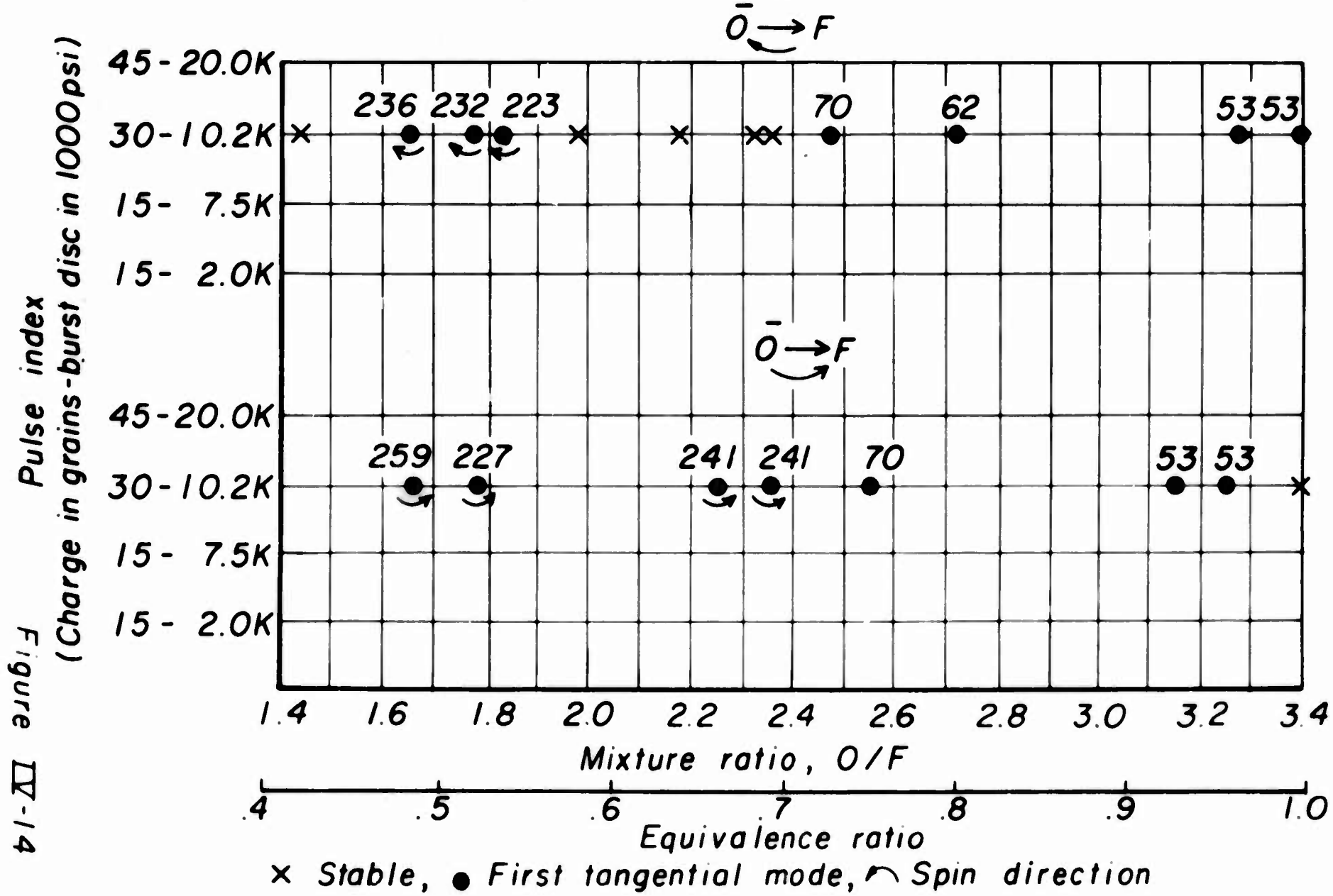

Figure IX-14

Mixture ratio distribution at 3" from the injector face for the (6×2) .2 L on L 1.4T- $\bar{O}$ injector, 9" dia. chamber, 7" dia. injector, 1.4 mixture ratio flow.

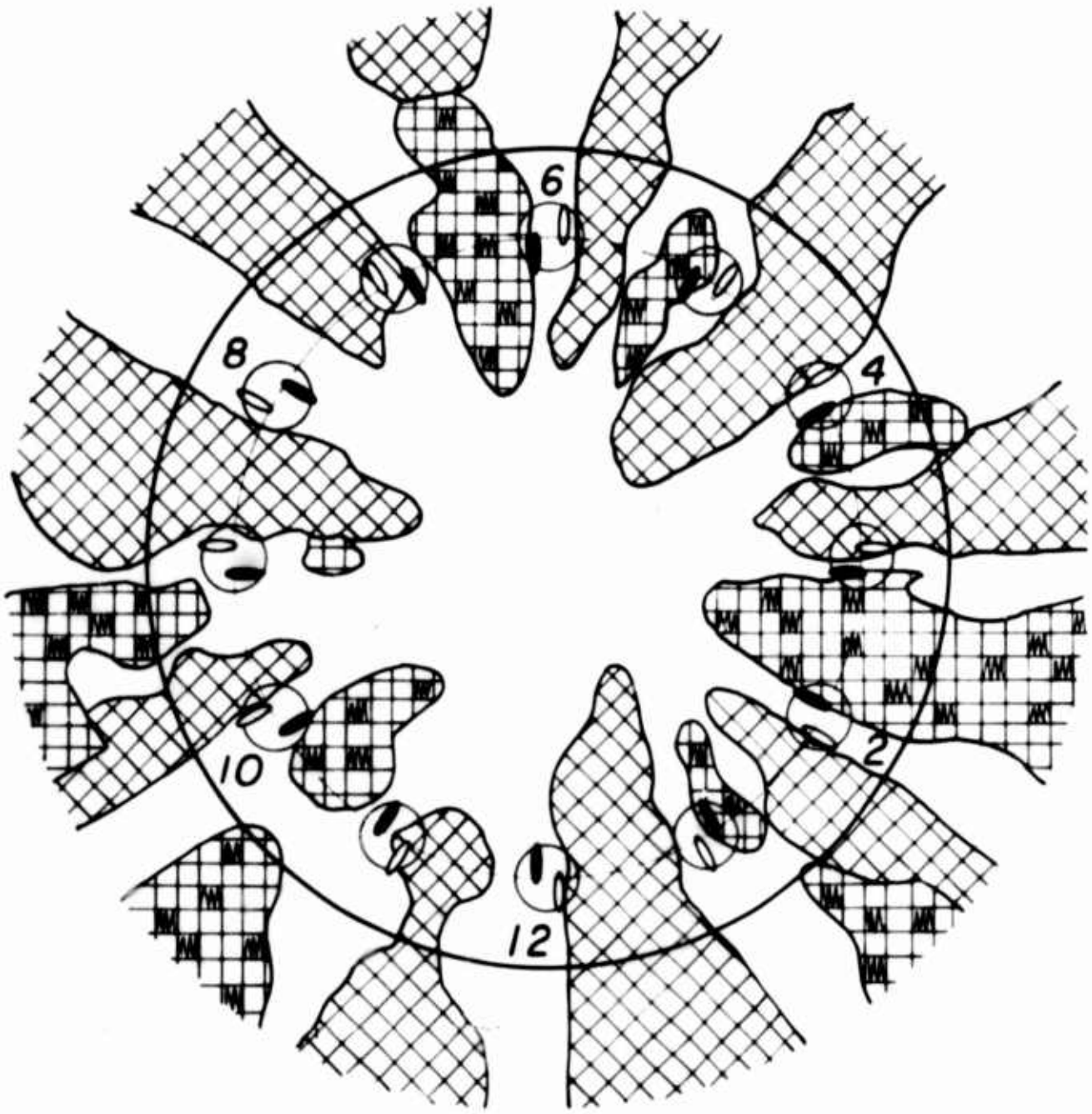

● = Fuel

○ = Lox

⨯ = over 5.0 mixture ratio

▦ = < 1.0 mixture ratio

Figure IV-15

Mixture ratio and relative mass distribution at 3 inches from the injector face along the circumference of the propellant injection circle for a (6 × 2) .2 L on L 1.4 T - $\bar{O}$ injector, 1.4 mixture ratio.

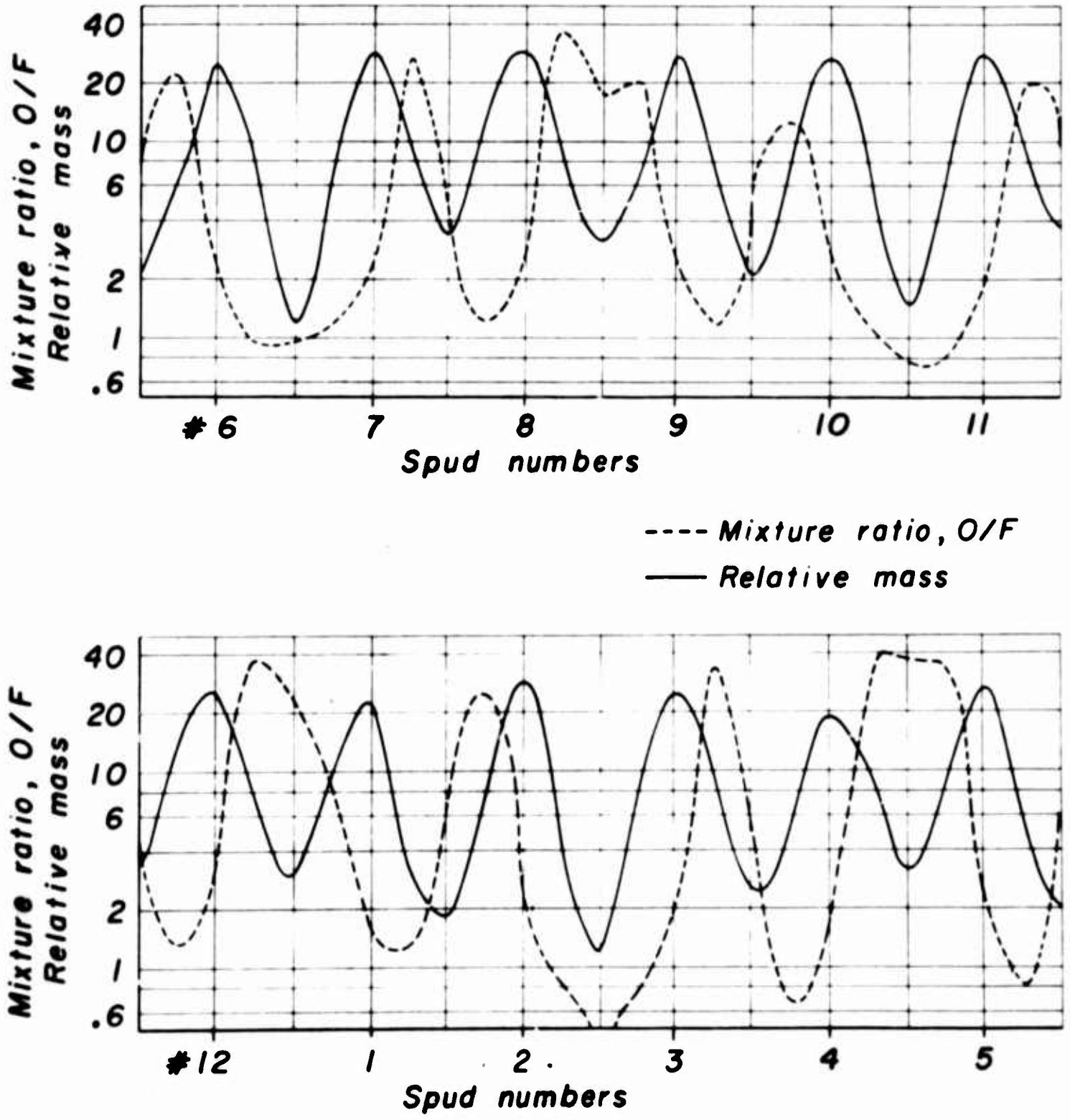

Figure IV-16

Mixture ratio distribution at 3" from the injector face for the (6×2) .2 L on L 1.4T- $\bar{O}$ injector, 9" dia. chamber, 7" dia. injector, 2.4 mixture ratio flow.

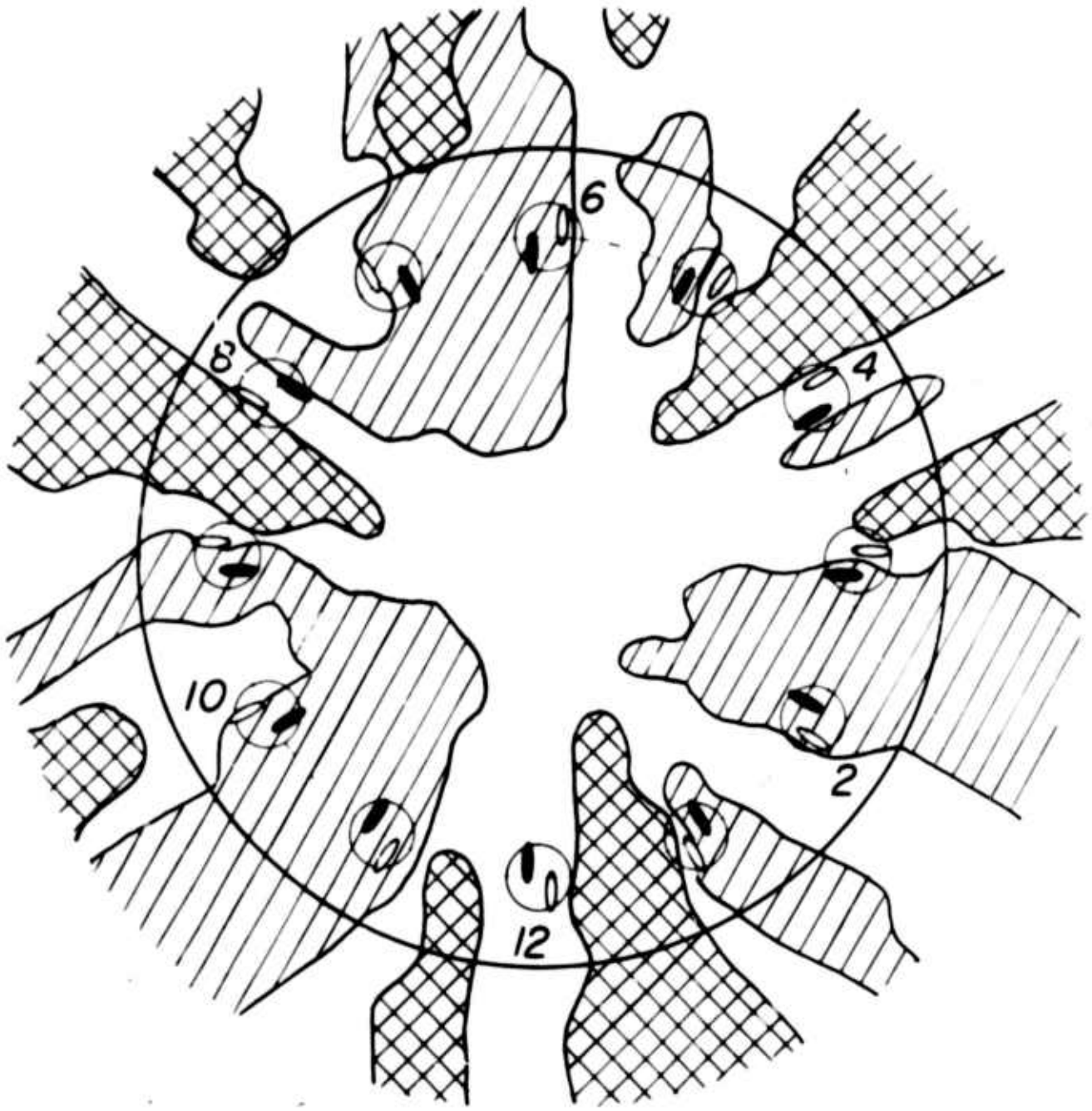

▮ = Fuel

▯ = Lox

⧄ = over 5.0 mixture ratio

/// = 1.0-5.0 mixture ratio

Figure IV-17

Mixture ratio and relative mass distribution at 3 inches from the injector face along the circumference of the propellant injection circle for a (6 × 2) .2 L on L 1.4 T-O injector, 2.4 mixture ratio.

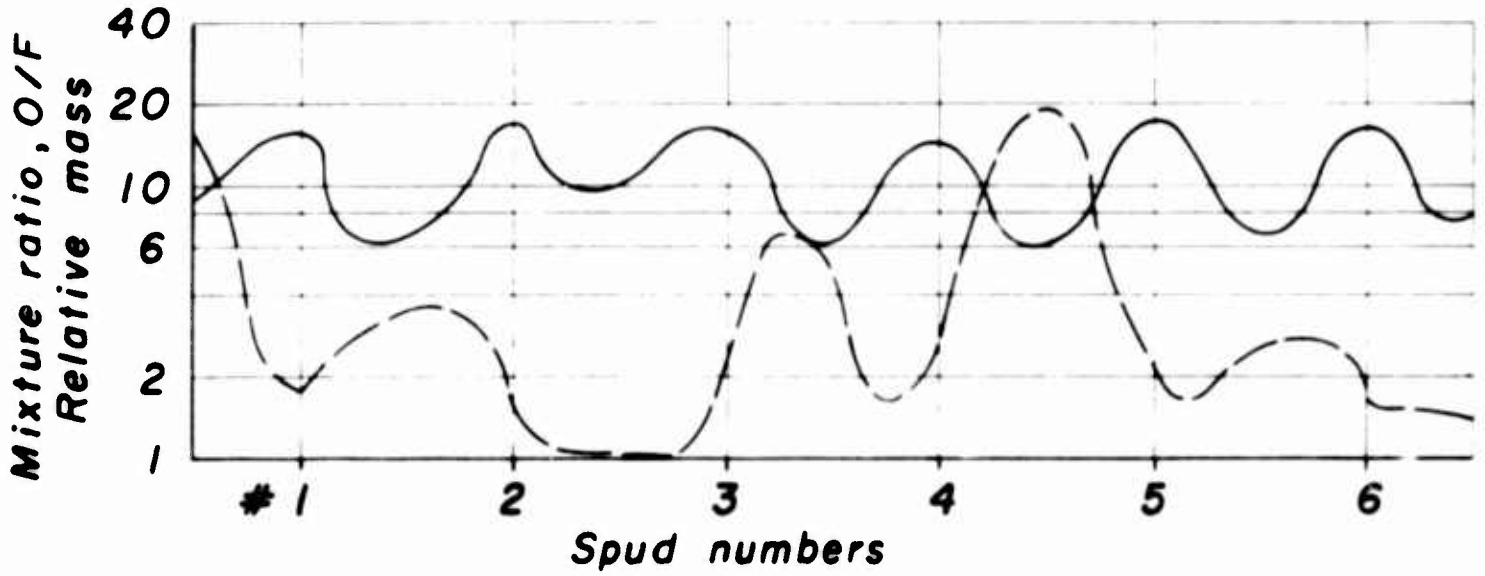

Figure IV-18

Four 4 x 4 injectors used in sq-motor testing

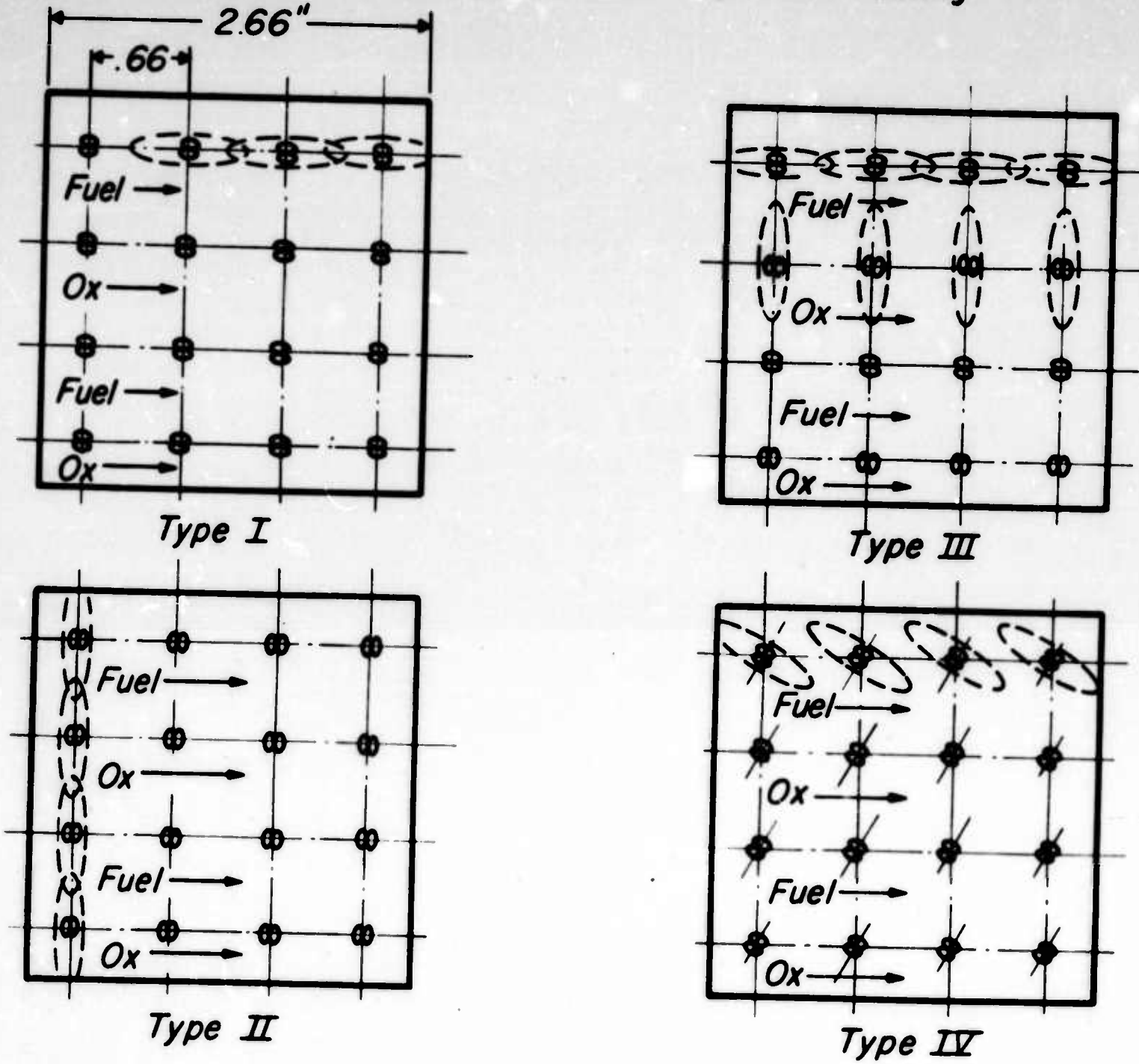

Figure IV-19

Variable - length, square - motor, 4x4 LonL Type III injector,
800 lb thrust, 300 psia, 15-1K pulsed 0→0
LOX, Alcohol

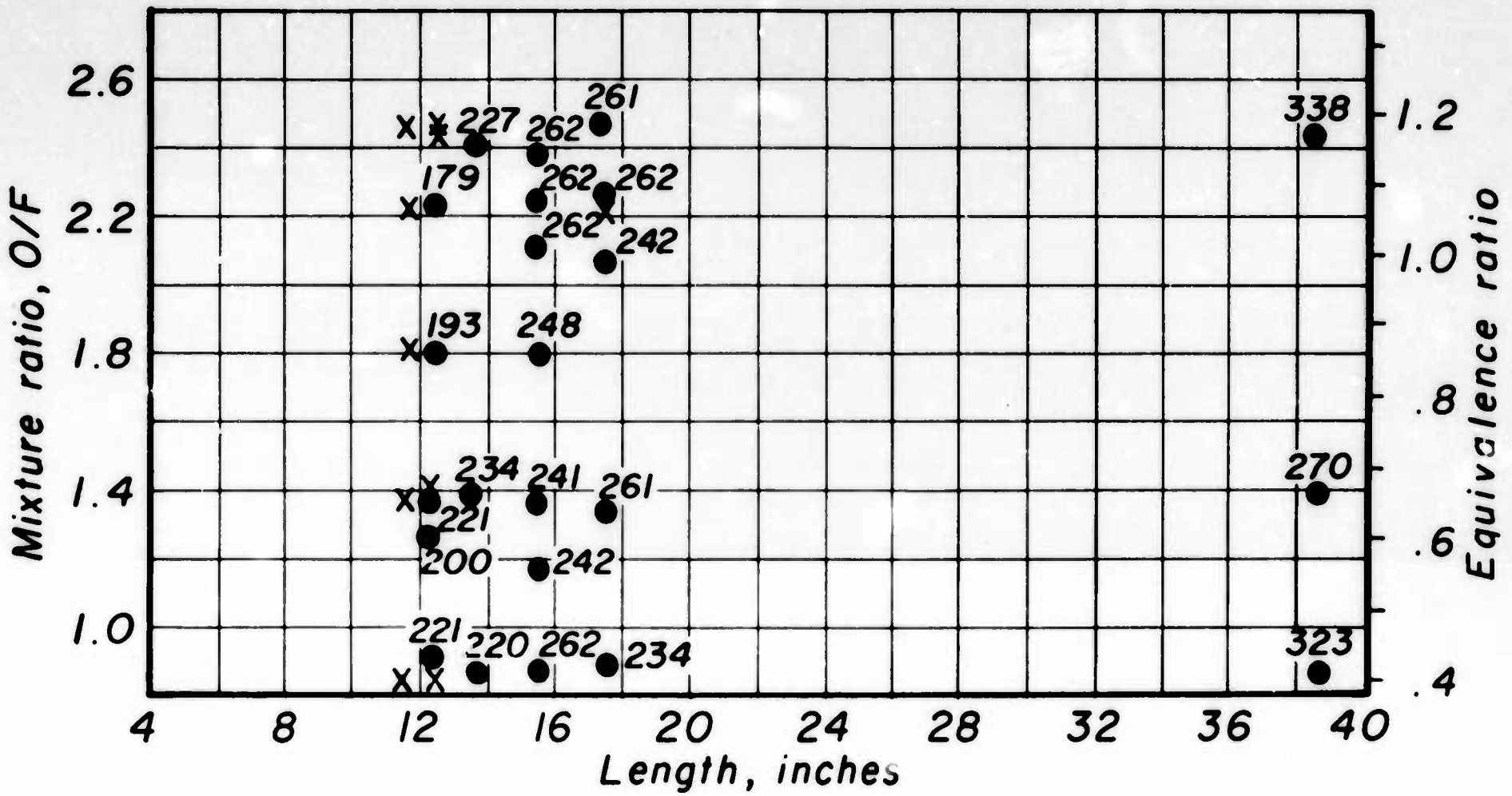

Key: ● = IL., x = stable

Figure II - 20

JPR 2183

Variable - length, square - motor, 4 spud Type IV (.120" dia.) injector,
800 lb thrust, 300 psia, non-pulsed
LOX - Alcohol

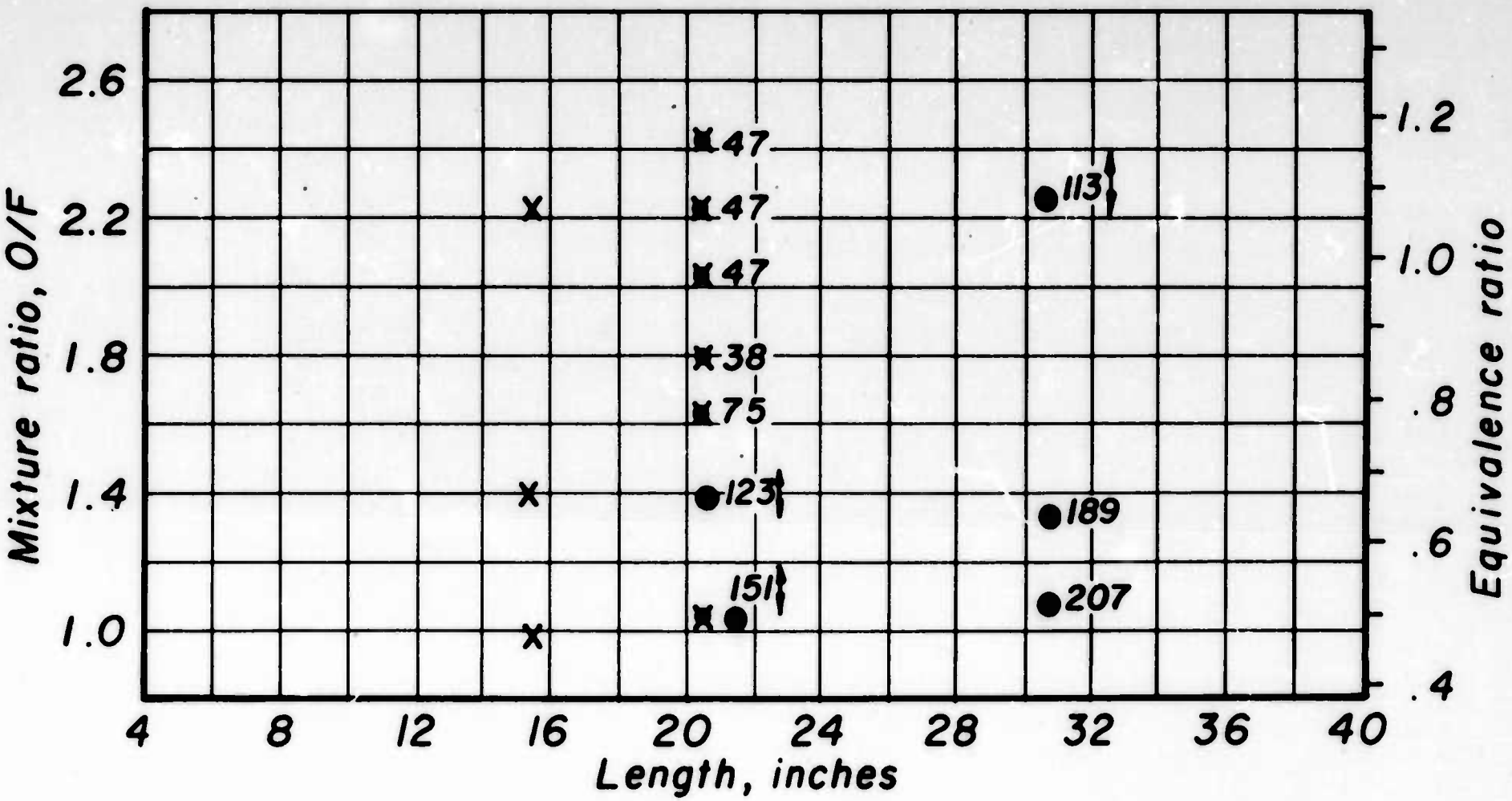

Key: ● = IL, x = stable, ✖ = in and out IL

Figure IV-21

Variable - length, square - motor, 4 spud L on L Type II injector,
800 lb thrust, 300 psia, limited pulsing
LOX, RP-1

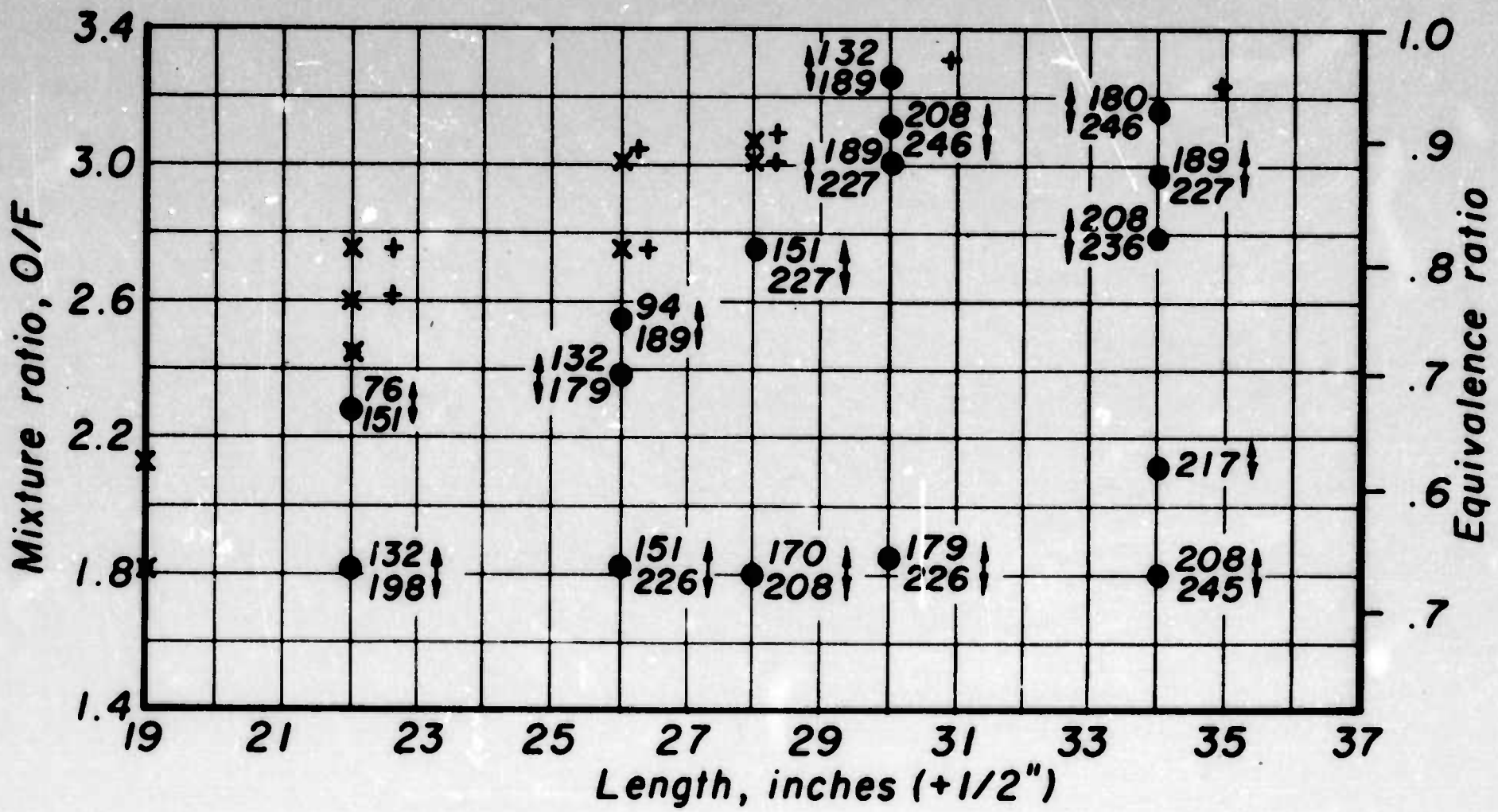

× Stable, ● IL, ✖ I & O IL, + Pulsed 30 - 10.1 K nozzle-end
↕ Max. amplitude, frequency and amplitude oscillating

Figure IV-22

Variable - length, square - motor, 4 spud L on L Type IV injector,
800 lb thrust, 300 psia, limited pulsing
LOX, RP-1

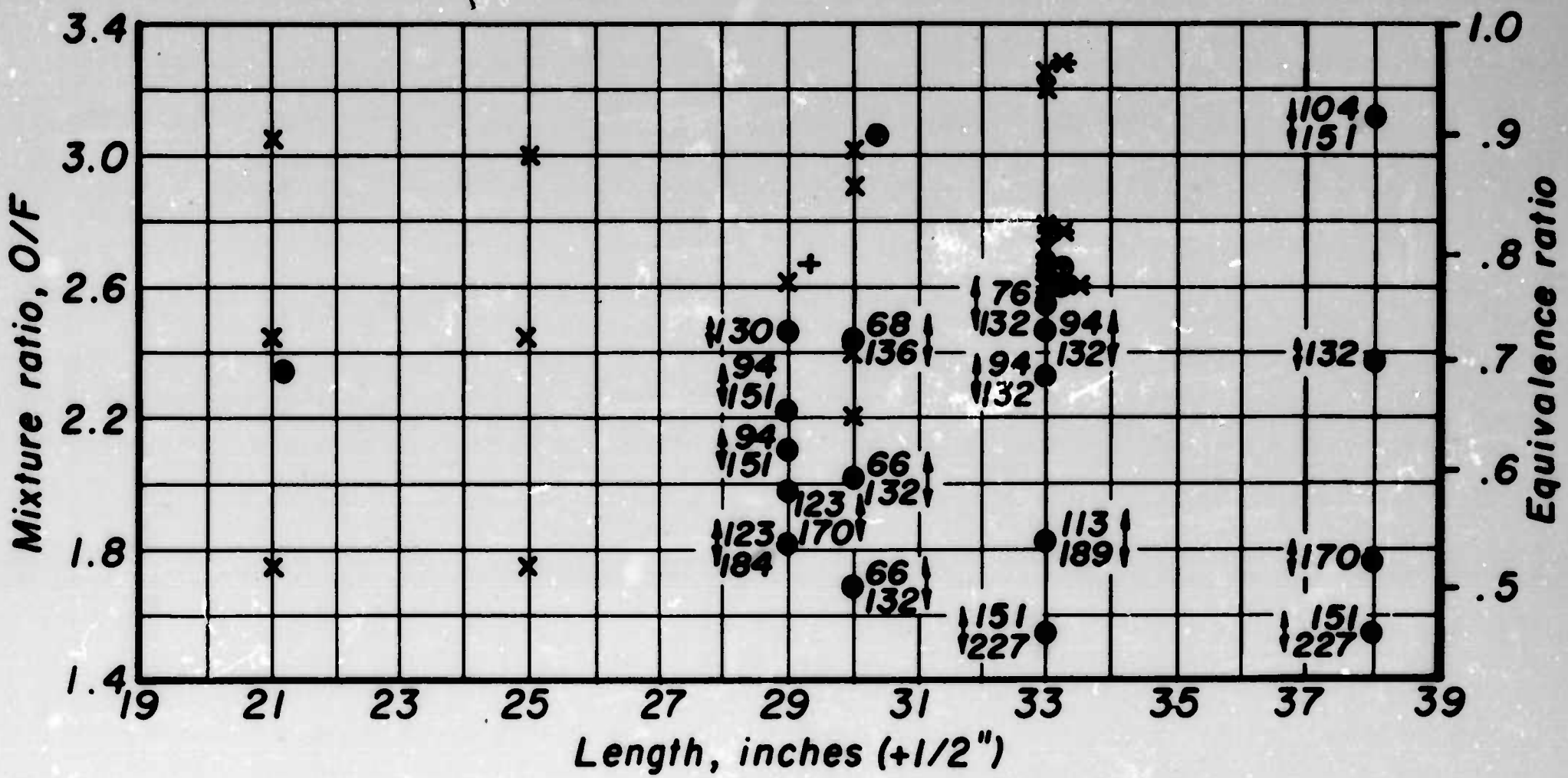

× Stable, ● IL, + Pulsed 30-10.1K nozzle-end,
✱ Pulsed 15-1K nozzle-end, ◉ Pulsed 15-1K injector-end,
⟊ Max. amplitude, frequency and amplitue oscillating

Figure IV-23

Performance vs chamber length for the Type IV - 4 spud injector with LOX orifices of .12 and .17 inches diameter

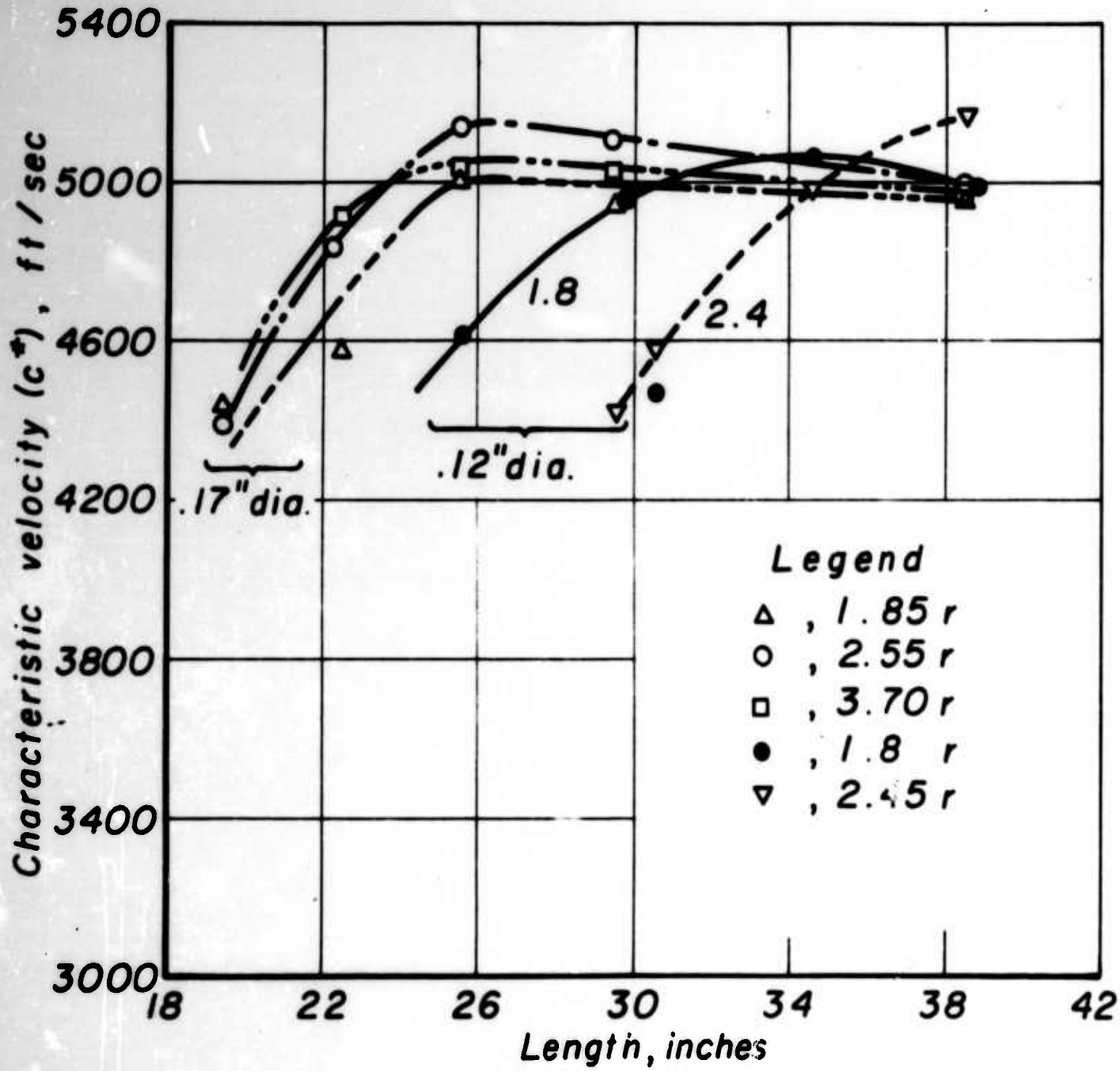

R 2403

Schematic of "Pseudo" rocket motor

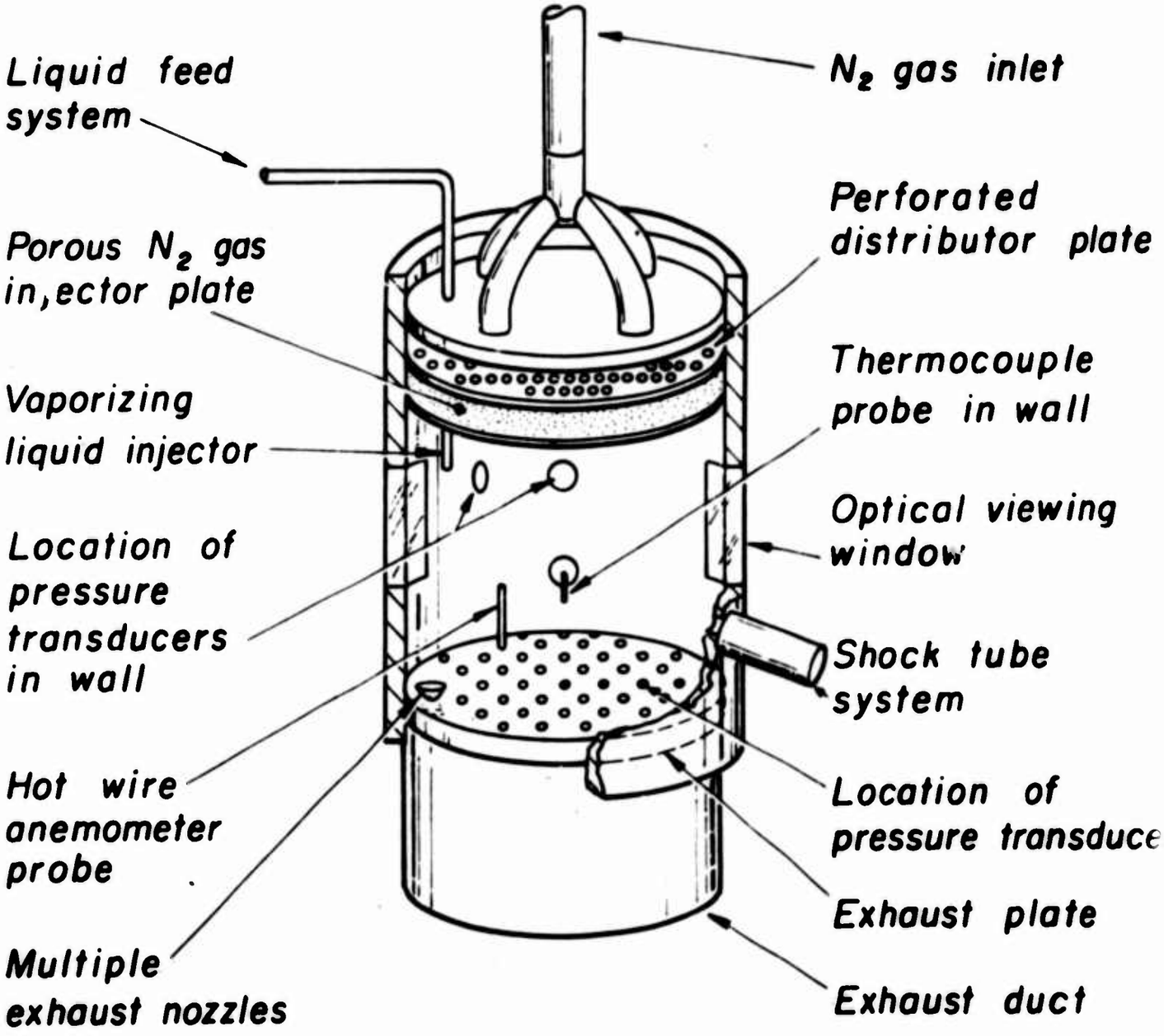

Figure IV - 25

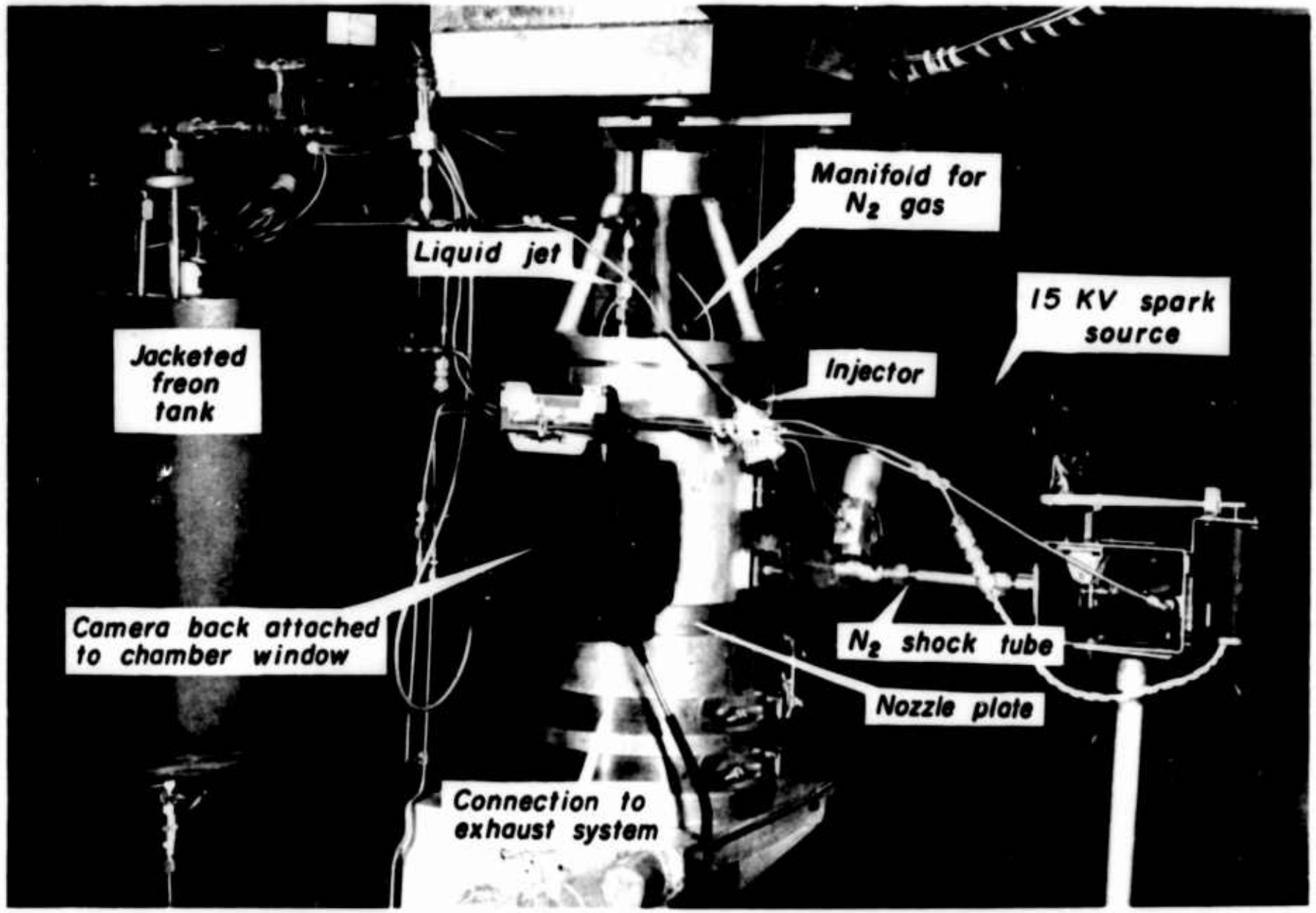

"Pseudo" rocket motor for vapor displacement studies

Figure IV-26

JPR 2405

Oscillographic record of vapor displacement test

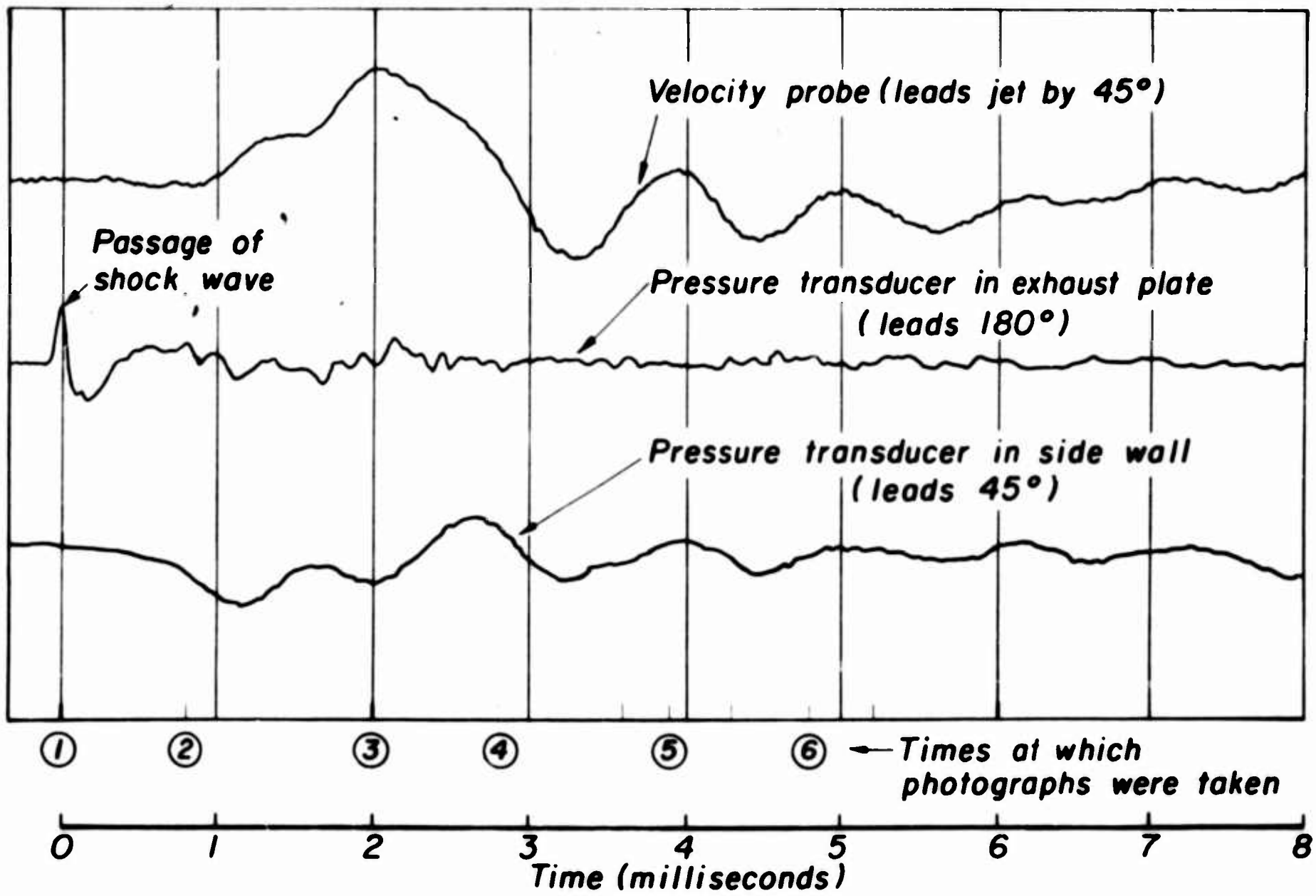

Figure IV-27

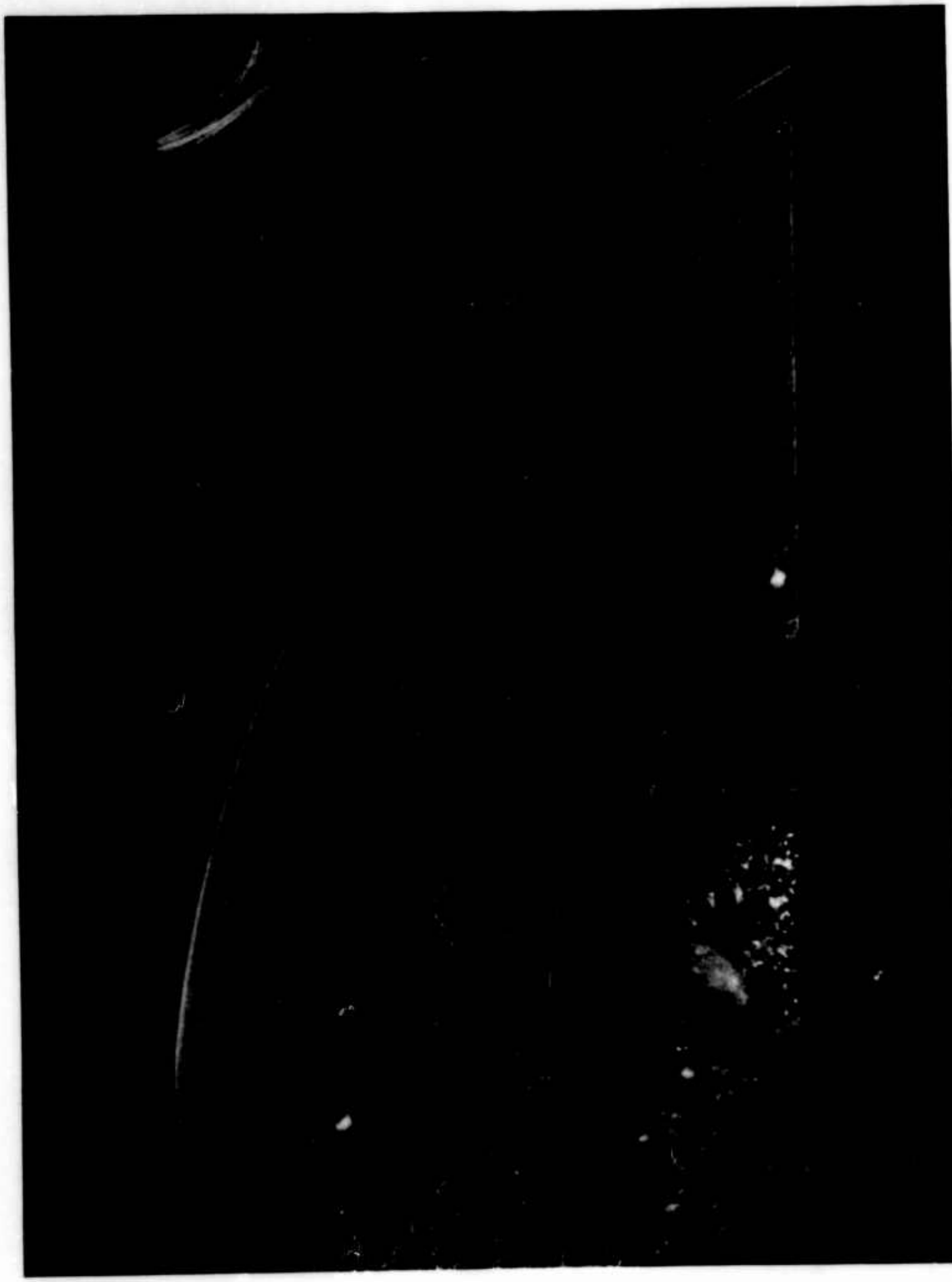

Figure IV-28

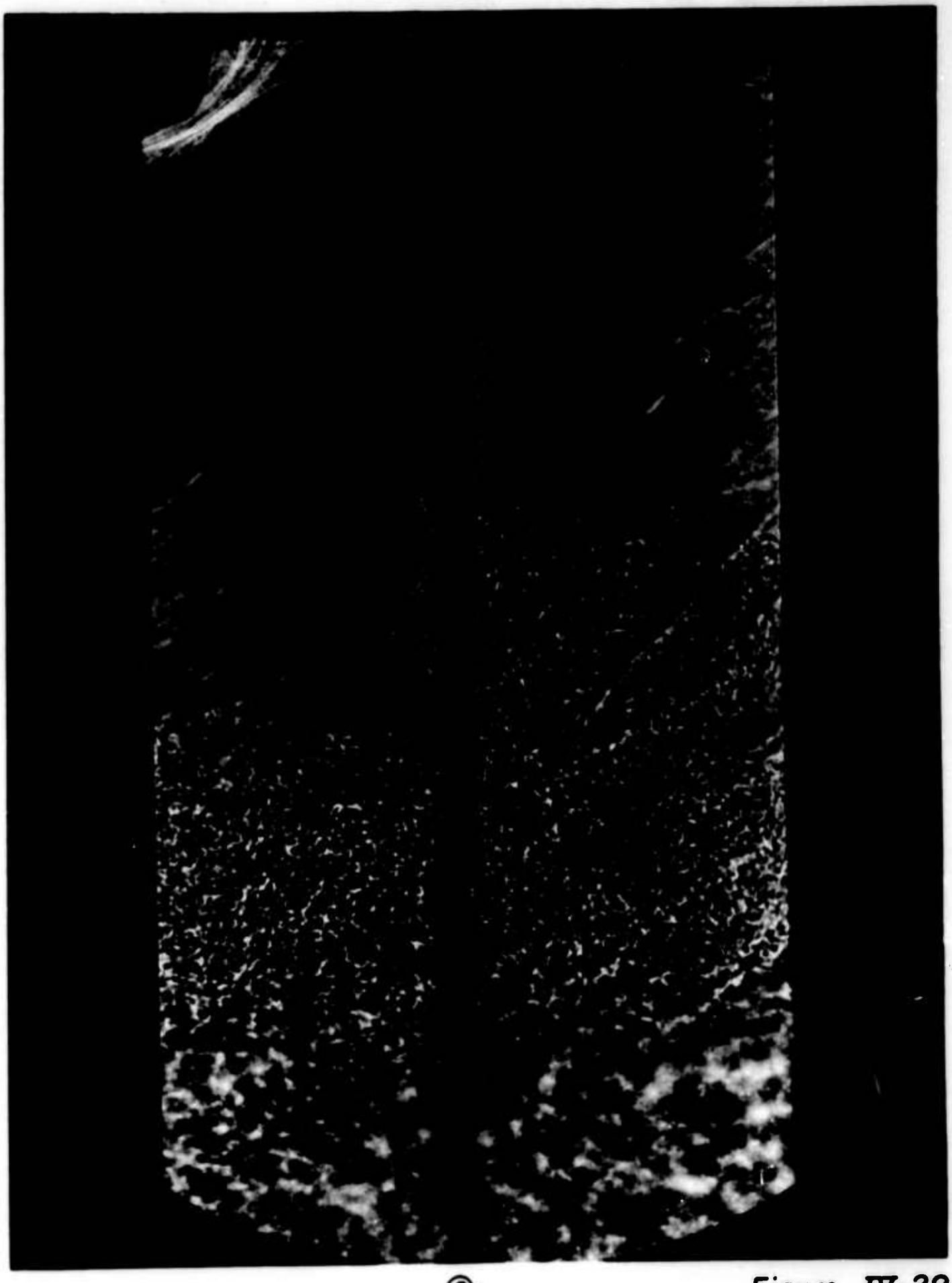

Figure IV-29

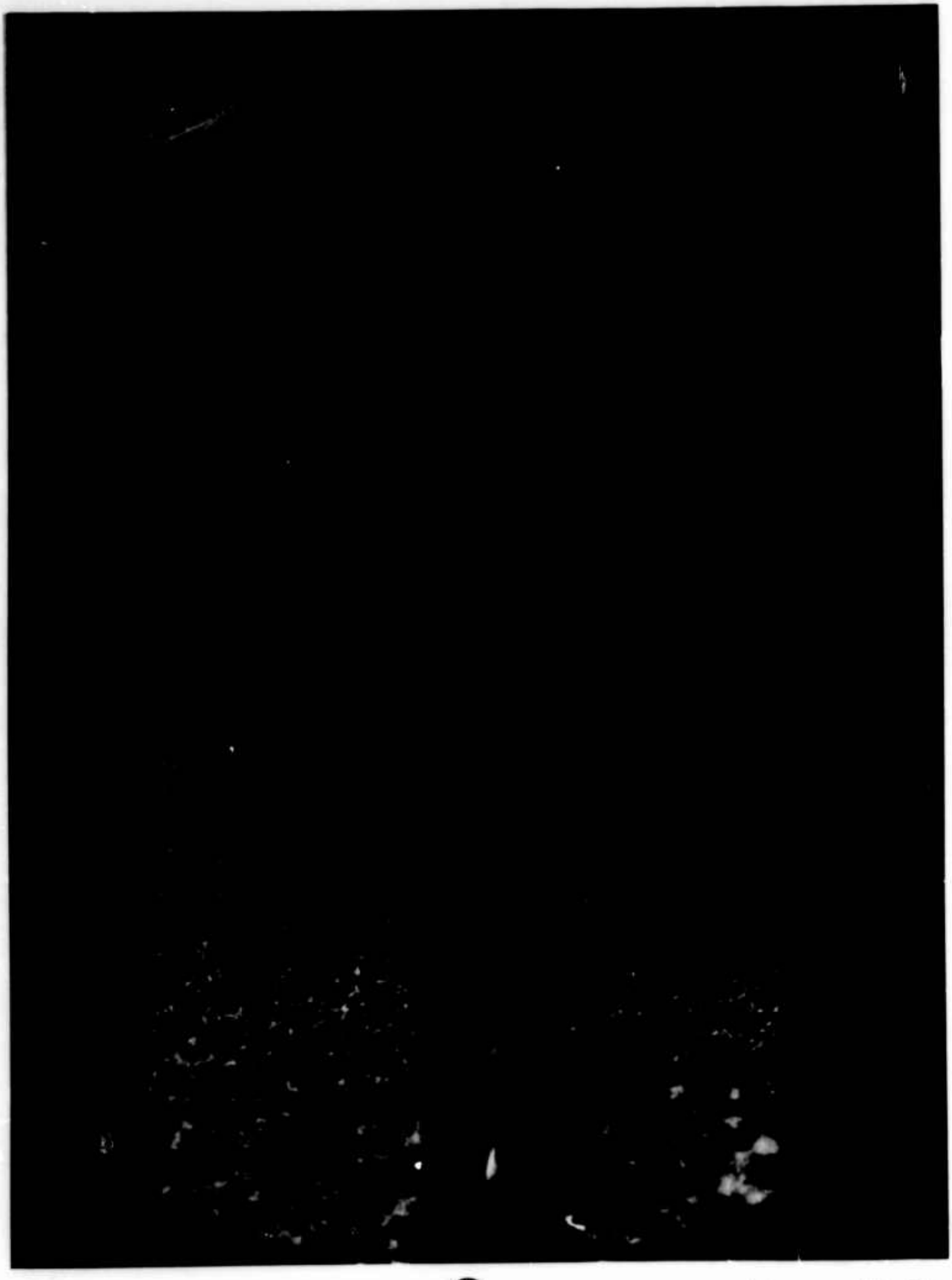

③

Figure IV-30

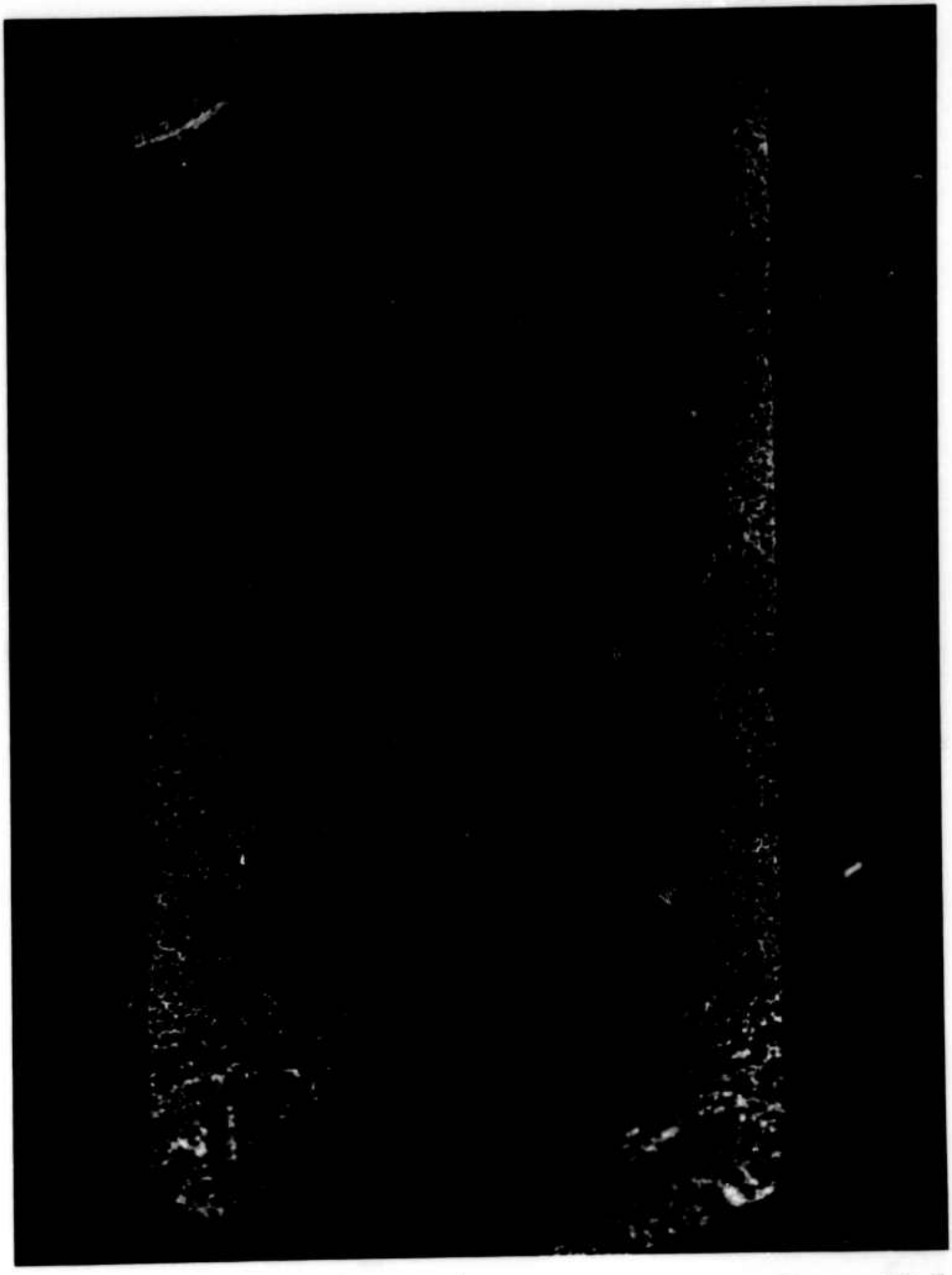

④

Figure IV-31

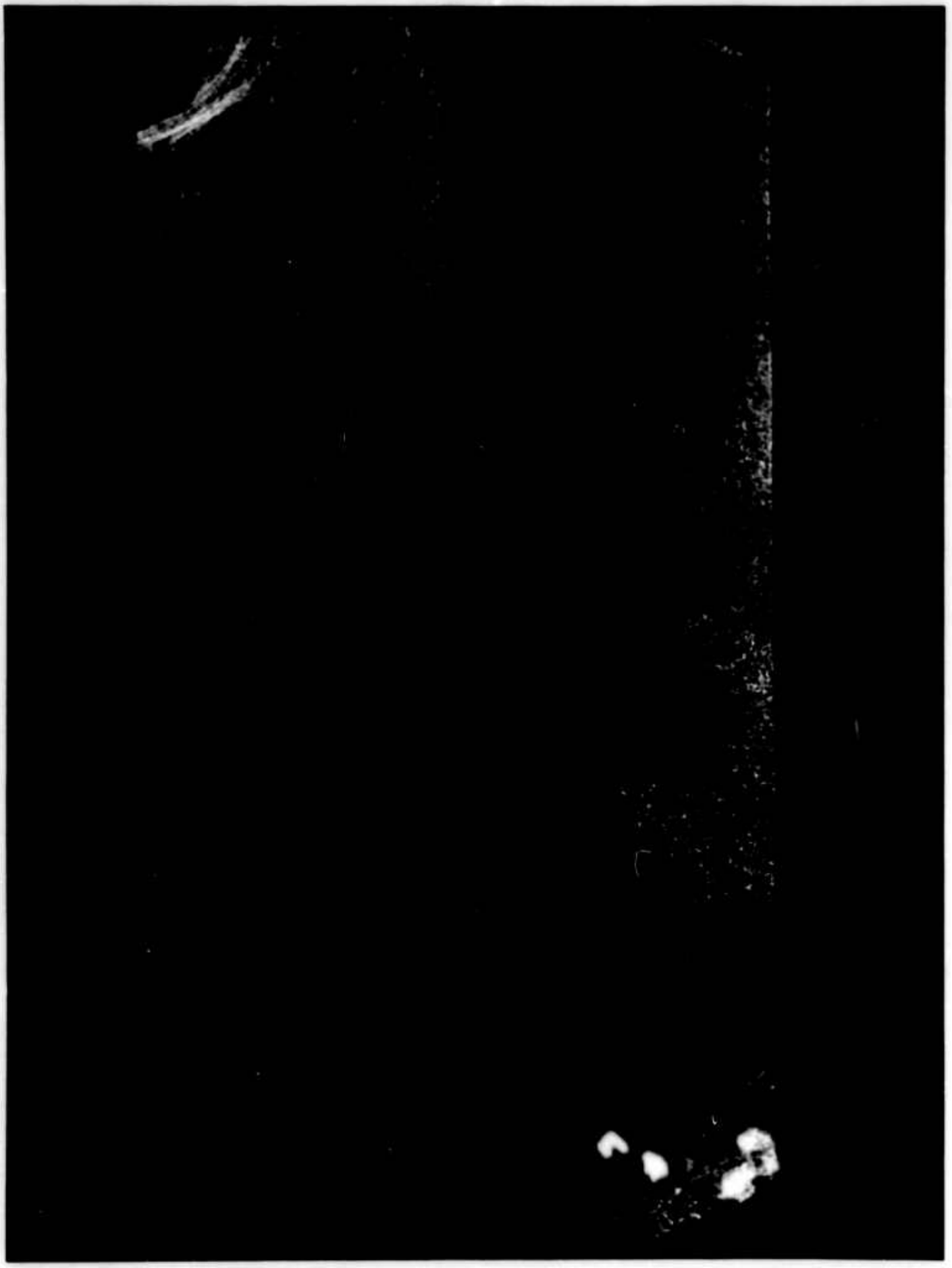

⑤

Figure IV-32

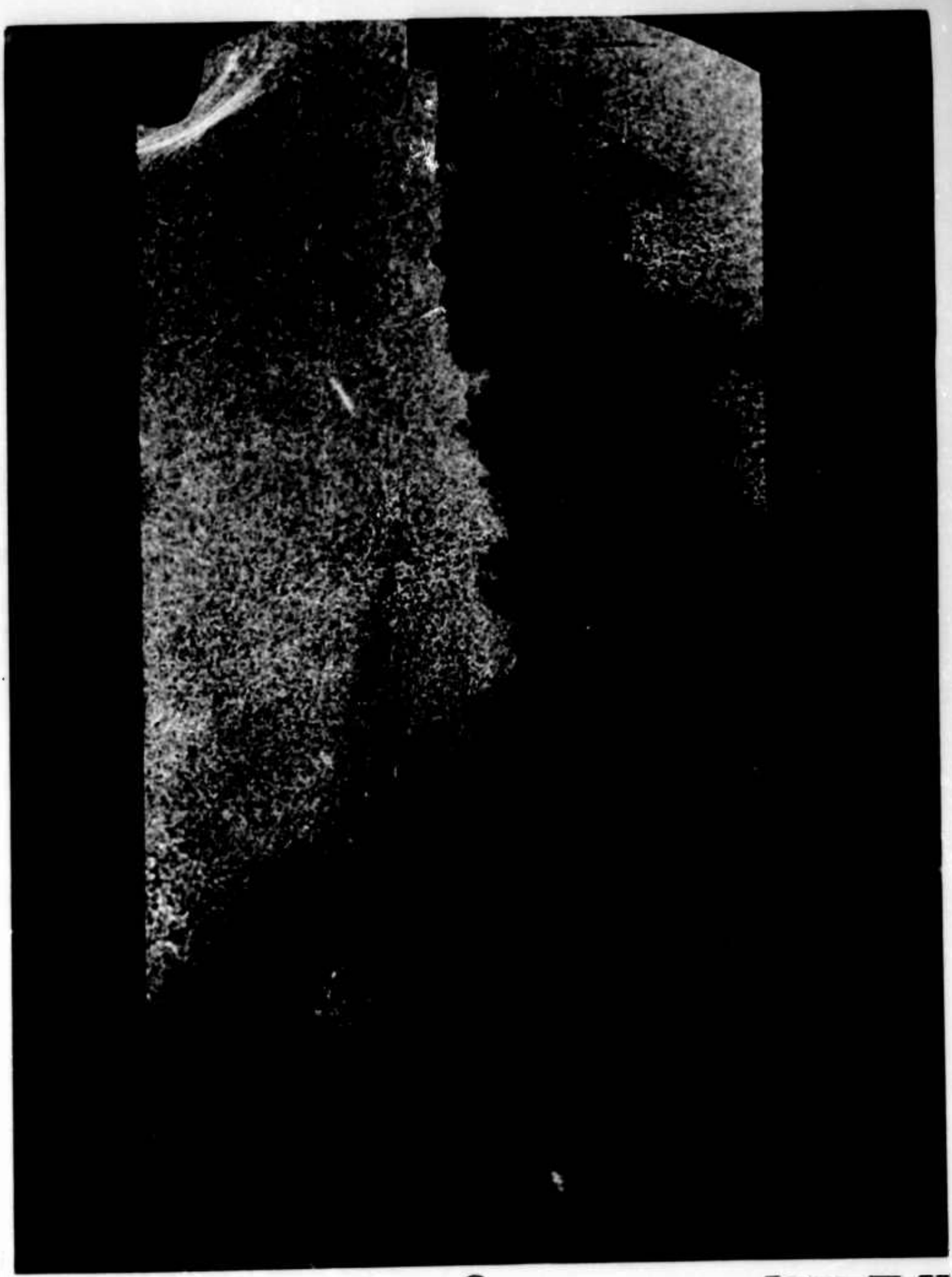

⑥

Figure IV-33

Schematic of resonating chamber

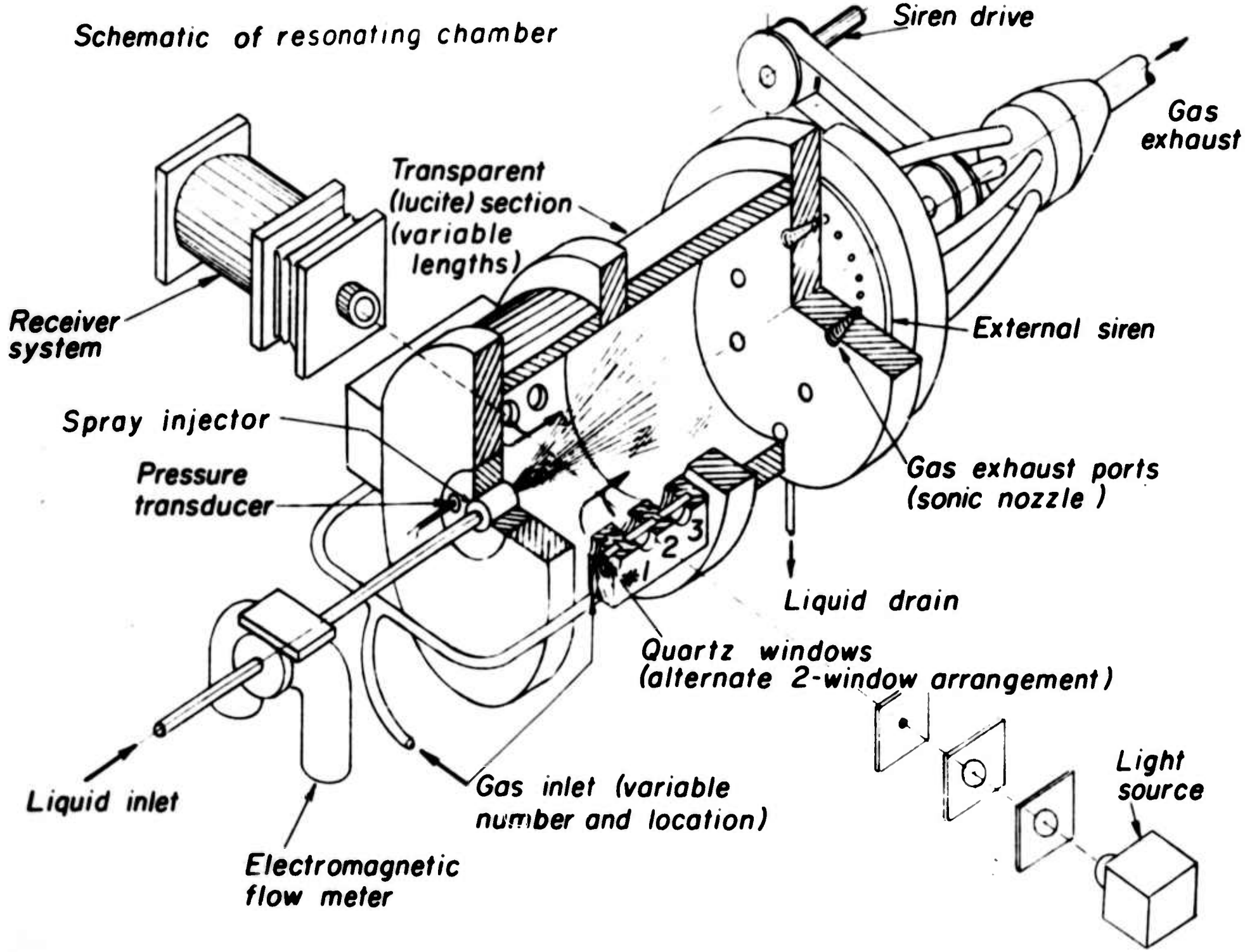

Figure II-34

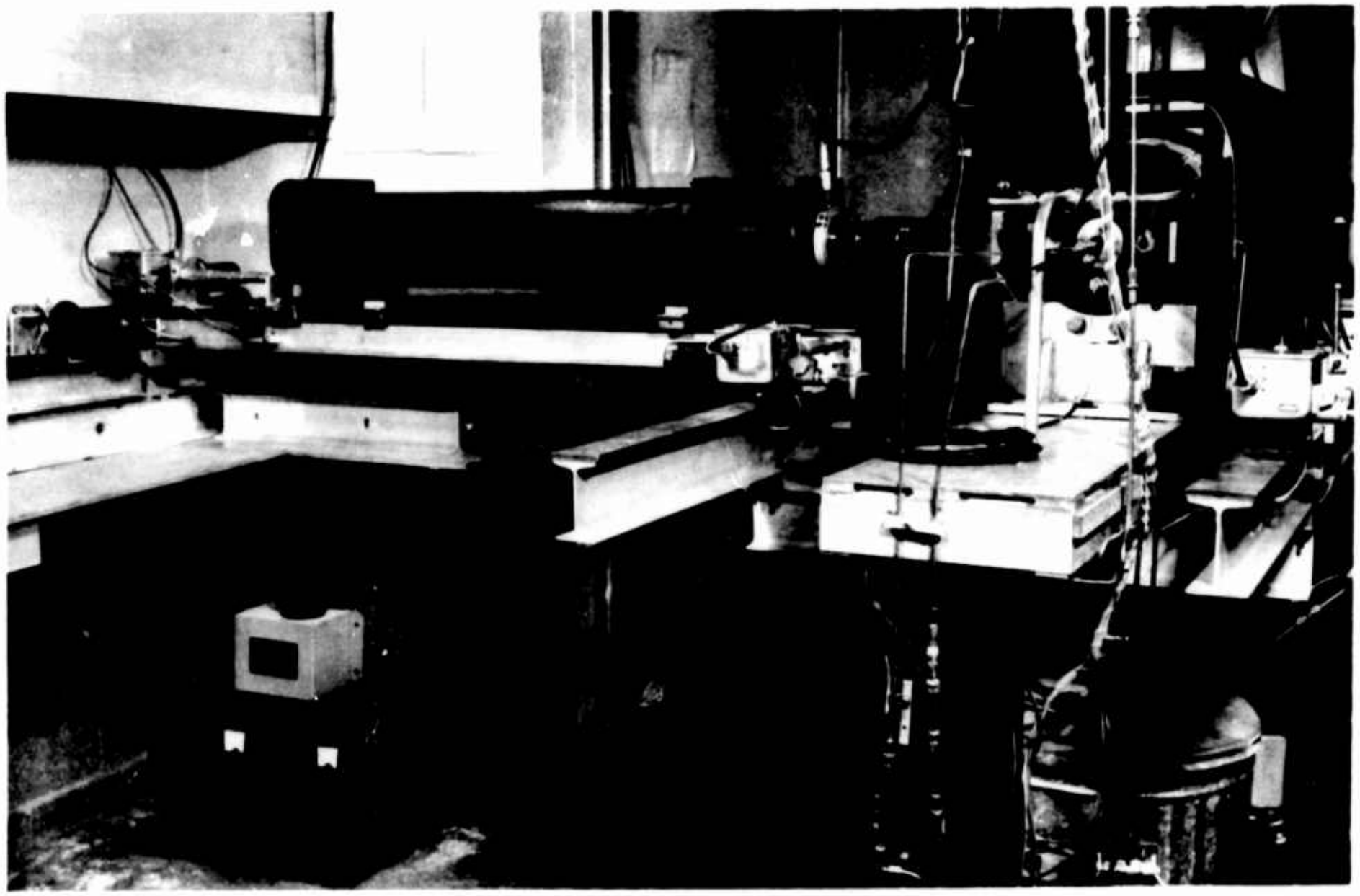

Resonating chamber, light receiving, & light source systems

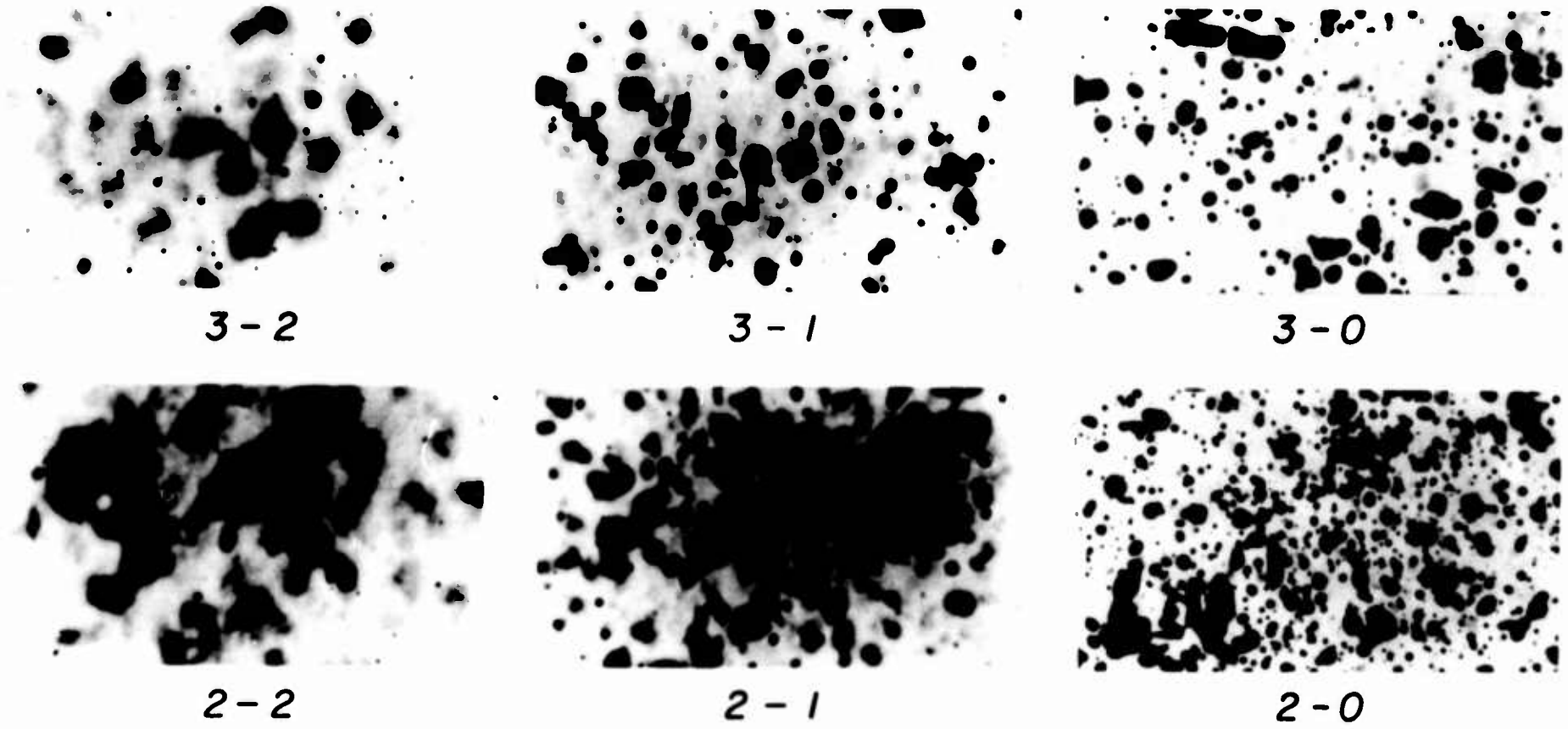

3-2 3-1 3-0

2-2 2-1 2-0

1-1/2 1-0

Legend

See Figure IV-34 for window numbers

1-2 indicates window no. 1, 2" from the ℄ of spray

Typical steady-state photomicrographs of drop distributions, magnification 5 ×

Drop-size distributation curves resulting from various data processing methods

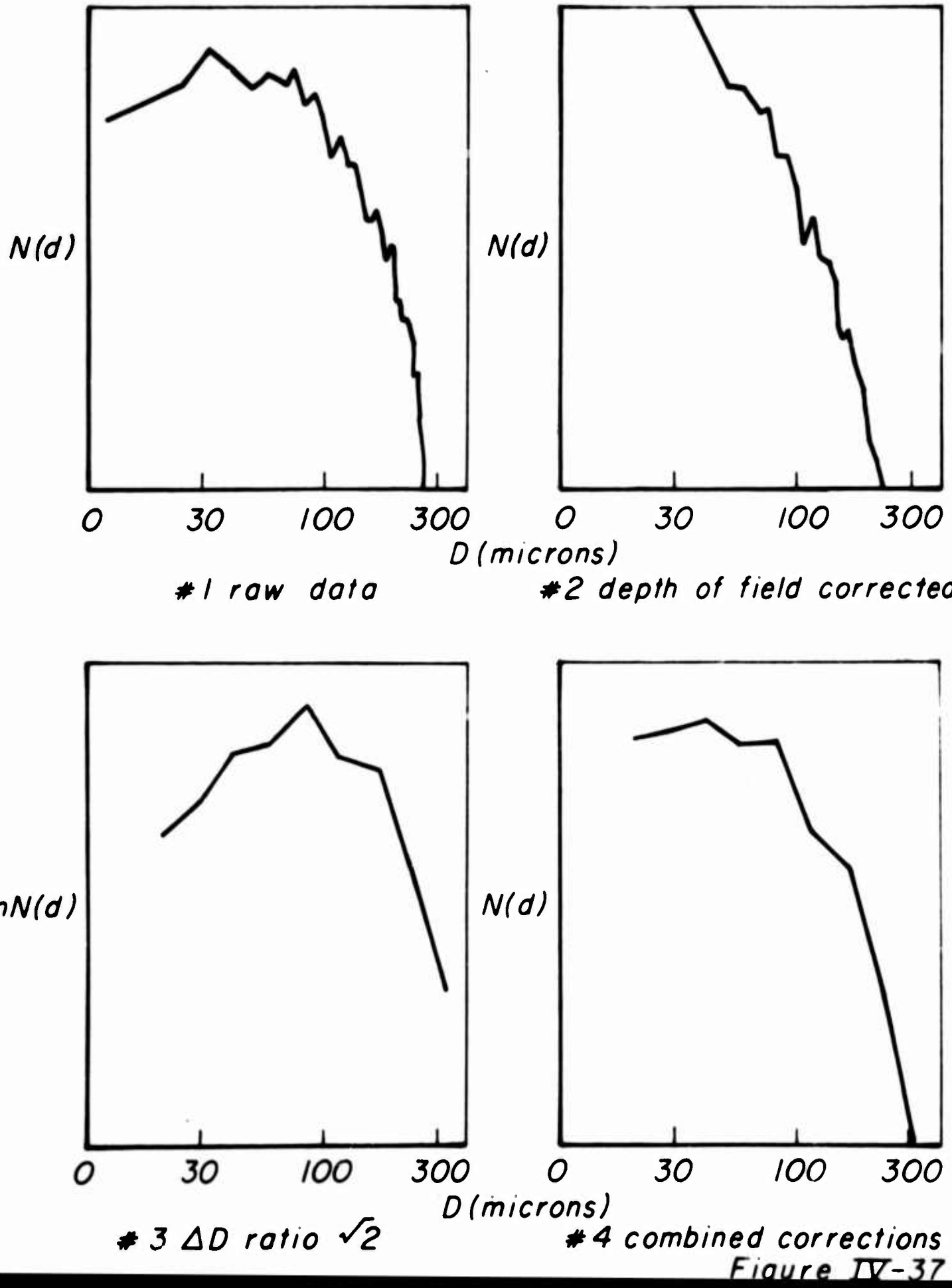

Figure IV-37

Table I

Inject dia	Smaller mode mean dia (microns)	Larger mode mean dia (microns)	Ref
.089	180-190	500-700	3
.060	65	200	3 & 4
.040	33	73	—

Table II

	D30 (microns)		
	Raw data	Δ_s Corrected	
Nukiyama-Tanasawa Expression	77-90	50-70	
Empirical Equation			196
$\frac{\Sigma nd^3}{\Sigma n}$	118	82.4	

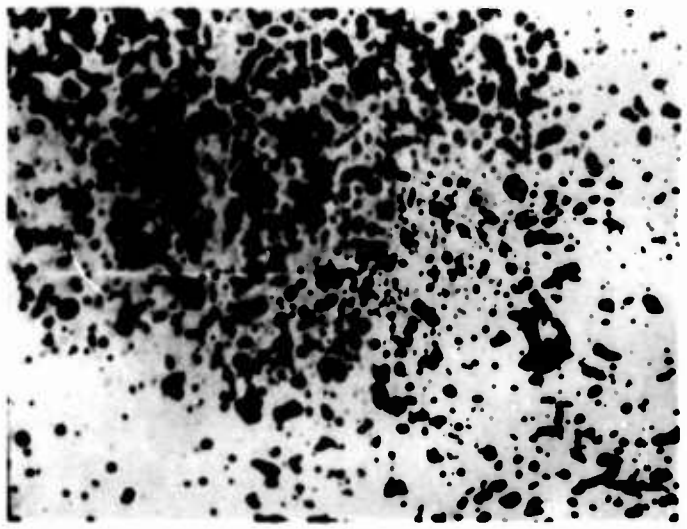

C

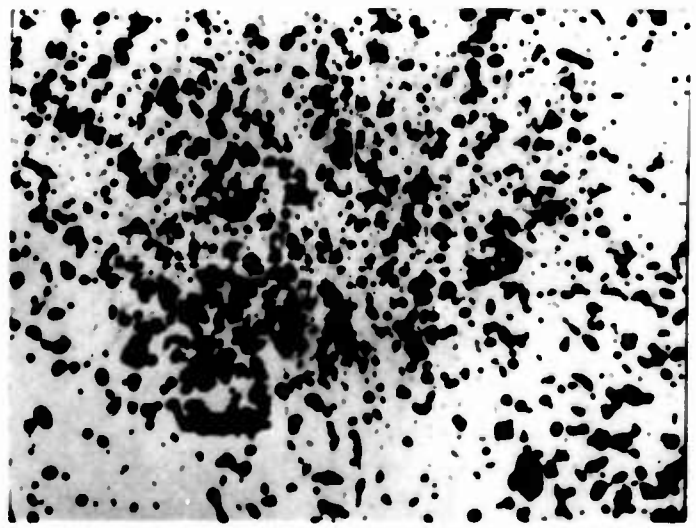

D

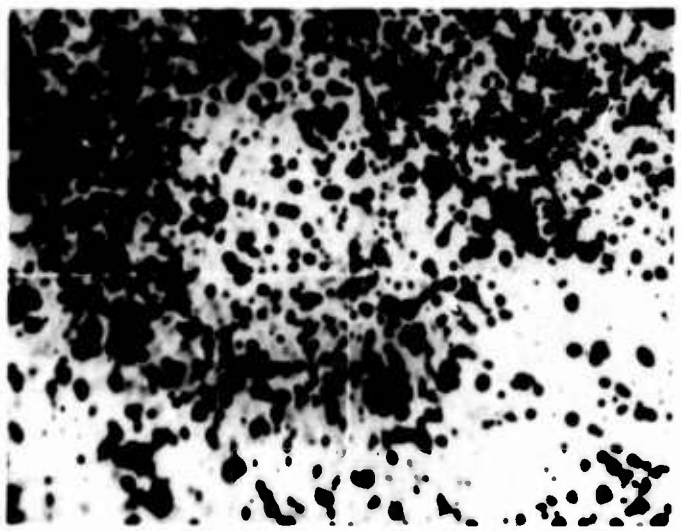

A

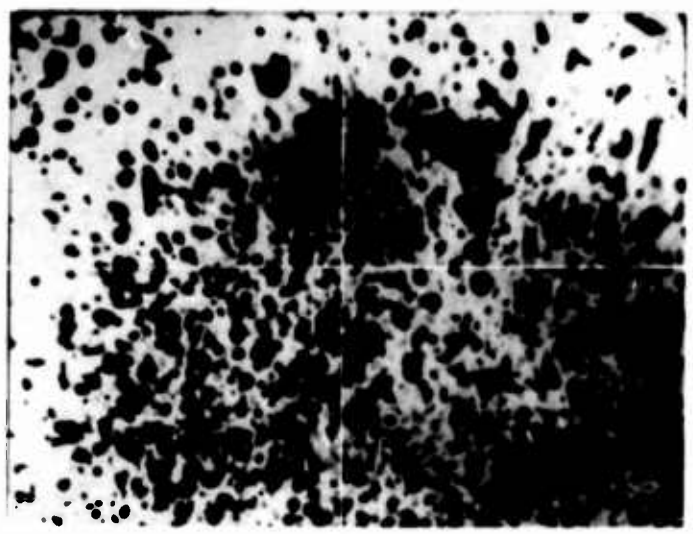

B

Magnification 5X

Frequency 500cps, .040" diameter, 90° impinging jet injector, chamber pressure 100psig, injection pressure drop 50psi, 2 1/8" downstream of the injector face

Typical photomicrographs of spray in oscillating flow field

JPR 2408

Number-size distributions based on photographs shown on Figure IV-39
Preliminary data

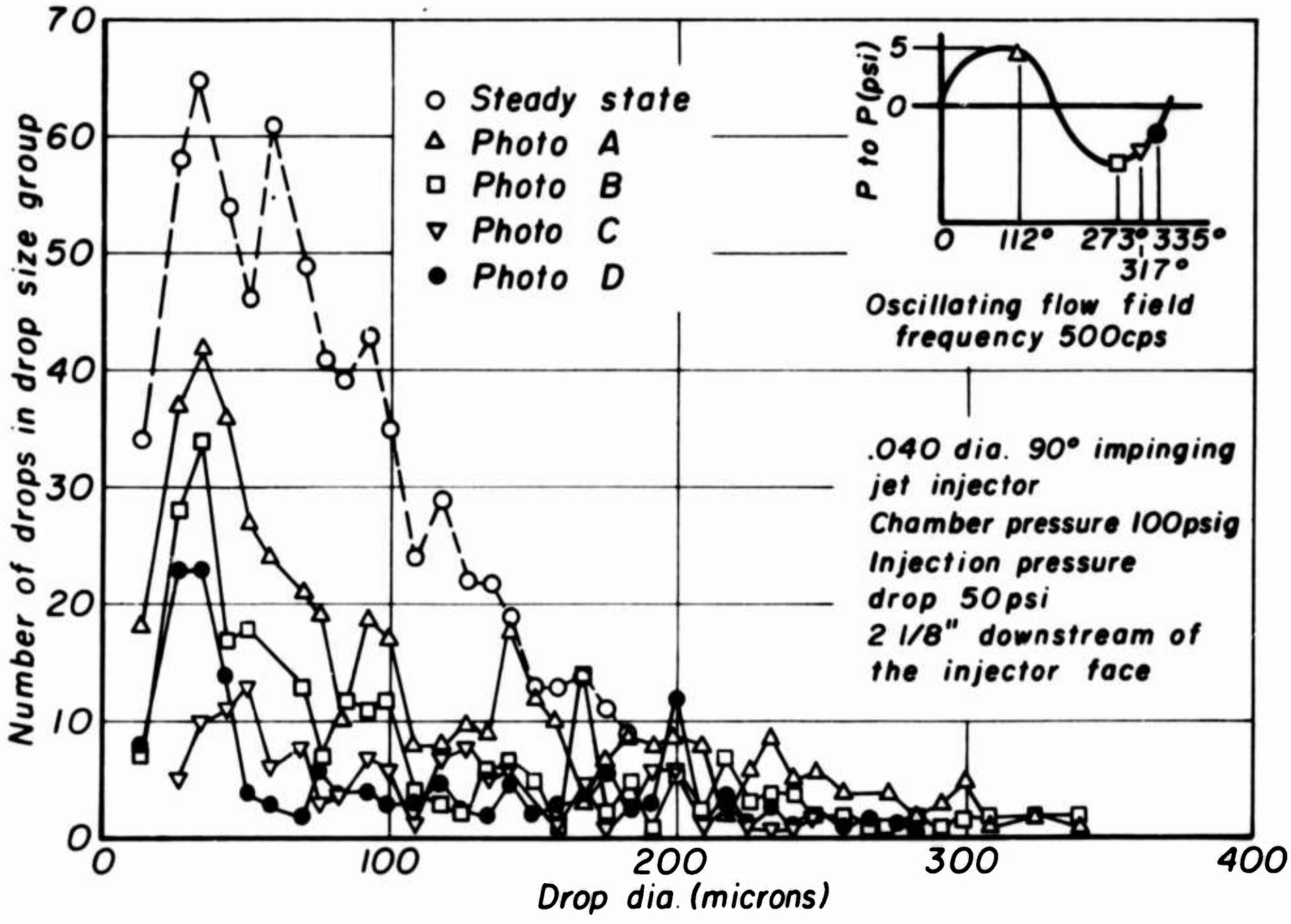

Figure IV-40

Schematic of the burning droplet wake

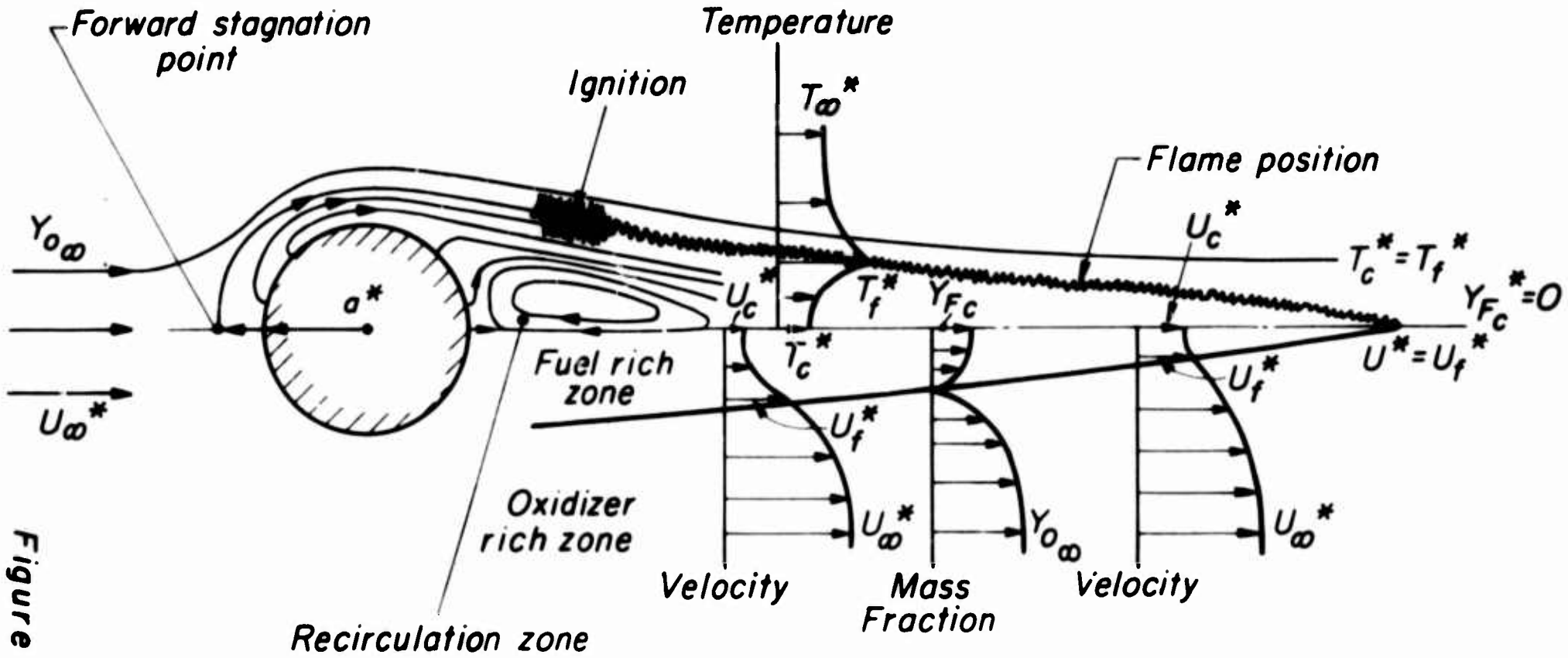

Figure IX - 1

Neutral stability line.
Frequency vs. interaction index

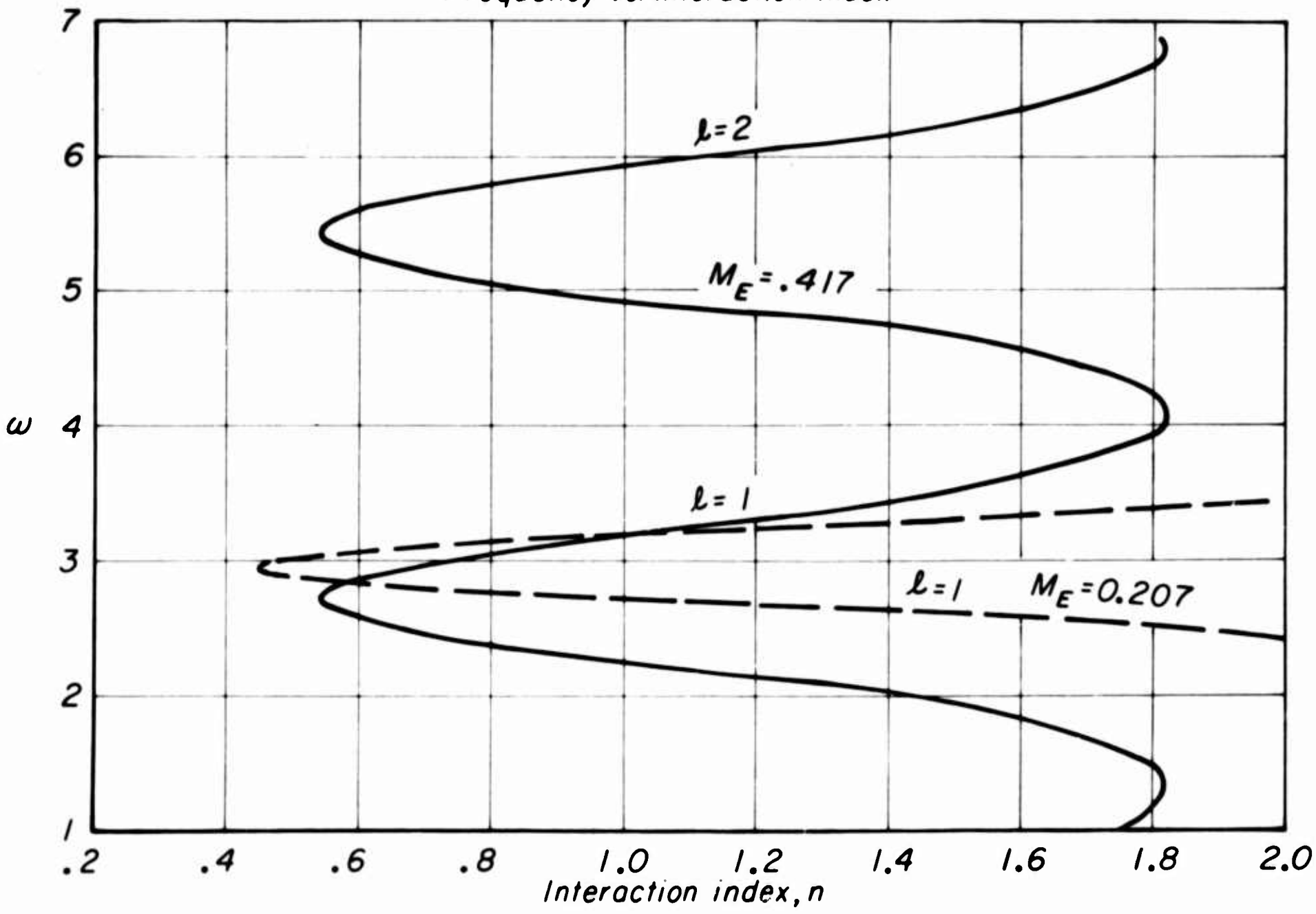

Figure III - 1

Neutral stability line.
Frequency times time-lag vs. interaction index

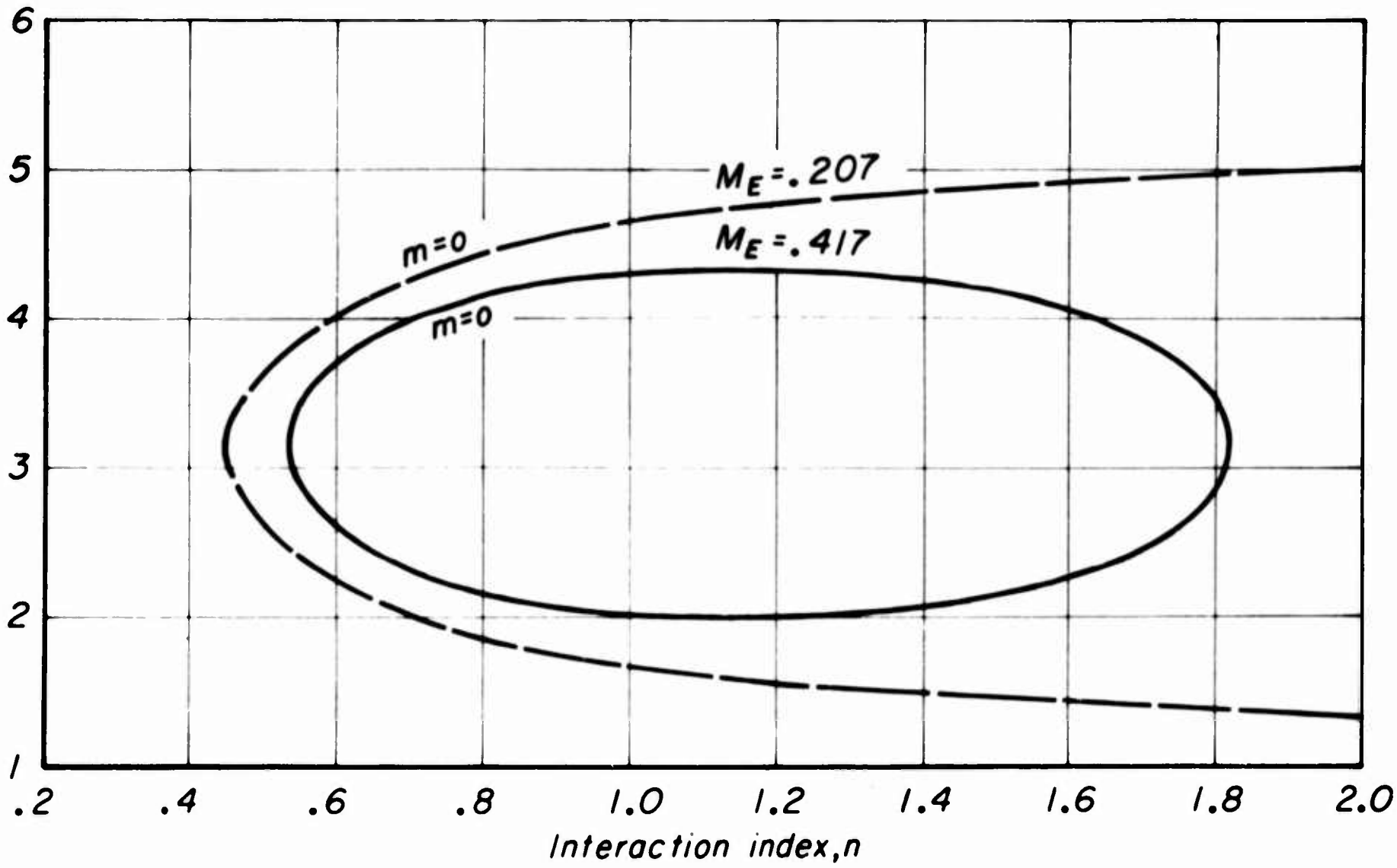

Figure II-2

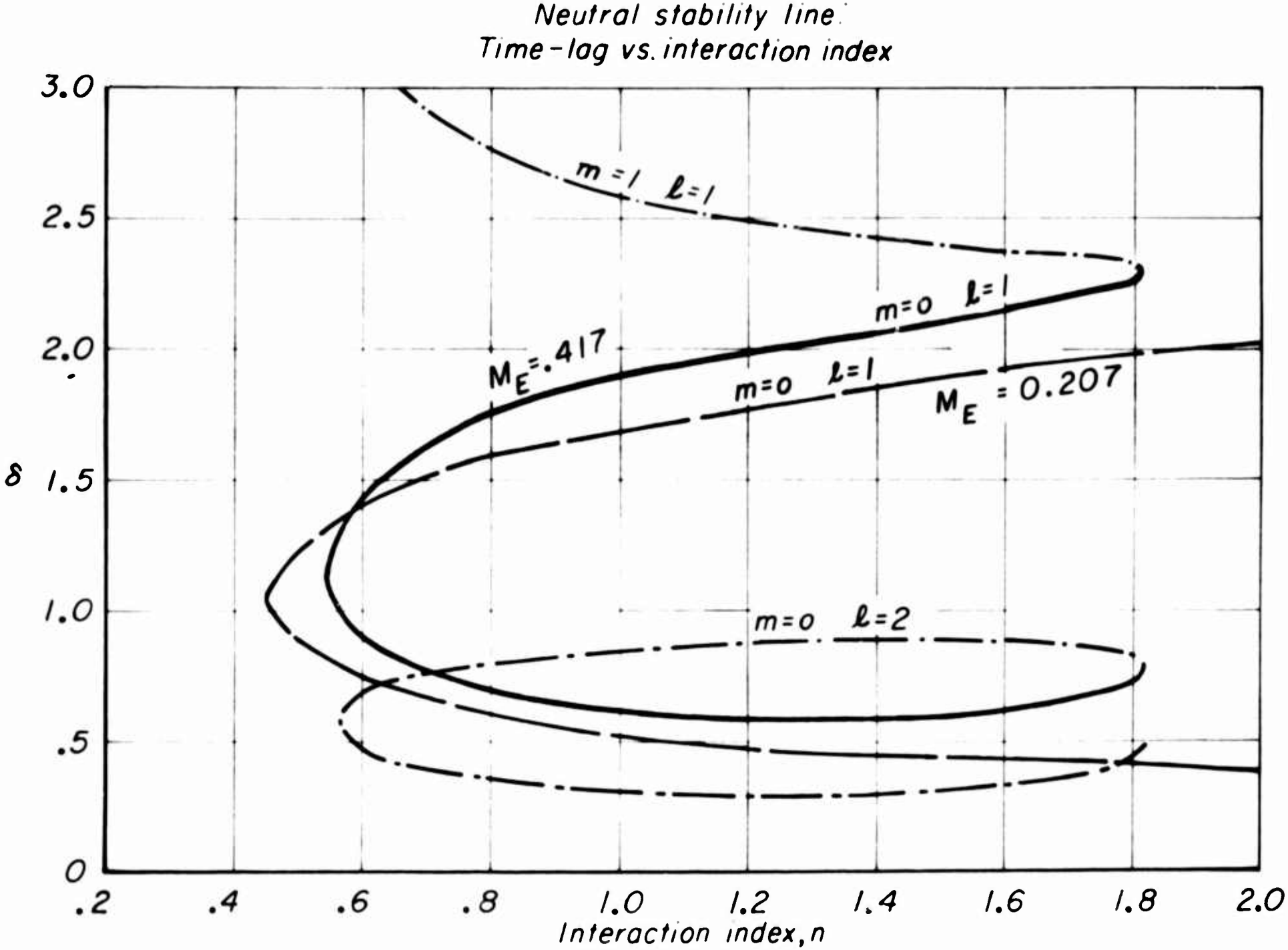
Neutral stability line
Time-lag vs. interaction index
3.0
2.5
2.0
1.5
1.0
.5
0
δ
m = 1 ℓ = 1
m=0 ℓ=1
M_E = .417
m=0 ℓ=1
M_E = 0.207
m=0 ℓ=2
.2
.4
.6
.8
1.0
1.2
1.4
1.6
1.8
2.0
Interaction index, n

Figure II - 3

Geometrical configuration

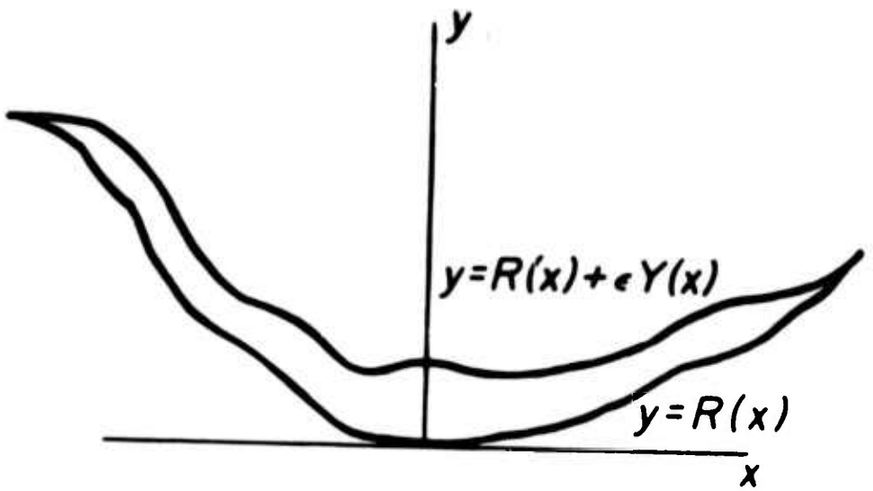

Figure B1

A possible baffle configuration

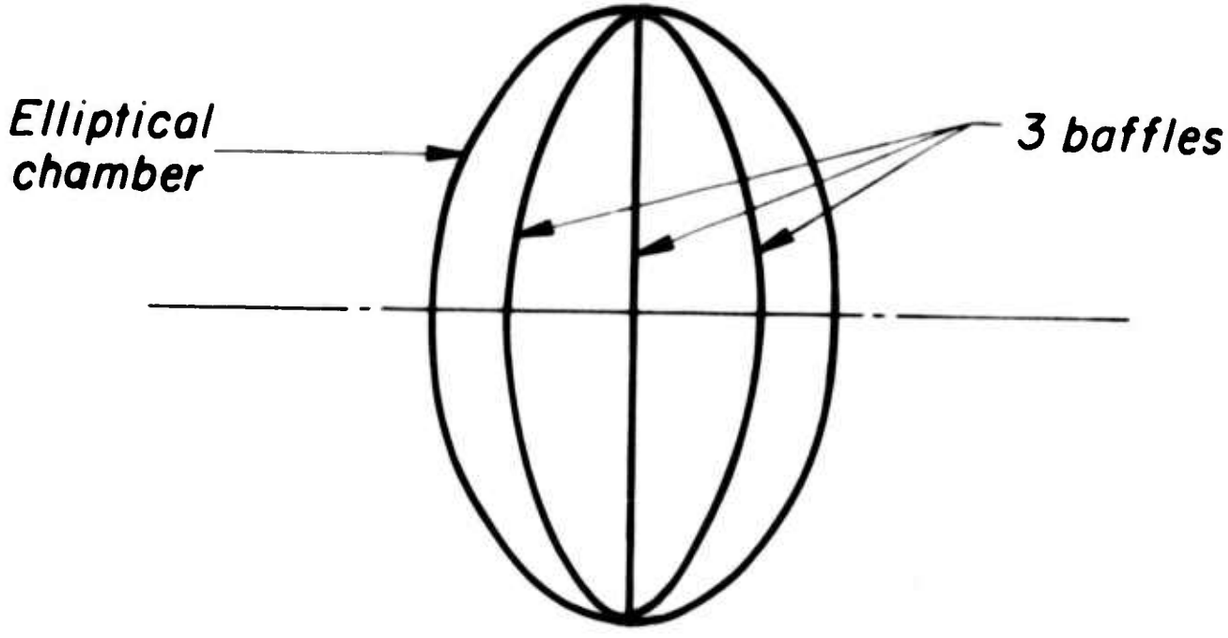

Figure B2